High Inclination X-Ray and Cataclysmic Binaries

by

T. Naylor

St. John's College
Oxford

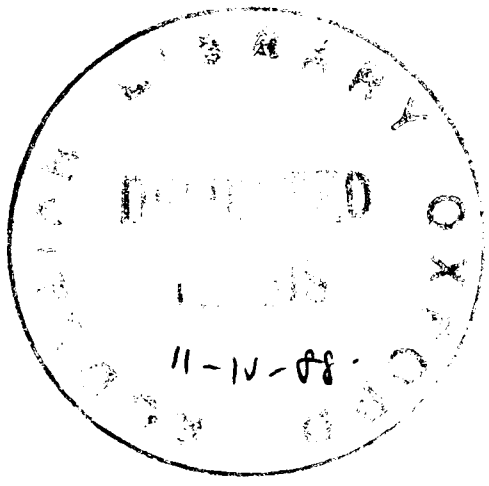

A thesis submitted to the University of Oxford in partial fulfilment of the requirements for the degree of Doctor of Philosophy.

Michaelmas Term 1987

To my parents, and others like them, whose profession is not astronomy, but who still find time to take in interest in the stars. Their enthusiasm helps make astronomy worthwhile.

High Inclination X-Ray and Cataclysmic Binaries

Timothy Naylor

St. John's College
Oxford

A thesis submitted to the University of Oxford in partial fulfilment of the requirements for the degree of Doctor of Philosophy.

Michaelmas Term 1987

Abstract

An introduction is given to the fields of X-ray and cataclysmic binaries, low mass X-ray binaries (LMXBs) and globular clusters. New observations of the W Vir star AC5 (=V86) are used show that it is probably the source of Hα emission previous authors have found in core of the globular cluster M15.

The first phase resolved optical spectroscopy of AC211, the optical counterpart of the X-ray source in M15, are presented, and its binary period discovered to be 9.1±0.5 hours. A re-analysis of archive ultraviolet (UV) spectra of M15, shows spectral features which are attributed to AC211. These observations are combined with those of other authors, to prove AC211 is probably an "accretion disc corona" (ADC) source.

After reviewing the superoutbursts of the SU UMa class of dwarf novae, X-ray, UV, optical and infrared observations of the SU UMa star OY Car are used to show that during superoutburst there is extensive vertical structure in its accretion disc, similar to that in the ADC and "dipping" LMXBs. Archive UV data from the 1978 outburst of WZ Sge shows that it had similar vertical structure. UV observations presented of EX Hya during a bright outburst may have the same explanation. From the OY Car data, a temperature and area for the region which produces the "superhump" light are derived, of 8 000K and $\sim 10^{20} cm^2$, respectively. It is found that during OY Car's superoutburst, the size of the O-C variations of the eclipse timings are significantly smaller than was previously thought, and that it has an extended X-ray source whose size is comparable to the binary separation.

The results are discussed with respect to models of the superhump phenomena in SU UMa stars, and possible causes of vertical disc structure in X-ray and cataclysmic binaries.

Contents

Chapter 1

Introduction

1.1 The standard models

Accretion discs are one of the most active areas of research in modern astronomy. They are thought to play a part in processes as diverse as planetary formation and the powering of active galactic nuclei. The objects studied in this thesis are galactic binaries, where a white dwarf, neutron star or black hole accretes matter via an accretion disc from a companion star.

Figure 1.01 shows some typical geometries of interacting binaries where one of the stars is a compact object. A mass-losing star which fills its Roche lobe (see Kopal 1959 for a description of Roche geometry) loses matter through the inner Lagrangian point, forming a stream. If the compact object has a strong magnetic field the matter is channelled along the field lines onto the accreting star (figure 1.01c).

If the magnetic field is negligible, an accretion disc is formed around the compact object. The transferred matter moves through the accretion disc as it loses angular momentum via viscous forces (Shakura & Sunyeav 1973). The final stage of accretion, the transfer of matter from the inner edge of the disc to the compact object, is assumed to take place in a boundary layer, where the material acquires the angular velocity of the compact object (see, for example, Pringle & Savonije 1979).

The point where the stream impacts the disc is known as the bright spot (or occasionally, and rather misleadingly, as the hot spot). In some circumstances it has an anisotropic radiation pattern, such that light

(a)

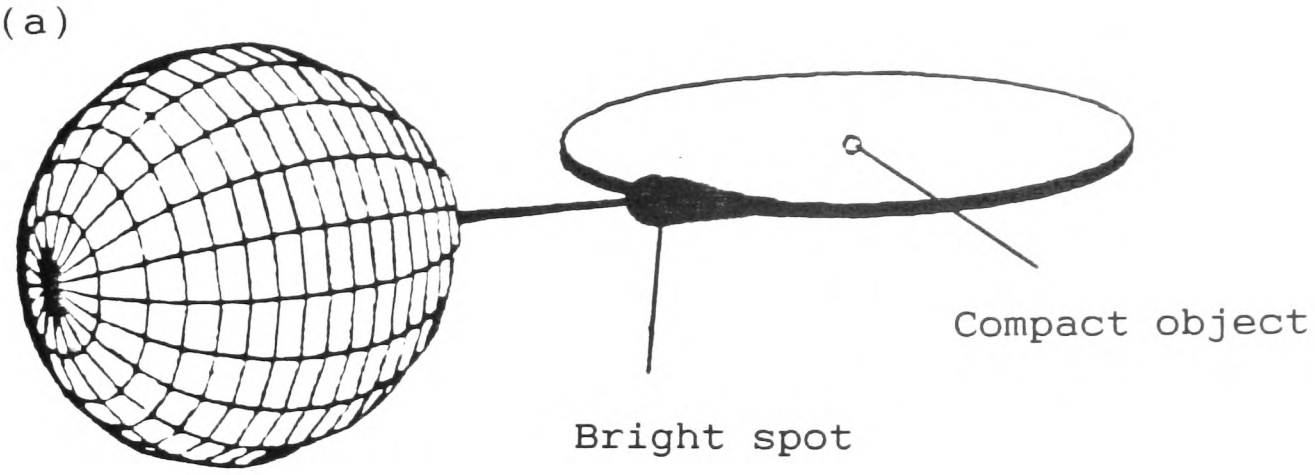

(b)

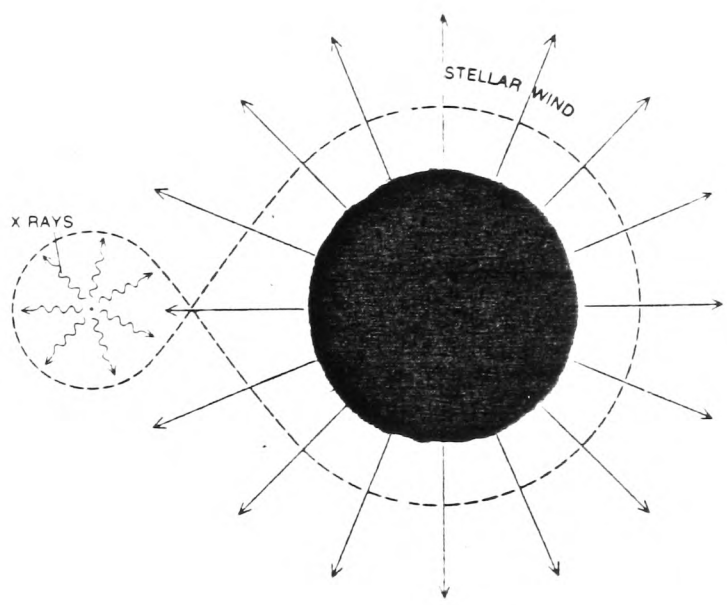

(c)

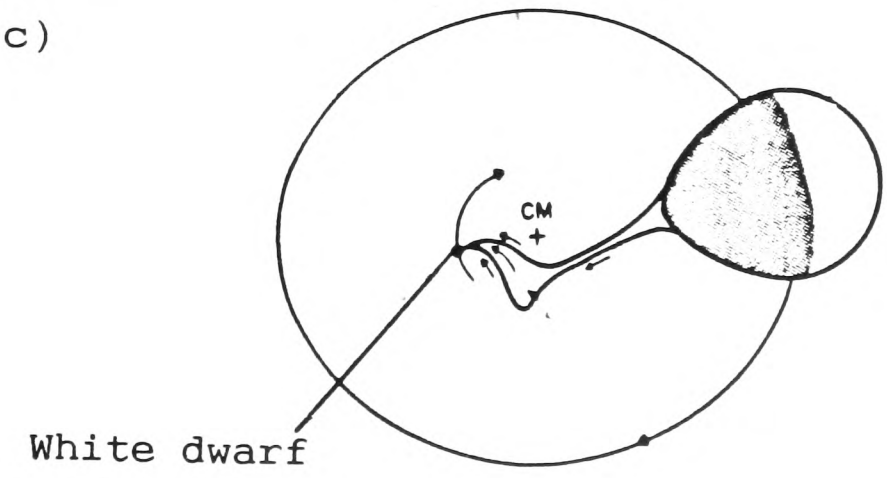

Figure 1.01 Typical geometries for X-ray and cataclysmic binaries.
a) A Roche-lobe filling secondary losing matter to a compact object via an accretion disc. This geometry is typical of cataclysmic variables and low mass X-ray binaries. (From an original by K. Horne.)
b) A massive X-ray binary where the mass losing star does not fill its Roche-lobe, but loses matter via a powerful wind. (From Gursky & van den Heuvel 1975.)
c) An AM Her system. A Roche-lobe filling star is losing matter to a white dwarf. The accretion stream is funnelled and controlled by the white dwarf's magnetic field. (From Liebert & Stockman 1985.)

is beamed away from the centre of the disc, and approximately in the plane of the disc. Thus, if the system is viewed at inclination angles greater than $\simeq 60^{o}$ (i.e. "edge on") there is a light-house effect, where the system brightens every time the bright spot moves along the side of the disc closest to the observer.

In cases of intermediate magnetic fields, an outer disc is formed. At some point this is disrupted by the field to form a stream-like flow along the field lines to the compact object. The gravitational energy is released in non-magnetic systems as electro-magnetic energy during its passage through the disc and in the boundary layer. In the magnetic systems the energy is released in shock regions above the "accretion poles".

1.2 The broad divisions

The major division of these binaries is the cataclysmic binaries, or cataclysmic variables (CVs), where the accreting objects are white dwarfs, and the massive X-ray binaries (MXBs) and low mass X-ray binaries (LMXBs) where the accreting objects are neutron stars or black holes.

1.3 Cataclysmic variable classification

The divisions presented here (largely following those of Wade & Ward 1985, also see Table 1.1) are useful working classifications of the CVs, although there are objects which do not fit into the scheme. However, the classification has entered the vocabulary of the subject, and greatly simplifies discussion of the systems.

Table 1.1 Cataclysmic variable classification

Class	Disc	Magnetic	Mag	Period	Outburst Behaviour
U Gem	Yes	No	14.0-9.1	> 2hrs	Wide and narrow outbursts
Z Cam	Yes	No	14.8-10.5	> 2hrs	Occasionally remains on for long periods
VY Scl	Yes	No	12.9-18.5	> 2hrs	Occasionally in faint state
UX UMa	Yes	No	≈12	> 2hrs	
DQ Her	Yes	Yes	≈14	> 2hrs	
SU UMa	Yes	No	11.2-15.0	< 2hrs	Wide and narrow outbursts
AM Her	No	Yes	12.0-15.5	< 2hrs	Occasionally in faint state

Notes
"Magnetic" refers to whether or not the accretion flow is magnetically confined.
"Mag" is the normal magnitude range of the class prototype, excluding eclipses, taken from Ritter, 1987.

A typical CV might have a white dwarf of $\simeq 1M_{\odot}$, and a companion of $\simeq 0.3M_{\odot}$. The separation between the stars is $\simeq 1R_{\odot}$, and the binary period is usually in the range 1.5 to 20 hours. One of the most intriguing divisions occurs if a histogram of the number of systems with a given orbital period is plotted (see figure 1.02). There is a gap in the distribution between 2 and 3 hours. Above the period gap there exists a wide variety of systems. The U Gem stars, systems which have accretion discs, show outbursts (i.e. the system brightens by ~5 optical magnitudes) which are either wide, lasting $\simeq 14$ days, or narrow lasting $\simeq 4$ days. Stars which show outbursts like this (I shall discuss more sub-classes later) are called dwarf novae. The Z Cam stars are similar, except that after the peak of some outbursts their optical brightness remains at a level only slightly fainter than at peak for a long period (~months) before returning to quiescence. The VY Scl stars are usually in a bright state, but occasionally change to faint states which last for many weeks, hence their alternative name of "anti-dwarf novae". The UX UMa stars are non-magnetic systems in permanent outburst. The magnetic systems above the period gap all appear to have outer discs, and hence are called intermediate polars, or DQ Her stars.

The old novae are CVs where hydrogen on the surface of the white dwarf has been seen to undergo sudden nuclear burning (the recurrence time is $>$ 100 years). There are both non-magnetic and intermediate polar systems. Since the UX UMa and DQ Her stars which have not undergone nova explosions are indistinguishable from old novae, it may well well be that the former two classes are simply novae whose eruptions have not been observed.

By contrast, behaviour below the period gap is simpler. The stars are

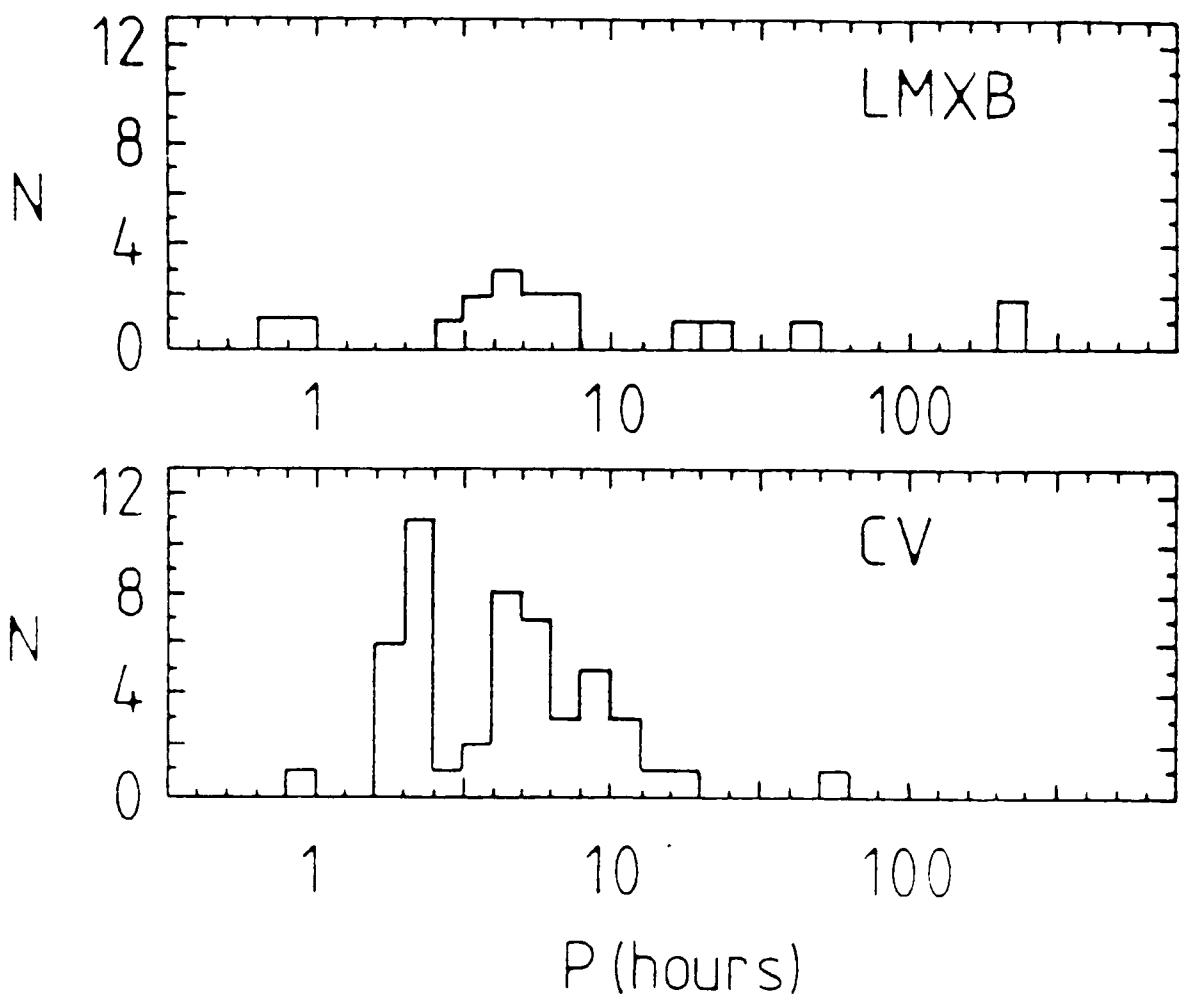

Figure 1.02 The orbital period distributions of CVs and LMXBs taken from White (1986). Note that the period scale is logarithmic.

either in the fully magnetic AM Her class, or the non-magnetic SU UMa class. The former spend most of their time in high states, occasionally switching off for periods of order months. The SU UMa stars show a bimodal distribution of outburst lengths, analogous to the U Gem stars, but their wide outbursts are much rarer than their narrow ones. The SU UMa stars are reviewed more extensively in Chapter 4.

Finally, the phrase "nova-like" is used to refer to the DQ Her, UX UMa, VY Scl and AM Her stars, i.e. all those systems usually in high states.

1.4 The outburst mechanism

The possible causes of dwarf nova outbursts have been reviewed by Bath & Pringle (1985). A controversy centres around whether the outburst is instigated by a burst of mass transfer from the secondary into the disc, or whether the disc itself is unstable. In the latter case mass is thought to be continuously transferred from the secondary into the disc, and when the disc reaches a critical density the viscosity of the disc changes from a low to a high value. An outburst then ensues as the matter moves through the disc and is accreted onto the white dwarf.

1.5 LMXBs and MXBs

Systems where a neutron star or black hole is gaining material from a high mass companion are called massive X-ray binaries. Often mass exchange between these stars occurs by accretion of the massive star's wind, rather than by Roche-lobe overflow. The low mass X-ray binaries have dwarf companions, and geometries similar to the non-magnetic CVs.

The common feature of the LMXBs and MXBs is that they are bright in X-

rays, but they can be differentiated by several methods. A study of their distribution in the galaxy (see van Paradijs 1983) suggests that LMXBs are associated with population II stars, and MXBs with population I. Hence MXBs are sometimes referred to as Type I sources, and LMXBs as Type II or bulge sources. The LMXBs also have softer X-ray spectra than the MXBs, and larger ratios of X-ray to optical luminosity (L_x/L_{opt}). For the LMXBs L_x/L_{opt} is usually greater than 10^1, whilst for the MXBs it is usually less than 10^1 (see Bradt & McClintock 1983 for the standard wavebands used).

I shall review the LMXBs in more detail in 1.6.3 and 1.6.4, and in Chapter 2.

1.6 The eclipses of X-ray binaries

Primary eclipses of X-ray binaries take several different forms, depending on the precise inclination and classification of the binary. I shall discuss here each those relevant to this thesis.

1.6.1 Disc eclipses

Often an accretion disc produces significant flux at optical wavelengths over almost its entire surface. If the secondary can obscure every part of the disc (though not simultaneously), the optical eclipse will show a smooth ingress and egress, whose precise length depends on the relative sizes of disc and secondary. Such an eclipse is usually symmetric. These conditions apply for optical light curves during the outbursts of dwarf novae such as Z Cha and OY Car, and such an eclipse is shown in figure 3.07. Such eclipses are usually symmetric.

1.6.2 Quiescent dwarf nova eclipses

During quiescence the outer disc of eclipsing dwarf novae is not the major contributor to the optical light; the white dwarf and bright spot dominate. If the inclination of the system is such that the central object cannot be eclipsed but the bright spot can, the result is an eclipse whose shape is unstable from one cycle to the next, such as that of U Gem.

If the inclination is such that the compact object can be eclipsed, then the bright spot is eclipsed also. The result is the eclipse of a relatively small object (the white dwarf and boundary layer) which results in a rapid ingress and egress, superimposed on the bright spot eclipse. The relative sizes and positions are such that the order of the eclipse is normally central source ingress, bright spot ingress, central source egress, bright spot egress.

1.6.3 LMXB dips

The situation in the LMXBs is complicated by the prescence of extended vertical disc structure (see Mason 1987 for a review). The precise form of the structure is unclear, but it is probably in the form of a rim around the outer edge of the disc. In the case where the observer can see the compact object directly, but the structure occasionally obscures the view, the result is "dips", as seen in the X-ray light curves of these objects. Dips occur in two distinct groups. One group of dips stretches across the phase range 0.6 to 0.0, and sometimes beyond, and the other, which is not always present, is centered around phase 0.2. The mechanism which supports the structure is still a subject for debate, but the dips near phase 0.8 are probably associated with the

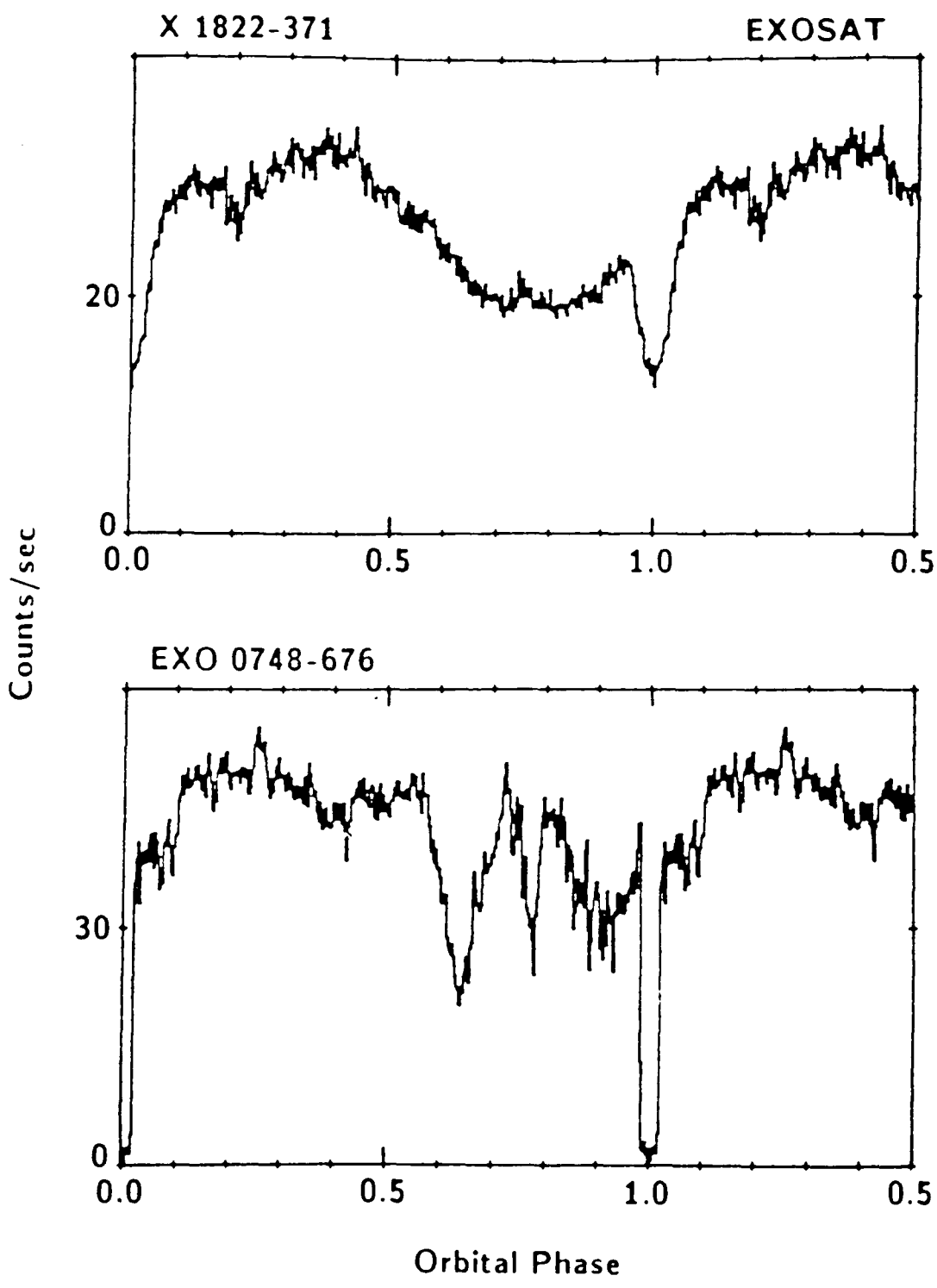

Figure 1.03 A comparison of the X-ray light curves of the ADC source X1822-371 (upper panel) and the dip source EXO 0748-676 (lower panel), taken from Parmar *et al.* (1986). Note how the large size of the ADC broadens the eclipse and smooths the dips in X1822-371, compared with EXO 0748-676, where the X-ray source is point-like.

stream impact region. There is no convincing explanation of the dips near phase 0.2.

If higher inclination systems are studied, the companion star eclipses the compact object, causing an X-ray eclipse of a small object (comparable to the optical eclipse of the white dwarf in CVs) as well as dips (see the lower panel of figure 1.03).

1.6.4 The LMXB ADC sources

In the highest inclination systems the disc structure hides the X-ray source from view. In this case the accretion disc corona (ADC), becomes visible. The corona scatters X-rays from the region near the compact object into the observer's line of sight. This leads to the ADC sources being X-ray faint compared to other LMXBs, and thus they have a low L_x/L_{opt} of about 30.

There is a further important property of the ADC; it is much larger than the primary X-ray producing region, and hence the X-ray eclipse by the secondary is now the eclipse of an extended object. It is thus wider than the eclipse seen in the eclipsing dip sources, and only partial. Further, its obscuration by the disc structure appears much smoother. The result of these two effects in shown in figure 1.03.

References

Bath, G.T., & Pringle, J.E., 1985. In: *Interacting Binary Stars*, p. 177, eds. Pringle, J.E., & Wade, R.A., C.U.P.

Bradt, H.V., & McClintock, J.E., 1983. *Ann. Rev Astron. Astrophys.*, **21**, 13.

Kopal, Z., 1959. *Close Binary Systems*, Chapman & Hall Ltd., London.

Gursky, H., & van den Heuvel, E.P.J., 1975. *Scientific American*, 232, No. 3, p. 24.

Liebert, J., & Stockman, H.S., 1985. In: *Cataclysmic Variables and Low-Mass X-Ray Binaries*, p. 151, eds. Lamb, D.Q., & Patterson, J., Reidel, Dordrecht.

Mason, K.O., 1987. In: *Physics of Accretion onto Compact Objects, Lecture Notes in Physics*, vol. 266, p.29 eds Mason K.O., Watson, M.G. & White, N.E. Springer-Verlag, Heildelberg.

Parmar, A.N., White, N.E., Giommi, P., & Gottwald, M., 1986. *Astrophys. J.*, 308, 199.

Pringle, J.E., & Savonije, G.T., 1979. *Mon. Not. R. astr. Soc.*, 187, 777.

Ritter, H., 1987. *Astron. Astrophys. Suppl. Ser.*, in press.

Shakura, N. & Sunyeav, I.N., 1973. *Astr. Astrophys.* 24, 337.

van Paradijs, J., 1983. In: *Accretion-Driven Stellar X-ray Sources*, p.189 eds Lewin, W.H.G. & van den Heuvel, E.P.J., C.U.P., Cambridge.

Wade, R.A. & Ward, M.J. 1985. In: *Interacting Binary Stars* eds Pringle, J.E., and Wade, R.A. C.U.P., Cambridge.

White, N.E., 1986. In: *The evolution of Galactic X-ray Binaries*, eds. Truemper, J., Lewin, W.H.G., & Brinkman, W., D. Reidel Publishing Company, Dordrecht, Holland.

Chapter 2

A Review of Globular Clusters and Low Mass X-ray Binaries

2.1 Introduction to globular clusters

Globular clusters are spherically symmetric groups of stars whose density increases smoothly (on the large scale) towards the centre. They contain 10^5 to 10^7 stars, giving a total mass of 10^4 to $10^6 M_\odot$ (the mean stellar mass is $\sim 0.5 M_\odot$), and have radii ~10pc. Our galaxy has perhaps 200 of these clusters, in orbits which are not aligned with the disc of the Galaxy, so that they form an approximately spherical halo. As distance from the Galactic centre increases, the range of metallicity of clusters decreases. In the outermost regions there are only metal poor (F type) clusters whereas in the inner regions there are both metal rich (G type) and F type clusters (Harris 1976).

It is thought that when a cluster passes through the galactic plane (with a velocity of ~100km s^{-1}) the gas from the cluster is swept out by ram pressure. Gas is also lost by evaporation because of the low (~10km s^{-1}) escape velocity. The absence of gas inhibits further star formation, and so all the stars in a given cluster were formed, at essentially the same time. Thus within a cluster all the stars have the same metallicity and age (~10^{10} years). Coupled with the fact that the stars are all at the same distance, this makes the globulars much like a set of experiments where, within each experiment, the only parameter allowed to vary is the mass of the stars. Between experiments the metallicity and age is varied.

Studies of these "experiments" have concentrated on the evolution of individual stars (see Section 2), and explaining the density distribution of stars within the cluster (Section 3).

2.2 Stellar evolution in globular clusters

The age of the globular clusters means that all the remaining non-degenerate stars are low mass (less than ~$0.8M_{\odot}$), the shorter lived high mass stars having evolved into neutron stars and white dwarfs. In this section I shall outline the evolution of the low mass stars.

Figure 2.01 shows the Hertzprung-Russell (H-R) or colour-magnitude (C-M) diagram for the globular cluster M15, I have marked various branches on it corresponding to those in Table 2.1 (from Castellani 1980).

Table 2.1

Evolutionary phase	Structure	Lifetime
Main Sequence (MS)	Central H-burning	10^{10} years
First Giant Branch (FGB)	H-shell burning	10^{8} years
Horizontal Branch (HB)	Central He & H-shell burning	10^{8} years
Asymptotic Giant Branch (AGB)	Double shell burning	10^{7} years

Once the hydrogen core of the star is exhausted the envelope expands, and the star leaves the main sequence (MS) and begins to ascend the first giant branch (FGB). The point at which the star leaves the main sequence (the turn off) is marked in figure 2.01 (as TO). The lower luminosity region of the FGB is referred to as the sub-giant branch (SGB). A hydrogen burning shell develops around the degenerate helium core, as the star continues to brighten, moving through the upper part of the FGB, sometimes called the red giant branch. When the star is near the top of the giant branch the core ignites, and burns very rapidly - the helium flash.

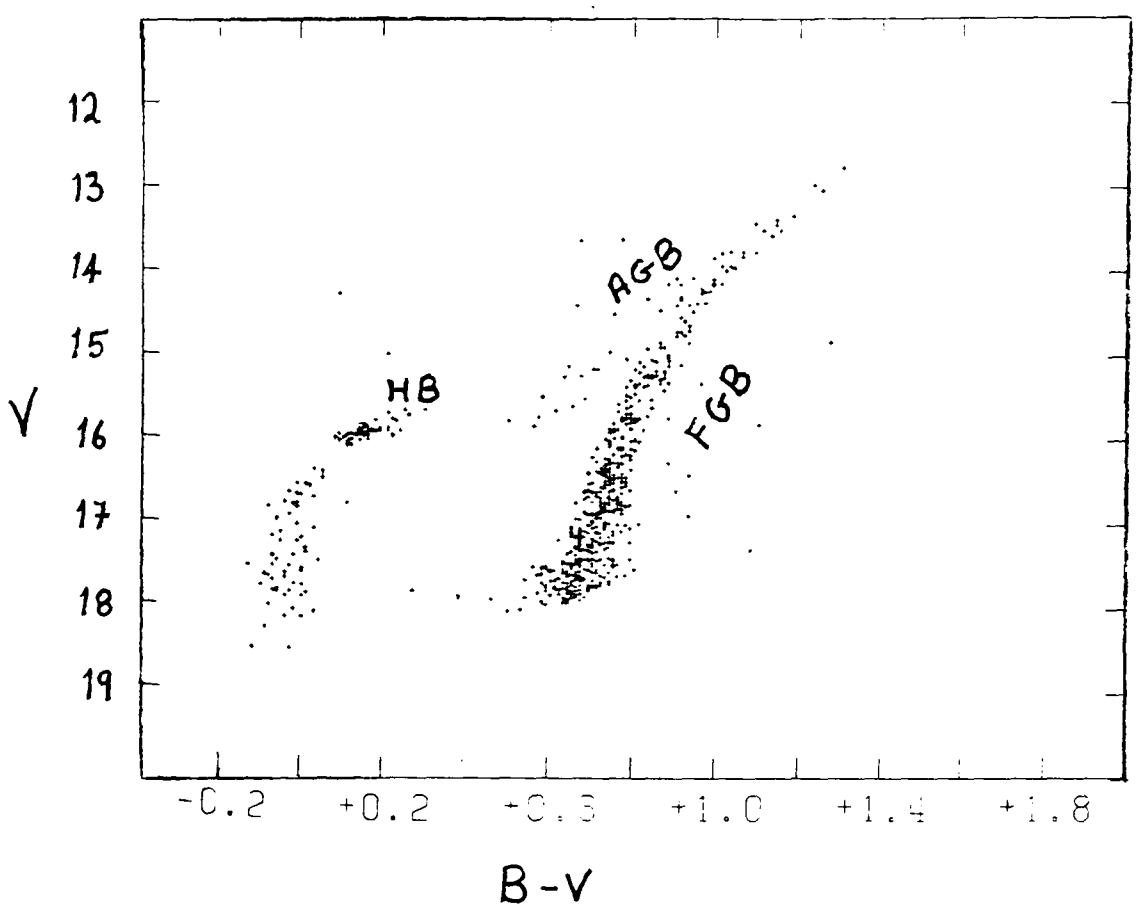

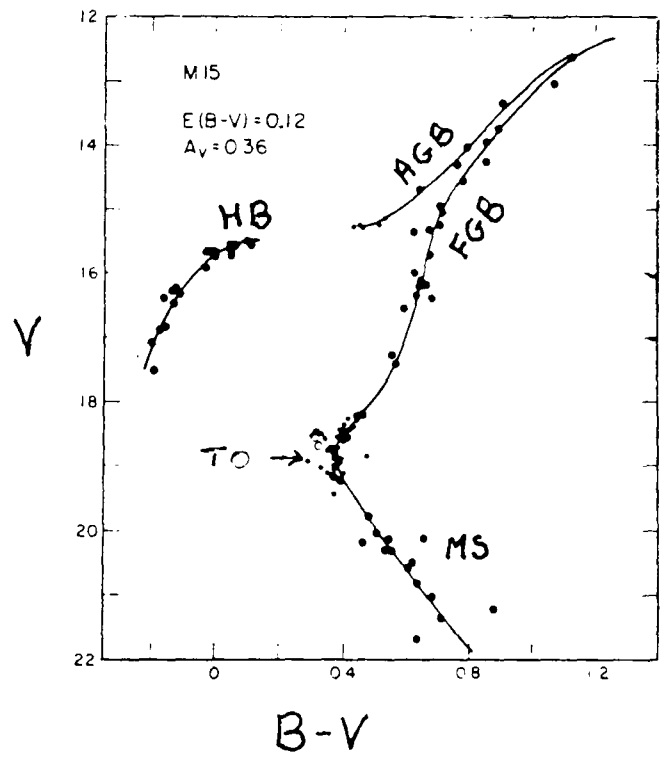

Figure 2.01 The H-R diagram for M15 taken from Battistini *et al.* (1985) (upper) and Sandage (1969) (lower). Note that the lower diagram has been corrected for reddening. Various branches are marked (see text).

During and immediately after the helium flash the star evolves very rapidly to a position somewhere on the horizontal branch (HB). The locus of these initial positions is the zero age horizontal branch (ZAHB). The HB is divided into a blue and red region (the BHB and RHB), the gap between being populated by the RR Lyrae stars which are pulsating variables. Whilst on the HB the star burns a hydrogen shell, and a helium core. When this core is exhausted helium and hydrogen burning continues in shells; the star is now referred to as a double shell source. It becomes hotter and more luminous, rising above the ZAHB, before ascending the asymptotic giant branch (AGB). This is the phase of evolution in which the Mira variables (periods of ~100 - 650 days) occur.

The cores of low mass stars do not reach temperatures high enough to ignite heavier elements, and so after reaching the tip of the AGB the star will contract, becoming bluer once again, and move towards the bottom left of the H-R diagram, evolving eventually into a white dwarf.

Fitting the results of stellar evolution codes to the main sequence and the horizontal branch yields information about the chemical composition, age, and stellar mass spectrum of the cluster. For such a study of M15 see Fahlman, Richter & VandenBerg (1985).

2.3 Stellar density functions

There are essentially two ways of determining how the density of stars in a cluster changes with radius; either count the number of stars, or measure the surface brightness, as functions of radius. Depending on whether a mass or number density is required, a mass-luminosity relation and/or the proportion of stars with a given luminosity must be assumed.

Obtaining reliable star counts or surface photometry has proved to be difficult (see King 1980 for a review), especially in the core, although the advent of CCDs has improved the situation.

King (1962) found that the surface density of globular clusters could be fitted with just 3 parameters. Such a fit is shown in figure 2.02. The luminosity becomes zero at the tidal radius (r_t), and tends to a finite maximum density, f_o. The relatively flat region (remembering this is a log/log plot) is called the core, and the core radius (r_c) is marked. The tidal radius is the radius at which the gravitational attraction of the Galaxy equals that of the cluster, and thus beyond this point stars are stripped from the cluster. This radius will change as the cluster's distance from the Galactic centre changes during its orbit of the Galaxy. Thus the tidal radius is, more properly, the minimum tidal radius.

Once such a radius has been imposed on the system, then the minimum number of parameters that can describe the system is 3: a term associated with the total energy (r_c); a richness factor (f_o); and r_t. As King pointed out, this means that the clusters are as nearly the same as external circumstances will allow, a situation only possible if there has been some method of relaxation or mixing in the cluster. Whilst it would be convenient if a globular cluster could be represented as an "isothermal gas sphere", Chandrasekhar (1942) has shown that the mean free path is much larger than the radius of the cluster. Thus the clusters probably relaxed by a process of spatial mixing at the time that the cluster was formed (see King 1962), and then evolved by encounters between states represented by the 3 parameters.

Due to the imposition of a tidal radius stars with a finite velocities

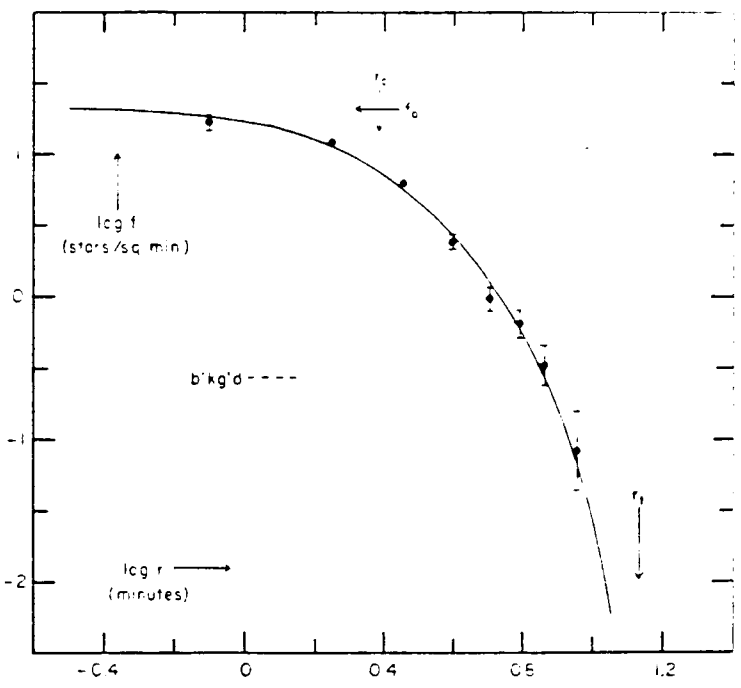

Figure 2.02 A Fokker-Planck velocity distribution single mass component model fitted to the number density of NCG5053, taken from King (1966). The core radius (r_c), tidal radius (r_t) and peak surface brightness (f_o) are marked.

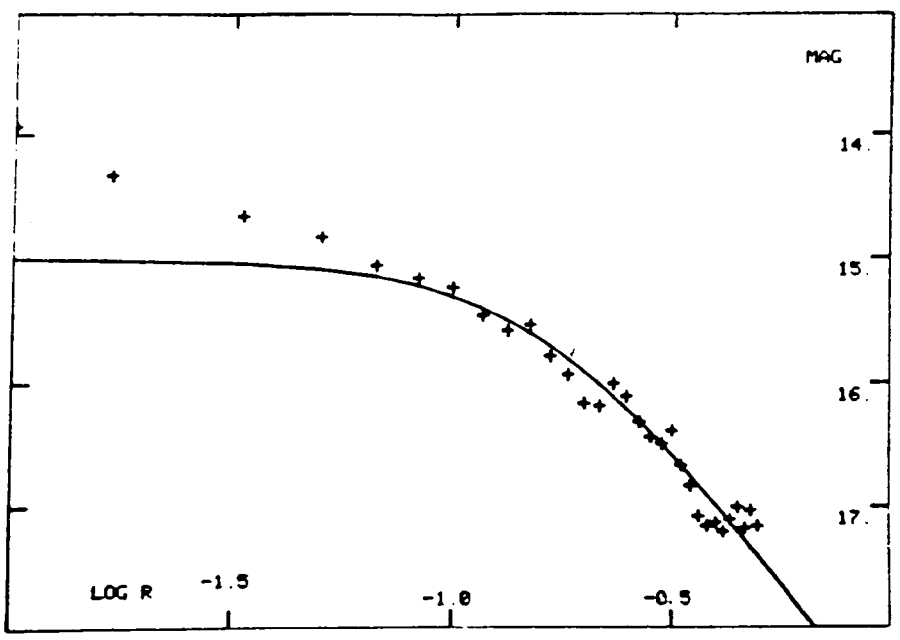

Figure 2.03 The variation of surface brightness with radius in the V band for M15, from Aurière and Cordoni (1981). The solid line is a King model. The x-axis in the logarithm of arcminutes, the y axis is in magnitudes per square arcsecond.

can escape the cluster. This modifies the Maxwellian velocity distribution that the relaxation alone would cause, into the Fokker-Planck distribution (see King 1965). If this distribution is combined with the assumption that all the stars have the same mass, the result is the model presented by King (1966), of which the fit to the data in figure 2.02 is an example. The density functions predicted by this model are nearly identical to the empirical models of King (1962).

Star counts to different limiting magnitudes and surface photometry in different bands will all sample different parts of the stellar population. It is important to note that these different measures can give different parameters for the same cluster. For example, King found that the core radius of NGC5053 increased when the star count had a fainter limiting magnitude, implying that stars of different luminosity have different distributions within the cluster. Models with a distribution of masses for the stars have been computed (e.g. Da Costa & Freeman 1976) and show that the parameters do change for the different mass components, the higher mass classes generally having a smaller core radius.

2.4 Core collapse

Using these models it can be shown that the dynamical evolution of globular clusters is unstable. By this epoch many should have undergone "core collapse", a process whereby the central regions of the cluster condense, whilst the envelope expands (for a theoretical review see Heggie 1979, and for a thermodynamical explanation Lynden-Bell & Wood 1968). Essentially, as the cluster evolves, the stars with the most kinetic energy (the "hottest" stars) are ejected from the core of the

cluster into the envelope. This process can be thought of as the core cooling by evaporation. As the cluster cools, it contracts, and the interaction time between stars shortens. Thus the cooling process speeds up, as does the collapse. Certain clusters cannot be fitted by King models due to a light excess near their centres, and this is thought to be a sign that core collapse has occurred (for an observational review, see King 1984). Figure 2.03 shows this effect in M15.

Our knowledge of the dynamical evolution from this point on is entirely theoretical, based on the results from numerical models. The collapse of the core is thought to be finally halted by the formation of "hard" binaries (binaries where the binding energy is greater than the mean kinetic energy of a cluster member). These binaries are formed by inelastic encounters, and then "hardened" by further encounters with cluster members. The binding energy thus released is sufficient to make the core re-expand, and it then undergoes more cycles of collapse and expansion.

2.5 Binaries in globular clusters

As binaries are important in the dynamical evolution of globular clusters (see Section 4) much effort has been expended in finding them. Spectroscopic studies have found just one binary, von Zeipel (vZ) 164 (in M3), which shows an amplitude ≥ 8 km s^{-1} and a period of a few years (Pryor, Latham & Hazen-Liller 1985). Photometric searches for eclipsing binaries have found ~50 in globular cluster fields, but none has been shown to be cluster members on the basis of radial velocity, proper motion or luminosity (Trimble 1980). Hesser *et al.* (1985) found a

"second main sequence" in M3 about 0.75 of a magnitude above the normal MS, which they thought may be composed of binaries, however this work has yet to appear in full. Finally, attempts have been made to associate types of stars with the effects of mass transfer in binaries, like the anomalous Cepheid in NGC 5466 (Zinn & Dahn 1976) and the blue stragglers. The latter are stars that lie near the turnoff point in the H-R diagram, but are bluer and more luminous than the turnoff. However, other explanations are possible, and the case for them being binaries is as yet unproven.

The conclusion that the globulars are short of detected binaries compared with the Galactic disc seems inescapable, and indeed a systematic survey of the giants in M3 compared with field giants seems to confirm this (Gunn & Griffin 1979). The survey covered the range of binary separations sufficiently hard not to be disrupted by encounters. Furthermore the authors believed they observed stars sufficiently close to the core that mass segregation would not account for the complete absence of binaries from the sample.

Although normal binaries are probably underabundant relative to the Galaxy, the LMXBs are overabundant by a factor of about 3000 (using modern figures and the method of Katz 1975). Their nature was originally deduced by the similarity of their X-ray properties to the LMXBs of the galactic bulge, and was confirmed by a statistical determination of their masses (Grindlay *et al.* 1984). In addition, there are two optically identified CVs in globular clusters; V101 in M5 (Margon, Downes & Gunn 1981) and V4 in M30 (Margon & Downes 1983).

2.6 The LMXBs

The LMXBs have been discussed in relation to other X-ray binaries in Chapter 1, section 5. In this section I shall review their properties most relevant for interpreting the M15 X-ray source.

2.6.1 Classification

The globular cluster LMXBs is one of 4 (non-exclusive) classes into which the low mass X-ray binaries are divided. The "bursters" are so called because they show bursts in their X-ray and optical light curves which last up to a few minutes. The "soft X-ray transients" are optical/X-ray novae whose outbursts last a few weeks, some of which are known to recur on timescales of months or years. They are "soft" since their X-ray spectra contrast with the hard spectra of the massive X-ray binaries. A "bright bulge source" refers to any persistent (non bursting) LMXB near the galactic bulge. That it is X-ray bright distinguishes it from the bursters, and that it is in the galactic bulge from the massive X-ray binaries. Since many bursters are also associated with the bulge the term "bulge source" is used to include both the bursters and the bright bulge sources. The overlap between classes in sometimes quite large, for instance most globular cluster sources are bursters, and they are often included in the term "bulge sources" because of their similarities with them.

2.6.2 X-ray bursts

This topic is reviewed extensively by Lewin and Joss (1983). X-ray bursts have rise times of the order of a few seconds, and decay on timescales of seconds to minutes. The peak burst flux is usually

several times the persistent flux. Most bursts which are observed occur in the surface layers of the neutron star, and are caused by light elements undergoing thermonuclear fusion. However, aside from these "Type I" bursts, there are also "Type II" bursts, from an LMXB called the "Rapid Burster" (MXB1730-335). Type II bursts occur too frequently (~20 seconds) to be thermonuclear flashes and are thought to be caused by accretion instabilities.

2.6.3 Optical properties

LMXBs have typical optical magnitudes of B~18, and absolute magnitudes M_v~2. Their spectra are intrinsically very blue, exhibiting almost featureless continua, on which HeII λ4686, the Bowen blend λλ4640-4650 and a some Balmer emission lines are usually superimposed (see figure 2.04).

The Bowen blend is a blend of lines of NIII, and possibly CIII and OII. Whilst it is possible that the above emission lines could be produced by a hot plasma, it seems more likely that the blend is primarily due to NIII Bowen fluorescence (McClintock, Canizares & Tarter 1975). The "Lyman α" line of HeII (λ304) coincides with a resonance line of OIII. From the excited state produced by the capture of a λ304 photon the OIII ion can decay to produce optical photons, and a λ374 UV photon. This wavelength coincides with an excited state of NIII, from which a possible decay produces photons in the range λλ4634-4641. As other lines are produced in this process it should be possible to choose between the two mechanisms, as suggested in McClintock *et al.* (1975).

There follows a brief description of those LMXBs for which radial velocity studies are available.

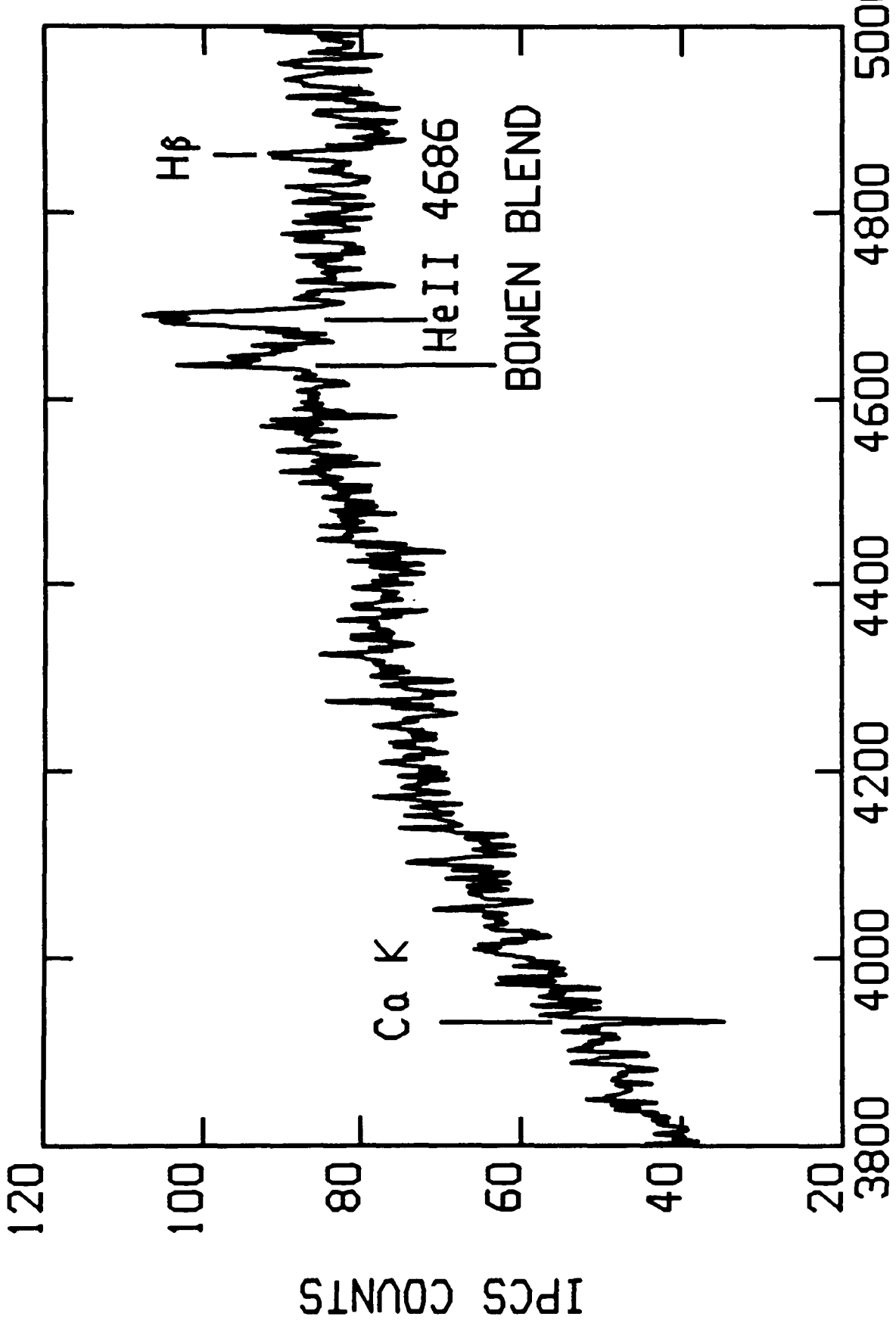

Figure 2.04 An IPCS spectrum of the LMXB GX339. Reproduced from data kindly supplied by R.H.D. Corbet.

X0921-630

The smooth X-ray eclipse (Mason *et al.* 1987) and low L_x/L_{opt} of X0921-630 show that this is an ADC source (see Chapter 1), and because of its long period (216.3 hrs) the mass-losing star must be a giant. Spectra (see Cowley, Crampton & Hutchings 1982a and Branduardi-Raymont *et al.* 1983) show HeII λ4686 and Balmer emission, and weak (sometimes absent) HeI λ4471 absorption. Compared with HeII λ4686 the Bowen blend is very weak. The G band and Ca II H and K lines are also seen, which are thought to be from the secondary star (Thorstensen & Charles 1980). The base (i.e. broad flat topped component) of the HeII line profile is thought to originate in the disc (hence its large width); and the narrow peak superimposed on the base, in the bright spot. This results in the base and peak moving out of phase with each other, producing apparently complex changes in line profiles.

Cyg X-2

The X-ray dips of Cyg X-2 demonstrate that this is an intermediate inclination source, and the long period (235 hrs) again requires that the mass losing star is evolved. The spectral lines of an early F giant are clearly visible in the spectra, and have been used for radial velocity studies (Cowley, Crampton & Hutchings 1979). By studying the phasing of the HeII λ4686 flux and position with respect to the secondary's spectral features, Cowley *et al.* (1979) showed that the majority of the flux, whose position was measured using the peak of the line, probably originates on the heated face of the giant. They also detected a weaker component in the HeII line that could have been either underlying broad emission, or a second, anti-phased line. This may

originate in the accretion disc (as they suggested), or in the bright spot.

There is emission infilling of the giant's Balmer lines. The Bowen blend is normally weak but occasionally (Bopp & Vanden Bout 1972) as strong as HeII λ4686.

Sco X-1

This is probably at low inclination. Its spectrum shows emission from the Balmer lines, HeII λ4686 and weaker Bowen blend emission. LaSala & Thorstensen (1985) used the phasing of the base of the HeII λ4686 to show that it moved with the compact object, a view which is supported by the fact that its width is consistent with it being formed in the outer disc. They also found that the peak of the HeII line, and the entire Hβ line lagged the HeII base in phase. They attributed this effect to an additional component in these lines due to the bright spot.

X2129+47

This object may have either a neutron star or a white dwarf as its compact object. A good spectroscopic study has been carried out by Horne, Verbunt & Schneider (1986). The spectrum shows HeII λ4686 and Bowen blend emission, of roughly equal strengths, with Ca H & K (probably interstellar) and Balmer absorption. The study showed that the HeII profiles can be interpreted as an "S" wave similar to those seen in cataclysmic variables (see for example, Brunt 1983), and thus probably has a broad (double peaked) component from the disc, and a sharp one from the bright spot. Hβ has a broad, apparently stationary component, and a narrow component from the heated face of the secondary.

The Bowen blend is constant with a narrow component from the secondary, and a broad (though not double peaked) base whose width is similar to ? that expected from the disc.

X1822-371

In the X-ray band X1822-371 shows broad eclipses of the ADC by the stream impact region, and sharper eclipses of the ADC by the secondary. The optical spectrum (Mason *et al.* 1982) shows HeII λ4686 and Bowen blend emission, Ca H & K (probably interstellar), and broad HeI λ4471, λ4387 and λ4026 absorption. There are also broad Balmer absorption lines, although Hα is in emission. From a radial velocity study Cowley, Crampton & Hutchings (1982b) showed that the base of the HeII line originates in the disc region, and that Hδ probably comes from the secondary, the latter result being supported by the line's flux modulation. From a study of the flux modulation of these lines Mason *et al.* (1982) supported the conclusion for HeII, but showed that the distribution in the disc may be quite complex.

X1735-44

The most complete spectroscopic study of this object is Smale (1986), although the data is also presented in Smale *et al.* (1984). The spectrum shows HeII λ4686 and Bowen blend emission, and Ca K absorption. There is weak NIII λ4100 and HeII λ4541 emission. The Balmer lines are not discernible. The HeII line position (measured by Gaussian fitting, and so reflecting a mixture of the base and peak position) moves with a large amplitude that implies it must either be from the secondary, or the bright spot.

A0620-00

The spectrum of this transient shows Hβ emission, and absorption lines which are associated with the late-type secondary. By following the radial velocity of these absorption lines McClintock & Remillard (1986), have shown that the compact object in this system is probably a black hole.

From this short survey two interesting points arise. Firstly, wherever its position can be found, a large fraction of the He II flux originates in the stream impact region. Secondly, the high inclination systems X1822-370 and X0921-630 show HeI lines in absorption, a feature they have in common with AC211 (see Chapter 3).

2.7 Ultraviolet studies of clusters

Van Albada, de Boer and Dickens (1979, 1981) carried out broad band UV photometry of 27 globular clusters, using the *ANS* satellite. The data were taken through a 2.5 x 2.5 arc minute aperture with band passes 100-200Å wide. After correction for reddening, the clusters form a sequence which they labelled extremely blue, blue, intermediate and red, with M15 falling in the blue group. They concluded that all the flux could be accounted for by horizontal branch stars. It is interesting that neither of the two X-ray clusters for which colours could be derived (NGC6624 and M15) were unusually blue.

Dupree *et al.* (1979) used the large aperture of *IUE* to take spectra of the central 10".0 x 20".0 of 6 globular clusters. In the cases of two of the three X-ray clusters studied the aperture should have included the X-ray source. NGC6624 showed a weak SWP spectrum

($\sim 2 \times 10^{-14}$ergs cm^{-2}s^{-1}Å^{-1}) that was consistent with a point source. As the authors suggest, this probably a BHB star, but it should be noted that these are rare in this particular cluster. The other cluster where the X-ray source was within the aperture is M15. I have re-extracted all the archive M15 spectra, and they are discussed in Section 6 of Chapter 3.

2.8 The M15 X-ray source

An X-ray source near M15 was first detected by *Uhuru* (*SAS A*) and appears in the second *Uhuru* Catalogue (Giacconi *et al.* 1972) as 2U2134+11. In the 3U Catalogue (Giacconi *et al.* 1974) it was tentatively identified with M15, and the more accurate position of the 4U Catalogue (Forman *et al.* 1978) confirmed this. The source was shown to be variable by a factor > 2 (in the 3-10keV band) on a timescale of months by *OSO-7* (Clark, Thomas & Li 1975) and irregularly variable by a factor > 3 (2-18keV) by the *Ariel V* Sky Survey Instrument (Cooke *et al.* 1978).

An optical candidate (AC211) was first proposed by Aurière, Le Fèvre & Terzan (1984). The identification was made on the basis that AC211 is highly variable and blue. Aurière *et al.* 1984) also pointed out that when compared with a list of non bursting LMXBs, the only sources with a similar magnitude (X0921-63, Her X-1 and X1822-37) also show large optical variability. In a subsequent paper, Aurière *et al.* 1986) suggested that the system was eclipsing and thus deduced the colours of the secondary from the colours at minimum light. They are consistent with a BHB or SGB star with some contribution from the accretion disc. As they pointed out, such a scenario has the added attraction that no LMXB with an evolving companion bursts. This is probably because the

mass transfer rates for systems where the mass transfer is evolution driven are higher than for other systems, and high mass transfer rates are thought to inhibit bursting (Ayasli & Joss 1982).

The photometric identification was confirmed by spectroscopy (Charles, Jones & Naylor 1986), which showed HeII λ4686 and Lyman α emission. There is no Bowen blend, and it is thought that the other Balmer lines are masked by the presence of Balmer absorption from other late type stars in the spectrograph slit. Charles *et al.* (1986) pointed out that L_x/L_{opt} was lower than for most LMXBs, but consistent with the ratio for the ADC sources. As the ADC only scatters a fraction of the intrinsic X-ray flux towards the Earth, the X-ray heating of the secondary may be a better guide to the true X-ray luminosity, and hence accretion rate. Using the B band modulation they derived an accretion rate of $\sim 10^{-8} M_\odot$/year, close to the Eddington limit for the $1.4 M_\odot$ neutron star that was assumed. It should be noted that this is only an upper limit to the accretion rate since some of the modulation may be due to an eclipse.

2.9 The W Vir star AC5

The presence of AC211 cannot explain all the curious observational facts which have been published about the core of M15. MacGregor, Phillips & Selby (1973) found a 10.2μ infra-red source using a 10" aperture centered on the core of the cluster. They considered the source was too strong to be either cool (50K) dust, or a normal planetary nebula. This idea was supported by the theoretical work of Caloi & Panagia (1974) who showed that the data are consistent with a blue star illuminating a dust shell. They suggested this could be a young planetary nebula.

In a follow up study Peterson (1976) carried out slitless spectroscopy to search for the emission lines that would be expected from such a planetary. His data show an object with narrow Hα emission in the core of the cluster, that outshines everything else in the cluster in Hα light. Grindlay & Liller (1977) placed a 15" diameter circular aperture over the core of M15, and measured the light through a narrow (16Å) Hα filter. They found that it varied by 10% on a timescale of days, which a planetary nebula should not.

However, it is now widely accepted that the McGregor *et al.* detection, which was at the limit of their sensitivity, was not real (Longmore, private communication). In the IRAS point source catalogue M15 has a flux of only 0.74 Jy in the 60μm band, and is absent in the 12μm (0.41 Jy upper limit), 25μm (0.27 Jy) and 100μm (1.15 Jy) bands (see Schaefer 1986 for a discussion of the possible sources of this flux).

The Hα source is probably the W Vir Cepheid variable AC5 (= V86, see Aurière & Cordoni 1981 and Rosino 1950). Such a star (see Fusi-Pecci, Rosino & Voli 1980, and Joy 1949) has a period of ~20 days (17 days for AC5, Fusi-Pecci *et al.* 1980), with phase zero defined as the time of maximum brightness. The Balmer lines are normally blue shifted around the time of maximum light, and red shifted near minimum. On the rising branch of the light curve (phases 0.5 to 1.0) they are in emission, and at their strongest, whilst in the later stages of decline to minimum (0.2 to 0.4) they are seen in absorption. This picture is confirmed for AC5 by Ford *et al.* (1978), who found strong emission lines near phase 0.6.

In figure 2.05 and 2.06 I show IPCS and CCD spectra of AC5, with the details of the observations given in Table 2.2. The observations were

Table 2.2

Observations of AC5 made with the RGO Intermediate Dispersion Spectrograph on the 2.5m Isaac Newton Telescope at the Observatorio del Roque de los Muchachos during August 1987.

Date	Mid Exposure (UT)	Exposure(s)	Detector	Camera	Phase	Heliocentric Velocity (km s^{-1})
17	05:03	2x360	CCD	500mm	0.21	-91±41
19	02:45	600	IPCS	235mm	0.32	-61±6

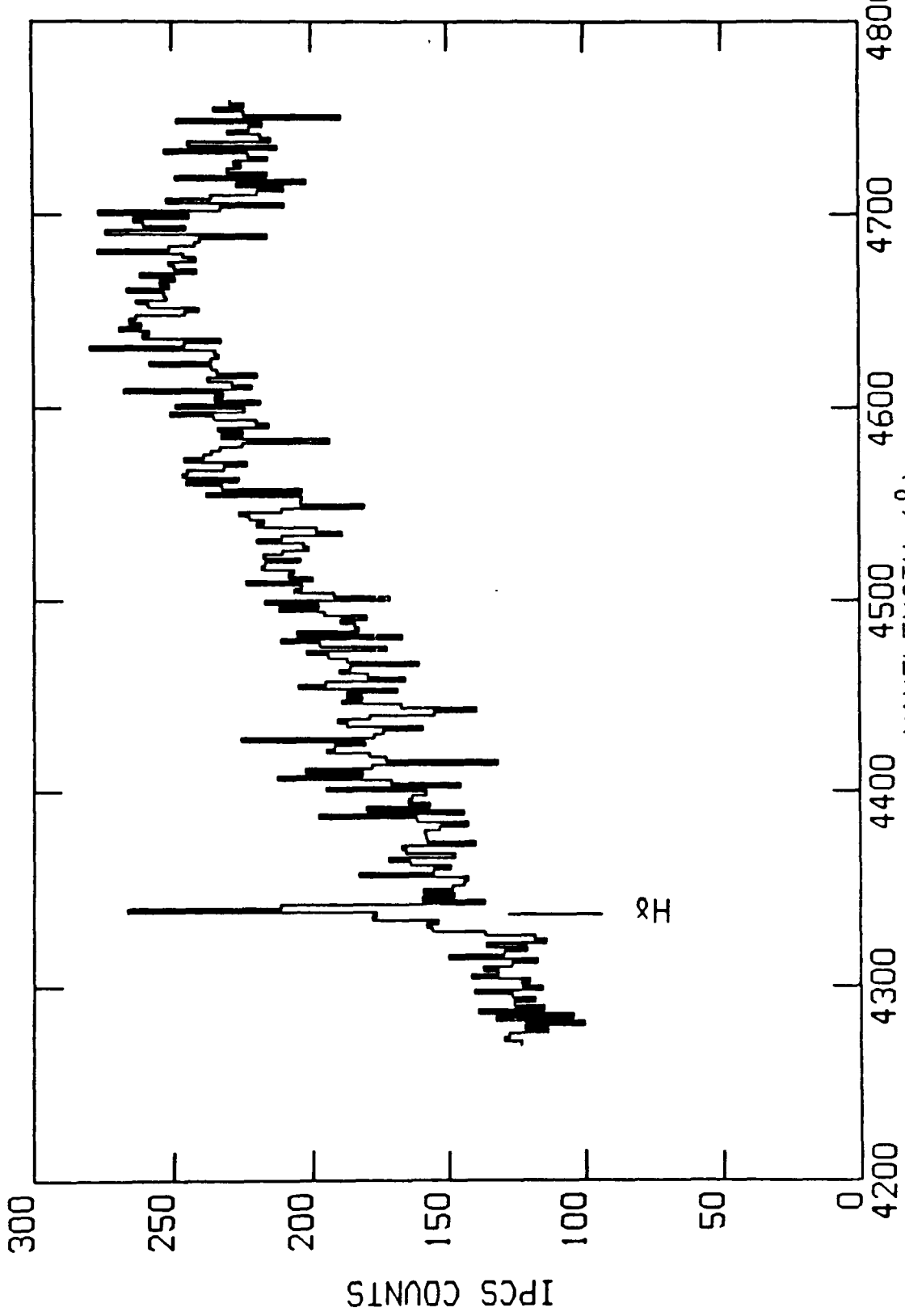

Figure 2.05 An IPCS spectrum of AC5. The data has been rebinned from the original 0.5Å pixels into 2Å bins in order to reduce the noise. No "sky" subtraction has been attempted since the background cluster light varies rapidly with position in this region. However less than 1/3rd of the continuum is likely to come from other stars. The exposure time was 600 seconds, although the IPCS counts are not a good indicator of the stellar flux as AC5 was a serendipitous source in this observation and was probably not centered on the 0".5 slit.

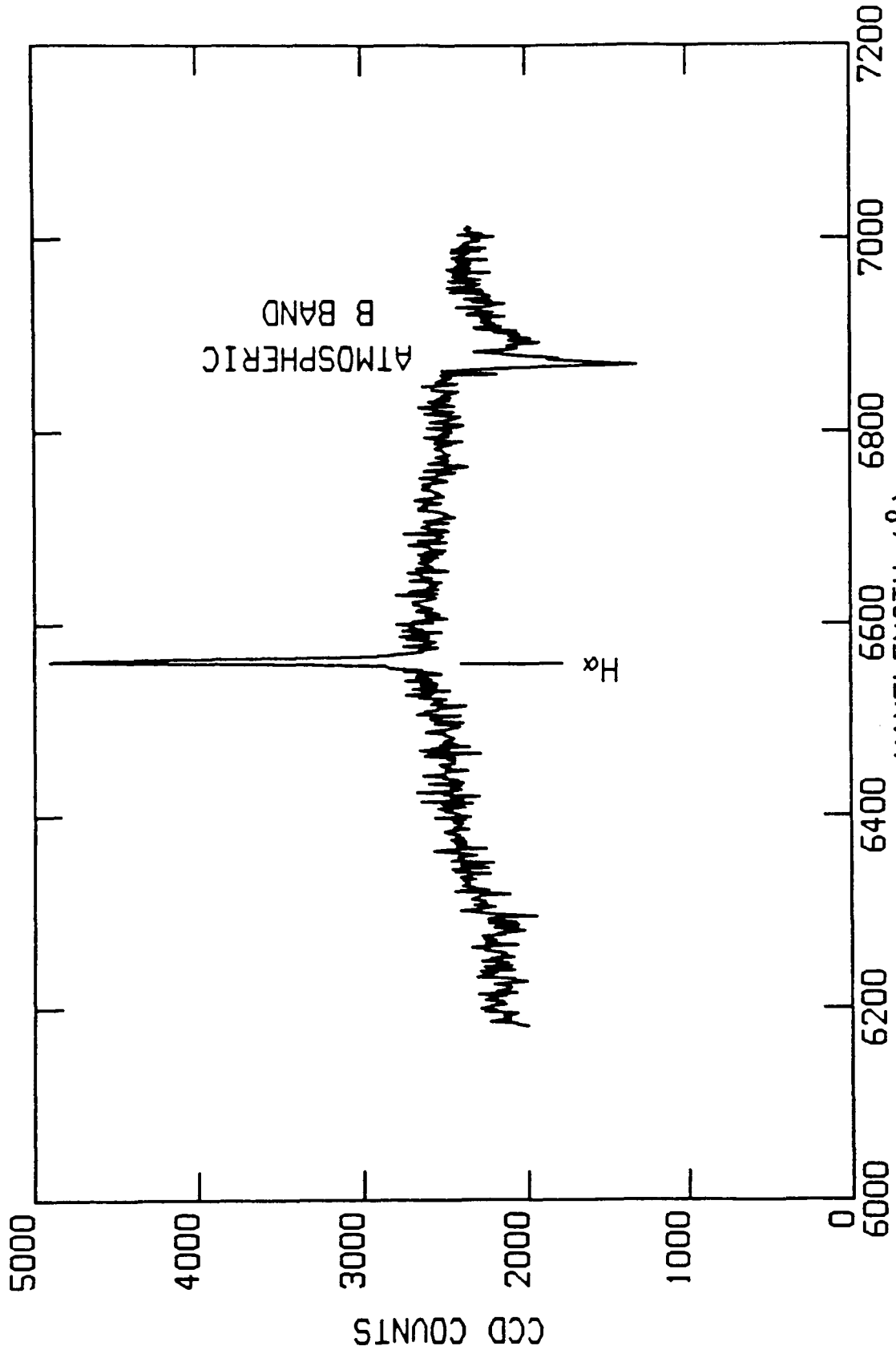

Figure 2.06 A CCD spectrum of AC5. No "sky" subtraction has been attempted since the background cluster light varies rapidly with position in this region (see figure 2.07). There is a small gap in the spectrum near 6846Å where a charge particle event occurred.

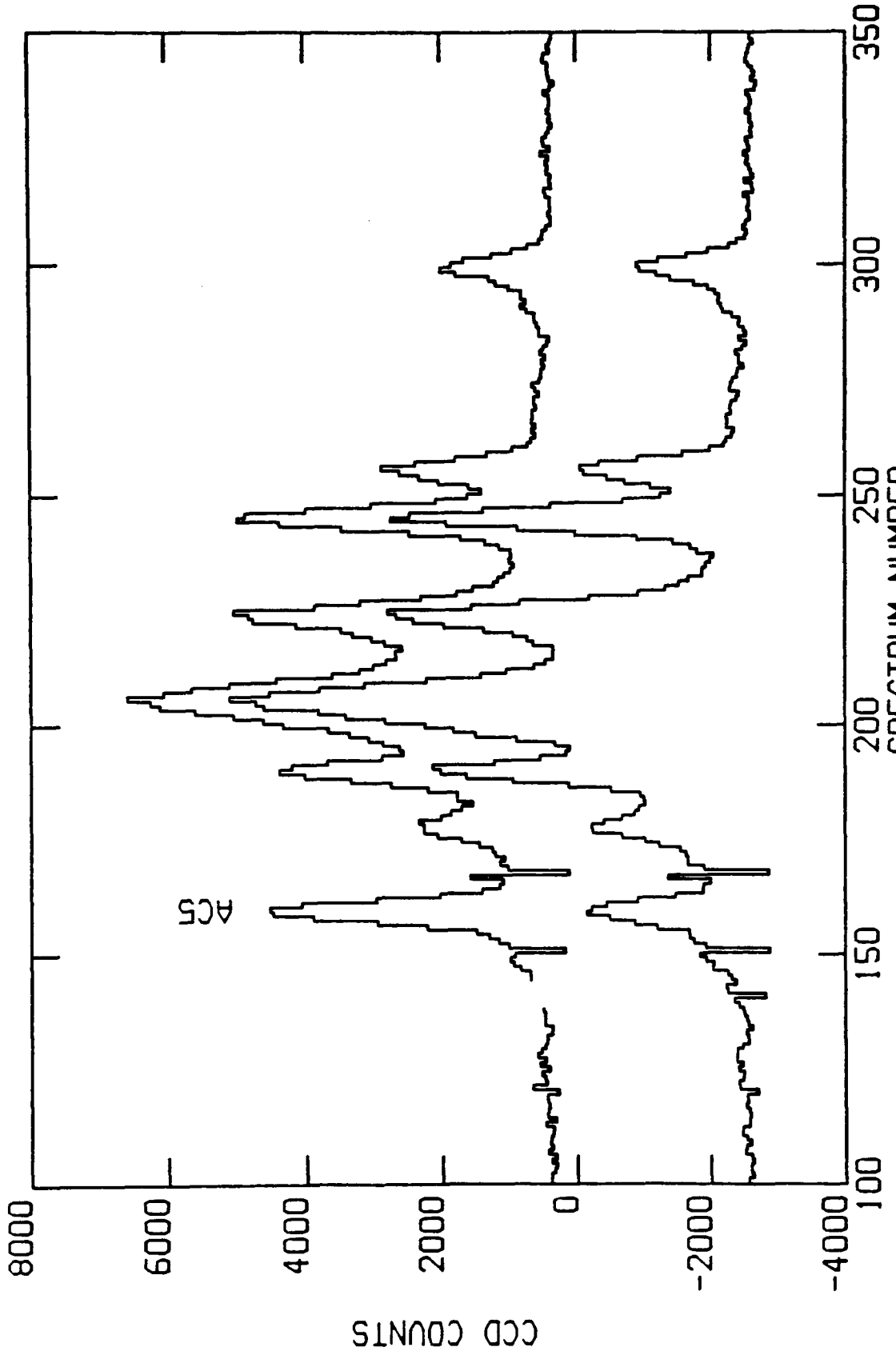

Figure 2.07 Cross sections near the cluster core in Hα light (above) and a nearby continuum band (below). The lower data are offset by -3000 counts, and points have been omitted in the upper curve around a charged particle event. The sharp features in the cross sections are due to "dead columns" on the CCD chip.

made near phase 0.35, when the Balmer absorption should be observed; in fact the lines are in emission. As expected at this phase, the velocity of Hα in the CCD observation is red shifted from the cluster, whose heliocentric velocity is 105 km s^{-1} (Peterson, Olszewski & Aaronson 1986). The velocity derived from the IPCS spectrum is consistent with this. Why AC5 should show emission at this phase is unclear, and no other observations of emission at this time have been published. This may, however, be because the observations presented here are the most sensitive to date.

During the CCD observations part of the slit was within 3" of the core. Figure 2.07 shows cross sections through the detector in Hα and continuum light. AC5 is approximately half as bright as the cluster peak in the Hα cross section. Since the observations are at what is probably a relatively weak phase for the Hα emission, AC5 probably outshines the core in Hα at certain phases. Thus it could well be the object observed by Peterson (1976), and the cause of the changes in Hα flux found by Grindlay & Liller (1977).

References

Aurière, M., & Cordoni, J.- P., 1981. *Astr. Astrophys. Suppl. Ser.* **46**, 347.

Aurière, M., Le Fèvre, O., & Terzan, A., 1984. *Astr. Astrophys.* 138, 415.

Aurière, M., Cordoni, J.P., & Koch-Miramond, L., 1985. IAUC 4101. (Note correction in IAUC 4112.)

Aurière, M., Maucherat, A., Cordoni, J.P., Fort, B., & Picat, J.P., 1986. *Astr. Astrophys.* **158**, 158.

Ayasli, S., & Joss, P.C., 1982. *Astrophys. J.*, **256**, 637.

Battistini, P., Bregoli, G., Fusi Pecci, F., & Lolli, M., 1985. *Astr. Astrophys. Supp. Ser.* **61**, 487.

Bopp, B.W., & Vanden Bout, P.A., 1972. *Pub. Ast. Soc. Pac.* **84**, 68.

Branduardi-Raymont, G., Corbet, R.H.D., Mason, K.O., Parmar, A.N., Murdin, P.G., & White, N.E., 1983. *Mon. Not. R. astr. Soc.* **205**, 403.

Brunt, C.C., 1983. *Ph.D. Thesis,* Cambridge.

Caloi, V., & Panagia, N., 1974. *Astron. Astrophys.* **36**, 139.

Castellani, V., 1980. In: *Globular Clusters* p. 65 eds. Hanes, D. & Madore, B., C.U.P. Cambridge.

Chandrasekhar, S. 1942. *Principles of Stellar Dynamics* Dover Publications Inc., New York.

Charles, P.A., Jones, D.C., & Naylor, T., 1986. *Nature* 323, 417.

Clark, G.W., Markert, T.H., & Li, F.K., 1975. *Astrophys. J.*, **199**, L93.

Cooke, B.A., Ricketts, M.J., Maccacaro, T., Pye, J.P., Elvis, M., Watson, M.G., Griffiths, R.E., Pounds, K.A., McHardy, I., Maccagni, D., Seward, F.D., Page, C.G., & Turner, M.J.L., 1978. *Mon. Not. R. astr. Soc.* **182**, 489.

Cowley, A.P., Crampton, D., & Hutchings, J.B., 1979. *Astrophys. J.*, **231**, 539.

Cowley, A.P., Crampton, D., & Hutchings, J.B., 1982a. *Astrophys. J.*, **256**, 605.

Cowley, A.P., Crampton, D., & Hutchings, J.B., 1982b. *Astrophys. J.*, **255**, 602.

Da Costa, G.S., & Freeman, K.C., 1976. *Astrophys. J.*, **206**, 128.

Dupree, A.K., Hartmann, L., Black, J.H., Davis, R.J., Matilsky, T.A., Raymond, J.C. & Gursky, H., 1979. *Astrophys. J.*, **230**, L89.

Fahlman, G.G., Richer, H.B., & VandenBerg, D.A., 1985. *Astrophys. J. Suppl. Ser.*, **58**, 225.

Ford, H., Margon, B., Jenner, D., & Klemola, A., 1978. IAUC 3306.

Forman, W., Jones, C., Cominsky, L., Julien, P., Murray, S., Peters, G., Tananbaum, H., & Giacconi, R., 1978. *Astrophys. J. Suppl. Ser.*, **38**, 357.

Fusi-Pecci, F., Rosino, L., & Voli, M., 1980. *Astron. Astrophys.* **85**, 269.

Giacconi, R., Murray, S., Gursky, H., Kellogg, E., Schreier, E., & Tananbaum, H., 1972. *Astrophys. J.* **178**, 281.

Giacconi, R., Murray, S., Gursky, H., Kellog, E., Schreier, E., Matilsky, T., Koch, D., & Tananbaum, H., 1974. *Astrophys. J. Suppl. Ser.*, **27**, 37.

Grindlay, J.E., & Liller, W., 1977. *Astrophys. J.*, **216**, L105.

Grindlay, J.E., Hertz, P., Steiner, J.E., Murray, S.S., & Lightman, A.P., 1984. *Astrophys. J.*, **282**, L13.

Gunn, J.E., & Griffin, R.F., 1979. *Astron. J.*, **84**, 752.

Harris, W.E., 1976. *Astron. J.*, **81**, 1095.

Heggie, D.C., 1979. In: *IAU Symposium 85; Star Clusters* ed. Hesser, J.E., Reidel, Dordrecht.

Hertz, P., & Grindlay, J.E., 1983. *Astrophys. J.*, **275**, 105.

Hertz, P., & Wood, K.S., 1985. *Astrophys. J.*, **290**, 171.

Hesser, J.E., McClure, R.D., Stetson, P.B. & Stryker, L.L., 1985. *J. R. Astron. Soc. Canada.* **79**, 237.

Horne, K., Verbunt, F., & Schneider D.P., 1986. *Mon. Not. R. astr. Soc.* **218**, 63.

Joy, A.H., 1949. *Astrophys. J.*, **110**, 105.

Katz, J.I., 1975. *Nature* **253**, 698.

King, I.R., 1962. *Astron. J.*, **67**, 471.

King, I.R., 1965. *Astron. J.*, **70**, 376.

King, I.R., 1966. *Astron. J.* **71**, 64.

King, I.R., 1980. In: *Globular Clusters* p. 249 eds. Hanes, D. & Madore, B., C.U.P. Cambridge.

King, I.R., 1984. In: *IAU Symposium 113; Dynamics of Star Clusters* eds. Goodman, J. & Hut, P., Reidel, Dordrecht.

LaSala, J., & Thorstensen, J.R., 1985. *Astron. J.*, **90**, 2077.

Lewin, W.H.G., & Joss, P.C., 1983. In: *Accretion Driven Stellar X-ray Sources* p. 41, eds. Lewin, W.H.G., & van den Heuvel, P.J., Cambridge University Press.

Lynden-Bell, D., & Wood, R., 1968. *Mon. Not. R. astr. Soc.* **138**, 495.

MacGregor, A.D., Phillips, J.P., & Selby, M.J., 1973. *Mon. Not. R. astr. Soc.* **164**, 31p.

Margon, B., Downes, R.A., & Gunn, J.E., 1981. *Astrophys. J.*, **247**, L89.

Margon, B., & Downes, R.A., 1981. *Astrophys. J.*, **274**, L31.

Mason, K.O., Murdin, P.G., Tuohy, I.R., Seitzer, P., & Branduardi-Raymont, G., 1982. *Mon. Not. R. astr. Soc.* **200**, 739.

Mason, K.O., Branduardi-Raymont, G., Cordova, F.A., & Corbet, R.H.D., 1987. *Mon. Not. R. astr. Soc.* **226**, 423.

McClintock, J.E., Canizares, C.R., & Tarter, C.B., 1975. *Astrophys. J.*, **198**, 641.

McClintock, J.E., & Remillard, R.A., 1986. *Astrophys. J.*, **308**, 110.

Peterson, A.W., 1976. *Astr. Astrophys.* **53**, 441.

Peterson, C.J. & King, I.R., 1975. *Astron. J.*, **84**, 427.

Peterson, R.C., Olszewski, E.W., & Aaronson, M., 1987. *Astrophys. J.*, **307**, 139.

Prior, C.P., Latham, D.W., & Hazen-Liller, M.L. 1985. In: *IAU Symposium*

113; Dynamics of Star Clusters eds. Goodman, J. & Hut, P., Reidel, Dordrecht.

Rosino, L., 1950. *Astrophys. J.*, **112**, 221.

Sandage, A., 1969. *Astrophys. J.*, **162**, 841.

Schaefer, B.E., 1986. *Publs. astr. Soc. Pacif.*, **98**, 556.

Smale, A.P., 1986. *D.Phil. Thesis.* Oxford.

Smale, A.P., Charles, P.A., Tuohy, I.R., & Thorstensen, J.R., 1984. *Mon. Not. R. astr. Soc.* **207**, 29p.

Thorstensen, J.R., & Charles, P.A., 1980. *Bull A.A.S.*, **11**, 721.

Trimble, V.L., 1980. In: *IAU Symposium 85; Star Clusters* p. 259, ed. Hesser, J.E., Reidel, Dordrecht.

van Albada, T.S., de Boer, K.S., & Dickens, R.J., 1979. *Astr. Astrophys.* **75**, L11.

van Albada, T.S., de Boer, K.S., & Dickens, R.J., 1981. *Mon. Not. R. astr. Soc.* **195**, 591.

Zinn, R., & Dahn, C.C., 1976. *Astron. J.*, **81**, 527.

Chapter 3

Spectroscopic Observations of AC211

3.1 Observations

AC211 was observed on the nights of 1986 August 1, 2 and 3 (hereafter Nights 1, 2 and 3), at the Observatorio del Roque de los Muchachos using the IPCS and 235-mm camera attached to the RGO Intermediate Dispersion Spectrograph on the 2.5m Isaac Newton Telescope. On Night 1 a grating with 632 lines mm^{-1} and a 0".7 slit were used, which gave a resolution of 1.5Å FWHM and a spectral range of λλ3250-5175. During the remaining two nights a 1200 lines mm^{-1} grating and 0".5 slit were used yielding 0.8Å resolution and a spectral range of λλ3950-4975. On Night 1 a 0.3ND filter was also used.

Normally the IPCS is used with about 60 resolution elements along the slit, and 2000 in the wavelength direction. In this mode the spectra cover approximately 1".5 each. However, for these observations the resolution along the slit ("X-gain") was set to give 0".4 pixels, and hence 192 spatial elements along the slit. This mode was used in order to oversample the seeing so that individual stellar profiles could be distinguished against the overall cluster light. During all three nights the seeing was never worse than 1".0, and once was 0".6. All the IPCS images were flat-fielded.

Differential atmospheric refraction at extreme zenith distances (greater than 50^{o} at the beginning and end of each night's observations) could have caused a severe problem with such a narrow slit. In order to counteract this the slit was rotated about 8 times during the night so as to follow the parallactic angle. I will refer to each set of

exposures at the same slit position angle as an observation, since such groupings are useful during spectrum extraction.

Each exposure lasted 600 seconds, and in addition about 10 Cu-Ar arc spectra were obtained during each night that were later used for wavelength calibration.

3.2 Spectrum extraction and calibration

Figure 3.01 shows cross-sections along the slit from an observation during Night 1; one is in blue light, the other in red. The positions of the stars in this figure demonstrate the major problem of the extraction; the position of a star changes with wavelength. The reasons for this, and the solution, are described in detail in Appendix 1. The result of the extraction process is a set of arc and object spectra (the latter without background subtraction) similar to those which would result from a more conventional extraction. The only exception to this is that the statistical errors are smaller by a factor ~1.05 than the square root of the number of counts. To account for this factor the values of χ^2 quoted have been increased by 10%, but the values of errors quoted have not been corrected, since it would only decrease them by 5%.

About 12 lines in each arc spectrum were fitted with a 5th order polynomial, which gave a reliable wavelength calibration in the range λλ3950-4950 for Night 1 and λλ4100-4950A for Nights 2 and 3. In order to estimate the error in the wavelength calibration I show, in figure 3.02, the wavelength associated with a particular channel as a function of time for each night. The positions scatter over about $\pm$0.2Å for Night 1 and $\pm$0.1Å for Nights 2 and 3.

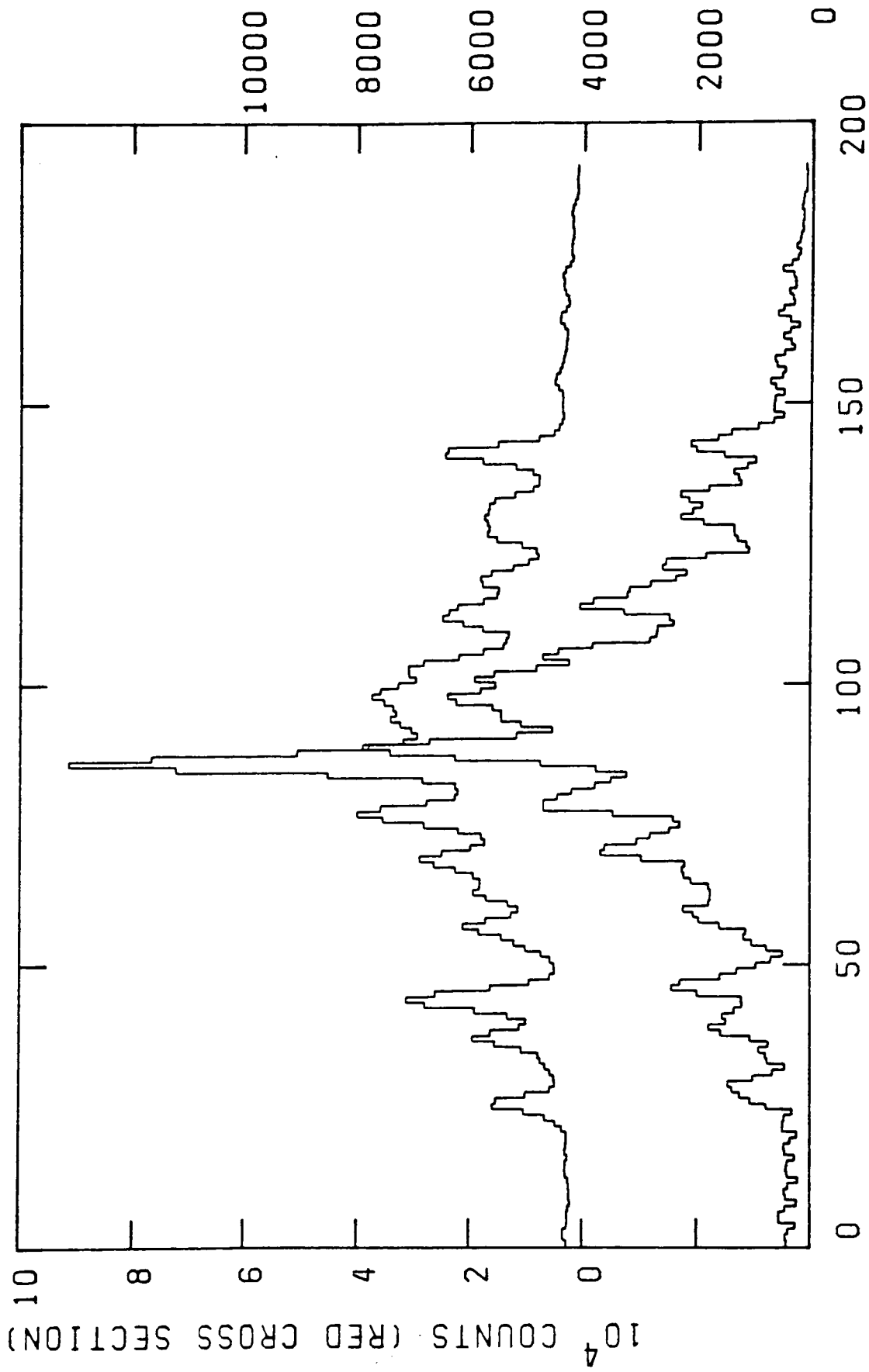

Figure 3.01 Two cross sections of a typical IPCS frame taken perpendicular to the dispersion direction. The lower is a sum over λλ3305-3738, and the upper λλ4693-4986. The position of AC211 is marked for the upper cross section.

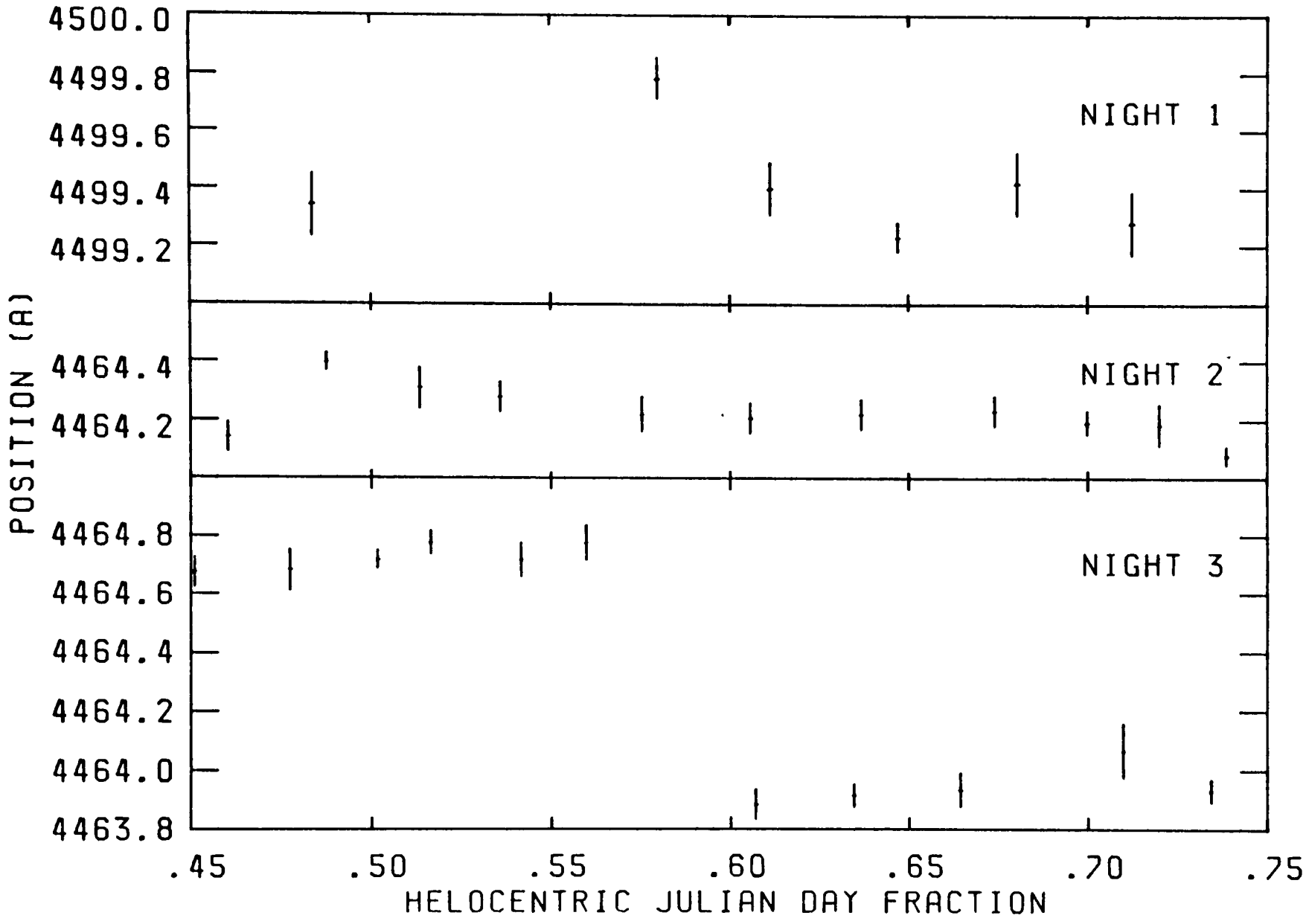

Figure 3.02 The wavelength corresponding to channel 1300 (Night 1) or 1000 (Nights 2 and 3) as a function of time. The horizontal bars are the length of the integration, the vertical bars the root-mean-square residual from the 5th order polynomial fitted to the arc lines. The break during Night 3 is when the grating angle was moved.

A second check was performed using the planetary nebula K648, which lies in M15. At some time during all three nights the slit was oriented such that this nebula was in the same IPCS image as AC211, and the nebula was also observed separately on the first night. These spectra were extracted and arc calibrated in the same way as AC211. A Gaussian profile was then fitted to the Balmer emission lines in order to determine the position of the line (see Table 3.1). The errors from the fitting process were so small (<0.04Å for Night 1 and <0.01Å for the other two nights) that the errors in the velocity determination are dominated entirely by the error in the arc calibration itself. I therefore assumed that the errors for each line were the same (in wavelength space) and performed a least squares fit of all the measured wavelengths of the lines to their laboratory wavelengths, leaving only the radial velocity as a free parameter. The assumed errors were adjusted until the reduced χ^2 was 1. The resulting errors were 0.3Å (Night 1) and 0.1(An (Nights 2 and 3).

These errors are a factor 2 or 3 larger than the root-mean-square residuals from the polynomials fitted to the arc lines. However, they are negligible compared with the uncertainties in the line fitting discussed below, and so arc calibration errors will henceforth be ignored.

Flux calibration was carried out in the normal way, correcting for the narrow slit and extraction window as detailed in Appendix 1. By following stars other than AC211 it was found that the instrumental response function went through periods (~1 hour) when the number of counts per unit flux declined and then recovered. Further, the effect was differential across the detector, the blue being more badly affected

Table 3.1 Heliocentric velocity of K648

	Hβ	Hγ	Hδ	Fitted Mean
Night 1 (a)	-141	-95	-148	
Night 1 (b)	-120	-105	-104	-119±8
Night 2	-130	-128	-129	
Night 3	-125	-119	-110	-124±3

Notes: All velocities are in km s^{-1}.
Night 1 (a) was not observed simultaneously with AC211.

Table 3.2 Velocities of HeI lines

Line	Heliocentric Velocity	Full Width Half Max'm	χ^2
4921	-241±9 km s^{-1}	151±7 km s^{-1}	0.91
4471	-254±8 km s^{-1}	259±5 km s^{-1}	1.35
4713	-178±11 km s^{-1}	162±9 km s^{-1}	1.48
4144	-155±11 km s^{-1}	146±8 km s^{-1}	1.81
4388	-292±21 km s^{-1}	387±22 km s^{-1}	1.99

Table 3.3 HeI ephemeris

Gamma	4467.56 ± 0.14 Å
Amplitude	0.59 ± 0.22 Å
	JD 2 446 645.367 ± 0.019 (Change from red to blue shift.)

Table 3.4 Log of *IUE* observations

Image #	Date	Exposure	Comments
SWP1479	May 1978	210 mins	
SWP1641	May 1978	?	Almost no flux, useless.
SWP10161	Sept 1980	160 mins	HeII 1640 clearly visible.
LWR1457	May 1978	100 mins	Some over exposure.
LWR1820	July 1978	60 mins	
LWR7589	Apr 1980	60 mins	
LWP1382	Nov 1981	60 mins	Over exposed.

than the red, though the effect was always less than 20% between 4471Å and 4686Å. The spectra which were calibrated were chosen so that they did not coincide with these events, and the various standard star observations checked with each other for consistency. It should be emphasised that these events had no effect upon wavelength information in the data.

3.3 The summed spectra

Figure 3.03 shows the sum of all spectra from the first night, and figure 3.04 the sum of Nights 2 and 3. The spectra show Balmer absorption, HeII (4686) emission and λ4026, λ4144, λ4388, λ4471, λ4713 and λ4922 HeI absorption. There is an unidentified absorption feature at 4225Å.

Table 3.2 shows the velocities for the HeI lines obtained by fitting a Gaussian to the sum of all the spectra from Nights 2 and 3. The velocities of the two strongest lines agree, but the three weaker ones show a scatter much larger than their errors. As they also have the highest values of χ^2 their parameters are unreliable. The gamma velocity measured from the two strongest lines is $\simeq$-150 km s^{-1} with respect to the cluster. (The velocity of the cluster is -105 km s^{-1}, see Peterson, Olszewski & Aaronson 1986.) The velocity of K648 measured from some of the same IPCS images as AC211 is only 15 km s^{-1} with respect to the cluster, giving an independent check of the accuracy of our velocity measurements. Thus I believe the radial velocity for AC211 is correct.

An enlargement of the Balmer lines is shown in figure 3.05. There is also a blue shifted component in each of these lines, in addition to

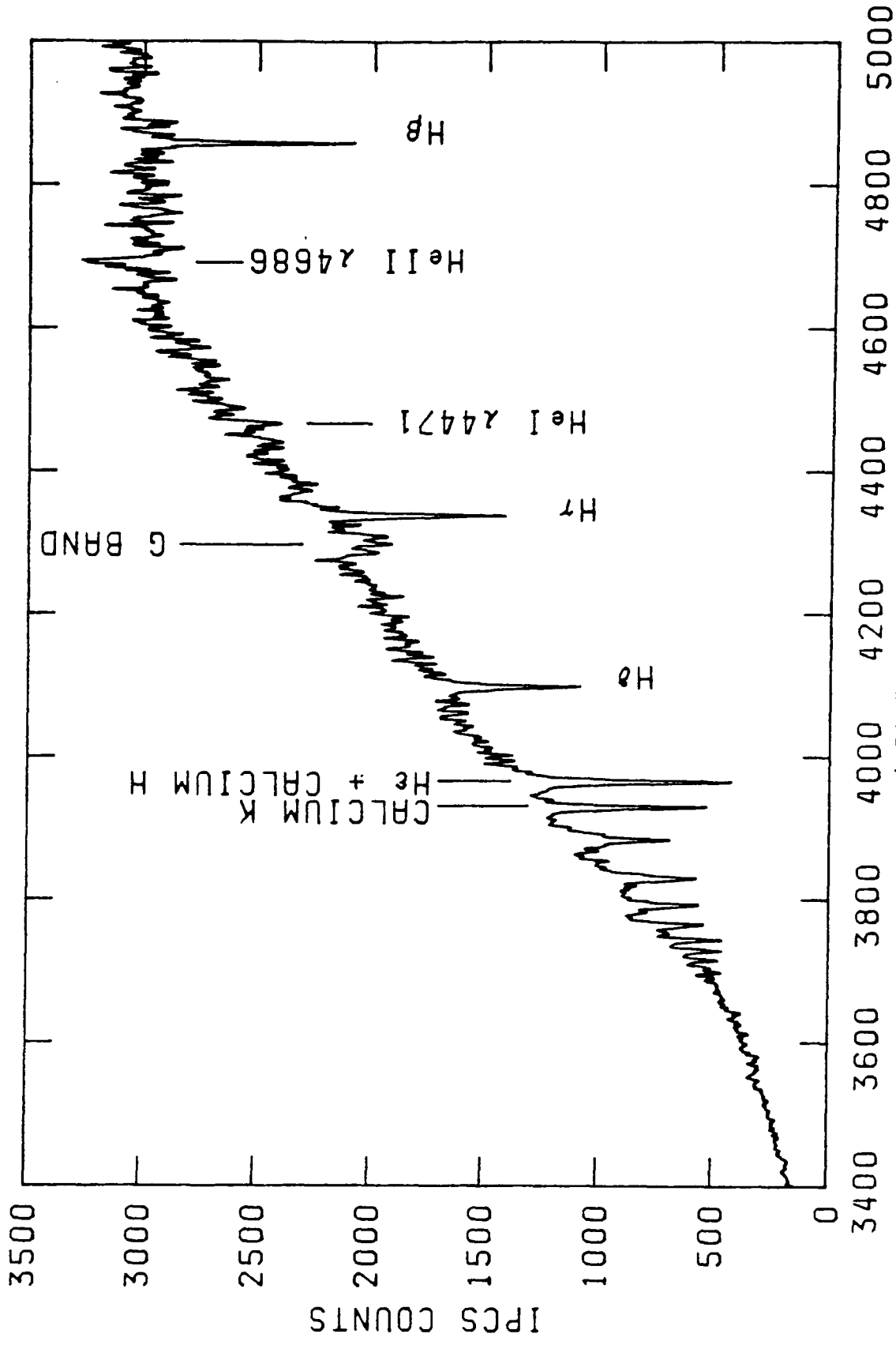

Figure 3.03 Sum of all the spectra from Night 1.

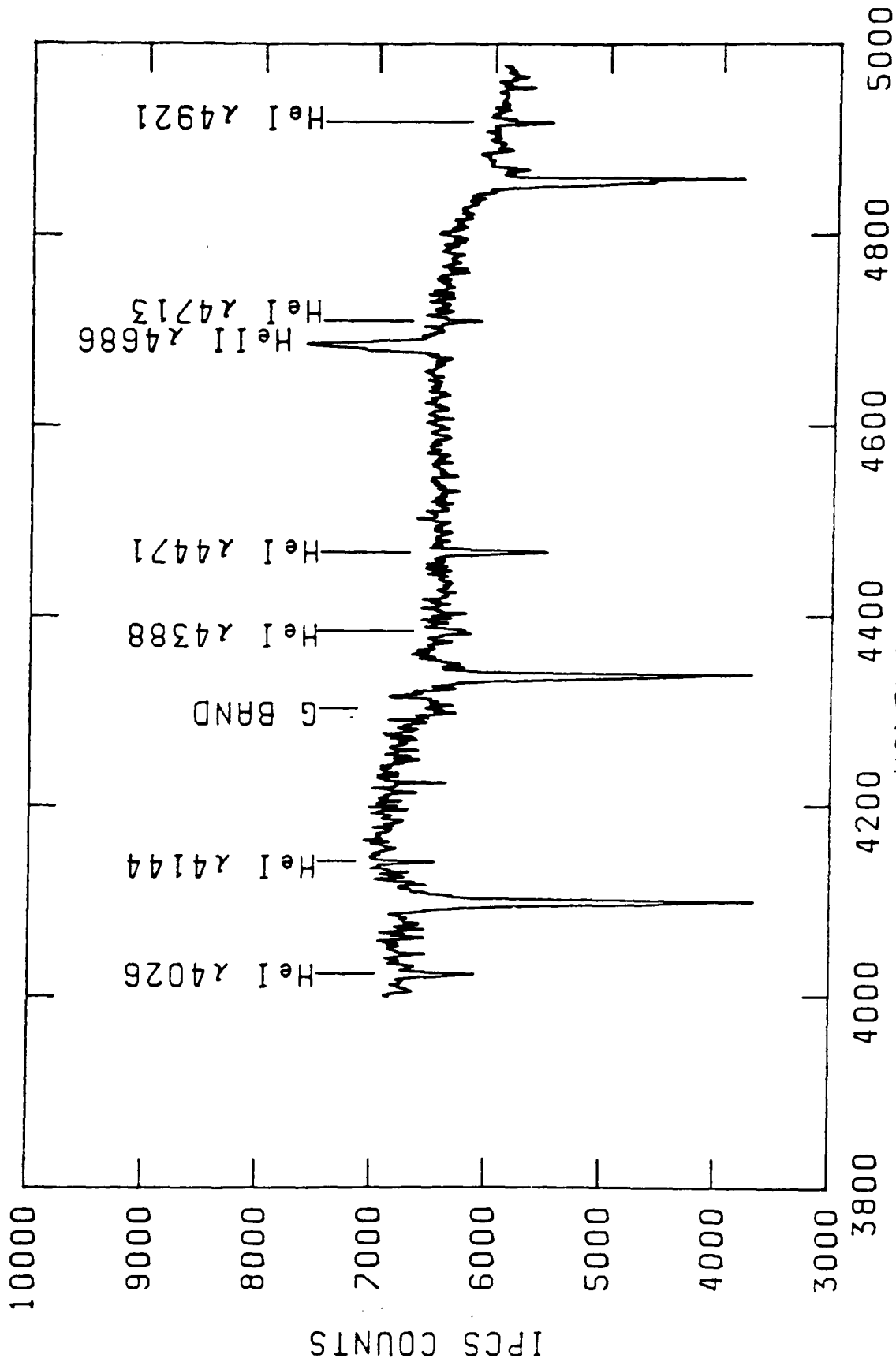

Figure 3.04 Sum of all the spectra from Nights 2 and 3.

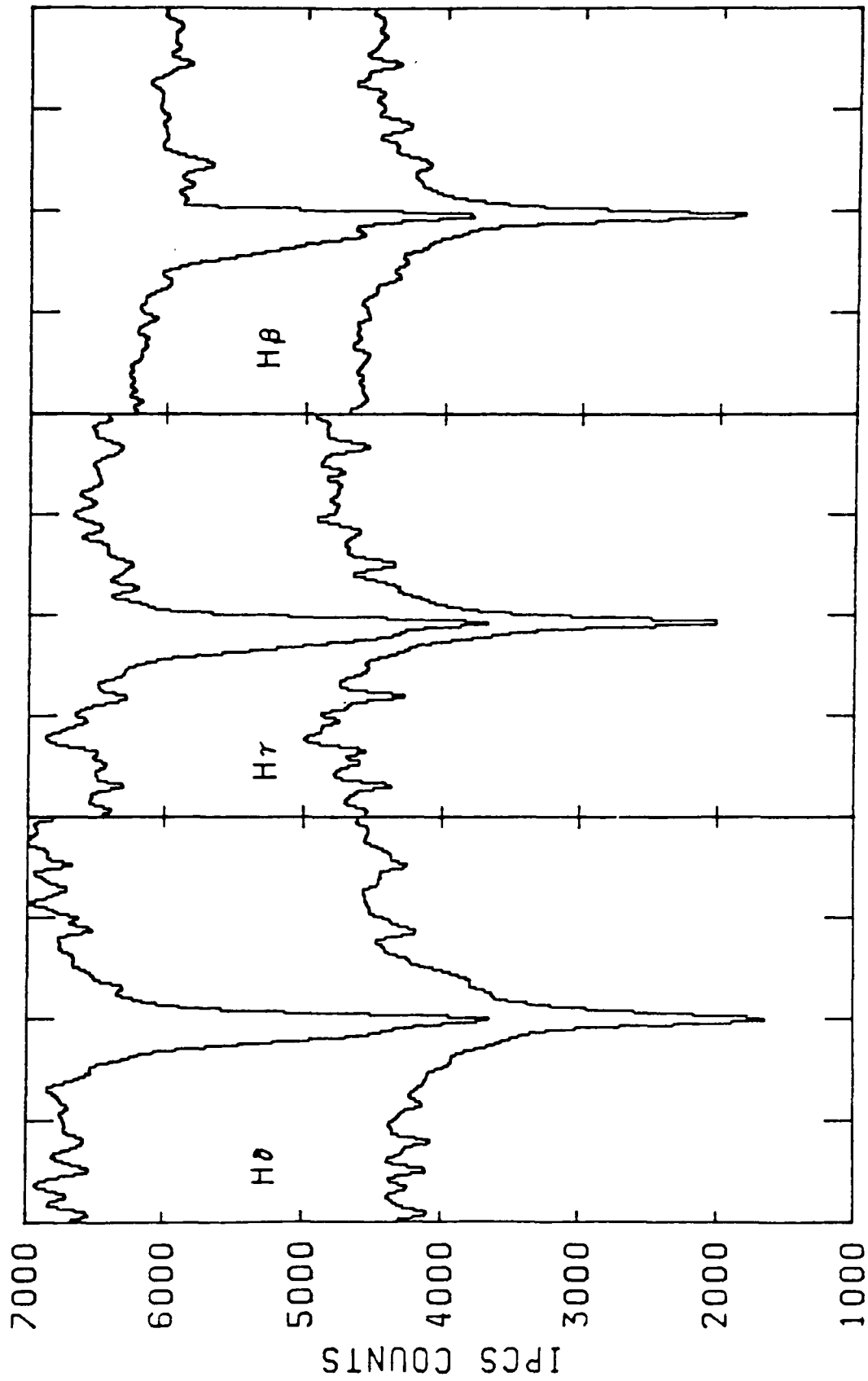

Figure 3.05 An enlargement of the Balmer line profiles of figure 3.04 (upper curves) compared with a mean profile from the core region. The latter have had 1000 counts subtracted from them. Emission infilling of the red wing declines moving from Hβ to Hδ. There is also a second blueshifted absorption component in the profiles of AC211.

emission infilling of the red wing. The infilling declines from Hβ to Hδ. The sharp, rest wavelength component is probably due to the background cluster stars, as is the G band at λλ4290-4315.

HeII λ4686 shows a broad (≃800km s^{-1}) base approximately at rest with respect to the cluster, and a peak which is redshifted by ≃100 km s^{-1}.

3.4 The HeI λ4471 line

The signal to noise in the 600 second integrations was too low to allow a study to be made of the HeI λ4471 velocity on this timescale. I therefore summed them in such a way that the elapsed time between the the start of the first and the end of the last spectrum in each sum was about an hour. These will be referred to as the "1 hour" sums.

In order to find the position of HeI λ4471 a Gaussian profile was fitted to each 1 hour spectrum using a non-linear least squares method. One of the 1 hour sums from Night 3 was too weak to be fitted, and only the last two sums from Night 1 could be fitted. The positions obtained for the lines are shown in figure 3.06.

A Fourier transform of the time dependence of the velocity shifts showed peaks at 56, 14, 9 and 6 hours. The data were fitted by sine functions near each of these periods. The periods at 56 and 6 hours have unacceptably high reduced χ^2 values of 1.7 and 2.1 respectively. The remaining two periods are 14.03±0.25 hours, and 9.1±0.5 hours. Figure 3.07 shows the data folded on these two periods.

The 14 hour fit does not reproduce the trend of the points near phase 0.1 well, which is reflected in the marginal change of the reduced χ^2 from 1.04 (14 hours) to 0.98 (9 hours). For this reason the

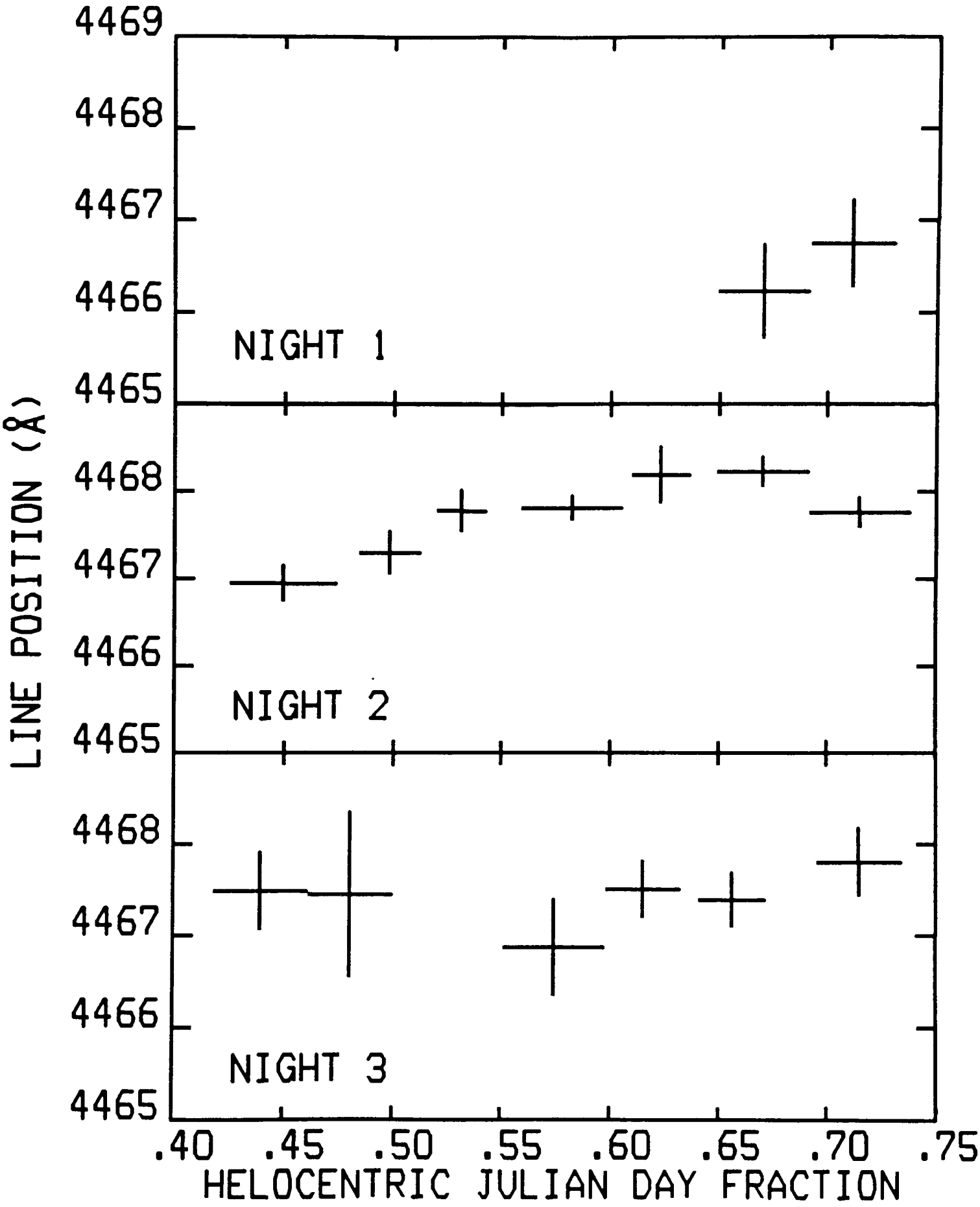

Figure 3.06 The HeI radial velocity points from each night.

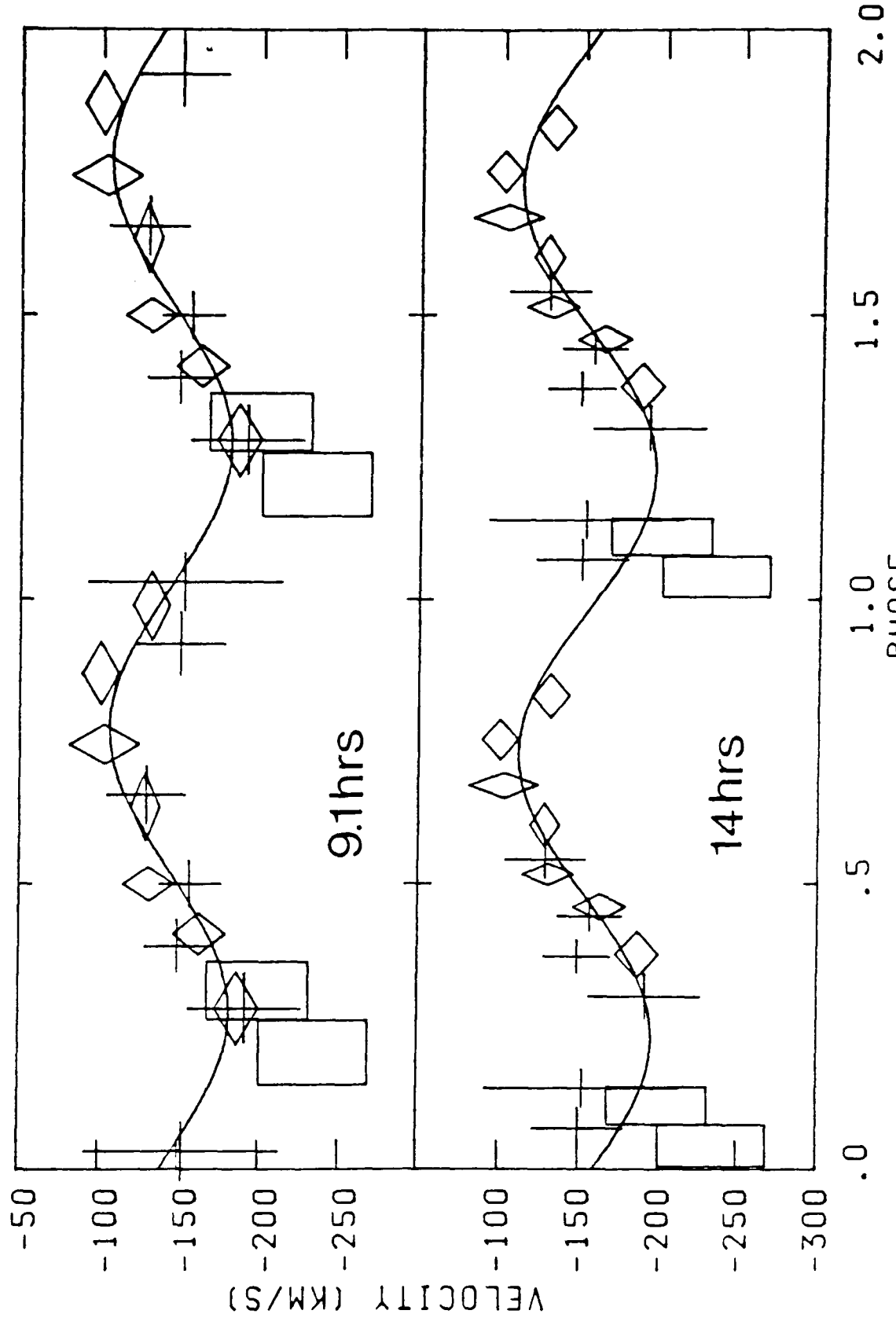

Figure 3.07 The radial velocity curve folded on both the 9 and 14 hour periods. The points from Night 1 are shown as boxes, those from Night 2 diamonds, and Night 3 as crosses. In all cases the extent of the symbol in the x direction is the phase covered by the 1 hour sum, and the extent in the y direction is the error in position.

spectroscopy alone suggests that the 9 hour period is the correct one.

Since the discovery of this period (Naylor *et al.* 1986) the same period has been discovered in optical photometry (Ilovaisky *et al.* 1986, 1987) and in archival X-ray data (Hertz 1986, 1987) neither of which suffer from the 14 hour alias. The most accurate period is now the X-ray period of 8.66 hours, since the optical photometry suffers from a 1 year alias problem. Hence the HeI line velocities were fitted to a sinusoid with the period fixed at 8.66 hours. The results for the other parameters of the fit are presented in Table 3.3.

I will define the point where the velocity of the HeI line is midway between maximum red and blue shift as phase zero. The spectroscopic phasing is chosen such that if the HeI velocity shift is due to the compact object, the latter will be eclipsed by the secondary at phase zero.

3.5 The phase folded data

The data from Nights 2 and 3 were folded on the X-ray period into 8 phase bins. The resulting HeII profiles (figures 3.08 and 3.09), show that the line appears to drift to the red with time. Figure 3.09 shows how the HeII flux suddenly turns on at phase 0.22, and then gradually declines, finally disappearing near phase 0.94. It was found that at similar phases the gross structure of the HeII line was the same during Nights 2 and 3, but that there are changes in detail. This is shown in figure 3.10, where profiles from the same phase, but different nights, are plotted. The HeII flux in the Night 3 spectra in the phase 0.71 sum was evaluated by numerical integration as 9.9×10^{-15}ergs $cm^{-2}s^{-1}$, with an uncertainty ~20% due to systematics in the flux calibration.

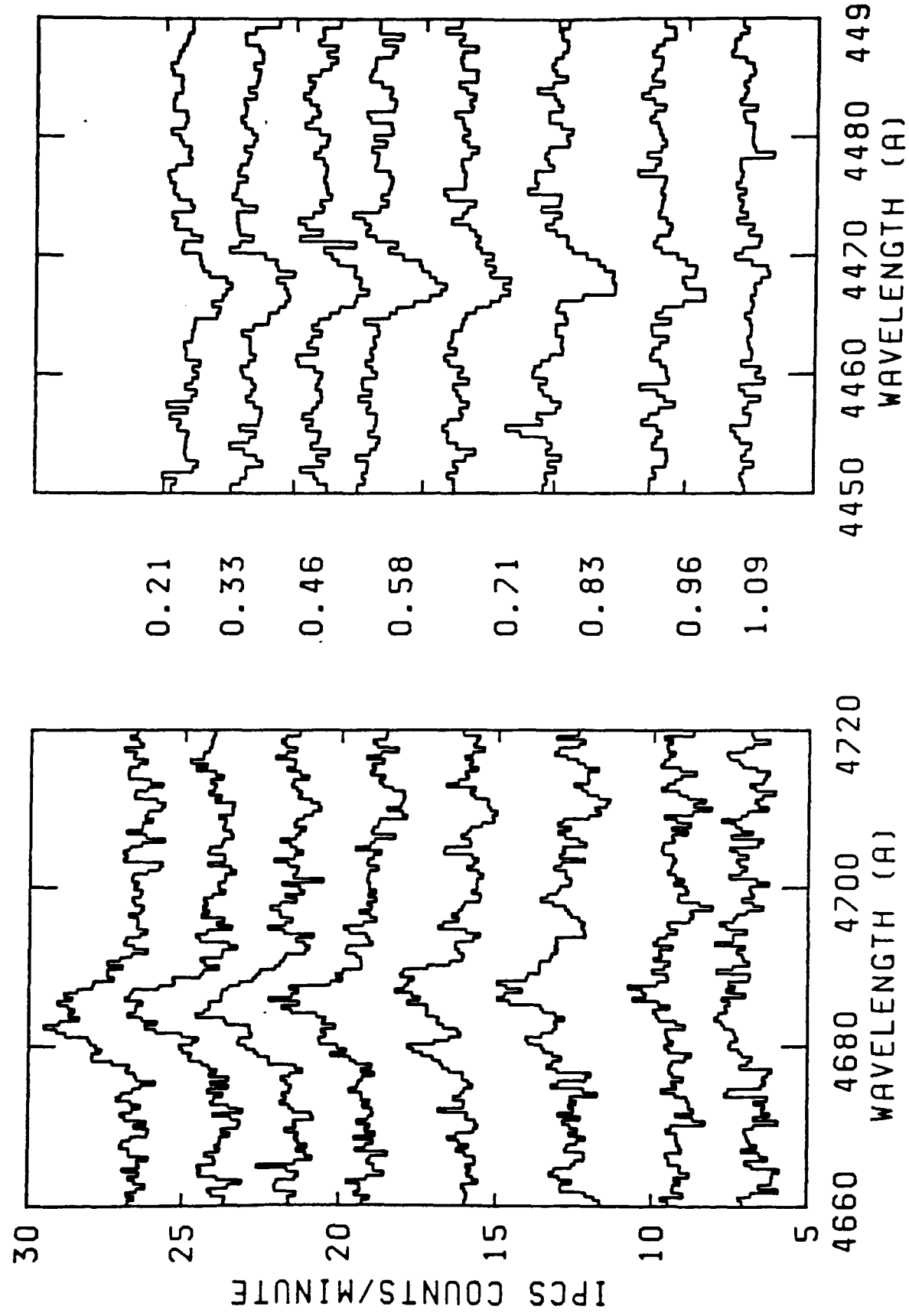

Figure 3.08 The HeI (right) and HeII (left) line profiles folded on the orbital period. The numbers between the panels are the orbital phase of each spectrum.

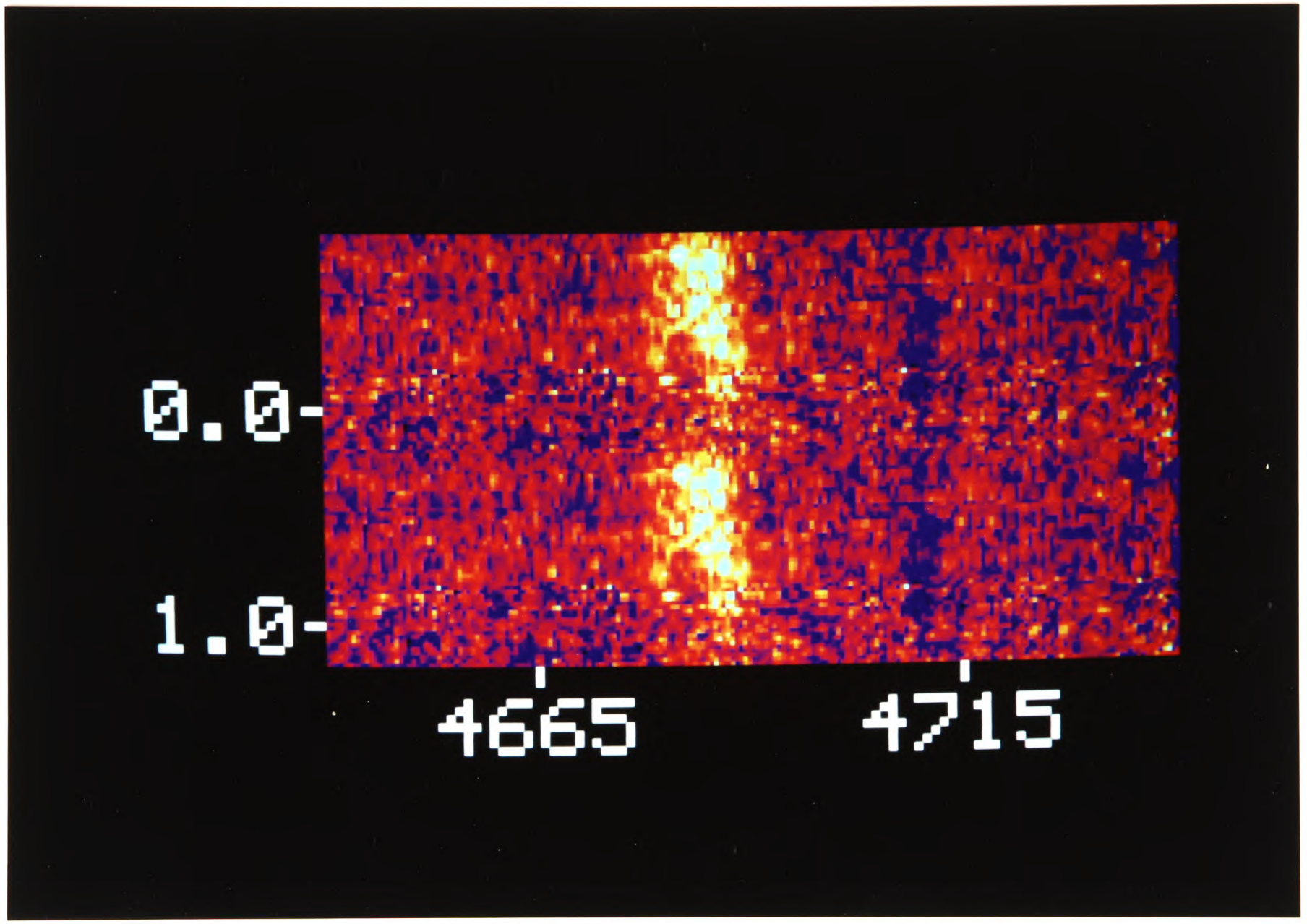

Figure 3.09 A colour coded plot of the phase folded spectra of the HeII λ4686 line. The data have been repeated for clarity. Each wavelength bin is 0.5Å, each time bin 10 minutes. HeI λ4713 can be seen as a dark vertical bar. The colour coding is (from low to high counts), blue, red, yellow, cyan, white.

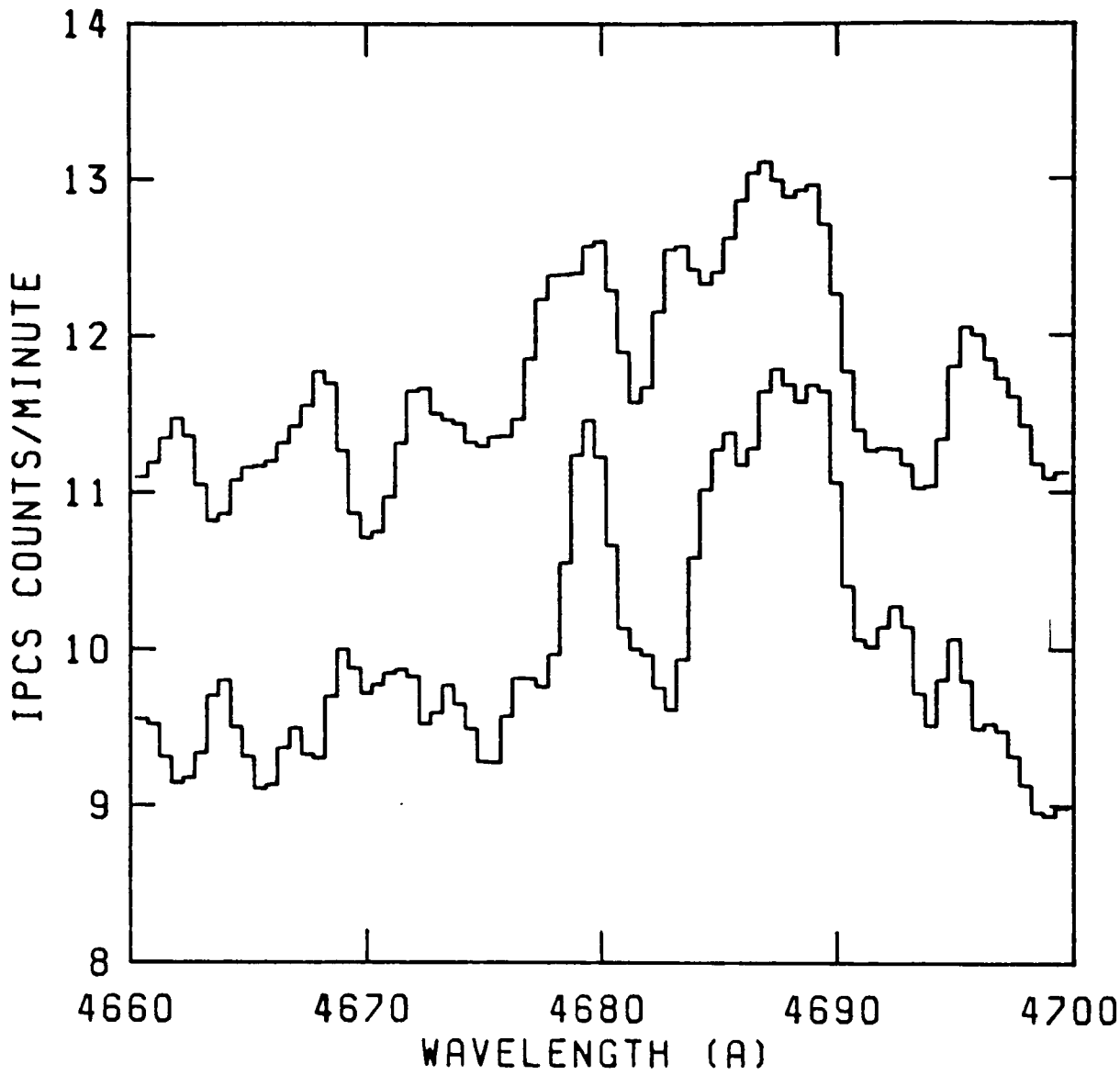

Figure 3.10 The sum of the spectra from Night 3 (upper) and Night 2 (lower) which were summed to make the phase 0.71 sum in figure 3.08. Both spectra have been smoothed 3 times, and the lower one has been offset by -10 counts.

In an attempt to follow the movement of the blue wing in the Balmer lines the profile of the underlying stars was first estimated by fitting a Voigt profile to a sum of spectra from the core of M15, excluding the region around AC211. The Voigt profile and a blue shifted Gaussian were then fitted to the phase folded spectra. The pressure width, Doppler width and position of the Voigt profile were fixed to the values found in the overall cluster core spectrum. The results for Hδ are shown in figure 3.11, with the velocities of the HeI λ4471 lines overlaid. Hδ was chosen so that the emission contamination of the red wing of the Voigt profile would be small. Although the positions of the Balmer and HeI lines differ, this difference is probably not significant as emission contamination will have some effect. I therefore conclude that the radial velocity curve of the blue component in Hδ is consistent with that for HeI λ4471.

3.6 IUE spectroscopy

Table 3.4 lists the *IUE* exposures using the large (10"x20") aperture placed over the center of light of the cluster. The standard (IUESIPS) reduction of the data produces an image similar to an IPCS image, with pixel boundaries running parallel and perpendicular to the dispersion direction (the line-by-line-spectrum). I re-extracted the spectra using 15 lines of this image, which is the normal extraction for an object which fills the aperture. All the spectra except SWP1461 and LWR1457 were used to make the summed spectrum shown in figure 3.13. The absorption feature at 1300Å is probably a combination of OI, SiII and SiIII. The feature is present in the cluster's horizontal branch stars, but might also be expected from LMXBs, hence its origin is unclear.

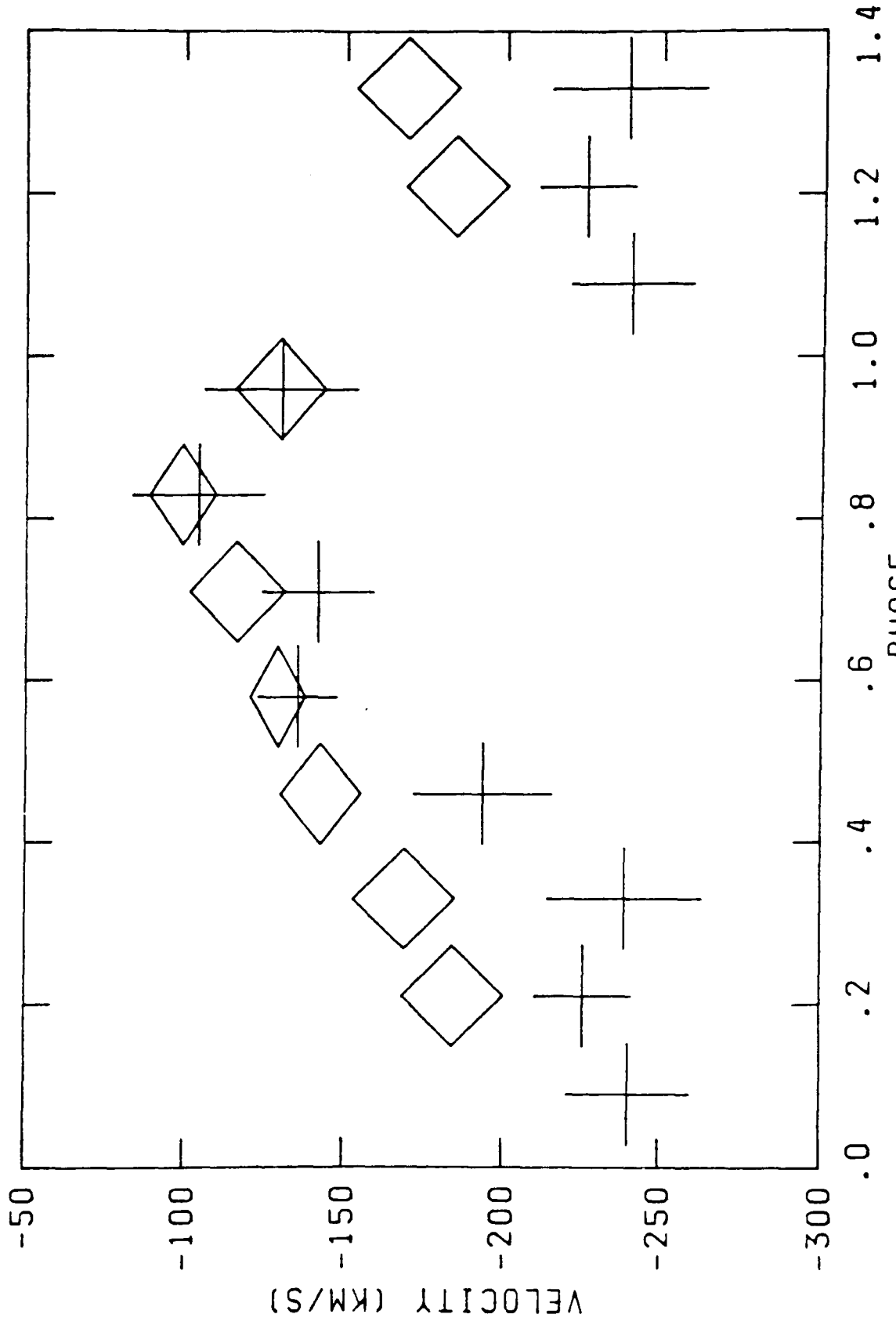

Figure 3.11 The positions of the blueshifted Gaussians fitted to H6 (crosses), and those fitted to HeI λ4471 (diamonds) as a function of phase. The extent of the symbol in the x direction is the duration of the phase bin, and the extent in the y direction is the error in velocity.

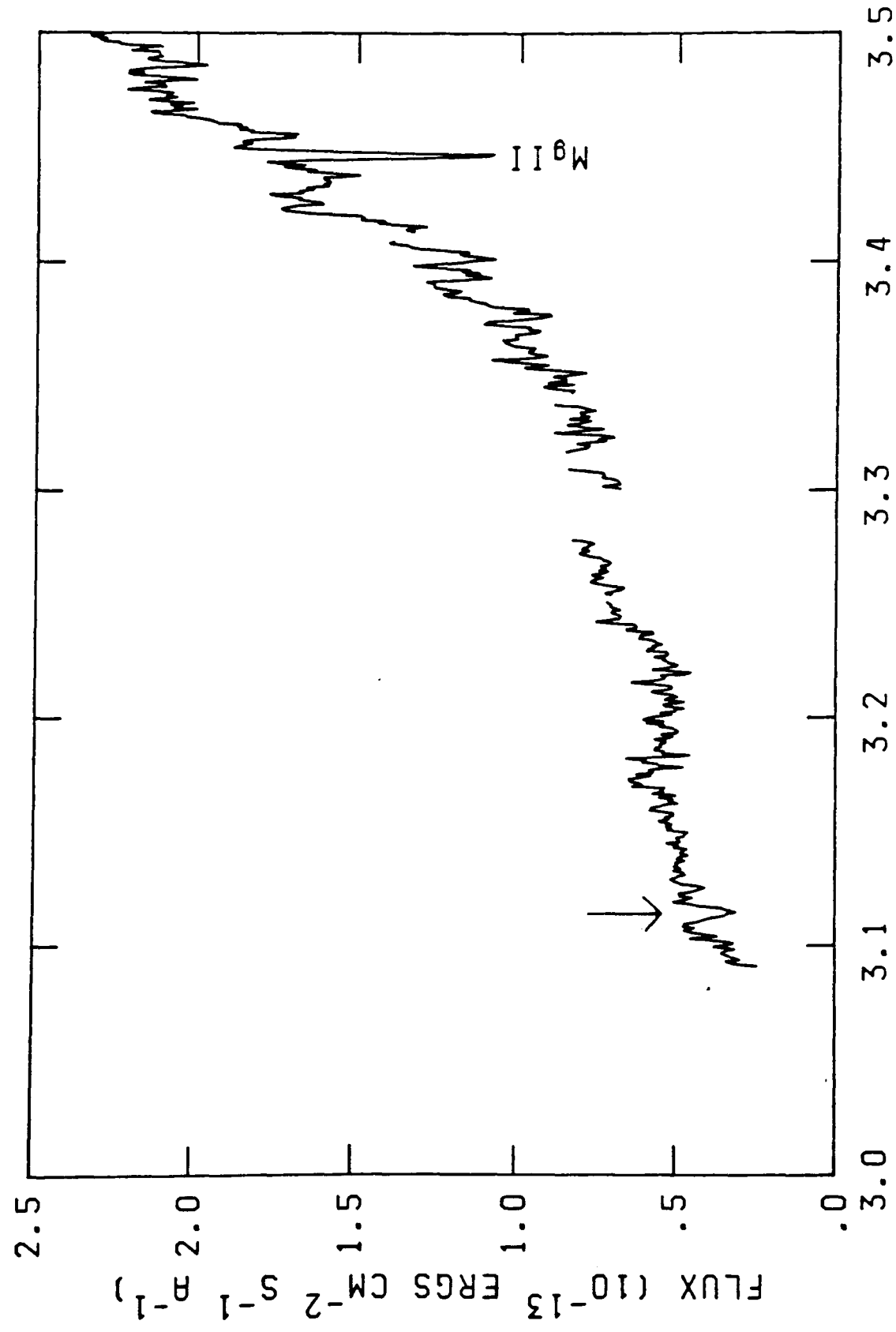

Figure 3.12 The summed IUE spectra. The absorption feature marked with the arrow is probably a combination of OI, SiII and SiIII.

The 3 LWP spectra show no significant variation. SWP10161 is, however, bluer than SWP1479, and shows HeII λ1640 emission. The spectra are shown in figure 3.13, together with the difference between them. There is a ridge-like feature in the SWP10161 image which has the effect of increasing the flux in the region 1265-1420Å by $\sim 1 \times 10^{-14}$ergs $cm^{-2}s^{-1}Å^{-1}$, although this clearly cannot account for the entire difference between the 2 spectra.

The most likely source for the HeII emission is AC211. This is supported by the HeI λ1640 flux (1.1×10^{-13}ergs $cm^{-2}s^{-1}Å^{-1}$ which is 11 times that in AC211's HeII λ4686 line. This compares favourably with the theoretical ratio of 7 (Seaton 1978) remembering the known variability of the HeII λ4686. Although the aperture was centered on the cluster's center of light for the two exposures, the position angle varies by about 20^{o}. This means AC211 (<3" from the cusp) should be well within the aperture in both exposures, and thus the variation in the HeII λ1640 line is intrinsic to the source.

It is possible that the difference in continuum level between the two spectra could be due to a horizontal branch star falling within the aperture for SWP10161, and outside in SWP1479. Alternatively, it might be due to AC211 varying. If this is the case then the flux from AC211 in the brighter of the two spectra is in the range $(1-6) \times 10^{-14}$ergs $cm^{-2}s^{-1}Å^{-1}$.

If the continuum flux variation is not due to AC211, the flux in SWP1479 represents an upper limit to the flux from AC211.

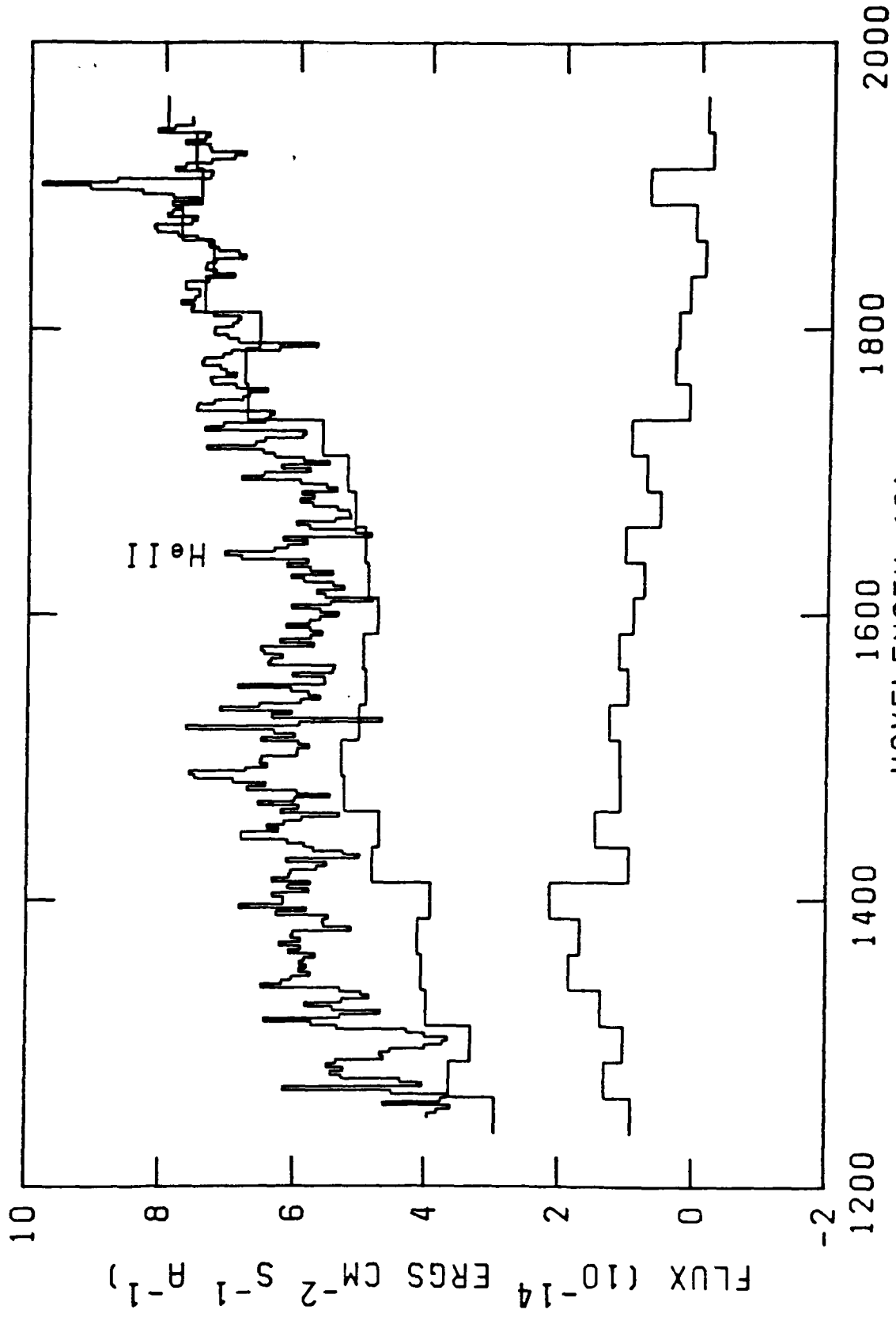

Figure 3.13 SWP10161 (upper curve), SWP1479 in 25Å bins (middle curve) and their difference in 25Å bins (lower curve).

3.7 Discussion

3.7.1 An ADC model of AC211/4U2127+11

The interpretation of AC211 that follows is an expansion of that suggested by previous authors (Aurière *et al.* 1984, 1986, Charles *et al.* 1986, Hertz 1987). In this framework the system is considered to be an eclipsing, or near-eclipsing binary with an inclination $>80^{o}$. The accretion disc has considerable vertical structure, probably in the form of a rim around the outer edge. The height of this wall varies with position around the disc, being highest at the point where the accretion stream impacts the disc edge (see figure 3.14). The thickness of the disc and the high inclination of AC211 effectively obscure the compact object from us. The X-rays we detect are therefore from an "accretion disc corona" (ADC) which surrounds the compact object, but which is sufficiently large to be visible from Earth despite the disc structure. This ADC scatters only a fraction of the X-rays from the compact object and inner disc into our line of sight. This explains the low ratio of the X-ray to optical flux, $L_x/L_{opt}\simeq 50$ (Hertz 1987), compared with the more typical value of ~500 for LMXBs (van Paradijs, 1983). Just such an ADC model has been proposed for 2A1822-371 (White *et al.* 1981), 4U2129+470 (McClintock *et al.* 1982), 2S0921-630 (Mason *et al.* 1987) and Her X-1 in its low state (Jones & Forman 1976).

Hertz (1987) suggested that, as the height of disc wall obscuring the ADC varies, it will modulate the X-ray flux. Two types of variation will occur; a periodic minimum, every time the stream impact region intercepts our line of sight to the source, and a random fluctuation, since the wall structure will not be stable. This is indeed what is observed. Hertz (1987) found a factor 3 variability in 3.5 hours,

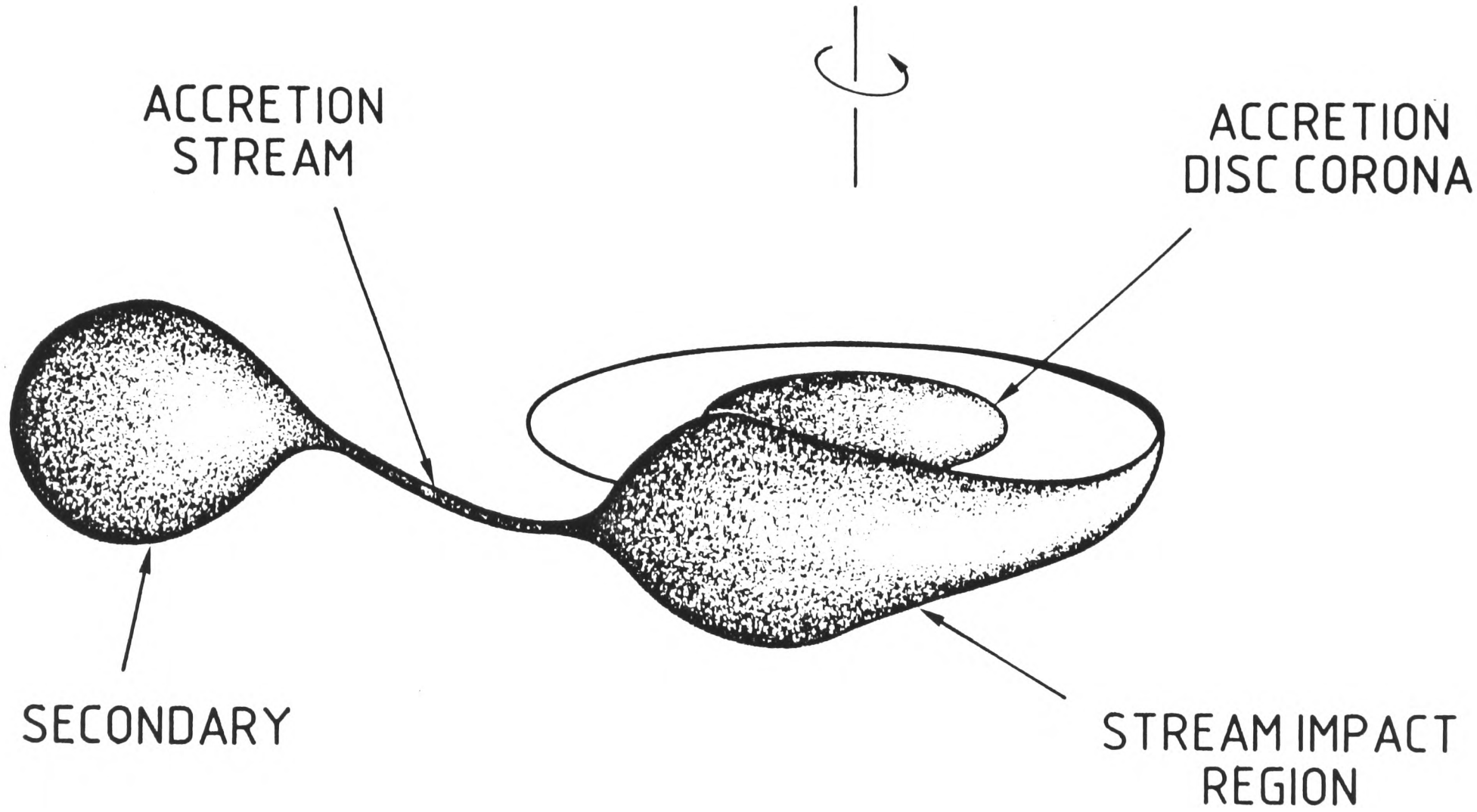

Figure 3.14 A schematic of AC211 near spectroscopic phase 0.75. The relative sizes of the disc structure, accretion disc and accretion disc corona are uncertain, but the figure illustrates how the blue shifted (left hand) side of the corona can be obscured more than the red.

compared with only a 24% orbital modulation. The random fluctuations will also conceal the orbital modulation in the short (~2 orbital cycle) EXOSAT observations (Callanan *et al.* 1987).

However, AC211 does not fit simply into the ADC model as described above. All the other sources mentioned above show X-ray eclipses, in addition to the modulation caused by the stream impact region. There are three possible reasons why this is not seen in AC211. Firstly, as I shall argue in 3.7.3, the secondary is smaller compared with the size of the disc structure than in other LMXBs, and thus the eclipse is less easily distinguished from obscuration of the ADC by the disc structure itself. Secondly, as Fabian, Guilbert and Callanan (1987) pointed out, the low metallicity of M15 means that the ADC will be larger than in other LMXBs. Thus, at the time of eclipse the secondary will cover a smaller area of the ADC, and the eclipse will be shallower. This effect will be accentuated by the small secondary. Finally, the high X-ray variability of the source will tend to mask any periodic modulation.

Ilovaisky *et al.* (1987) discovered a periodic modulation in the optical light curve, but do not discuss its origin. In fact, disc structure could explain the shape of their light curve. It is never quite the same from one orbital cycle to the next, the dip is large and lasts about 0.5 of a cycle, and has a slower ingress than egress. This behaviour is due to the shape of the stream impact region (see figure 3.14). The one major difference between the X-ray and optical modulation is that whilst in the X-ray band only the ADC is luminous, in the optical both the disc and stream impact region will also contribute significant flux. The stream impact region will be relatively cool, which means that the optical modulation should be greater at shorter

wavelengths, since hot regions are being obscured by a cooler region. Again, observations support this interpretation, the U band modulation is substantially deeper than that in the V band (Aurière *et al.* 1986).

An alternative explanation of the optical light curve may be afforded by analogy with 4U2129+470, a source that shows a large modulation in the optical, which is thought to be due to the changing aspect of the X-ray heated face of the secondary (Thorstensen *et al.* 1979). However, it must be remembered that in AC211 all deviations from the mean light curve would have to be explained by variable X-ray emission, or disc structure shadowing the secondary. The photometric data of Ilovaisky *et al.* from 1986 July 10 showed the source to be constant for 5.5 hours, including the normal time of minimum or "dip". If this were due to the X-ray heating turning off, the optical flux should fall to the level observed at the bottom of the dip. In fact the source was steady at a level 0.6 mag above this.

Whilst not ruling out the X-ray heating model, I feel that it is an unnecessary addition, since the stream impact bulge would still be required in order to explain the periodic X-ray modulation. Furthermore, it offers no convincing explanation of the random variability, which in the stream impact bulge model is due to changes in disc structure.

If some of the HeII emission comes from the disc or a corona, then it should be obscured in the same way as the optical continuum. Further, as the stream impact region will always be higher on the side of the disc moving towards the observer, it will always obscure the blue wing of the HeII line more heavily than the red (see figure 3.14) This is the effect seen in figures 3.08 and 3.09. From the profile labelled phase

0.58 onwards the HeII flux declines and shifts redwards. The relatively rapid reappearance of the HeII (< 0.1 of an orbital cycle) probably occurs when the secondary moves out of the line of sight. If this is so then the blue wing should re-appear before the red wing. There is marginal evidence for this (see figure 3.09) but higher time resolution data are needed.

Finally, it is possible to estimate the intrinsic X-ray luminosity of AC211/4U2127+11. For the ADC systems 2A1822-371 and 4U2129+470 L_x/L_{opt} is 20 and 30 respectively, whereas it is 1.6 for 2S0921-630 (Bradt & McClintock, 1983). If the optical luminosity is due to reprocessing of X-rays in the disc, then the long orbital period of 2S0921-630 may explain this difference. It has a period of 9 days whilst 2A1822-371 and 4U2129+470 have periods of 5.6 and 5.2 hours respectively, and since the disc radius increases as $P^{2/3}$ for a given compact object mass, 2S0921-630 should be particularly bright optically. As these systems are viewed at high inclination, the disc rim will mean that the projected area of the disc varies linearly with the radius. Correcting the 2S0921-630 L_x/L_{opt} to that for a 5.5 hour period it becomes 18. Scaling the L_x/L_{opt} for AC211 to a 5.5 hour period yields 37, and thus a mean value of 27 is within a factor 1.5 of all the corrected values for the ADC sources. L_x/L_{opt} for "normal" LMXBs is ~350 (van Paradijs, 1983), with a standard deviation of a factor 2.7. This gives an intrinsic X-ray luminosity of 8×10^{37}ergs s^{-1} for AC211/4U2127+11, with an accumulated error of a factor 3.0.

An alternative method of estimating the X-ray flux, which is also independent of the distances to other sources, has been proposed by Charles *et al.* (1986). They used the observed HeII flux as an indicator

of intrinsic X-ray flux, which gives an L_x of $1.5x10^{38}$ergs s^{-1}.

3.7.2 The site of the HeI absorption

HeI absorption lines have been seen in the spectra of the ADC sources 2S0921-630 (Cowley, Crampton & Hutchings 1982; Branduardi-Raymont *et al.* 1983), and 2A1822-371 (Mason *et al.* 1982) whereas Sco X-1, which we observe at a lower inclination, shows HeI emission (Westphal, Sandage & Kristian 1968; Sandage *et al.* 1966). I therefore suggest that the HeI absorption in 2S0921-630, 2A1822-371 and AC211 is due to relatively cool disc edge material which is back-illuminated by the ADC and inner disc. As the light passes through this structure, HeI absorption will occur.

To test the plausibility of this idea I carried out an LTE analysis for material at the disc edge. Since the HeI λ4471 line is visible in the spectra, the optical depth to λ=4471Å photons must be $\gtrsim$1. This a lower limit to the HeI line optical depth since there is an unknown contribution to the continuum light in the spectra from other cluster stars. To produce $\tau \gtrsim 1$ in a column of $\lesssim 10^9$ cm (the Roche Lobe radius is $\sim 10^{11}$ cm), the calculation showed that an electron density, n_e $\gtrsim 10^{13}$ cm^{-3} and an ambient temperature between 20000K and 30000K was needed. Such material at the disc edge would be within 10^{11} cm of at least a $6x10^{36}$ erg s^{-1} X-ray source (this corresponds to the observed luminosity of AC211), and so it is necessary to check that this does not have a serious effect on the ionisation structure. For the above density limit, the ionisation parameter, $\xi = L/nr^2$ is $\lesssim$60, for which Kallman & McCray's (1982) optically thin nebular models predict $T_e \lesssim$ 30000K, and $He^+/He \simeq 5x10^{-3}$. These conditions correspond to the X-ray irradiated (inward facing) surface of the the disc edge. The ratio

He^+/He would fall to approximately 1 when the helium column density from the surface was 10^{20} cm^{-2} (corresponding to a physical length of 10^8 cm), much less than the column required to produce the absorption. Thus the LTE analysis is relevant for the majority of the disc edge material, and provides an order-of-magnitude estimate of the column required.

Although Kallman & McCray's models are concerned with low interstellar densities and solar abundances this is unlikely to mean that our estimates should be changed by more than a factor of a few. A more serious objection is that the disc edge may see the intrinsic rather than the observed X-ray luminosity. This would make $\xi \sim 1000$, which means that the lower limit on the density in the absorbing region would have to be increased to $>10^{14}$ cm^{-3}. However, if we assume that this density is typical of the disc, and that the disc height is a tenth of the Roche Lobe radius, we arrive at a disc mass of $<10^{-11}$ $M_\odot$. This is quite in keeping with current theories of disc structure (see for example Petterson 1983).

If the HeI is from the disc edge then one might expect that as the HeII emission disappears, and more of the disc is obscured by the stream impact region, the amount of HeI absorption relative to HeII will increase. At first sight figure 3.08 may give the impression that the HeI and HeII fluxes decline together. However, it should be remembered that the narrow slit means that our data is not photometric, and absolute fluxes may be dominated by systematic effects such as seeing. Thus, in figure 3.15 I have plotted the ratio of HeI λ4471 to HeII λ4686 for each of the phase folded spectra. It shows that the HeI absorption does indeed strengthen relative to HeII near phase 0.8. The point near phase 0.1 does not follow the trend of the other points.

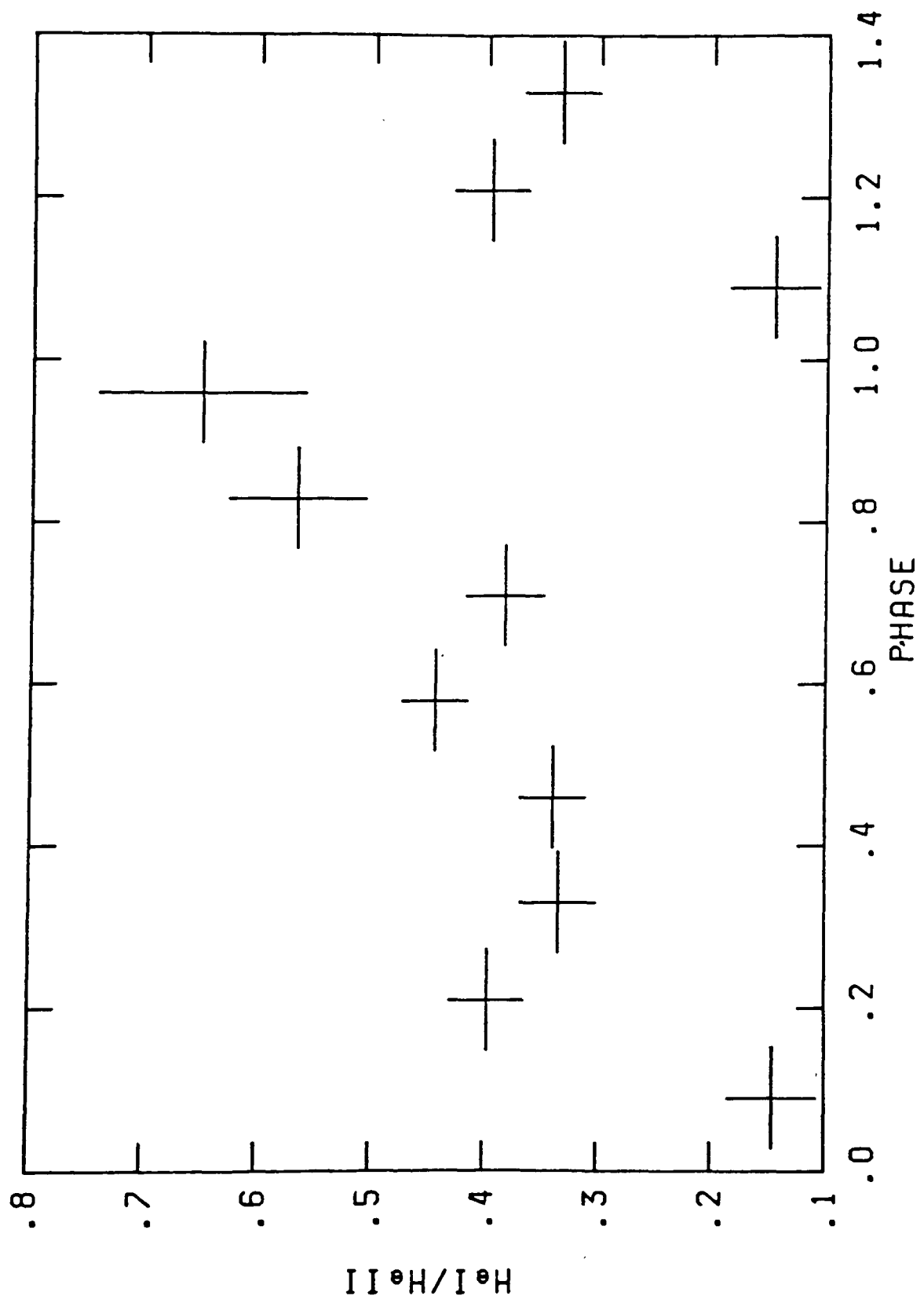

Figure 3.15 The ratio of HeI λ4471 counts to HeII λ4686 as a function of orbital phase.

This is probably because the lines in the spectrum are very weak (see figures 3.08 and 3.09), which in turn might be caused by the disc structure completely obscuring the central regions of the disc.

Finally, I have measured the position of HeI λ4471 in the 2S0921-630 data of Branduardi-Raymont *et al.* (1983). Its velocity is -11±19 km s^{-1} with respect to the HeII base profile (i.e. the compact object). This greatly strengthens the interpretation of the HeI absorption in the ADC sources generally, and in AC211 in particular. An important consequence of this interpretation is that the absorbing column must follow the orbital motion of the compact object.

3.7.3 The stellar masses

If the radial velocity variation of HeI λ4471 represents the motion of the compact object, and if the system inclination is assumed to be 90^{o}, then, as the binary period is known, the mass function can be calculated. The upper and lower bounds are $6.2x10^{-3}$ $M_{\odot}$ (55 km s^{-1}) and $5.8x10^{-3}$ $M_{\odot}$ (25 km s^{-1}) respectively, which are plotted as functions of the component masses in figure 3.16. This shows that quite modest masses for the secondary lead to rather massive primaries. Indeed, if the primary is not a black hole ($<3M_{\odot}$), the secondary must be $<0.4M_{\odot}$. Placing the HeI region elsewhere in the system exacerbates this effect. The motion of the secondary, for instance, is larger than the primary, (as long as the latter is the more massive object) so were the HeI located on the secondary, the implied radial velocity of the primary would be even smaller than 40km s^{-1}.

If the HeI arises from within the stream impact region then its velocity would show a roughly sinusoidal modulation, with a semi-amplitude equal

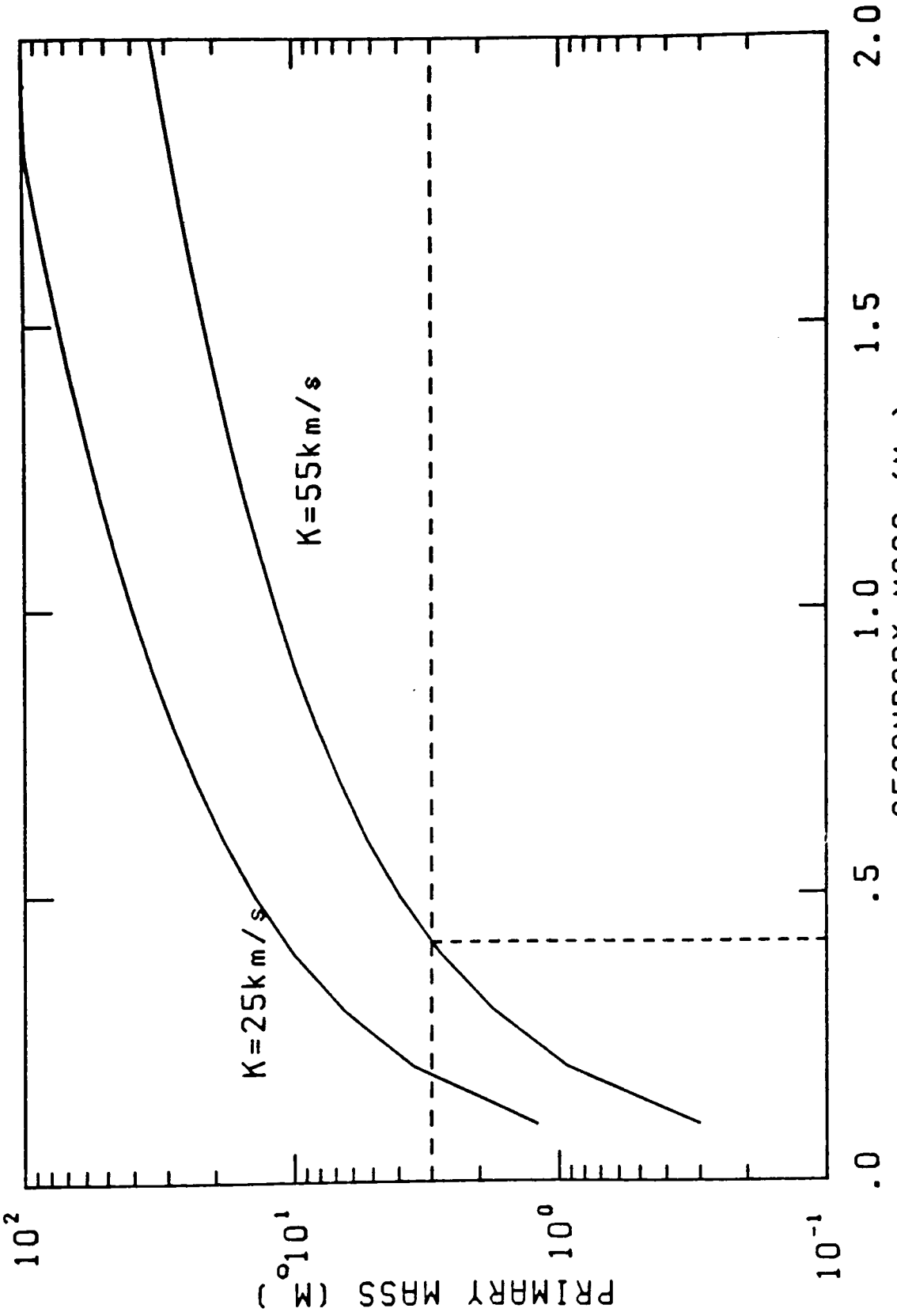

Figure 3.16 The mass function for AC211 assuming an orbital inclination of 90^o. The solid lines are the extreme ($\pm 1\sigma$) values of the radial velocity. The dotted horizontal line marks a primary mass of $3M_\odot$, and the vertical line the largest possible secondary mass if a black hole ($> 3M_\odot$) solution is to be avoided.

to the outer Keplerian disc velocity. This effect is well known as the "S-wave" in dwarf novae. However, the amplitude of the S-wave is always much greater than the amplitude of the motion of the primary. So, were the HeI located within the stream impact region itself, the implied velocity of the primary would again be even smaller than 40km s^{-1}.

This means that if the HeI comes from a single site, the lowest mass estimates for the primary will be arrived at by assuming it reflects the orbital motion of the compact object. If we then also assume the empirical main sequence mass-radius relation for CV secondaries proposed by Patterson (1984), and set this radius equal to the Roche lobe radius, we find that the secondary mass must be $1.05M_{\odot}$. Using the period and velocity amplitude gives a primary of $21M_{\odot}$.

Such a main sequence solution is not possible in M15, since the turn-off mass is about $0.8M_{\odot}$ (see for example VandenBerg 1983). This means that no main sequence star in M15 would fill its Roche lobe in this binary; so the secondary must be evolved. A star ascending the first giant branch would have a mass roughly equal to the turnoff value, giving a primary of $14M_{\odot}$. Such a secondary, in combination with a neutron star, has been suggested by Aurière *et al.* (1986). In this case the mass transfer would be driven by the evolution of the secondary, and so would be high, explaining the high X-ray luminosity (see 3.7.1). This would then explain why 4U2129+11/AC211 does not burst, since high mass transfer rates inhibit bursting on neutron stars (Ayasli & Joss 1982). Alternatively, if the compact object has a mass of $14M_{\odot}$, the mass accretion rate must be lowered by a factor 10; but X-ray bursts will still not occur since the accreting object is a black hole.

Finally, using the upper limit to the radial velocity, a black hole

solution can be avoided if the secondary is less massive than $0.4M_{\odot}$. A main sequence star of this mass would not fill its Roche-lobe, but mass loss after the turn-off might be thought sufficient to bring an evolved star down to this mass. This is not the case in M15 since the lightest evolved stars are those of the horizontal branch, whose mass is given as $0.65\pm0.05M_{\odot}$ (Cox, Hanson & Clancy 1983). This result assumes that all horizontal branch stars in M15 have essentially the same mass (Rood 1973). The horizontal branch mass allows us to place a lower limit on the mass of the compact object of $10M_{\odot}$, if the secondary is a near-normal cluster member.

The compact object will be $< 3M_{\odot}$ only if the secondary is not a normal cluster member. It would then have to be a giant of $<0.4M_{\odot}$, which had presumably reached this evolutionary state by mass loss onto the primary. It is intersting to note that such a $\simeq 0.5\ M_{\odot}$ giant probably exists in 2S0921-630 (Mason *et al.* 1987). However, if AC211 is only $\sim 10^3$ years old (see 3.7.4) it is unlikely that a normal cluster star could have evolved to this state in the lifetime of the system. Unless it can be proved conclusively that AC211 is very young, or until we have an independent measurement of the mass ratio, the precise nature of the primary and secondary in this system will remain an open question.

The extreme mass ratios implied by all these models, but especially the black hole scenarios, will make the secondary very small compared with the primary's Roche lobe. If the opening angle of the disc is the same as for other LMXBs, the secondary will be smaller compared to the size of the disc structure than in other systems. Taking, for instance, a $0.8M_{\odot}$ secondary, and a $14M_{\odot}$ primary, the secondary's Roche lobe surface subtends an angle of 20° at the position of the primary, compared with

30^{o} for q (= primary mass/secondary mass) = 4. Thus, if the disc structure extends about 10^{o} above and below the plane of the disc, as is suggested by the inclinations of the X-ray dippers (Mason 1986) the X-ray eclipse of the ADC in AC211 may become indistinguishable from its occultation by the disc structure, as suggested in 3.7.1.

3.7.4 AC211 as a globular cluster member

The high γ velocity of the HeI lines with respect to the cluster implies that it has a high translational kinetic energy. The ratio of the binding energy of the binary to its kinetic energy is

$$\frac{\text{Binding Energy}}{\text{Translational Kinetic Energy}} = \frac{M_1}{M_2}\left(\frac{v_1}{v_o}\right)^2 \qquad \ldots(3.1)$$

where subscript 1 refers to the primary, 2 to the secondary, and v_o is the systemic velocity. The inverse of the ratio of the square of the velocities is ~14, and in the models discussed above M_1/M_2 varies in the range 7 to 26. Thus the apparent translational energy is of the same order as the binding energy of the binary. The translational kinetic energy deduced from the γ velocity is only the component of the translational velocity perpendicular to the plane of the sky, and thus the true energy must be larger.

The effect that binaries may have on the dynamical evolution of a cluster has been discussed in Chapter 2. Since M15 is a core-collapse cluster, AC211 may be a core collapse binary, especially as its binding energy is sufficient to halt the collapse. However, until the velocity of the primary, and the mass ratio are known to greater accuracy, it is impossible to say how much of that binding energy has been released to

the rest of the cluster; although it should be noted that the mere ejection of AC211 will make the total energy of the cluster less negative, and may help halt the collapse (see Goodman 1984). The high γ velocity suggests that AC211 was formed by the interaction of a single star with a binary, in which the latter was "hardened", and the potential energy released converted into kinetic energy of the single and binary (see Statler, Ostriker & Cohn 1987).

If AC211 was formed in the central cusp of the cluster, and we assume its velocity in the plane of the sky is similar to its radial velocity, its distance from the center of the cluster (2" to 3", depending on definition; see Aurière & Cordoni, 1981) implies it is $\sim 10^3$ years old; a result that should, perhaps, be treated with some scepticism. The time to reach the tidal radius of the cluster is $\sim 3 \times 10^5$ years.

An alternative explanation for AC211's high systemic velocity is offered by the behaviour of the SU UMa star Z Cha during its superoutbursts (see Chapter 4, specifically 4.3). Its apparent γ velocity varies by about 300 km s^{-1} with a period of 2 days. The origin of this effect is still controversial, but the lines showing the velocity shift are probably formed in the disc edge, as in AC211. If the γ shift period scales with the orbital period, then the γ shift period in AC211 should be approximately 11 days. Further observations of the HeI lines should test this possibility more thoroughly.

3.7.5 Wind and common envelope models

Two other models have been invoked for the M15 X-ray source. One suggests a large corona and a massive wind from the disc (Fabian, Guilbert & Callanan 1987, hereafter FGC) and the other a common envelope

for both the primary and secondary (Bailyn & Grindlay 1987).

In the FGC model, the low L_x/L_{opt} is explained by a corona which "backheats" the disc. In order to achieve this, the corona must be larger than those seen in other LMXBs. Its size is explained by the inefficient cooling of metal-poor plasmas (the metal abundance in M15 is ~1% solar). The outer region of the corona is cool, supersonic wind, with which FGC seek to associate the HeI and HeII lines.

If, as FGC suggested, the HeI and HeII lines originate in the wind it is hard to understand why their profiles are so very different; the HeII line is much broader (contrary to their expectation) and more complex than HeI. Yet, in an optically thick wind model we would expect the HeI to be associated with the larger expansion velocity. Alternatively, if the wind is not opaque in the continuum there should be no HeI absorption at all. One might invoke a decelerating flow, or suppose that the HeII emission is not produced in the wind at all. In the latter case there is no longer any compelling reason to argue for a thick wind with a mass loss rate $\sim 10^{-7}\ M_\odot yr^{-1}$. Finally the HeI lines are more or less Gaussian (at our resolution) with no emission, suggesting a photospheric rather than wind origin.

Bailyn & Grindlay (1987) have proposed that AC211 is a $1.2M_\odot$ neutron star with a $0.8M_\odot$ secondary. This yields $q \simeq 1.25$, leading to unstable mass transfer. The primary and secondary are thus embedded in a common envelope, and the accretion is Eddington-limited. The secondary mass is the turn-off mass in M15, and is chosen because, as I have already shown, a main sequence star will not fill its Roche lobe. The HeI line is then associated with the expanding envelope, thereby accounting for the large velocity shift. One problem with this model is obtaining HeII

λ4686 emission and HeI absorption within a single geometry. Another more serious difficulty arises from the fact that absorption in excited state transitions of HeI is only likely to occur if helium is mainly neutral. This places a constraint on the mass loss rate as follows. The HeI absorbing region must be illuminated by an X-ray flux corresponding to at least the observed L_x of 6×10^{36} ergs s^{-1}. From Kallman & McCray's (1982) models, we find that ξ must be $\lesssim 0.01$ for neutral helium to be the dominant species, which gives $nr^2 \gtrsim 6\times10^{38}$ cm^{-1}. We can substitute this into the the formula for a spherically symmetric wind,

$$N_H = \frac{\dot{M}}{4\pi r^2 \mu m_H v} \qquad \ldots(3.2)$$

to yield an approximate lower limit to the mass loss rate of 3×10^{-3} $M_\odot$ yr^{-1}. Collimation of the outflow could, of course, lower this estimate by a factor ~10. However, it is still not clear what mechanism could drive a mass loss rate of even $\sim10^{-4}$ $M_\odot$ yr^{-1}.

3.8 Conclusions

The orbital period of AC211 has been discovered by following the radial velocity variations of HeI λ4471. The γ velocity of the line suggests that AC211 will leave the cluster rapidly (~10^5 years), and that the object in its present configuration is very young.

The spectroscopy presented here and other published optical and X-ray photometry have been drawn together into a model for AC211. It is most probably a high inclination accretion disc corona source, where disc structure causes the periodic X-ray and optical modulations. Wind and

common envelope models can be ruled out by the HeI and HeII line profiles.

The high inclination suggests that the HeI absorption lines originate at the disc edge, and thus reflect the motion of the compact object. This allows us to calculate the mass function, and if the secondary is assumed to be a normal cluster star, implies that the compact object is a black hole. The alternative is that the secondary is a giant of $\lesssim 0.4$ $M_\odot$, and that the γ velocity is not indicative of the age of the system.

The next major step in understanding this object will be to relate the X-ray photometric and spectroscopic phasing. In the ADC model outlined in 3.7.1 the time of the X-ray and optical minima should coincide. If the deepest part of the optical/X-ray minimum is caused by the secondary it must occur at spectroscopic phase zero. If it is caused by disc structure then it should occur near spectroscopic phase 0.8.

The circularization time for AC211 (assuming component masses of $0.8M_\odot$ and $14M_\odot$, and that the secondary has a convective envelope) is $\sim 3\times10^4$ years (see equation 6.2 of Zahn 1977). Thus if the object was formed by an encounter $\sim 10^3$ years ago, the orbit should still be elliptical, which could be tested by further observations. If the velocity in the plane of the sky is similar to the radial velocity, AC211 should move 0".1 in ~30 years, providing a further test of its age.

The nature of the primary and secondary make AC211 an interesting LMXB in its own right. Its importance is enhanced by its evolutionary history, and consequent effects on the dynamical evolution of the host cluster. AC211 is not an easy object to observe, but further observations will reap rewards in helping to unravel the nature of the

primary, and in testing theories of LMXB and globular cluster evolution.

References

Aurière, M., & Cordoni, J-P., 1981. *Astr. Astrophys. Supp. Ser.* **46**, 347.

Aurière, M., Le Fèvre, O., & Terzan, A., 1984. *Astr. Astrophys.* **138**, 415.

Aurière, M., Maucherat, A., Cordoni, J.P., Fort, B., & Picat, J.P., 1986. *Astr. Astrophys.* **158**, 158.

Ayasli, S., & Joss, P.C., 1982. *Astrophys. J.*, **256**, 637.

Bailyn, C.D., & Grindlay, J.E., 1987. *Astrophys. J.*, **316**, L25.

Branduardi-Raymont, G., Corbet, R.H.D., Mason, K.O., Parmar, A.N., Murdin, P.G., & White, N.E., 1983. *Mon. Not. R. astr. Soc.* **205**, 403.

Bradt, H.V.D., & McClintock, J.E., 1983. *Ann. Rev. Astron. Astrophys.*, **21**, 13.

Callanan, P.J., Fabian, A.C., Tennant, A.F., Redfern, R.M., & Shafer, R.A., 1987. *Mon. Not. R. astr. Soc.* **224**, 781.

Charles, P.A., Jones, D.C., & Naylor, T., 1986. *Nature*, **323**, 417.

Cowley, A.P., Crampton, D., & Hutchings, J.B., 1982. *Astrophys. J.*, **256**, 605.

Cox, A.N., Hodson, S.W., & Clancy, S.P., 1983. *Astrophys. J.*, **266**, 94.

Fabian, A.C., Guilbert, P.W., & Callanan, P.J., 1987. *Mon. Not. R. astr. Soc.* **225**, 29p (FGC).

Goodman, J., 1984. *Astrophys. J.*, **280**, 298.

Hertz, P., 1986. *IAUC* 4272.

Hertz, P., 1987. *Astrophys. J.*, **315**, L119.

Ilovaisky, S.A., Chevalier, C., Angebault, P., Koch-Miramond, L., &

Cordoni, J.-P., 1986. *IAUC* 4263

Ilovaisky, S.A., Aurière, M., Chevalier, C., Koch-Miramond, L., Cordoni, J.-P., & Angebault, L.P., 1987. *Astr. Astrophys.* **179**, L1.

Jenkins, C.R., 1987. *Mon. Not. R. astr. Soc.* **226**, 341.

Jones, C., & Forman, W., 1976. *Astrophys. J.*, **209**, L131.

Kallman, T.J., & McCray, R., 1982. *Astrophys. J. Suppl.*, **50**, 263.

Mason, K.O., 1986. In: *Physics of Accretion onto Compact Objects* p. 29. eds. Mason K.O., Watson, M.G. & White, N.E. Springer-Verlag, Heildelberg.

Mason, K.O., Murdin, P.G., Tuohy, I.R., Seitzer, P., & Branduardi-Raymont, G., 1982. *Mon. Not. R. astr. Soc.* **200**, 739.

Mason, K.O., Branduardi-Raymont, G., Cordova, F.A., & Corbet, R.H.D., 1987. *Mon. Not. R. astr. Soc.* **226**, 423.

McClintock, J.E., London, R.A., Bond, H.E., & Grauer, A.D., 1982. Astrophys. J., **258**, 245.

Naylor, T., Charles, P.A., Callanan, P.J., & Redfern, R.M., 1986. *IAUC* 4263.

Patterson, J., 1984. *Astrophys. J. Suppl.*, **54**, 443.

Peterson, R.C., Olszewski, E.W., & Aaronson, M., 1987. Astrophys. J., **307**, 139.

Petterson, J.A., 1983. In: *Accretion-driven stellar X-ray sources* p.367, eds. Lewin, W.H.G., & van den Heuvel, E.P.J., C.U.P.

Rood, R.T., 1973. *Astrophys. J.*, **184**, 815.

Sandage, A.R., Osmer, P., Giacconi, R., Gorenstein, P., Gursky, H., Waters, J., Bradt, H., Garmire, G., Sreekantan, B.V., Oda, M., Osawa, K., & Jugaku, J., 1966. *Astrophys. J.*, **146**, 316.

Seaton, M.J., 1978. *Mon. Not. R. astr. Soc.* **185**, 5p.

Statler, T.S., Ostriker, J.P., & Cohn, H.N., 1987. *Astrophys. J.*, **316**,

626.

Thorstensen, J., Charles, P., Bowyer, S., Briel, U.G., Doxey, R.E., Griffiths, R.E., & Schwartz, D.A., 1979. *Astrophys. J.*, **233**, L57.

Vandenberg, D.A., 1983. *Astrophys. J. Suppl.*, **51**, 29.

van Paradijs, J., 1983. In: *Accretion-driven stellar X-ray sources* p. 189, eds Lewin, W.H.G., & van den Heuvel, E.P.J., C.U.P.

Westphal, J.A., Sandage, A., & Kristian, J., 1968. *Astrophys. J.*, **154**, 139.

White, N.E., Becker, R.H., Boldt, E.A., Holt, S.S., Serlemitsos, P.J., & Swank, J.H., 1981. *Astrophys. J.*, **247**, 994.

Zahn, J.-P., 1977. *Astr. Astrophys.*, **57**, 383.

Chapter 4

The Superoutbursts of the SU UMa Stars

4.1 Introduction

Reviews of the SU UMa stars and their superoutbursts include Vogt (1980, 1983) and Warner (1985a). However, the field has progressed sufficiently far since the lastest of these, to justify the review presented here.

The SU UMa stars are the cataclysmic variables below the period gap where the magnetic field of the white dwarf does not significantly affect the accretion flow (see Chapter 1). All those with known orbital periods are listed in Table 2.1. The SU UMa stars are dwarf novae, and their outbursts show a bimodal distribution of outburst lengths, clustering around 3 days for the "normal" outbursts, and 2 weeks for the "superoutbursts". The recurrence times are ~weeks for normal outbursts, and a few months for superoutbursts. Typical outburst light curves are shown in figure 4.01.

Superoutburst light-curves (see also figure 5.01) have sharp rises of less than two days and then decline slowly for about two weeks (the "plateau") before a final decline to quiescence lasting one or two days. Sometimes, a day or so after the initial rise the system will fade by about a magnitude, before rising to a new, even higher maximum. This gives the impression of a "precursor" normal outburst before the onset of the superoutburst.

There is one system, WZ Sge, which I shall refer to as though it is an SU UMa star, but whose precise classification is still unclear. It was

Table 4.1 The SU UMa stars

Name	Visual Magnitude quiescent	superoutburst	Inter-outburst period normal	super	Orbital Period	Comments
TU Men	>16	11.6	37	194	0.1176	
YZ Cnc	14.1	10.5	6-16	134	0.0864	
TY Psa	16	12			0.08063	
WX Hyi	14.7	11.4	14	140	0.074813	
Z Cha	15.3	11.9	82	287	0.074499	Eclipses
VW Hyi	13.4	8.5*	27	179	0.074271	
HT Cas	16.4	10.8	30-35		0.073647	Eclipses
AY Lyr	18.4	12.3	8-43	205	0.0730	
TY Psc	15.3	11.7	11-35	370	0.071	
IR Gem	16.3	11.2	22-48	150	0.0684	
RZ Sge	16.9	12.2	62-93	266	0.067	
EK Tra	>17	12.0	231	487	0.0636	
OY Car	15.3	11.4	25-50	318	0.063121	Eclipses
V436 Cen	15.3	11.3	32	335	0.062501	
SW UMa	16.5	9	459		0.05681	Also a DQ Her
WZ Sge	14.9	7	11876		0.056688	Bright spot eclipsed

* Normal outburst magnitude

"Eclipses" in the comment column means that both the bright spot and the white dwarf are eclipsed.

All periods are in days.

The data is from Ritter (1987).

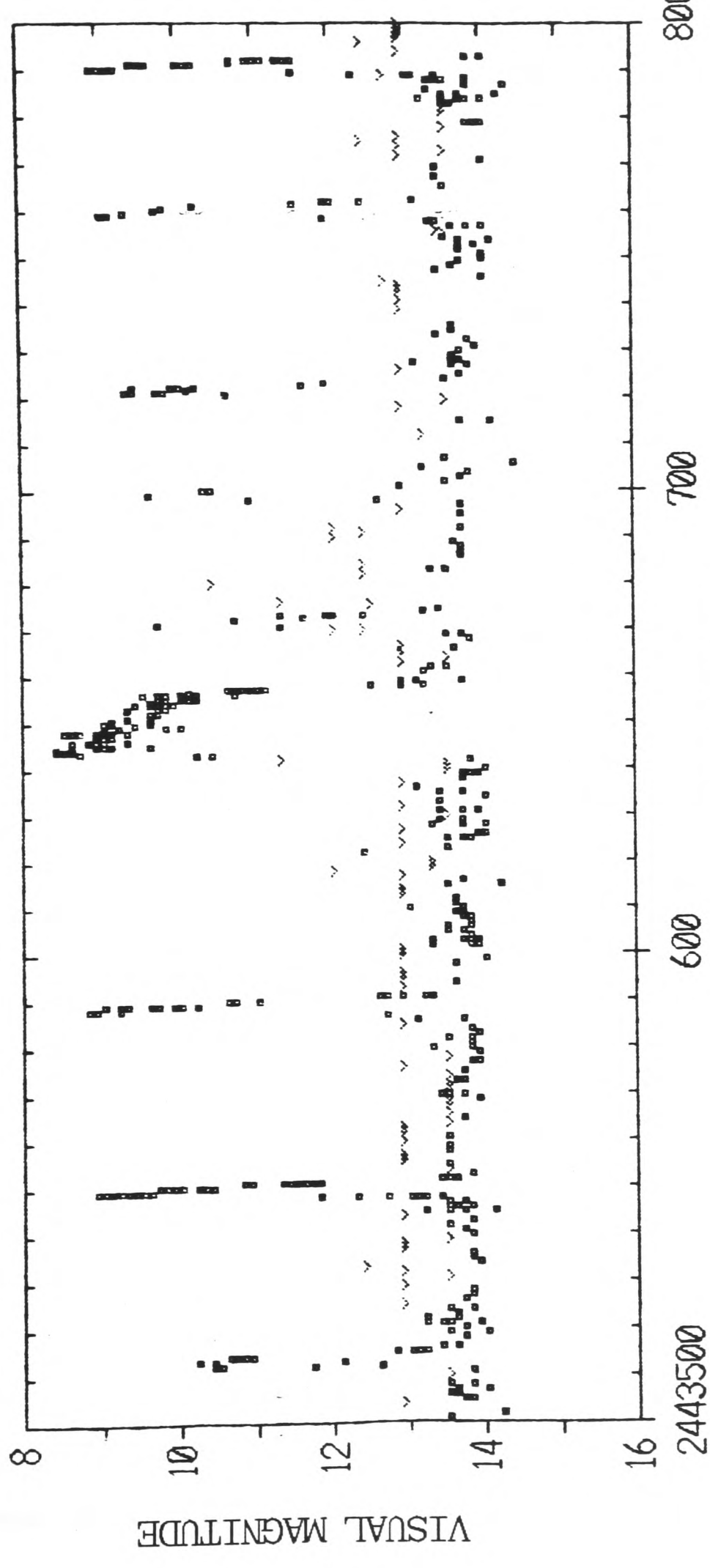

Figure 4.01 A light curve of the SU UMa star VW Hyi, taken from Bateson & McIntosh (1986). The arrowheads are upper limits to the star's brightness.

thought to be a recurrent nova (its interoutburst period is close to 33 years), until its December 1978 outburst when it showed many of the characteristics of an SU UMa superoutburst. Thus it appears to be an SU UMa which only undergoes rare, but prolonged, superoutbursts.

4.2 Superoutburst photometry

4.2.1 The superhump phenomenon

Within ~2 days of reaching the plateau stage of a superoutburst, SU UMa stars begin to show large (~0.5 magnitude) humps in their optical light curves, which recur with a period slightly (≃3%) longer than the orbital period (see Vogt 1974 and Warner 1975). This is known as the "superhump", and has become the defining characteristic of superoutbursts, and thus of the whole SU UMa class. Superhumps are seen irrespective of the orbital inclination of the system, in contrast with quiescent orbital humps (see Chapter 1). Superhumps are clearly visible in the light curves of figures 5.03 and 5.07. From such light curves a superhump phase can be defined; conventionally phase zero is the peak of the hump.

As the superoutburst progresses the humps become fainter with respect to the overall system light, and broader. Also their period decreases, so that it becomes closer to the orbital period.

2.2.2 Eclipse effects

In the eclipsing systems, since there is a difference between the orbital and superhump periods, the orbital phase at which superhump maximum occurs changes with time. It returns to the same orbital phase

every "beat cycle", which is approximately 2 days. The orbital phase of the superhump maximum is known as the beat phase, though occasionally the definition is reversed to be the superhump phase of the eclipse. However, I shall use the former definition throughout this thesis.

When part of the superhump profile coincides with the eclipse, its effect on the eclipse is approximately that which might be expected if the superhump light were uneclipsed. Thus the depth of the eclipse (measured in flux) remains the same, although the flux at eclipse bottom changes as the hump moves through it (Whitehurst, Bath & Charles 1984). If the eclipse depth is measured in magnitudes, then it varies with beat phase, since at the time superhump maximum coincides with the eclipse, the eclipse depth is a smaller portion of the total system light than when the superhump is well away from the eclipse. This is probably the explanation of the eclipse depth's dependence on beat phase found by Krzeminski & Vogt (1985).

The superhump also distorts the shape of the eclipse, as shown in figure 4.02 where Gaussian eclipses of the same depth (in intensity) have been superimposed on linearly rising and falling light curves. If the eclipse lies on the superhump decline (i.e. after the hump) the result is a rapid ingress and a slow egress. If it lies on the rise (i.e. before the hump) the ingress is slow and the egress rapid. I suggest that this is probably the cause of the ΔT effect (an eclipse asymmetry) noted by Krzeminski & Vogt (1985).

The changing shape of the eclipse also has the effect of changing the time of minimum light. The standard method of measuring this is to find the observed (O) time of minimum, minus the time predicted or calculated (C) known as O-C. If the superhump is uneclipsed, then O-C should show

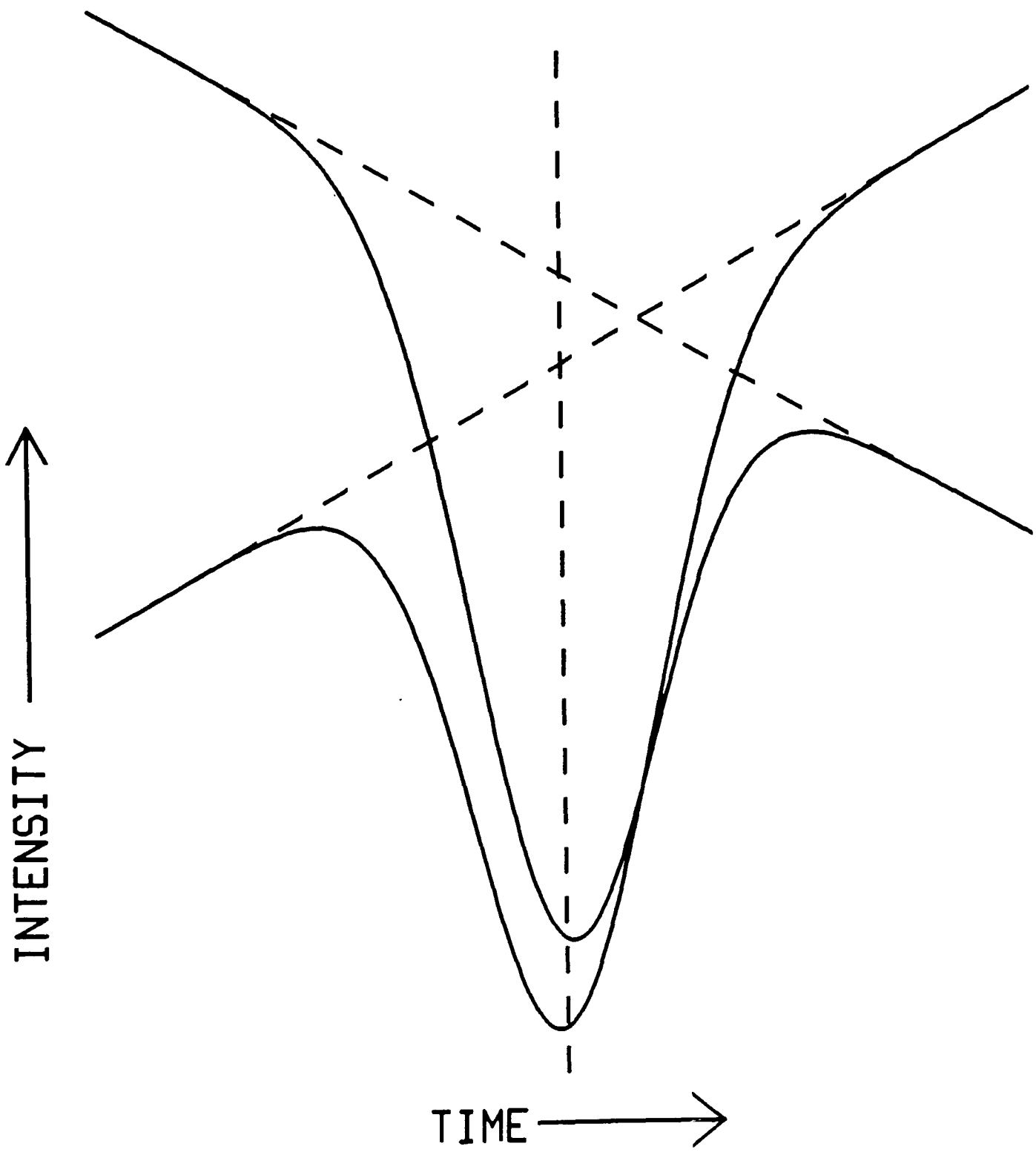

Figure 4.02 Gaussian eclipse profiles superimposed upon rising and falling backgrounds, their y-axes have been shifted so that the minimum of the eclipse can be examined. The dotted line would correspond to the time of eclipse minimum were the eclipses on constant backgrounds. These profiles show the effect that the superhump has on an eclipse if it is just before (rising background) or after (falling background) superhump maximum. The slopes of the ingress and egress, and the time of minimum are all affected.

the behaviour predicted by Whitehurst *et al.* (1984). Their figure 3 should be directly comparable with figure 11 of Krzeminski & Vogt (1985), since both use the same definition of beat phase. However, the method of analysis used by the latter is open to criticism (see Chapter 5), and the O-Cs for Z Cha (see figure 5 of Warner 1985a) have a different form from both the prediction, and those measured by Krzeminski & Vogt. (Note that Warner uses a different definition of beat phase.)

Thus, supposing that the superhump is uneclipsed will explain the eclipse depth and ΔT effects, and may explain the O-C effect. This does not prove, however, that the superhump is uneclipsed. Other explanations are possible (see, for example Krzeminski & Vogt 1985), and the O-C evidence is far from unambiguous. Also the superhump could be partially eclipsed and produce all the effects noted above (see, for example, Horne 1985). I shall return to these points in 4.5.

4.2.3 System luminosity

Schoembs (1986) noted that the mean luminosity of OY Car away from both eclipse and superhump is modulated with a period close to the beat period. The maximum intensity occurs at beat phase 0.5, and the amplitude is ~30%. Whitehurst (1987) pointed out that this, in conjunction with superhump, causes the modulation of the flux at eclipse bottom on twice the beat period seen by Schoembs (1986). At beat phase zero the flux at eclipse minimum will be high, because of the superhump (see 4.2.2), and it will also be high at beat phase 0.5 because of the overall system light modulation. There is some evidence for a similar, overall modulation in the lower inclination system VW Hyi (Bath,

Edwards, & Mantle 1983).

Many dwarf novae show low coherence ($\dot{P}\simeq10^{-5}$) oscillations with periods ~20 seconds during outburst (see Cordova & Mason 1983 for a review). The best superoutburst data are probably that of Schoembs (1986) for OY Car. The oscillations were observed during the rapid decline, and their presence seemed to correlate with the times of superhump, or late superhump (see 4.2.4) maximum. The oscillations were eclipsed, though the eclipse was slightly later than the primary eclipse, implying that they are associated with the position of the quiescent bright spot.

4.2.4 Late superhumps

During and after the rapid decline of VW Hyi the orbital hump re-appears. In addition there is a hump which seems to be a remnant of the superhump. It appears, however, that this remnant (called the "late superhump") is phase shifted with respect to the normal superhump by 180^{o}. The light curves of Schoembs & Vogt (1980) show this best, but it has also been reported by Vogt (1977) and Schoembs & Vogt (1980). The same effect may have been observed in V436 Cen (Warner 1983).

4.3 Superoutburst spectroscopy

The optical superoutburst spectra of the low inclination SU UMa stars EK TrA (Hassall 1985) and WX Hyi (Hassall *et al.* 1983) have weak Balmer absorption, except for Hα which is in emission. WX Hyi also has weak HeI absorption. In contrast the high inclination systems (for Z Cha see Vogt 1982 and Honey *et al.* 1987; for WZ Sge see Crampton, Hutchings & Cowley 1979, Gilliland & Kemper 1980, Walker & Bell 1980, Brosch, Leibowitz & Mazeh 1980 and Ortoliani *et al.* 1980) have double peaked

Balmer emission lines, with the central absorption increasing relative to the emission up the series. They also show HeII λ4686 and Bowen blend emission, and Ca H and K absorption.

Gilliland & Kemper (1979) noted that the γ velocity of WZ Sge varied between the nights of observation, and Vogt (1982) and Honey *et al.* (1987) found the same effect in Z Cha. The velocities used for these studies were those of the absorption lines; or absorption cores in double peaked lines. Compilations of the available γ velocities, plotted against beat phase, have been presented for WZ Sge (Vogt 1982) and Z Cha (Honey *et al.* 1987, reproduced in figure 4.03). Although the data from Honey *et al.* in figure 4.03 cluster around beat phases 0.2 and 0.7, the points are from different superoutbursts and beat cycles, suggesting that the γ velocity does vary systematically with beat phase.

4.4 Superhump models

Of the models proposed to explain superhumps, none offers obvious explanations for all the observational facts. I shall here present an outline of each of them in turn, and discuss their relative merits in Section 5.

4.4.1 An elliptical disc

In the elliptical or eccentric disc model (Vogt 1982 and Krzeminski & Vogt 1985) the accretion stream falls on an elliptical accretion disc with the white dwarf at one focus. The precession period of the disc is the beat period (approximately two days). The ellipticity of the disc results in the kinetic energy of the stream, when it reaches the disc,

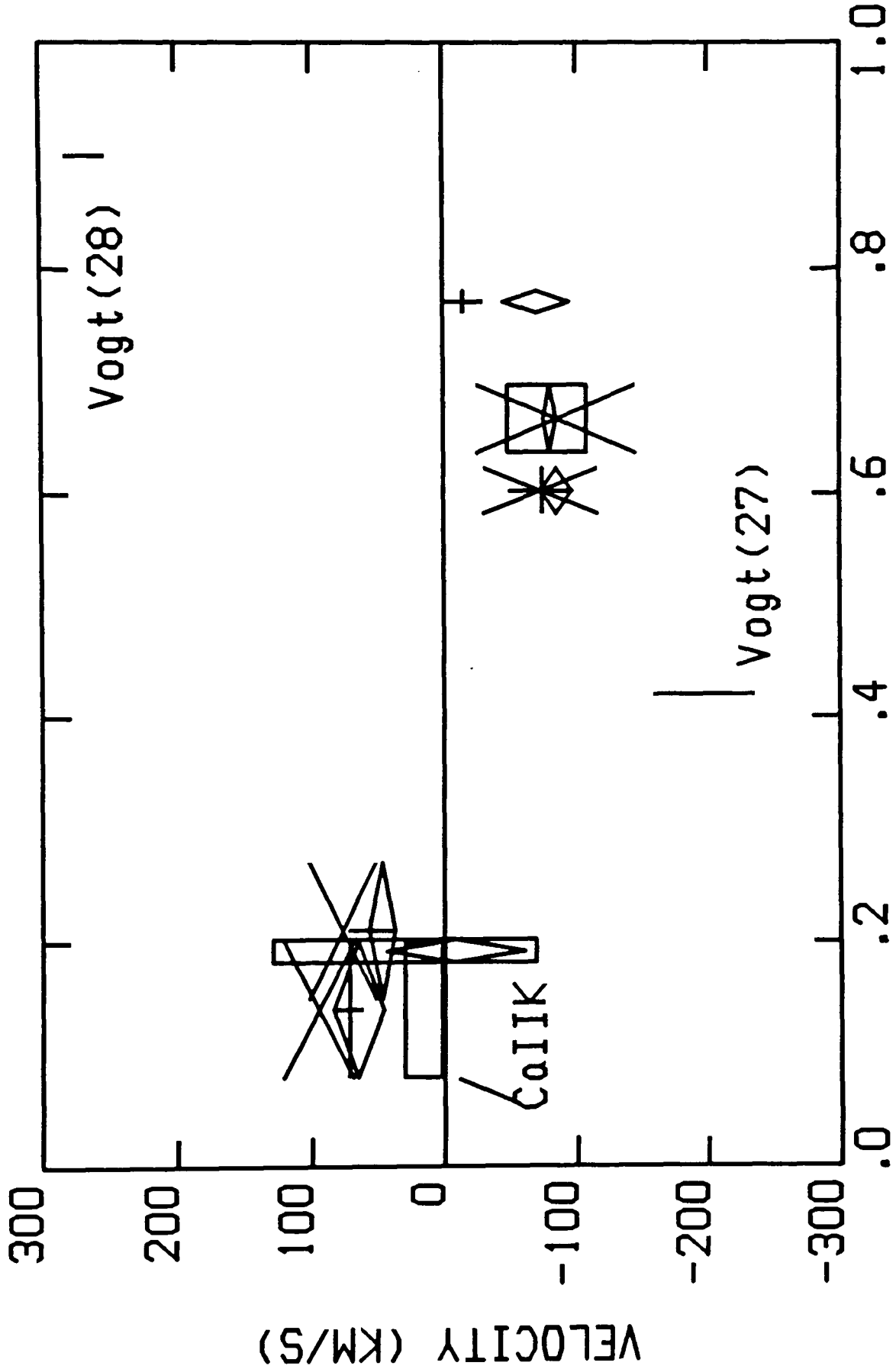

Figure 4.03 The γ velocity of the absorption lines of Z Cha as a function of beat phase, from Honey *et al.* (1987). The symbols for the Honey *et al.* data are: boxes=Hβ, bars=Hδ, diamonds=Hγ, crosses=HeI λ4471. The data for the Balmer lines from Vogt (1982) is also marked. The vertical extent of the symbol is the error in the velocity determination.

varying cyclically. This causes the energy released in the stream impact region to vary in the same way, and it is this varying bright spot that provides the superhump light. Furthermore, since the disc precesses in the frame of the observer with a period circa two days this extends the superhump period to a few percent longer than the orbital period. The model is sometimes referred to as an eccentric ring, since Vogt stated that the disc could be visualised as having a circular inner region, with an outer elliptical ring.

4.4.2 Osaki's model

Vogt (1982) sought to create the elliptical disc by a burst of mass transfer lasting less than 1 orbital cycle which would occur sometime after the outburst had begun. However, Whitehurst (1984) showed, by considering single particle orbits, that elliptical rings were unstable for more than a few orbital cycles.

Kato (1983) points out that, in general, waves in the disc's plane will have short wavelengths, but that one long wavelength mode can exist. This results in an elliptical disc which precesses slowly (compared with the orbital motion) in the observer's frame of reference. Osaki (1985) proposed a model which would excite this mode of the disc by modulated mass transfer. If the disc was initially assumed to be elliptical, then the X-ray irradiation of the secondary would be greatest when it passed the small side of the disc, and least at the large side. If the irradiation resulted in a burst of mass transfer occurring at some later time in each cycle, so that the extra material was dumped on the large side of the disc, it would remain elliptical. He showed that the predicted value of the precession period of the disc was close to the

observed beat period for SU UMa stars.

The superhump is then caused by the energy released in the bright spot, as in Vogt's model. However, in this case the superhump maximum occurs at the time of maximum mass transfer, not the time of the bright spot's closest approach to the compact object.

4.4.3 The tidal model

Whitehurst (1987) found that, under certain conditions, this long wavelength mode occurs in 2-dimensional hydrodynamic disc simulations, i.e. there was no need to call upon a specific mechanism to excite the wave. Furthermore he found that tidal dissipation in the disc would result in a peak in the disc's light output once per superhump cycle, removing the need for a bright spot modulation.

4.4.4 A starspot

The starspot model (Warner 1974, Vogt 1977, Bath, Edwards & Mantle 1983 and Whitehurst, Bath & Charles 1984) suggests that there is a bright active region on the secondary star. Were the active region to remain at the same place on the secondary's surface it would come into view once per orbital cycle, and it's extra light would produce the superhump. In order to give the observed superhump period, the secondary asynchronously rotates with respect to the binary rest frame with the beat period.

4.4.5 Intermediate polar model

Warner (1985a) suggested that the beat period may be the spin period of

the white dwarf. If it is further assumed that the white dwarf is magnetic the superhump can be produced by light from the magnetic poles illuminating the bright spot. However, Warner (private communication) has pointed out that since the discovery that the white dwarf spin period of SW UMa (Shafter, Szkody & Thorstensen 1986) is not equal to the superhump beat period (Robinson *et al.* 1986) the model cannot be correct.

4.4.6 Modulated mass transfer

Finally there is the modulated mass transfer model (Papaloizou & Pringle 1979). If the binary orbit is slightly elliptical ($e \sim 10^{-3}$) then the mass transfer from the secondary is modulated with the orbital period, the rate of Roche Lobe overflow being at its greatest at closest approach. This leads to a modulation of either the hot spot (Clarke, Mantle & Bath 1985) or the whole disc on the orbital period. Such an orbit should also precess and with a period that changes the hot spot modulation period into the superhump period (Papaloizou & Pringle 1979).

4.5 A critique of the models

Only the elliptical disc models convincingly account for the γ velocities. They are thought to arise because some of the inner disc and boundary layer are seen through relatively cool material at the edge of the disc. If this material has any radial motion, it will manifest itself as the radial velocity of the absorption lines. Figure 4.04 is a beat phase diagram for an SU UMa system, and shows why this material has a radial velocity.

The figure is drawn in a frame which co-rotates with the elliptical

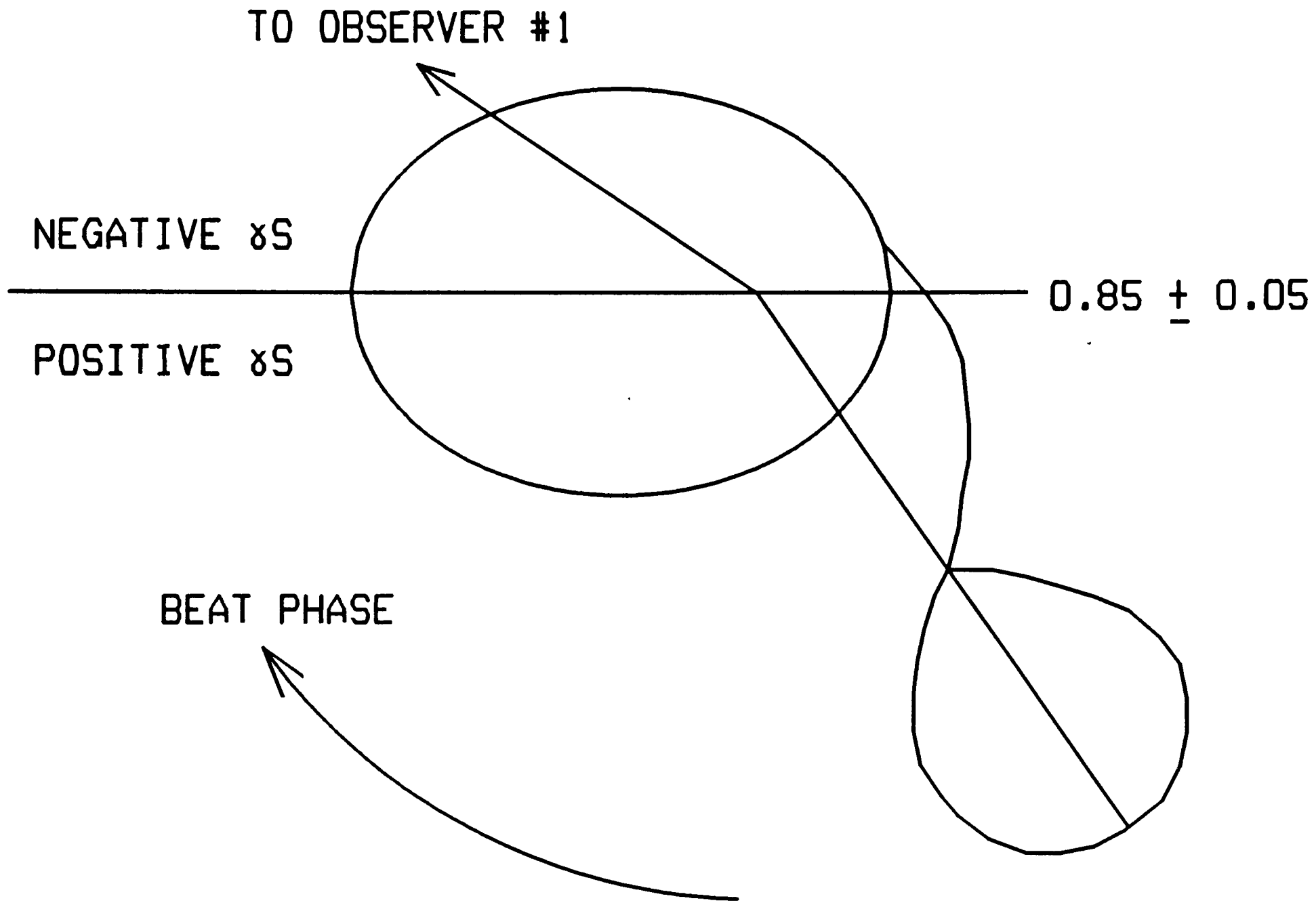

Figure 4.04 Beat phase diagram for an SU UMa star. As the observer moves around the system it is observed at different beat phases, but always at superhump phase zero.

disc, and thus the position of the observer must be moved to represent different beat phases. I shall assume the system is always viewed at superhump phase zero. If a line is drawn from the observer (observer #1) to the compact object it will cut the disc edge as shown. The radial position vector from the compact object to the disc edge has a positive first derivative for the particle shown moving around the edge of the disc. This radial motion will lead to an observed blue shift (negative radial velocity). Had the system been viewed from the lower half of the diagram a red shift would have been observed.

This line of argument, combined with the measured γ velocities, allows us to define the beat phase of a given disc orientation in a model independent fashion. Since beat phase (and thus time) increases as the observer moves anti-clockwise, the switch from negative to positive γ velocities occurs as the right hand side of the horizontal line is passed. Reference to figure 4.03 shows that this must occur between beat phases 0.8 and 0.9. This constrains the position of the secondary on the diagram, since it must lie on the beat phase zero line, which is now constrained to be in the range 0.1 to 0.2 of a cycle anti-clockwise from the right hand side of the horizontal line. Thus figure 4.04 must be approximately the beat phase zero configuration for all elliptical disc models.

As can be seen from the diagram the orientation corresponds roughly to that at which the bright spot releases the most energy per unit mass (depending on precisely how large an angle the stream swings through before it impacts the disc, and thus on the mass ratio), and so is correct for the Vogt model. It also corresponds to the finding of Whitehurst (1987) that the switch from positive to negative γ velocity

occurs at beat phase 0.78±0.05 (see his equation 5-6 and figure 5-24).

In order to maintain the disc in Osaki's model, the enhanced mass transfer, and thus superhump maximum, must occur when the bright spot is furthest from the compact object (see 4.4.2), i.e. when it is on the left hand side of figure 4.04. The data points of Honey *et al.* (1987), which were not available to Osaki, therefore seem to rule out his model.

Whether or not the superhump light is eclipsed, is still a matter of contention. Whitehurst *et al.* (1984) deduced that it was uneclipsed, whilst Smak (1985) concluded that the light is 20% eclipsed. Both the methods are inaccurate because the authors had not realised that the system brightness varies with beat phase (see 4.2.3 above). So the question remains an open one. However it is obvious even from the raw data (see for instance Schoembs 1986) that the superhump light is largely uneclipsed. This tells us that if the superhump source is located in the disc as in the tidal model, its area is probably quite large, and thus only suffers a partial eclipse as described by Horne (1984). If the bright spot is large, it too might avoid being eclipsed, and so the eclipse constraints are consistent with all 3 elliptical disc models.

Since all the eclipse effects can be interpreted as the superhump remaining largely uneclipsed there is no need to invoke a separate mechanism to explain them as Krzeminski & Vogt (1985) did. Vogt's elliptical disc model is consistent with the data, without having to resort to this mechanism.

The change in superhump period through superoutburst (see 4.2.1) remains difficult to explain using any of the models. Whitehurst (1987) thought

that changes in disc structure through a superoutburst might change the precession period of the disc, though this has yet to be proven. Warner (1985b) showed that if the disc's eccentricity declined through the outburst, and that if the angular momentum of the disc is conserved then the timescale for the period change is correct.

Whitehurst (1987) suggested that the Osaki mechanism might be invoked to explain the late superhump in his model, since (as shown above) the phasing of the humps in the two models is different by ~180^{o}. The same mechanism might be invoked for the late superhump in Vogt's model.

So we are left with two strong candidate models for superhumps, Vogt's and Whitehurst's. It is no accident that these models are very similar, the constraints placed by the data force them to be so. This also makes tests that can differentiate between them difficult to devise. The best tests are probably eclipse studies of the disc during superoutburst, which might discover where in the disc the hump light originates. Unfortunately Whitehurst (1987) does not state where the extra light in his simulations arises from, and the answer to this question will probably have to wait until the disc simulations can be performed with greater precision and detail.

4.6 UV observations of superoutbursts

UV spectroscopy of SU UMa stars in superoutburst, obtained using the *International Ultraviolet Explorer* (*IUE*), has been published for VW Hyi (Verbunt *et al.* 1987), WX Hyi (Hassall *et al.* 1983) and EK Tra (Hassall 1985). The NV λ1240, SiIV λ1400 and CIV λ1550 resonance lines are broad (a few thousand km s^{-1}), strong, absorption lines, which are often blueshifted. HeII λ1640 has a similar profile. Sometimes there is

also redshifted emission associated with these lines, resulting in P-Cygni profiles.

The UV resonance lines probably originate in an outflowing wind, and have been modelled as such (e.g. Drew 1987). In the face-on systems, light from the disc passes through the wind, and as it does so photons at the wavelengths of the resonance lines are scattered out of the observer's line of sight, producing an absorption line. A radiatively driven wind will acquire ever higher velocities as it moves outwards, and the absorption will occur at shorter wavelengths. This produces the observed blue shifted absorption profile.

If the system is edge-on, the wind is not seen projected against he disc, and the wind will scatter photons into the observers line of sight, and the system is then seen in emission. This effect has been seen in nova-like variables (e.g. RW Tri, Cordova & Mason 1985), which seem, in many respects, to be like dwarf novae in perpetual outburst.

4.7 EUV observations of superoutbursts

Polidan & Holberg (1987) present an EUV (1050Å) light curve of the October/November 1984 superoutburst of VW Hyi. The initial rise is delayed by about 0.5 days compared to the optical light curve, but the flux then dips before rising to a second peak, at ~100 times the quiescent flux, 1.8 days after the first. This dip was not seen in the optical data. However, it is thought that optical precursors occur only when the EUV dip is even more pronounced than it was in this case.

4.8 X-ray observations of superoutbursts

X-ray light curves have been published of VW Hyi during its November 1983 (van der Woerd, Heise & Bateson 1986) and October/November 1984 (van der Woerd & Heise 1987) superoutbursts. The soft X-ray flux (7-300Å) is generally a factor 100 or so above its quiescent value, whereas the hard X-ray flux (1-20keV) remains approximately at its quiescent value. During the two outbursts observed, the soft X-ray decline is similar to the optical decline.

During the October/November 1984 superoutburst two X-ray data points were obtained on the rise, approximately 2 and 2.5 days after the beginning of the optical rise. The second data point shows that the system has faded in X-rays relative to the first, and coincides with a dip in the EUV light curve (Polidan & Holberg 1987). Thus the X-ray may also show a precursor outburst. In the November 1983 superoutburst there is only one point before the peak of the outburst. The flux is almost a factor 10 below the peak flux, despite being 3 days after the commencement of the optical outburst. It may, in fact, be in the dip between the precursor and main outburst.

Soft X-ray oscillations are sometimes present in VW Hyi during superoutburst (van der Woerd *et al.* 1987). Their amplitude is around 15%, but variable, and their periods are near 14 seconds. Sometimes they are coherent, and at other times they show phase jitter. Their origin is still unclear, although the periods are similar to the Keplerian timescale of the inner disc, and they may originate there or in the boundary layer. They may well be related to the low coherence optical oscillations sometimes present during outbursts of dwarf novae (see 4.2.3).

4.9 Normal outbursts and quiescence

The first few days of a superoutburst are virtually indistinguishable from a normal outburst. In neither case are there superhumps (except the superhumps reported during the decline of a normal outburst by Marino & Walker 1979), and the EUV precursor light curve of VW Hyi is similar to that of a normal outburst (Polidan & Holberg 1987). Throughout a superoutburst the published UV and optical spectra are almost identical to those of normal outbursts. However, in a careful comparison for VW Hyi, Verbunt *et al.* (1987) showed that the equivalent widths of the UV absorption lines are smaller during superoutburst.

The quiescent spectra of the SU UMa's are radically different from those during outburst. The Balmer lines and HeII λ4686 are present in emission as are some of the UV resonance lines (for the latter see Hassall, Pringle & Verbunt 1985, and Verbunt *et al.* 1987). In some spectra there are HeI emission lines. The spectra do not have such a blue continuum as the outburst spectra. These differences are probably because the disc becomes optically thin in quiescence, and the absorption from the wind becomes much less important.

References

Bateson, F.M., & McIntosh, R., 1986. *Publs var. star Sect. R. astr. Soc. N.Z.* **13**, 1.

Bath, G.T., Edwards, A.C., & Mantle, V.J., 1983. *Mon. Not. R. astr. Soc.*, **205**, 171.

Brosch, N., Leibowitz, E.M., & Mazeh, T., 1980. *Astrophys. J.*, **236**, L29.

Cordova, F.A., & Mason, K.O., 1985. *Astrophys. J.*, **290**, 671.

Cordova, F.A., & Mason, K.O., 1983. In: *Accretion-Driven Stellar X-ray Sources* p.147 eds. Lewin, W.H.G., & van den Heuvel, E.P.J., C.U.P., Cambridge.

Crampton, D., Hutchings, J.B., & Cowley, A.P., 1979. *Astrophys. J.*, **234**, 182.

Drew, J., 1987. *Mon. Not. R. astr. Soc.*, **224**, 595.

Gilliland, R.L., & Kemper E., 1980. *Astrophys. J.*, **236**, 854.

Hassall, B.J.M., 1985. *Mon. Not. R. astr. Soc.*, **216**, 335.

Hassall, B.J.M., Pringle, J.E., & Verbunt, F., 1985. *Mon. Not. R. astr. Soc.*, **216**, 353.

Hassall, B.J.M., Pringle, J.E., Schwarzenberg-Czerny, A., Wade, R.A., & Whelan J.A.J., 1983. *Mon. Not. R. astr. Soc.*, **203**, 865.

Honey, W.B., Charles, P.A., Whitehurst, R., Barrett, P.E., Smale, A.P., 1987. *Mon. Not. R. astr. Soc.*, in press.

Horne, K., 1985. *Nature*, **312**, 348.

Kato, S., 1983. *Publs. astr. Soc. Japan*, **35**, 249.

Krzeminski, W. & Vogt, N., 1985. *Astr. Astrophys.*, **144**, 124.

Marino, B.F., & Walker, W.S.G., 1979. *Proc. IAU Colloq. No. 45*, p. 29, ed. Smak, J.

Ortolani, S., Rafanelli, P., Rosino, L., & Vittone, A., 1980. *Astr. Astrophys.*, **87**, 31.

Osaki, Y., 1985. *Astr. Astrophys.* **144** 369.

Polidan, R.S., & Holberg, J.B., 1987. *Mon. Not. R. astr. Soc.*, **225**, 131.

Ritter, H., 1987. *Astron. Astrophys. Suppl. Ser.*, in press.

Robinson, E.L., Shafter, A.W., Hill, J.A., Wood, M.A., & Mattei, J.A., 1986. Quoted in: Shafter, A.W., Szkody, P., & Thorstenson, J.R., 1986. *Astrophys. J.*, **308**, 765.

Schoembs, R., & Vogt, N., 1980. *Astr. Astrophys.*, **91**, 25.

Schoembs, R., 1986. *Astr. Astrophys.*, **158**, 233.

Shafter, A.W., Szkody, P., & Thorstenson, J.R., 1986. *Astrophys. J.*, **308**, 765.

Smak, J., 1985. *Acta Astr.*, **35**, 1.

van der Woerd, H., Heise, J., & Bateson, F., 1986. *Astr. Astrophys.*, **156**, 252.

van der Woerd, H., & Heise, J., 1987. *Mon. Not. R. astr. Soc.*, **225**, 191.

van der Woerd, H., Heise, J., Paerels, F., Beuermann, K., van der Klis, M., Motch, C., & van Paradijs, J., 1987. *Astr. Astrophys.*, **182**, 219.

Verbunt, F., Hassall, B.J.M., Pringle, J.E., Warner, B., & Marang, F., 1987. *Mon. Not. R. astr. Soc.* **225**, 113.

Vogt, N., 1974. *Astr. Astrophys.*, **36**, 369.

Vogt, N., 1977. In: *IAU Coll. 42, The Interaction of Variable Stars with their Enviroment* eds. Kippenhahn, R., Rahe, J., Strohmeier, W., p. 227. Veroff. Dr. Remeis Sternwarte Bamberg.

Vogt, N., 1980. *Astr. Astrophys.*, **88**, 66.

Vogt, N., 1982. *Astrophys. J.*, **252**, 653.

Vogt, N., 1983. *Astr. Astrophys.*, **118**, 95.

Walker, M.F., & Bell, M., 1980 *Astrophys. J.*, **237**, 89.

Warner, B., 1974 *Mon. Not. R. astr. Soc.* **168** 235.

Warner, B., 1975 *Mon. Not. R. astr. Soc.* **170** 219.

Warner, B., 1983. *I.B.V.S.* No. 2397.

Warner, B., 1985a. In: *Interacting Binaries* p.367 eds. Eggleton, P.P. & Pringle, J.E. D. Reidel, Dordrect, Holland.

Warner, B., 1985b. In: *Proceedings of the Ninth North American*

Workshop on Cataclysmic Variables p.142 ed. Szkody, P., University of Washington.

Whitehurst, R., 1987. *D.Phil. Thesis.* Oxford.

Whitehurst, R., Bath, G.T. & Charles, P.A., 1984. *Nature,* **309**, 768.

Whitehurst, R., 1984. *Mon. Not. R. astr. Soc.*, **207**, 215.

Chapter 5

Optical and Infrared Photometry of the May 1985 Superoutburst of OY Carinae

5.1 Introduction

OY Car is an SU UMa with an orbital period of 91 minutes and a superhump period of about 93 minutes (Krzeminski & Vogt 1985, hereafter KV). The normal outbursts have a recurrence time of 25-50 days and the superoutbursts, 300 days. OY Car is one of only two known eclipsing SU UMa systems with frequent (~months) superoutbursts, and thus is an ideal target for superoutburst studies.

In this Chapter I present optical and infrared photometry of OY Car during the superoutburst of May 1985, leaving the complementary ultraviolet (*IUE*) spectroscopy and X-ray (*EXOSAT*) observations for Chapter 6. The data are presented in 5.2, and in 5.3 the colour temperature and emitting area of the superhump are estimated. The results of eclipse fitting are contained in 5.4. In 5.5, 5.6 and 5.7 various features of the light curves are discussed and 5.8 summarises the conclusions. The relationship between the results of this chapter, and other observations of disc structure are discussed in Chpater 8.

The collection of the data presented in the following two chapters involved many astronomers at sites scattered across the globe. Firstly, long term optical monitoring of OY Car was carried out by the Variable Star Section of the Royal Astronomical Society of New Zealand (VSS RAS NZ). When the star was observed to be beginning a superoutburst they informed P.A. Charles at Oxford, who co-ordinated the subsequent

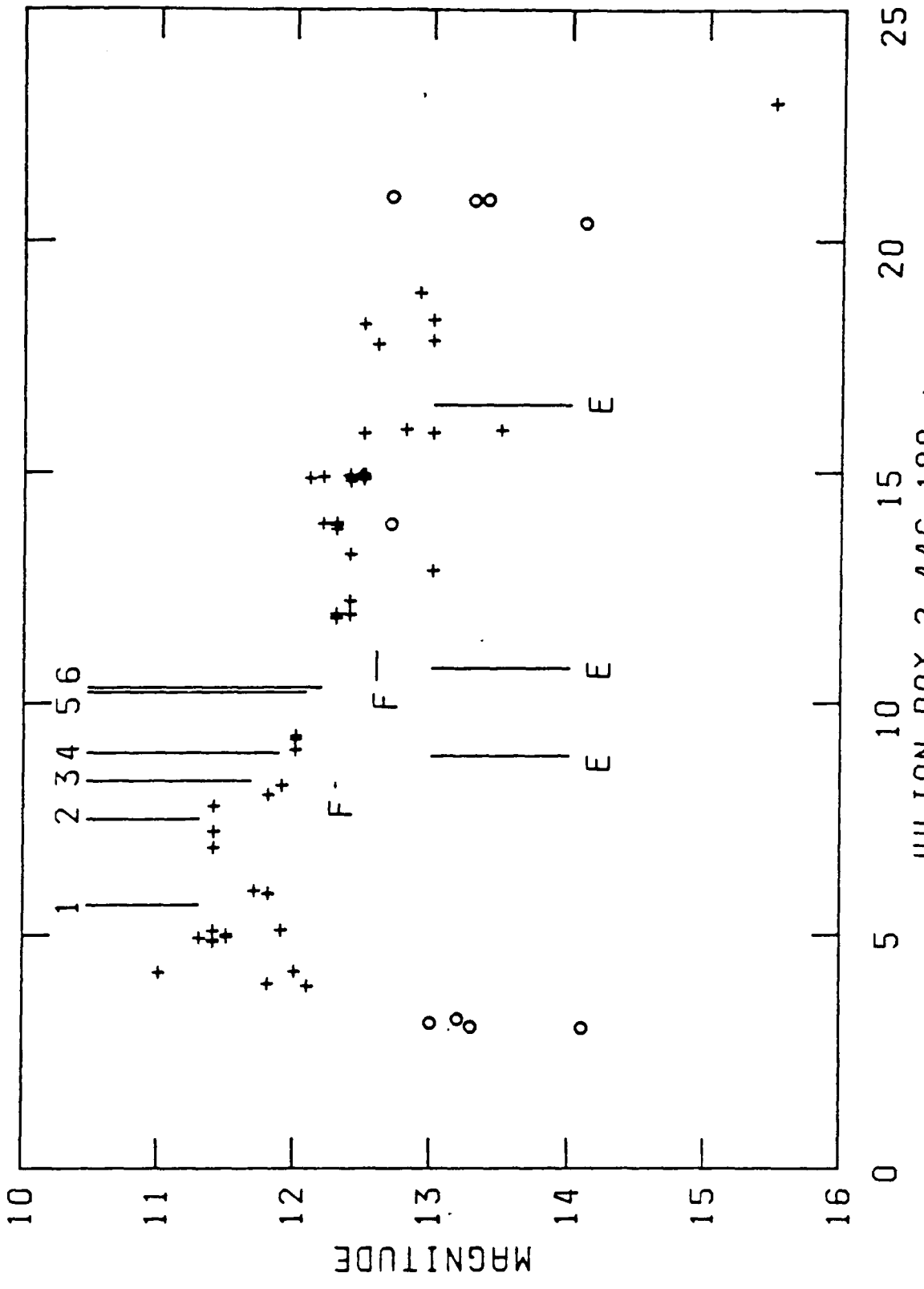

Figure 5.01 The light curve of OY Car during the May 1985 superoutburst. Crosses mark observations and circles upper limits from the observations of the VSS RAS NZ. The times of optical photometry (numbers) and *EXOSAT* (E) observations are marked. The length of the *IUE* observations are shown by horizontal lines (F) that lie at the mean FES magnitude.

Table 5.1 Log of obervations

Obs #	JD +2440 Start	JD +2440 End	Cycle Number Start	Cycle Number End	Telescope	Band	Beat Phase	Observer
1	6185.61	6185.69	34727.9	34729.2	ESO 0.9m	Wal.	0.30	KR
2	6187.50	6187.52	34757.8	34758.2	ESO 0.9m	Wal.	0.87	KR
3	6188.24	6188.41	34769.5	34772.2	SAAO 1.0m	B	0.15	IMC
3	6188.26	6188.35	34769.9	34771.3	SAAO 1.9m	J	0.15	PAW
3	6188.36	6188.41	34771.4	34772.3	SAAO 1.9m	H	0.15	PAW
4	6188.89	6188.91	34779.9	34780.2	AAT	K	0.34	DA
4	6188.95	6188.97	34780.9	34781.1	AAT	J	0.34	DA
5	6190.09	6190.11	34798.8	34799.2	AAT	J	0.70	ARH
6	6190.30	6190.40	34802.2	34803.8	SAAO 1.0m	B	0.78	IMC
6	6190.33	6190.40	34802.5	34803.8	SAAO 1.9m	J	0.78	PAW

Table 5.2 Details of obervations

Telescope	Integration Time	Aperture	Standard Stars
ESO Dutch 0.9m	16s	16"	From Walraven list
SAAO 1.9m	40s	24"	SA4102
SAAO 1.0m	10s	16" (#3) & 21" (#6)	E & F region
AAT	17.17s (eclipses) & 200s (else)	7" (#4)	Allen & Cragg (1983)

Table 5.3 Eclipse simulation parameters for figures 5.09 and 5.10

Curve Number	Disc Radius[1]	Mass Transfer Rate $10^{-8} M_\odot$/year	T(Figure 5.09) 10^3K	T(Figure 5.10) 10^3K
1	0.25	10.5	112 - 18	79 - 14
2	0.30	2.9	79 - 14	17 - 25
3	0.35	1.8	69 - 13	15 - 20
4	0.45	1.25	62 - 11	13 - 17

[1] In binary separation.

Table 5.3 Eclipse simulation parameters for figure 5.11

Curve Number	Disc Radius[1]	Temperature 10^3K
1	0.35	17.0 - 24.45
2	0.35	12.5 - 17.7
3	0.45	11.0 - 14.45

[1] In binary separation.

programme of observations. The "Target of Opportunity" override was then invoked for the *IUE* observations which were carried out by B.J.M. Hassall and G. Sonneborn, and the *EXOSAT* observations which Hans van der Woerd and the author carried out. Optical observations were also carried out by collaborators in Australia, South Africa and Chile (see 5.2).

5.2 Observations

Figure 5.01 shows the magnitude of OY Car throughout the May 1985 superoutburst, as observed by the VSS RAS NZ. In order to decrease the scatter introduced by the eclipses, points within a tenth of a cycle of phase zero have been omitted. The time of the beginning of the outburst is uncertain, as the only observations early in the outburst are upper limits, but the peak was reached at JD 2 446 184.0. The upper limits from the previous day show that OY Car brightened by more than 3 magnitudes in under 1.2 days. The outburst decayed slowly over the next 15 days, and was followed by a rapid decay of 2.5 magnitudes sometime between JD 2 446 198.9 and 2 446 203.0. If the outburst was similar to other outbursts (Bateson & Dodson 1983) the final decay will have taken less than a day.

During the 5 days after the peak of the superoutburst a total of 6 sets of photometric observations were made with Johnson B and Walraven (W, U, L, B, V) filters in the visual, and J, H and K filters in the infrared. All the observations were made in fully photometric conditions. These have been assigned numbers in chronological order (see Tables 5.1 and 5.2). The plots of each run use the orbital ephemeris of Wood (1986) for cycle numbers ≥22230. The flux densities of zero magnitude stars

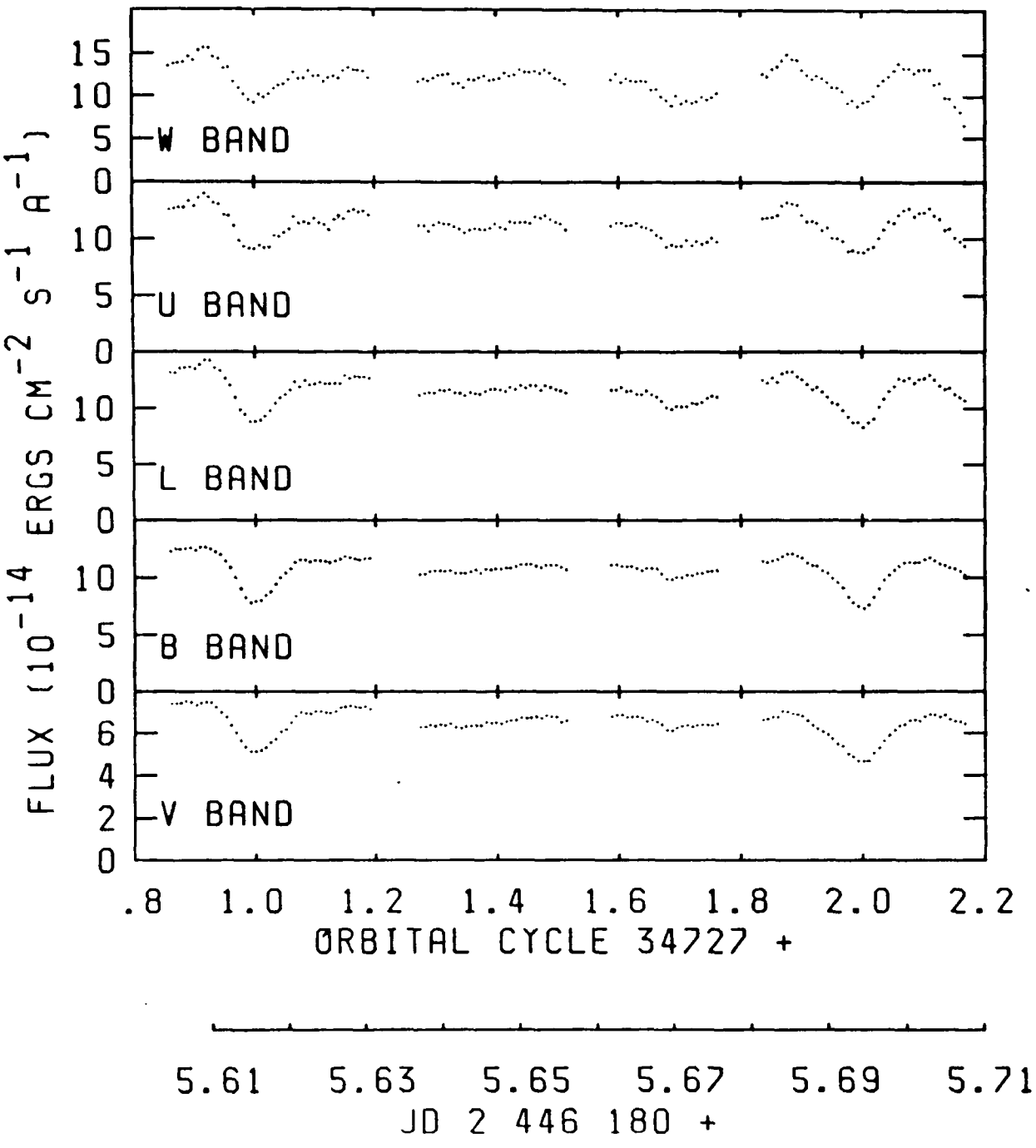

Figure 5.02 The Walraven light curves from observation 1.

given by de Ruiter & Lub (1986) were used to convert the Walraven data into fluxes.

Observation 1 (ESO; 0.9m, Walraven Photometry; figure 5.02)

Figure 5.01 shows that this observation (carried out by K. Reinsch) lies near the peak of the superoutburst. If we extrapolate the superhump ephemeris backwards (see Appendix 2 and Table 5.1) we find that any superhump should be at phase 0.3, but it is absent; the superhumps have not yet developed. The eclipses are smooth (apart from noise in the U and W band) and are slightly asymmetric; although the sense of the asymmetry is opposite in the two eclipses, it is the same in each band. Apart from the eclipses, the most prominent feature is the dip at phase 0.7, whose depth is greatest at the shortest wavelengths. In the W band the flux just before the eclipse is slightly higher than the flux away from the dip (e.g. at cycle 34728.4).

Observation 2 (ESO; 0.9m, Walraven Photometry; figure 5.03a)

By the time of this observation (2 days later, again carried out by K. Reinsch) the superhumps had started to develop. Their calculated time of maximum (using an ephemeris based on later optical observations, see Appendix 2), is phase 0.87. The flux is obviously greater before the eclipse than after it, in agreement with this prediction, although the asymmetry decreases at shorter wavelengths. Thus we attribute the extra light before eclipse to the superhump.

Observation 3 (SAAO; 1.0m, B; 1.9m J, H; figure 5.04)

Eighteen hours later the superhumps were well developed. P.A. Whitelock

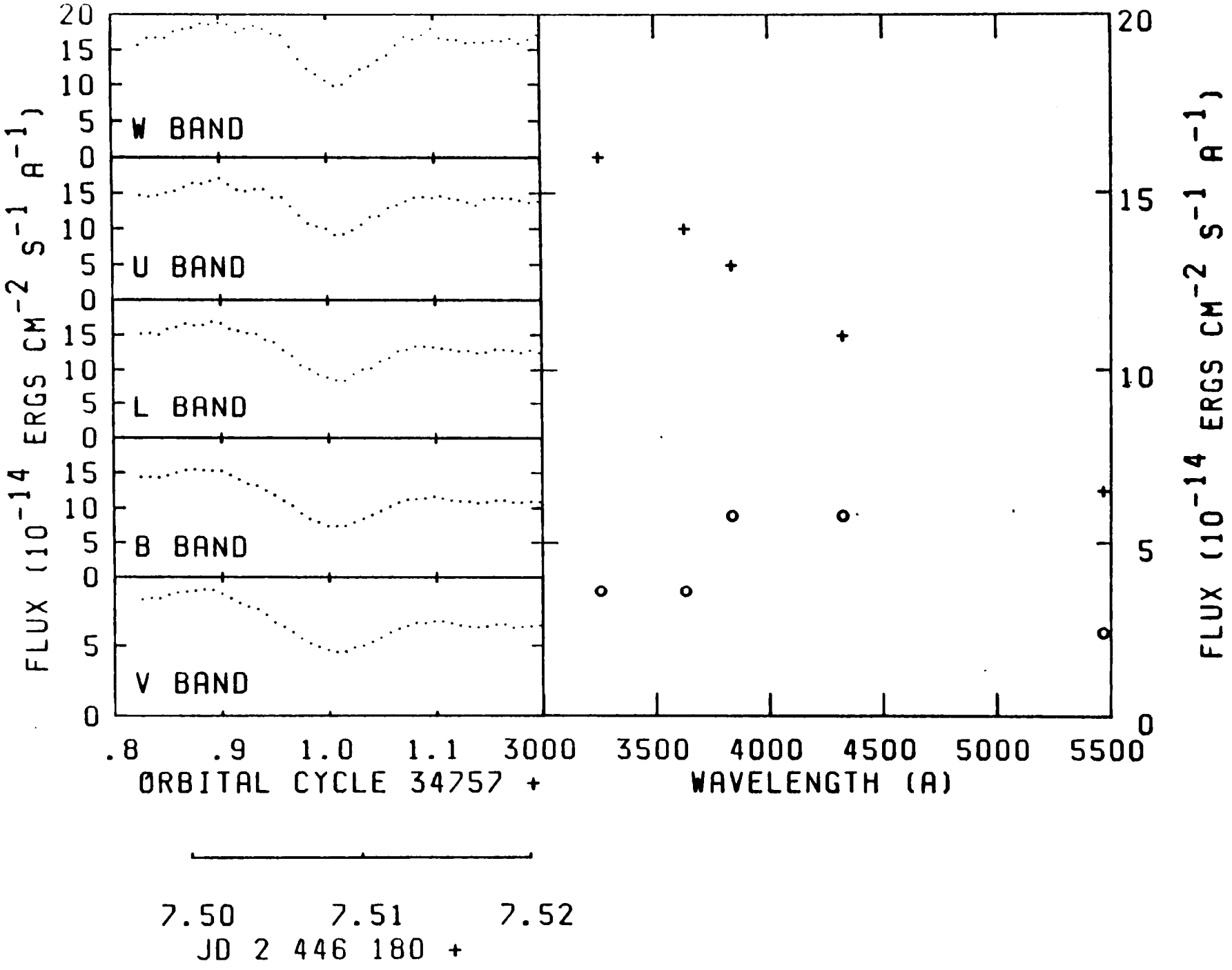

Figure 5.03 Left: a) The Walraven light curves from observation 2. Right: b) The derived spectral distribution for the disc (crosses) and superhump (circles).

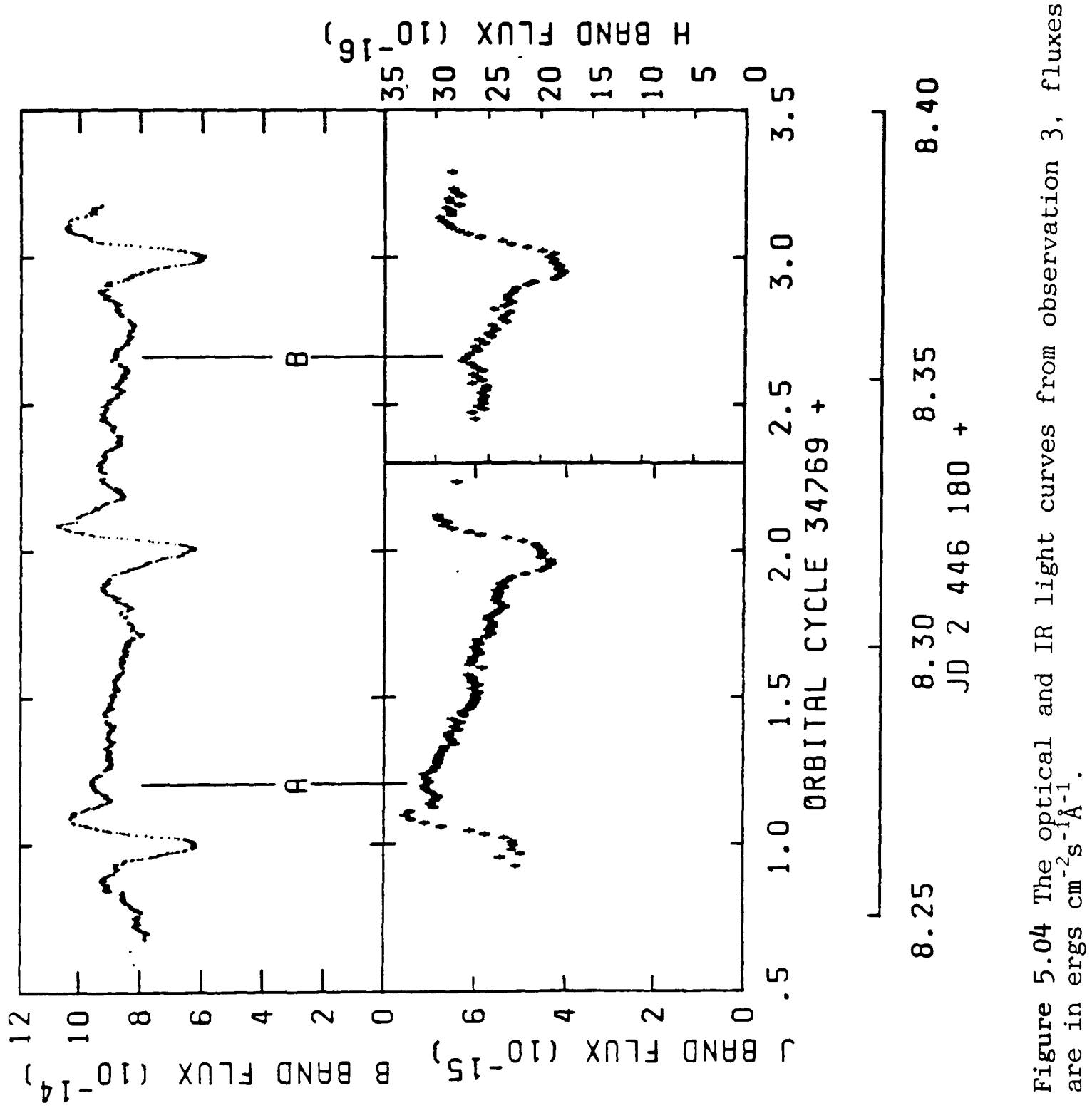

Figure 5.04 The optical and IR light curves from observation 3, fluxes are in ergs $cm^{-2}s^{-1}Å^{-1}$.

and I.M. Coulson observed two orbital cycles and three eclipses, the IR filter being changed after the second eclipse. The B band data show that superhump maximum occurs during or just after the eclipse. The most striking aspect is the difference between the gross optical and IR behaviour before the eclipse. Whilst the optical is increasing from about phase 0.8, the IR continues to fall until after the eclipse. The IR eclipses are relatively flat bottomed, as are two of the three optical eclipses. The remaining optical eclipse has a slower ingress than egress. In all the eclipses the IR ingress is complete before the optical ingress begins, but the egress begins at the same time in both bands. After the eclipse, there is structure (e.g. the features marked "A" and "B" in figure 5.04) on a timescale of 0.2 orbital cycles and with an amplitude of about 10% of the total system light. The IR data follow the optical structure closely, in contrast to their behaviour prior to the eclipse.

Observation 4 (AAT; J, H, K; figure 5.05)

Just twelve hours after observation 3, IR AAT observations (carried out in PATT service time) show that the flux away from the superhump had fallen by 15% to 20% in the H and J bands, and the superhump had moved away from the eclipse. High time resolution data of one eclipse (in J) and part of another (in K), and low time resolution J, H and K data during the rest of the orbital cycle were obtained. The IR eclipses are deeper and sharper than in observation 3. Eclipse 34781 is asymmetric, showing a slower ingress than egress.

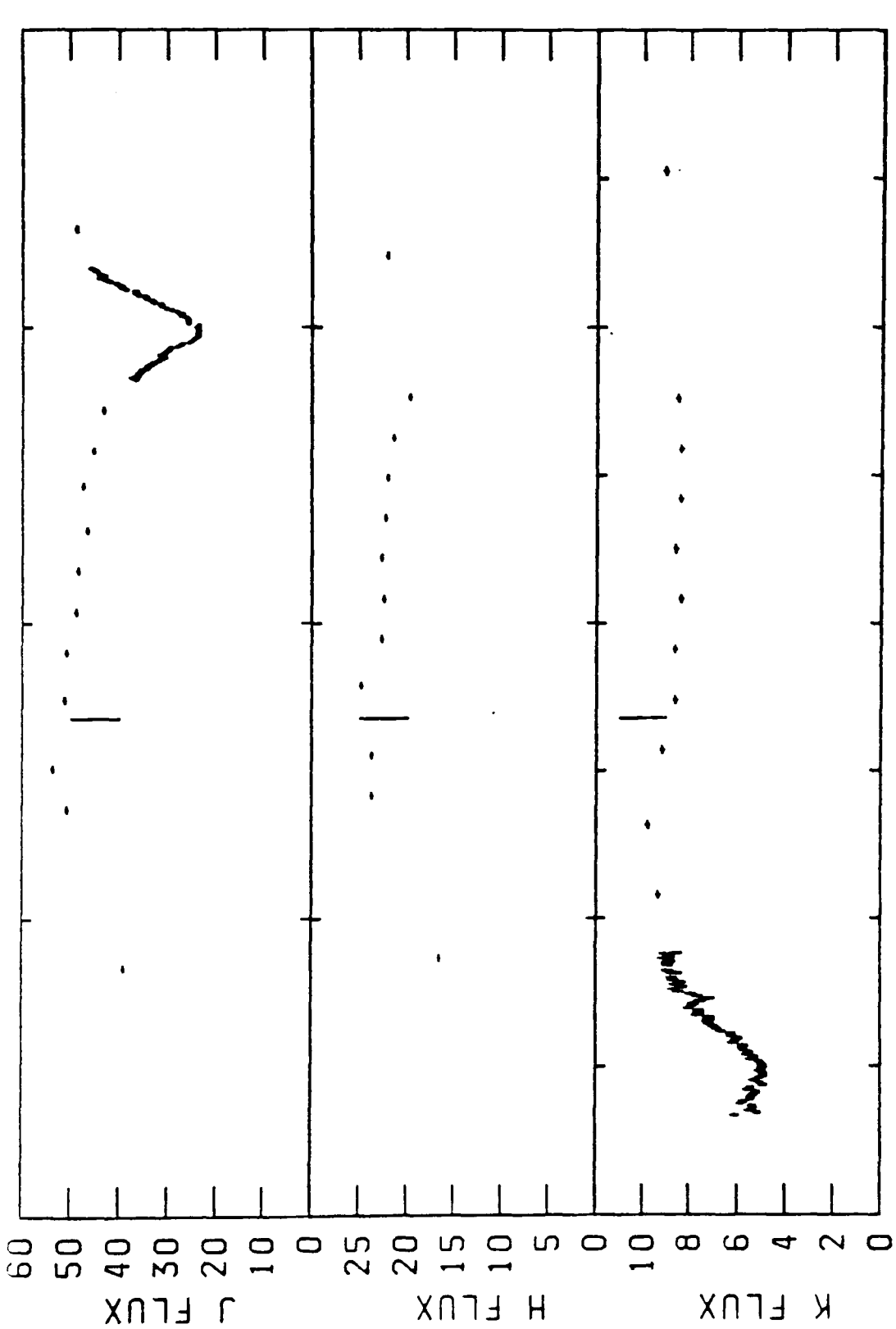

Figure 5.05 The IR light curves from observation 4, The vertical bars mark the calculated time of superhump maximum.

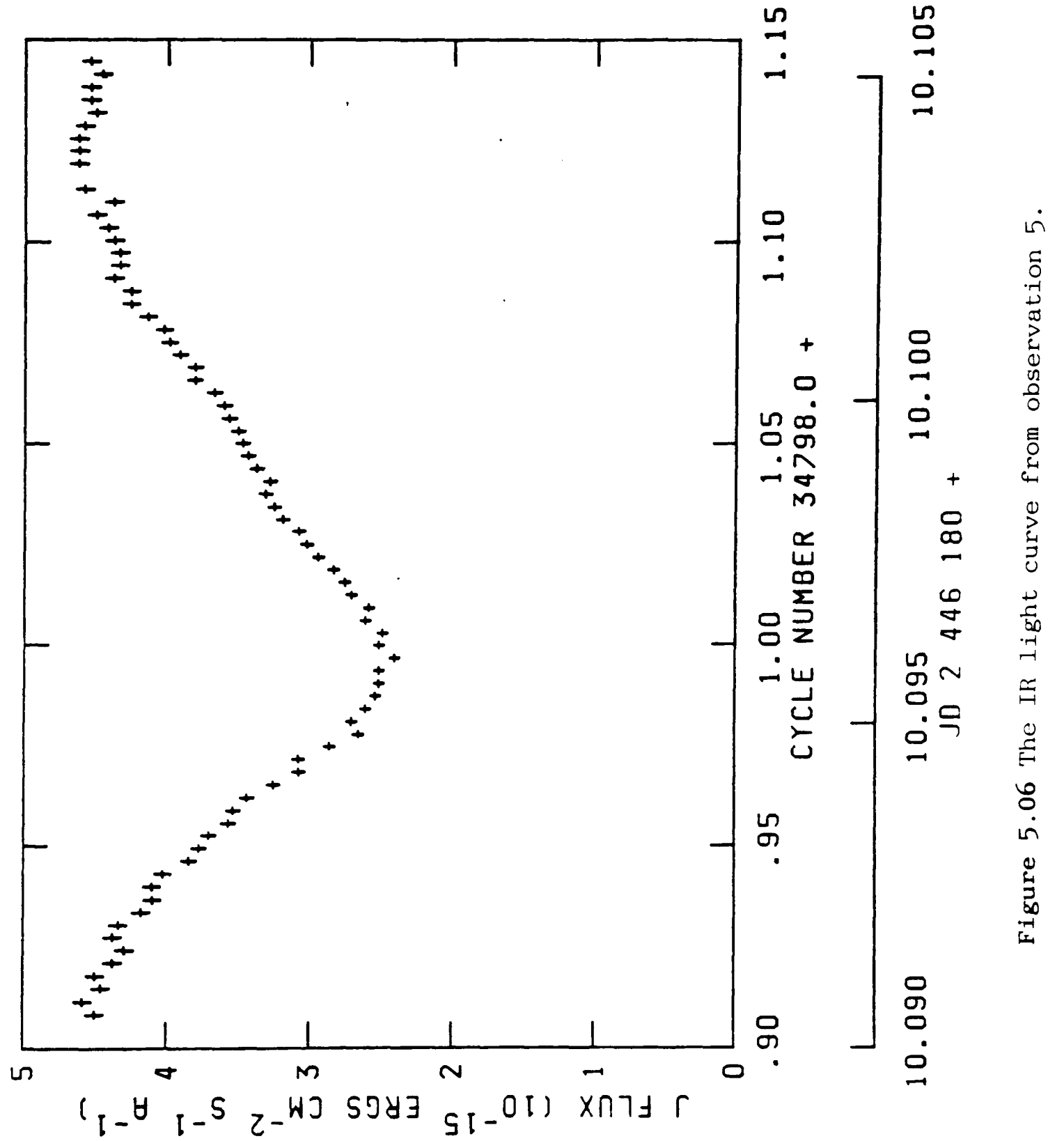

Figure 5.06 The IR light curve from observation 5.

Observation 5 (AAT; J; figure 5.06)

A further eclipse was observed with the AAT one day later by A.R. Hyland in the J band. Again the eclipse is fairly deep, but it now has a slower egress than ingress.

Observation 6 (SAAO; 1.0m, B; 1.9m, J; figure 5.07)

This observation consisted of simultaneous B and J band photometry, and was carried out by I.M. Coulson and P.A. Whitelock. In the B band the hump begins at orbital phase 0.5, peaks just before 0.8 and ends by phase 0.3. The superhump appears less structured than in observation 3. There is a sharp dip (marked "C"), which begins at orbital phase 0.6 in cycle 34802. At the same phase in cycle 34803 there are 2 or 3 smaller dips (the most prominent is marked "D"), which do not distort the superhump shape so significantly. The J band follows the optical, although the eclipse is wider than in the B band.

5.3 The superhumps

5.3.1 The optical spectrum

It was noted in Section 2 that in observation 2 the difference between the flux before and after the eclipse is probably due to the superhump. We have subtracted the peak flux before the eclipse (ϕ_o=0.9) from the mean flux between phases 0.1 and 0.2 to obtain the superhump flux shown in figure 5.03b. There are short term fluctuations in the Walraven light curves of ~10% of the superhump light, which is an estimate of the systematic error on these points. The spectrum has a Balmer jump in absorption, implying that the superhump is optically thick, allowing its

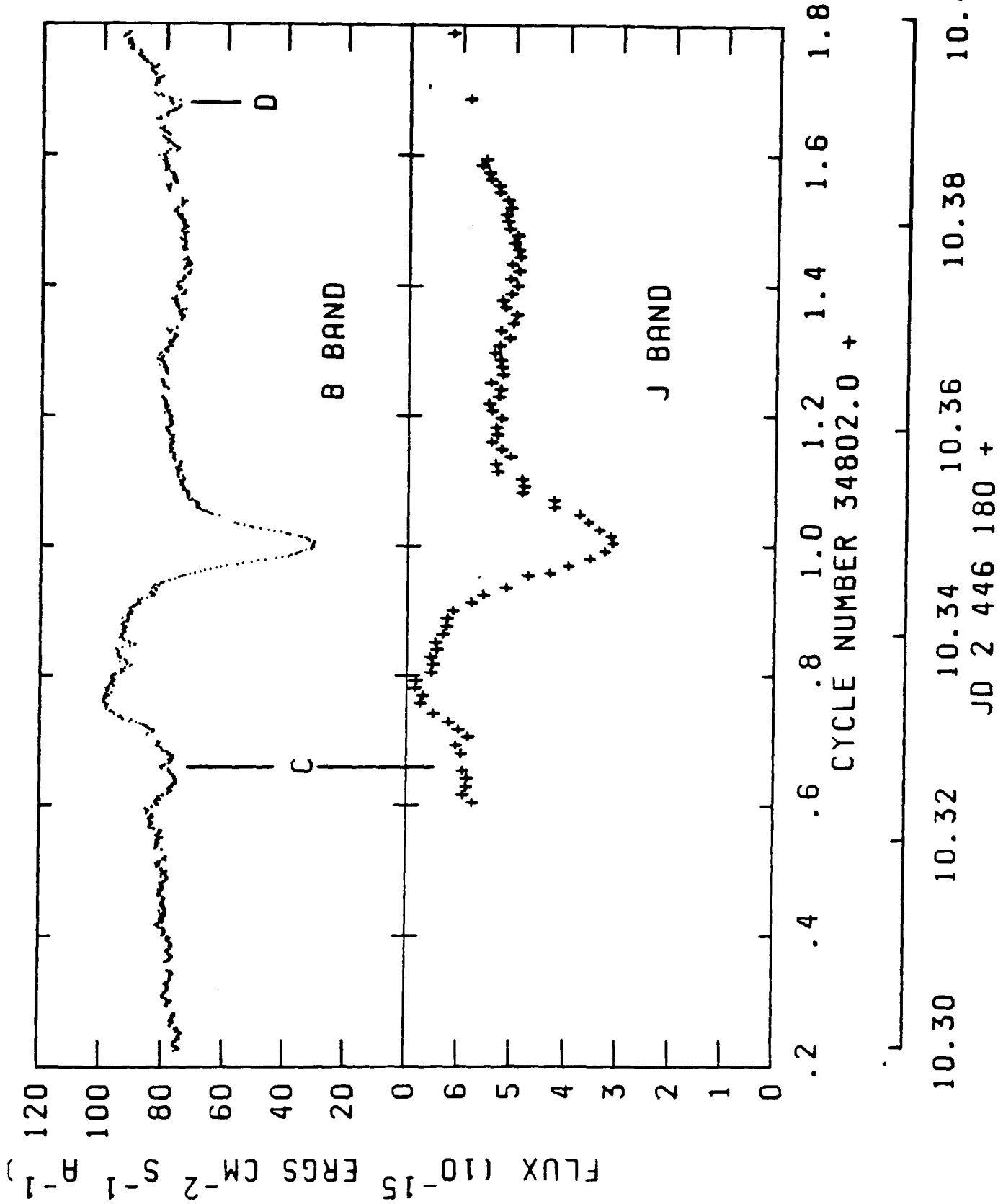

Figure 5.07 The optical and IR light curves from observation 6.

temperature and area to be estimated by the following colour temperature method.

5.3.2 The colour temperature and emitting area

To obtain a measure of the colour temperature, a wide wavelength baseline is needed, and light curves with a well defined superhump. This excludes observations 2 and 3. The best observation with which to derive a colour temperature is 6, which has B and J band data. Assuming the difference in flux between cycle 34803.5 and the peak near 34802.8 to be due entirely to the superhump we measure a superhump flux of 2.5×10^{-14} ergs $cm^{-2}s^{-1}Å^{-1}$ in the B band. The same times in the J light curve give a superhump flux of 1.8×10^{-15} ergs $cm^{-2}s^{-1}Å^{-1}$. The resulting B/J ratio of 14 ± 2 yields a blackbody colour temperature of 9200K ± 1200K, where the errors are due to the uncertainty in estimating the flux at superhump maximum and minimum. The corresponding blackbody area of the superhump when projected onto the plane of the sky is;

$$(11\pm3)\times10^{19}\left(\frac{d}{100pc}\right)^2 \ cm^2 \qquad \ldots(5.1)$$

where d is the distance to OY Car in parsecs.

An entirely separate estimate of the colour temperature and emitting area can be obtained using the low time resolution data from observation 4 since it shows a peak at about phase 0.3 in J and K and phase 0.4 in H. (It should be noted that this is a smaller wavelength range than was used above.) This coincides with the time of optical superhump maximum (see Appendix 2), and so we attribute the excess flux in this region to the superhump. Using the J/K ratio (5.8 ± 0.4) to derive a temperature we find a value of 6200 ± 700 K where the quoted error is due to a

combination of statistical errors and uncertainties in estimating the flux. The area given by observation 4 is also $(11\pm3)\times10^{19}cm^2$ at 100pc.

Although the areas derived from observations 4 and 6 agree, the temperatures are significantly different. As the two temperatures are derived from colour ratios of different pass bands I attribute the difference to temperature structure in the superhump, rather than to a true temperature change between the two observations. The Balmer jump in the Walraven data is consistent with model atmospheres in the range of temperatures found by the blackbody method.

The above calculation has made the implicit assumption that the superhump is only responsible for the light of the hump. It has been suggested (e.g. Smak 1985) that there is superhump light throughout the orbital cycle, and that it merely peaks at superhump phase zero. What we can say with certainty is that the superhump region produces at least as much light as there is in the hump in our light curves, and maybe more. Thus if lines of constant luminosity in a temperature-area diagram are drawn (figure 5.08), with a luminosity equal to that of the hump in various bands, the area and temperature of the superhump region must lie above and to the right of these lines. This is shown for the B and J data of observation 6. The point of intersection of the B and J band lines is the temperature and area calculated above. The total system luminosity in the UV (at 2650-2690Å, see Chapter 6) provides an upper limit. Since the superhump cannot be brighter than this its values of temperature and area are now limited to the region shown in the diagram. The minimum possible superhump area is the point where the UV line intersects the J band line, which is at about half of the area calculated above. This is because large areas will always be needed to

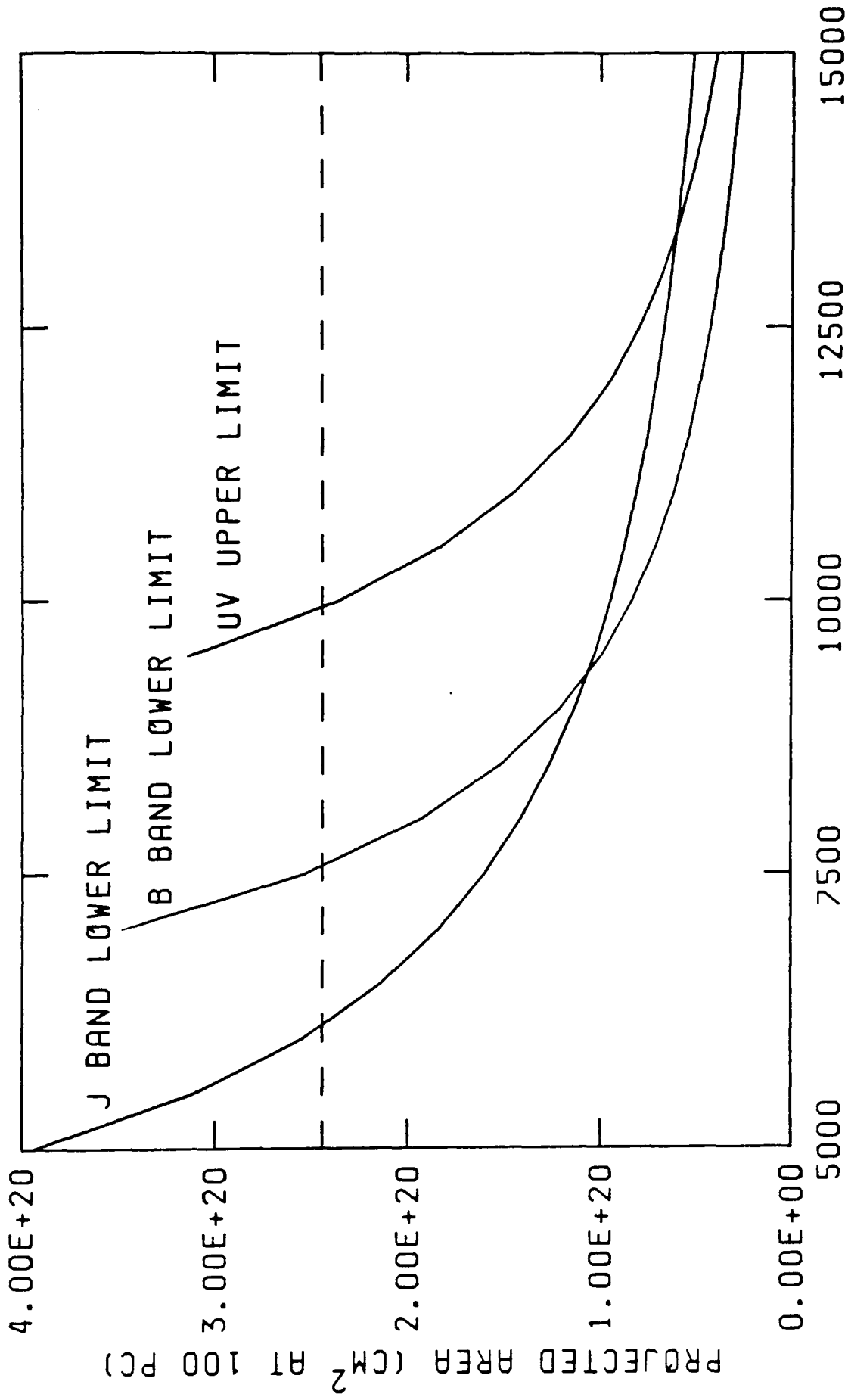

Figure 5.08 The range of possible temperatures and areas for the superhump using the fluxes of observation 6 and that in the LWP camera. The dotted line is the area of the red dwarf from Wood *et al.* (1987).

produce the observed IR flux, unless very high temperatures are invoked, which are ruled out by the UV flux.

The distance to OY Car is uncertain, but the minimum distance is 78pc (Wood 1986), and may be as much as a factor 2 larger. Also using Wood's radius for the red star and equation (5.1) gives the projected area of the superhump as 27% of the projected area of the red component. As I have used a lower limit to the distance, the area given is also a lower limit.

In summary, the projected area of the superhump is at least 27% of the projected area of the red star, under the assumption that the superhump provides no flux during superhump minimum. Relaxing the latter assumption will only allow smaller areas if the superhump is a very significant contributor to the system's UV light, which is unlikely (see Verbunt *et al.* 1987).

5.3.3 Consequences for superhump models

If the superhump source were on the red component, as it is in the starspot model, the limits make it obvious that a large proportion of the red star must be involved. Whitehurst *et al.* (1984) make no predictions about the size of the superhump region. In the elliptical disc and intermediate polar models the superhump is due to a modulation in the flux from the bright spot. If this is an isotropically radiating bulge on the edge of the disc our data suggest that the size of the bulge is of the same order as the red component.

In order to find whether the superhump source could lie in the plane of the disc I must first estimate the relative projected areas of disc and

red star. For the disc I used the largest possible area, that of the Roche lobe. Wood (1986) estimated the mass ratio and inclination independently of the (poorly understood) radial velocity variation as 9.8 and 83.3^{o} respectively. This gives the ratio of the surface area of the red star to the disc area as 1.1. So the superhump source must cover at least 25% of the white dwarf's Roche lobe, i.e. it is possible that the superhump source lies in the plane of the disc, although its area is large.

Bath *et al.* (1983) suggested that if the stream is dense compared to the outer regions of the disc (as may occur in a superoutburst), the stream will penetrate the disc. In a model where the stream penetration region is the source of the superhump light (i.e. all models where the bright spot is modulated) this means that the superhump source would lie in the plane of the disc. The large size of such a source means that it would be only partially eclipsed by the red dwarf, explaining the lack of a total superhump eclipse (see Horne 1984).

5.4 Eclipse fitting

In order to test the suggestion that there is superhump light throughout the entire superhump cycle G. Berriman used the methods described in Berriman, Kenyon & Bailey (1986) to produce synthetic light curves for steady state discs, and I have compared them with the data. If superhump light were present the model eclipses should be deeper than the observed eclipses. The models assume one-dimensional cylindrical symmetry, i.e. that the temperature at any point on the disc is only a function of distance from the centre of the white dwarf:

$$T_R = T_* R^{\beta} (1 - R^{-1/2})^{1/4} \qquad \ldots(5.2)$$

where T_* is the temperature at the white dwarf surface and R is in units of white dwarf radii. For a steady state disc $\beta=3/4$ and the mass transfer rate ($\dot{M}$) is related to T_* by $T_*=(3GM_{wd}\dot{M}\pi\sigma R^3)^{3/4}$ (Shakura & Sunyaev 1973). Each point is assumed to emit as a black body at a temperature T_R. The light curve for the eclipse of this disc by a Roche lobe filling secondary is then calculated.

An inclination of 81^o, a mass ratio of 7 and a secondary of $0.1M_\odot$ were used for all the models. The distance was found using the method of Bailey (1981) as in Berriman (1984), and assuming that the secondary has a K magnitude of 14.0. In fact, for a given inclination and K magnitude the calculated disc flux at the Earth is independent of the secondary mass since;

$$\text{flux at Earth} \propto \left(\frac{\text{disc radius}}{\text{distance}}\right)^2. \qquad \ldots(5.3)$$

The distance is from Bailey's method and is proportional to the radius of the red dwarf, and the disc radius is proportional to the binary separation. Thus the flux is proportional to the ratio of the binary separation to red dwarf radius, which is dependent only on the known mass ratio, not on the absolute masses.

The parameters which can be changed are the disc radius and the mass transfer rate. For a chosen disc radius, the mass transfer rate was adjusted so that the out-of-eclipse flux matched that of the observation.

It was decided to model the J band eclipse in observation 4 since this apparently suffers little interference from the superhump (see 5.2). Figure 5.09 shows the results for a steady state disc ($\beta=3/4$) and various values of mass transfer rate, superimposed on the data. In all

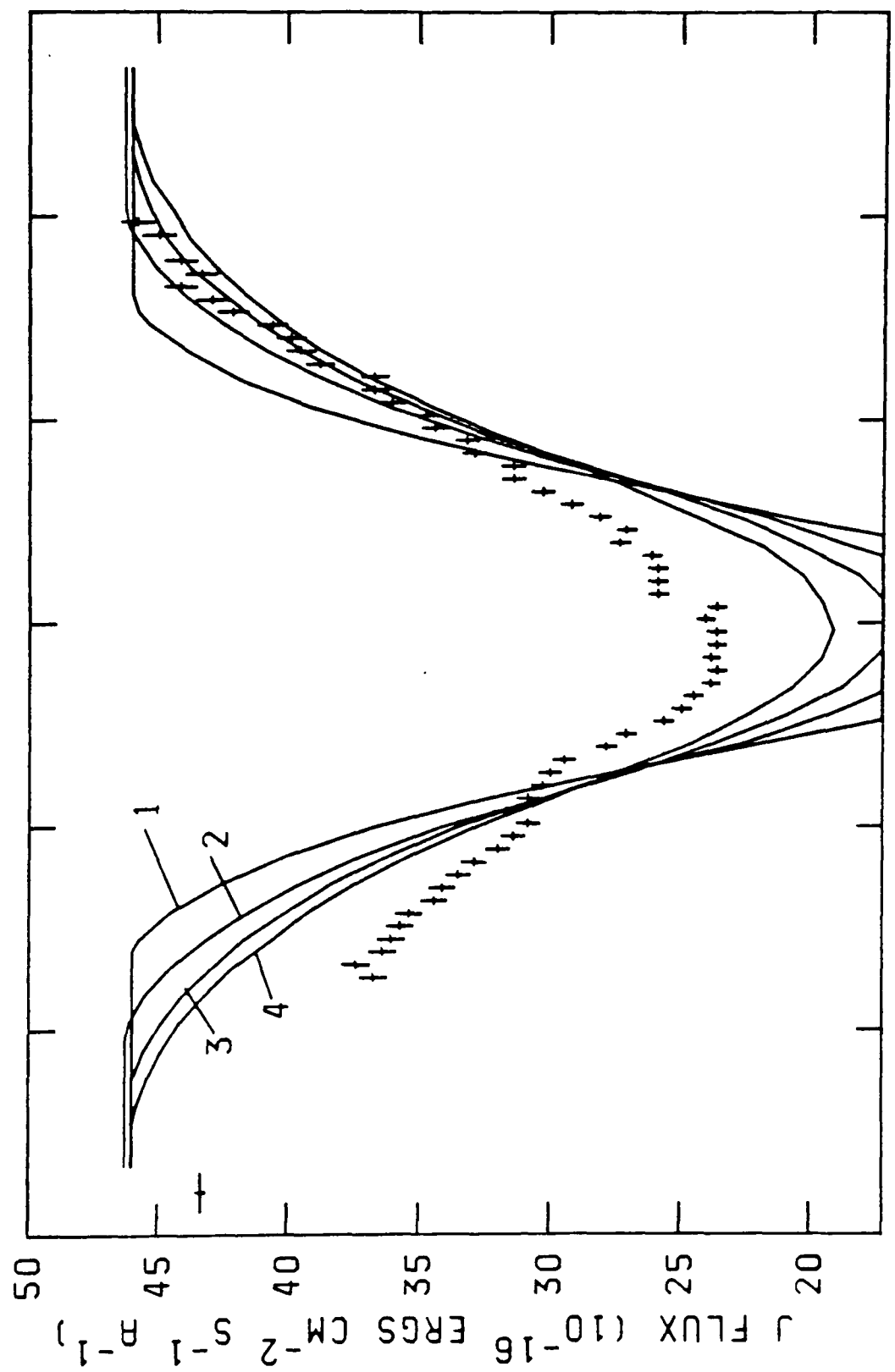

Figure 5.09 J Band simulations of a steady state disc compared with eclipse 34781. Table 5.3 lists the parameters for each simulation.

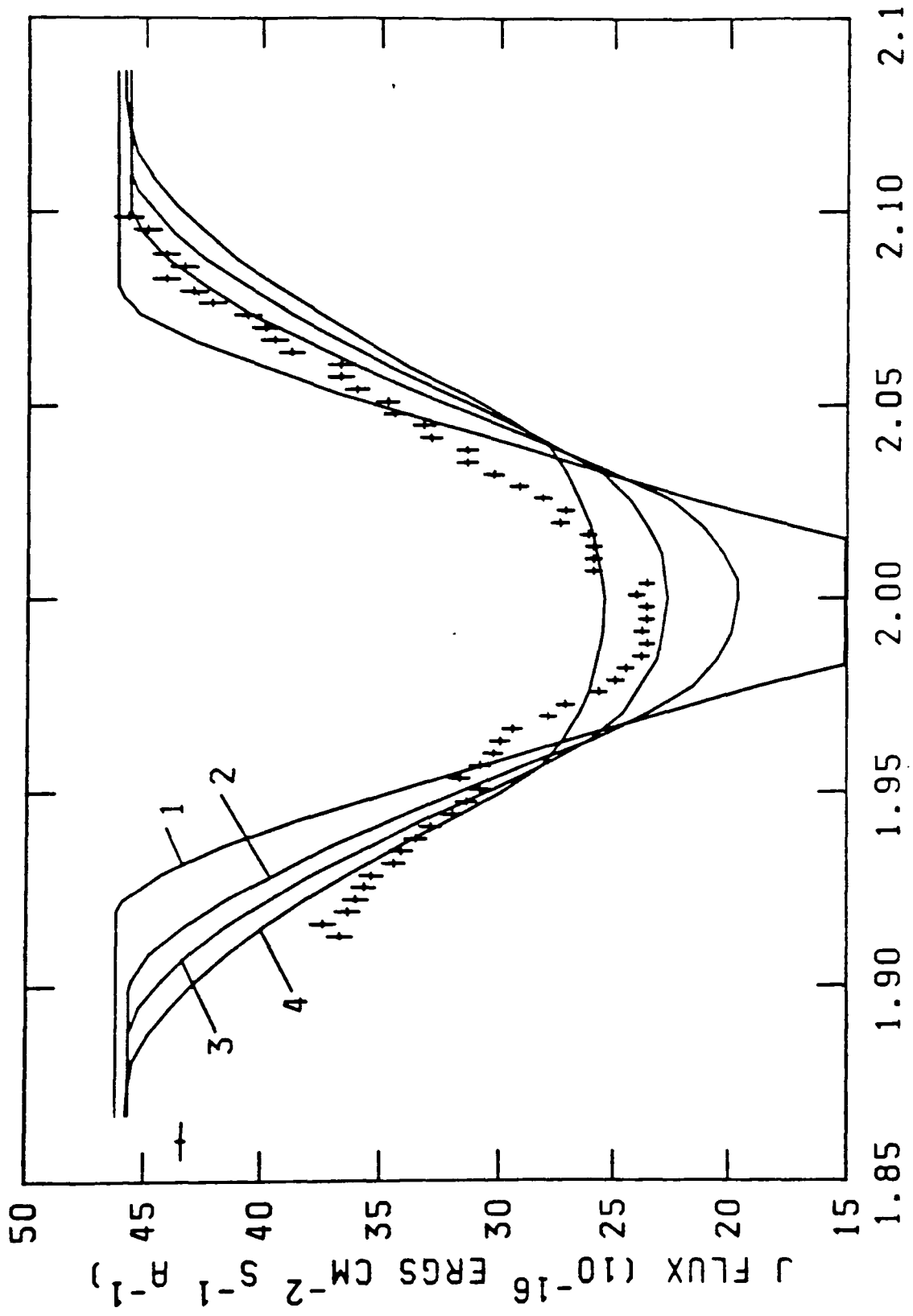

Figure 5.10 J Band simulations of a β=0 disc compared with eclipse 34781. Table 5.3 lists the parameters for each simulation.

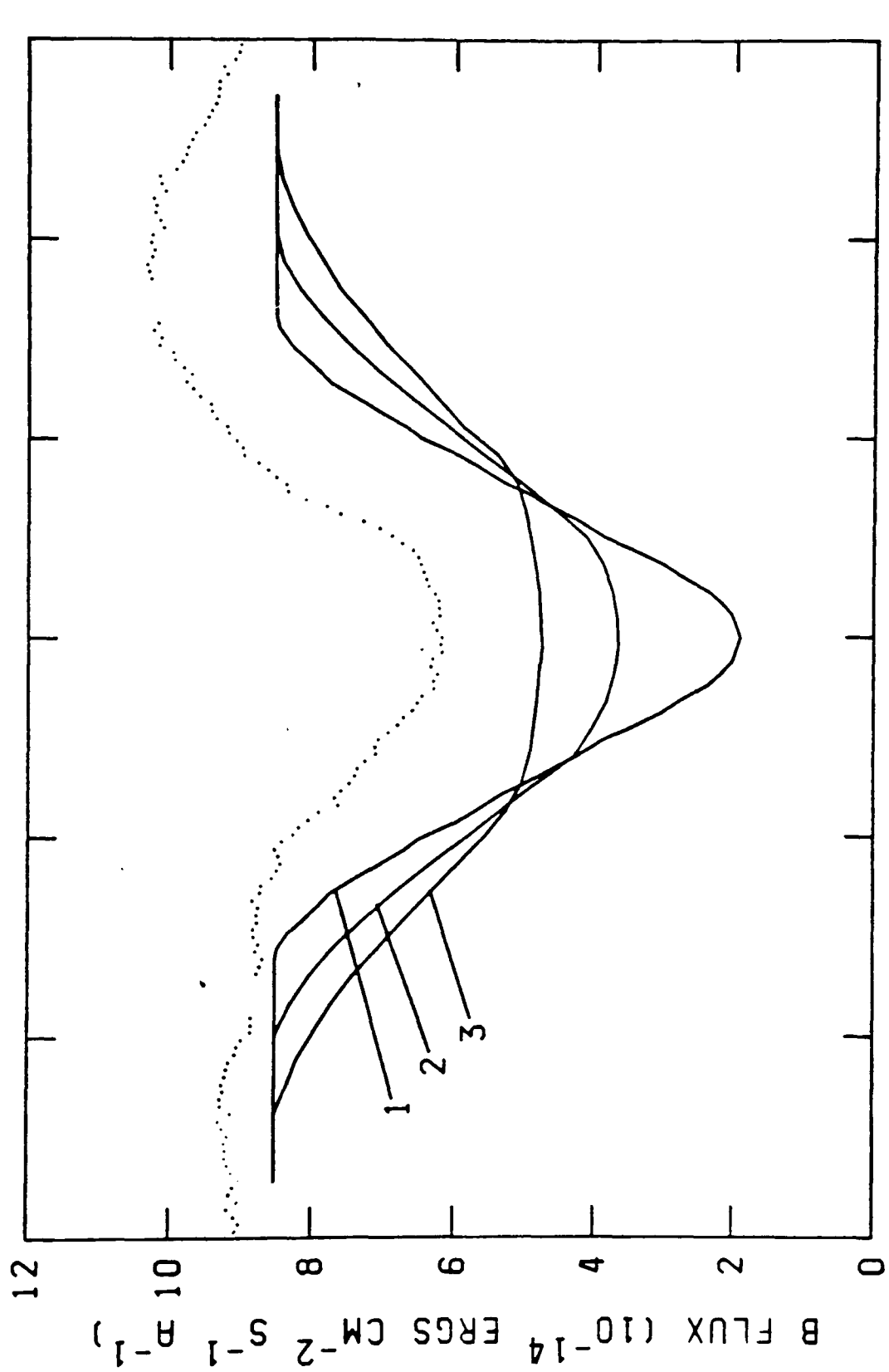

Figure 5.11 B Band simulations of a β=0 disc compared with eclipse 34770. Table 5.4 lists the parameters for each simulation.

the simulations the eclipses are too deep on a scale larger than the eclipse asymmetry. The only way to make them shallower is to make the disc larger, which will result in the model eclipse being too wide. In an attempt to resolve this the steady state assumption was relaxed, by setting β=0, although the physical significance of this is not obvious. Figure 5.10 shows the resulting fits for a range of values of T_*. These models can fit the egress, but are steeper than the observed ingress.

Synthetic eclipses for observation 3 will not fit the data even when β=0 (see figure 5.11). Attempts to widen or narrow the eclipse have the same effect as described for observation 4. Making β non zero will also deepen the eclipse.

Although the β=0 temperature distribution fits some of the eclipses, it must be remembered that this implies higher mass fluxes through the outer than through the inner disc. If this situation persisted for the duration of the outburst it would result in an increase in the mass of the inner disc. It also contrasts with the findings of Horne & Cook (1985), that the temperature distribution in Z Cha during a normal outburst was in fair agreement with a steady state disc, or a slightly higher mass flux in the inner disc. If the β=0 temperature distribution does not reflect the real radial temperature distribution, we must account for the reduction of the flux from the disc centre by about 50% relative to the outer edges. I will consider three possibilities; limb-darkening, obscuration of the inner parts of the disc and the effects of superhump light.

Real atmospheres, unlike black bodies, possess limb-darkening, which varies as a function of both temperature and wavelength. For the eclipse fitting we are interested in how the limb-darkening at a

particular wavelength varies with temperature. Early-type stellar atmospheres give some insight into the problem. However, it must be remembered that accretion discs have lower optical depths than stars, an uncertain and position dependent gravity, and produce some energy in the upper layers of their atmospheres (see Wade 1984).

Wade and Rucinski (1985) give quadratic limb-darkening coefficients for Kurucz model atmospheres. These have been plotted in figure 5.12 for 81^{o} inclination, a wavelength of 16500Å and for $2 \leq \log_{10}(g) \leq 5$. The maximum variation due to the combined effects of surface gravity and temperature is 25%, and most of that variation occurs for temperatures below 10^{4} K. Above this temperature the changes are in the sense that the hottest atmospheres (corresponding to regions nearer the centre of the disc) are the least limb-darkened; i.e. in the opposite sense to that required to explain the shallow eclipses. Gravity is expected to increase towards the centre of the disc, and this also decreases the limb-darkening. Indeed, only in the extreme condition of cool atmospheres approaching the Eddington limit will limb-darkening increase with temperature, and this effect is $\leq$10%.

A concave disc (i.e. a disc thicker at the edges than at the centre) would lead to a lower effective inclination in the inner than the outer regions of the disc. The resulting limb-darkening would tend to make the inner regions relatively brighter with respect to the outer disc. So, unless limb-darkening in accretion discs is dramatically different from that in stellar atmospheres, it cannot explain our results.

The absence of any X-ray eclipse (see Chapter 6) suggests that the white dwarf and innermost disc are permanently obscured in some way. If the opening angle of the disc were such that we could only see its rim, i.e.

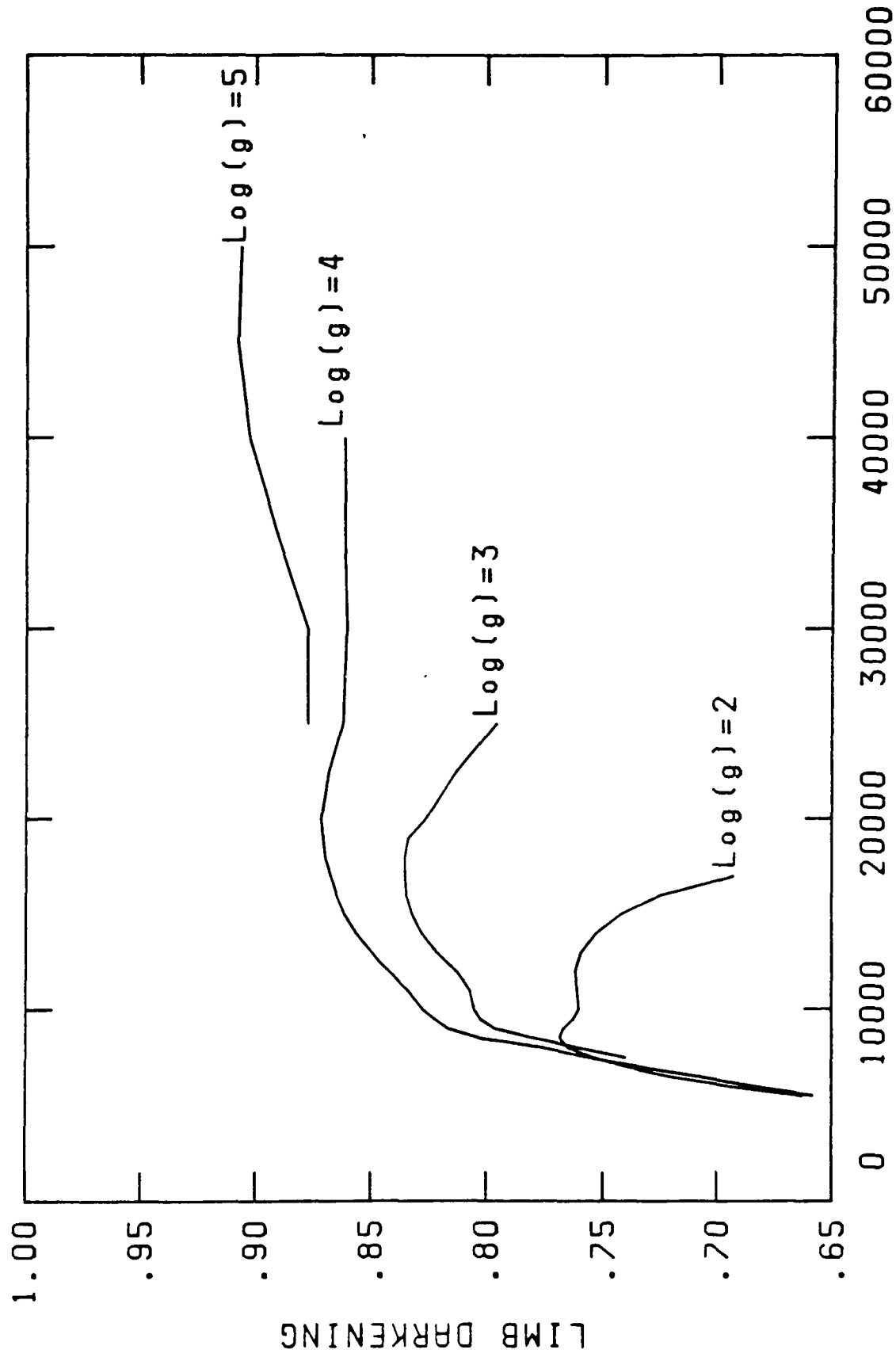

Figure 5.12 Limb-darkening calculated using Wade and Rucinski's (1985) quadratic co-efficents for Kurucz model atmospheres. The curves are for an inclination of 81^{o} and a wavelength of 16500Å.

a "wall", all at roughly the same temperature (~10^4 K), this would produce the required effect. However, this would completely occult the inner disc, and we would not see the observed UV continuum (see Chapter 4). This implies that either there is a bulge in the disc near the UV emitting region, that obscures the white dwarf and innermost regions of the disc, or the disc rim obscures only the front part of the disc and the white dwarf region, leaving the far side of the disc (and its UV region) visible. The results of Horne & Cook (1985) suggest that such a bulge or rim is absent during normal outbursts.

The failure to fit observation 3, even with a β=0 temperature distribution, may also be because of the presence of superhump light; this is the observation where superhump maximum is near the time of eclipse. If the superhump light is largely uneclipsed (see for example Whitehurst *et al.* 1984), we should subtract this light from the data before attempting to fit the eclipse. This would have the effect of making the eclipse deeper, which may then make it consistent with observation 4 (eclipse 34781).

One might go further and suggest that if there is superhump light present at all phases then this would explain why all the observed eclipses are too shallow, or too wide to be fitted by a steady state disc. At this point it is impossible to choose between this explanation and the idea of a thickened disc, except that the latter may explain other phenomena as well (see Section 8 and Chapter 6).

5.5 Eclipse parameters

The variations of the value of the observed time of eclipse minus the calculated time (O-C) is an important effect that any superhump model

must explain (see KV and Whitehurst *et al.* 1984). Table 5.5 shows values of O-C for all our eclipses with the observed eclipse time found by the standard method of bisecting chords. About 8 chords were drawn across each eclipse and the bisectors joined with a smooth curve that was extrapolated to the eclipse bottom. The intersection of the light curve and this line defined the observed time of eclipse. The quoted errors are the errors inherent in the measuring process; the systematic error is ~4 times larger.

These values cannot be compared directly with those of KV since there is an important difference between our definitions of O-C. Instead of subtracting the calculated time of conjunction ($T_{\phi=0.0}$) from the observed time of minimum (T_{min}) to find O-C, KV used the following procedure. They:

(1) defined the amplitude (A) of the eclipse by subtracting the average of the magnitudes at phases -0.1 and 0.1 from the magnitude at minimum,

$$A = m(T_{min}) - 0.5\{m(T_{\phi=-0.1}) - m(T_{\phi=0.1})\}; \quad ...(5.4)$$

(2) found the times when the magnitude was $m(T_{min}) - A/2$, and called these T_1 and T_2;

(3) calculated O-C as

$$(O-C)_{KV} = 0.5(T_1+T_2) - (T_{\phi=0.0}) \quad ...(5.5)$$

where the subscript KV indicates that this is the O-C calculated by the above method. They also defined an asymmetry parameter ΔT;

$$\Delta T = T_{min} - 0.5(T_1+T_2). \quad ...(5.6)$$

In order to compare my values of O-C with KV, I recalculated the

Table 5.5

Eclipse #	Band	O-C
34758	W	49
	U	49
	L	44
	B	40
	V	58
34770	B	22
34771	B	62
	J	-148
34772	B	9
	H	-153
34781	J	-12
34799	J	-22
34803	B	18
	J	35

N.B. All figures in $1x10^{-5}$ days, errors $\pm 8x10^{-5}$

Table 5.6

Eclipse #	$O-C_{KV}$	ΔT
34758	71	36
34770	-18	11
34771	4	67
34772	-16	44
34803	13	40

N.B. All figures in $1x10^{-5}$ days, errors $\pm 8x10^{-5}$

parameters for my B band light curves by the above method, having plotted the light curves in magnitudes (see Table 5.6). The Walraven B band data (which also have a slightly different band pass from Johnson B) were converted into magnitudes such that magnitude = -2.5log(flux).

My values for both of these parameters are consistent with those of KV, showing that at least the order of magnitude of these effects is similar for different superoutbursts, although there is not enough data to reproduce the beat cycle effects they noted. But $(O-C)_{KV}$ (Table 5.6) is significantly different from O-C calculated by the bisecting chords method (Table 5.5).

The higher time resolution of my data allows the morphology of the eclipse to be examined carefully. In the case of an asymmetric eclipse, i.e. one with a non zero ΔT, the observed time of eclipse calculated by KV's method does not coincide with the time of minimum light. Figure 5.13 shows this effect for eclipse 34771. The bisector of a chord at the half amplitude of an asymmetric eclipse will always be offset from T_{min} to the side of the eclipse with the smaller gradient. This means that an asymmetric eclipse with T_{min} at exactly the predicted time ($T_{\phi=0.0}$) would still show a non zero $(O-C)_{KV}$. Because of this I feel that the conventional definition of O-C, $T_{min} - T_{\phi=0.0}$, is a more useful parameter. This can be found from KV's data since,

$$T_{min} - T_{\phi=0.0} = \Delta T + (O-C)_{KV}. \qquad \ldots(5.7)$$

Figures 10 and 11 of KV show that ΔT and $(O-C)_{KV}$ are nearly in anti-phase, suggesting that the variation of $T_{min} - T_{\phi=0.0}$ should be smaller than $(O-C)_{KV}$, and that $(O-C)_{KV}$ is dominated by ΔT. In order to confirm this I calculated $T_{min} - T_{\phi=}0.0$ from KV's plots, choosing the I band data

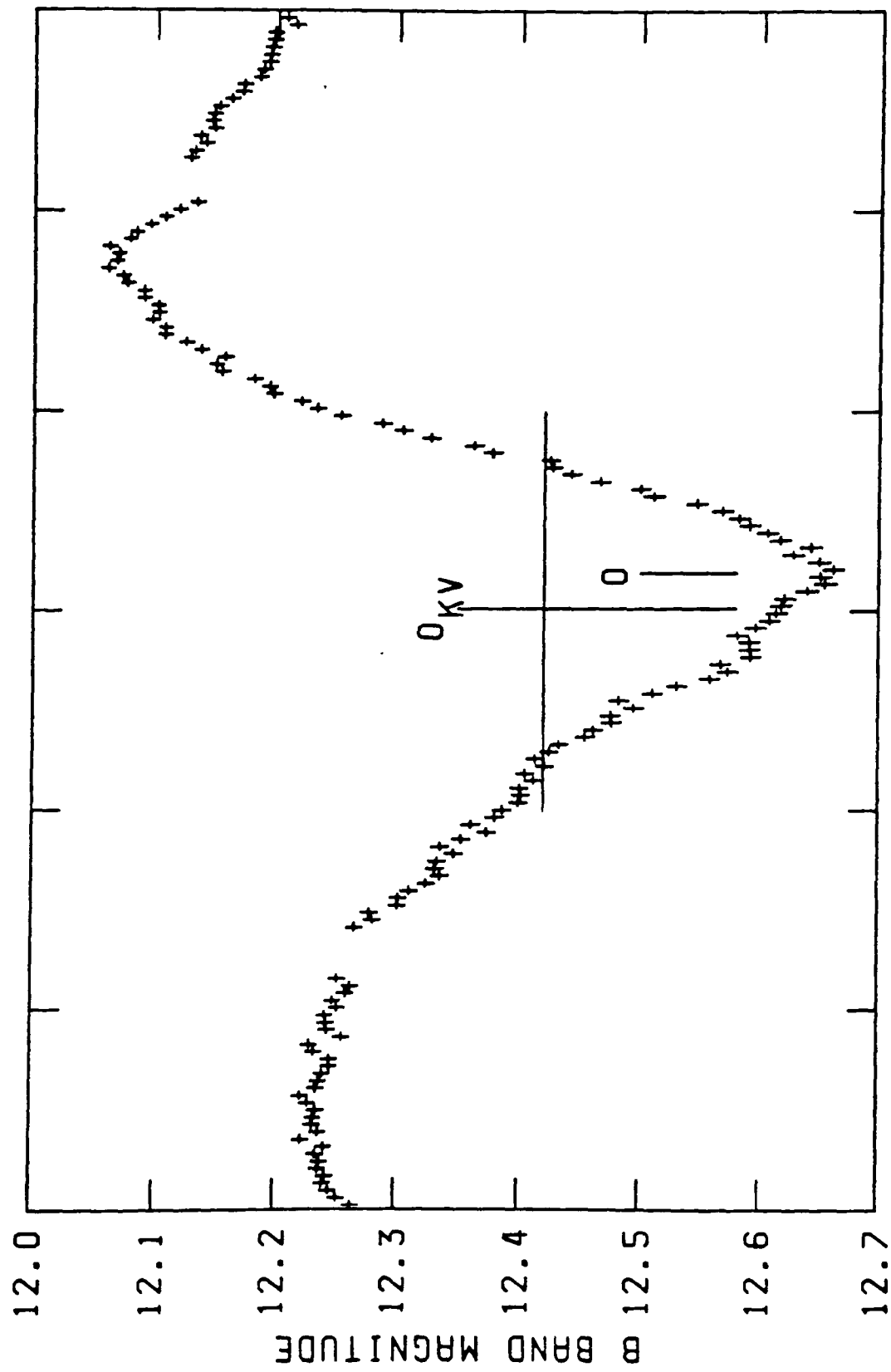

Figure 5.13 Eclipse 34771 plotted in B band magnitudes. The horizontal bar is at the half amplitude in magnitudes of the eclipse, and the vertical bar marked O_{KV} is the observed time of eclipse measured using the method of KV.

as these show the $(O-C)_{KV}$ and ΔT effects most clearly. The result is shown in figure 5.14. The range of values falls by a factor $\simeq 2$ with only a small systematic trend remaining.

These new O-Cs are in agreement with those of Z Cha (see Warner 1985), in contrast to $(O-C)_{KV}$. The apparent factor 3 difference remaining between OY Car and Z Cha is because figure 5.14 uses I band data. Figure 5.15 shows the B band data, where $T_{min} - T_{\phi=0.0}$ varies by $\leq 60 \times 10^{-5}$ day, but it is unclear whether there is a systematic trend. Hence there is no longer any evidence that the O-Cs of Z Cha and OY Car are systematically different.

KV used the change in position of T_{min} as evidence in favour of Vogt's elliptical disc model, but it is no longer clear that the position of T_{min} changes as suggested in their figure 12. However, no precise predictions have been made about the magnitude and form of the O-Cs in their model. The elliptical disc model is therefore still tenable, but the O-C variation is not such strong evidence as was previously thought.

By examining the flux at the bottom of superoutburst eclipses of Z Cha, Whitehurst *et al.* (1984) showed that because the superhump was not deeply eclipsed, the value of O-C should vary with a predicted semi-amplitude of approximately 0.009 of an orbital cycle ($= 60 \times 10^{-5}$ day) in the V band. However, the predicted O-Cs are for $T_{min} - T_{\phi=0.0}$, not $(O-C)_{KV}$, and relate to superhumps about 50% larger than those observed in Z Cha near the time of the eclipses (Whitehurst, private communication). Thus their predicted semi-amplitude of 0.009 of an orbital cycle should be reduced somewhat, and may be consistent with the observations.

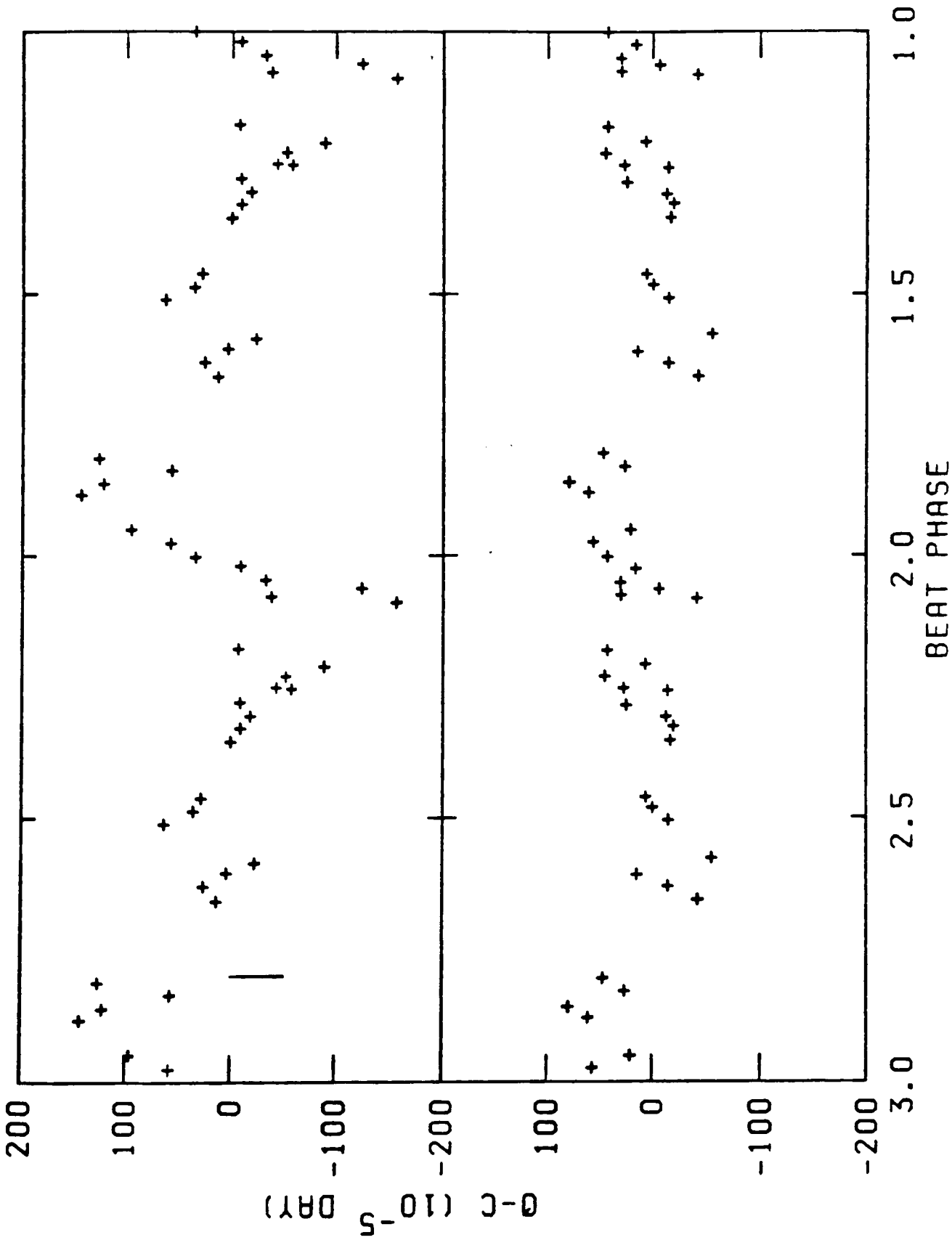

Figure 5.14 I band $(O-C)_{KV}$ from KV (upper panel) and $T_{min} - T_{\phi=0.0}$ calculated from the data presented in KV. The data is shown twice for clarity. The vertical bar represents half the filter cycle time. Note that although the x-axis is labelled with the beat phase defined in Appendix 2, the sense of the axis is reversed to give the appearance of KV's figures. This is because KV used a different definition of beat phase such that $\phi_b = 1 - \phi_{b(KV)}$.

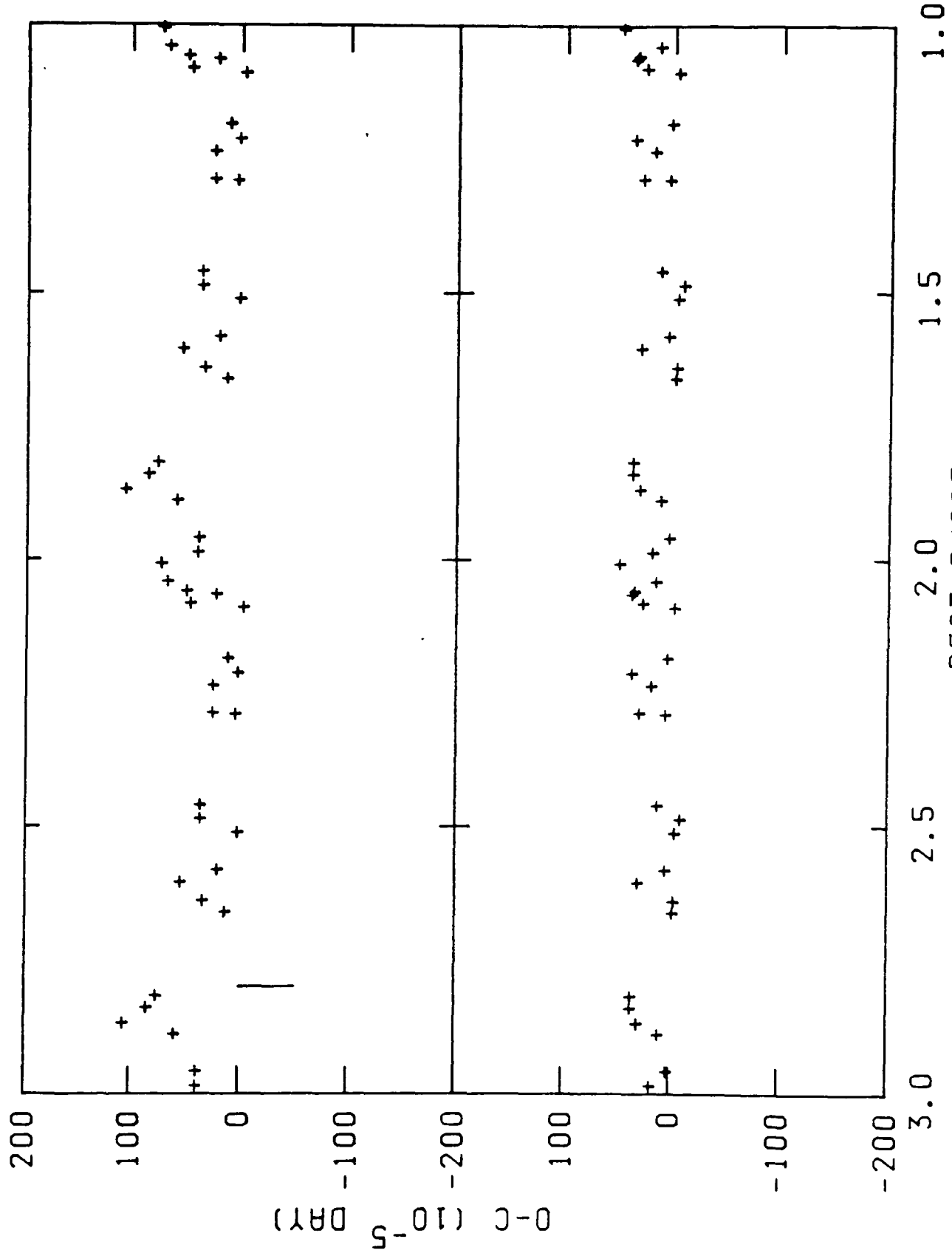

Figure 5.15 As figure 5.14, but for the B band.

ΔT itself must also be interpreted with some care. If the ratio of the gradients of the ingress and egress remain the same, but the eclipse becomes wider, then ΔT will increase. As we already know that the eclipse becomes wider at longer wavelengths, this might explain the increase in ΔT with wavelength seen by KV. A better asymmetry parameter may be to calculate ΔT in flux, rather than magnitudes, and divide by the width at half amplitude, again in flux.

5.6 The infrared structure during observation 3

In observation 6 the IR light curve follows the optical very closely, whereas in observation 3 from about phase 0.8 the superhump rises in the B band whilst the IR flux is generally declining. Either (a) the superhump colour temperature in observation 3 is much higher than in the later observations and thus there is little hump light in the IR, or (b) some other source of IR light is falling at the same time as the superhump, of colour similar to that in observations 4 and 6, is rising.

5.6.1 A hot superhump

If there is negligible hump flux in the J, say $<0.5\times10^{-15}$ ergs $cm^{-2}s^{-1}Å^{-1}$, and there is 2.6×10^{-14} ergs $cm^{-2}s^{-1}Å^{-1}$ in the B band, the resulting colour temperature is $>6\times10^{4}K$. Whilst such a colour temperature would explain the lack of IR light before the eclipse in observation 3, there would be no superhump light in the IR after the eclipse. Yet features A and B, and presumably all superhump structure, still appear in the IR. A modification is possible; that the superhump is initially at a high temperature and has cooled by the time structures A and B are reached. This appears contrived, as this time-dependence must have disappeared by

the time of observation 5 (only 10 cycles later) since the IR hump appears at the place expected by calculation from the optical data alone.

5.6.2 The eclipse of an IR region

Explanation (b) is only viable if the fall in IR flux coincides with the rise of the superhump. An eclipse of cool outer regions of the disc that contribute a lot of IR flux, but little in the optical, could have this effect. As the red star can only begin to eclipse the disc after phase 0.75, and would produce an eclipse centered on phase zero, the obvious candidate is an enlarged bright spot region. If present throughout the superoutburst, such a bright spot would always cause an early IR eclipse. But we only see the curious IR behaviour in the two eclipses of observation 3. Either the stream impact region is unusually large in observation 3, or there is an unusually large cool region of the disc that can be eclipsed. A large stream impact region may be expected if the mass transfer rate was abnormally high at this time, compared with any other observation.

In either Whitehurst's or Vogt's elliptical disc models (discussed in Chapter 4), at the beat phase of observation 3 (0.15), the disc's long axis is perpendicular to the observer and approaching on his left if the angular momentum vector of the secondary is upwards (see the right hand side of figure 9 of Vogt 1982). If the large side of the disc is cool, an eclipse of this region by the bright spot may produce the observed effect. Further, there would be no such effect expected at the other beat phases at which we observed. If this hypothesis is correct, however, the IR egress at beat phase 0.65 should show similar behaviour

to the ingress in observation 3. Conversely, if the high mass transfer hypothesis is correct, no such variations on beat phase would occur. Until this effect is observed again, and more extensively, no firm conclusions can be reached. More IR observations are needed to find out if, and how, the disc structure is changing.

5.7 The dips

In the January 1980 superoutburst, KV saw dips in their light curves, similar to those seen in observation 1, in every observation before the superhumps developed. The dips occur prior to the eclipse, and in the observations presented here their depths are greater at shorter wavelengths. The dips may be explicable by analogy with the dips seen in high inclination low mass X-ray binaries (LMXBs), or the eclipse of the accretion disc corona seen in LMXBs such as AC211 (see Chapters 1 and 3). Their phasing would suggest they correspond to the LMXB dips associated with the stream/disc impact region, that shadows the compact object. It might be that at this stage of the superoutburst there is mass transfer occurring at a high rate, which forms an isotropically radiating bulge, in contrast to the anisotropic quiescent bright spot. As this moves across the central disc it obscures the inner disc, producing the energy dependence observed in the Walraven data. Since the bright spot has an isotropic radiation pattern, and is cooler than the disc it is seen against, it produces less light than it obscures and its effect is that of a "dark spot" on the edge of the disc. This dark spot may also reprocess the X-rays into visible light, causing the X-ray oscillations (see Chapter 4, Section 8) to appear as visual oscillations near the position of the quiescent bright spot (Chapter 4, Section 2).

In observation 3 the superhump is extremely structured, pseudo-periodic on a scale of about 0.2 of a cycle and the structure may repeat from one cycle to another. In observation 6 the optical data show sharp dips just before the superhump maximum (marked C and D in figure 3.07), which are separated by exactly an orbital cycle. Schoembs (1986) has already attempted to distinguish between dips and structure, although his criteria for doing so are not enumerated, and he shows that the dips do coincide with superhump maximum. I therefore seek a common explanation for both effects.

Were the features in the light curve due to structure in the disc it should have a periodicity typical of a Keplerian orbit in the disc, instead of the binary period, and should be sheared out in approximately one Keplerian period. However, for reasons which are not clear, LMXB dips preserve their structure for ~10 orbital cycles, and have the binary periodicity. That the dips in the B band data of observation 6 are larger than those in the IR, as expected if the inner disc is being shadowed, also argues in favour of an LMXB dip analogy. I suggest that the reason the dips are associated with the superhump phase and not with orbital phase is that the entire outer edge of the disc is disrupted by the superhump, as might be expected a) in a mass transfer burst or b) in an elliptical disc model. What this idea fails to explain is why the structure is pseudo-periodic in observation 3.

5.8 Conclusions

From optical and IR light curves obtained during superoutburst three main conclusions have been drawn, First, there are three points which, taken together lead to the conclusion that there is vertical structure

in the disc, possibly in the form of a rim.

1) In observation 3 at beat phase zero, when we have simultaneous optical and IR photometry, the IR flux falls as the optical rises towards superhump maximum.

2) There are dips and other structure which seem to be associated with the superhump (observations 6 and 3 respectively, and Schoembs, 1986). There are also dips which occur prior to the eclipse before the superhumps have developed (observation 1 and KV), and can be attributed to a "dark spot".

3) Attempts have been made to fit the eclipses with a steady state geometrically thin disc where each element radiates as a blackbody. The model eclipses were either too deep or too wide. This may be because there is some superhump light present at all superhump phases, or because the inner regions of the disc are shadowed by an outer rim.

A study of the morphology of the eclipses has shown that the changes in the difference between the observed and expected time of eclipse (O-C) values for OY Car found by KV are dominated by an artifact in their method of measurement. When corrected for this, the amplitude of the O-C variations is actually found to lie in the range 80×10^{-5} day > O-C > -50×10^{-5} day, and shows no clear systematic behaviour. This is consistent with the values found for Z Cha.

By measuring the flux of the superhump in various optical and IR bands I find that the superhump light comes from an optically thick region at a temperature of approximately 8000K. This region has dimensions comparable with the projected area of the red star or accretion disc.

References

Allen, D.A., & Cragg, T.A., 1983. *Mon. Not. R. astr. Soc.* **203**, 777.

Bailey, J., 1981. *Mon. Not. R. astr. Soc.* **197**, 31.

Bateson, F.M. & Dodson, A.W., 1983. *Publs var. star Sect. R. astr. Soc. N.Z.* **11**, 1.

Bath, G.T., Edwards, A.C. & Mantle, V.J., 1983. *Mon. Not. R. astr. Soc.* **205**, 171.

Berriman, G., 1984. *Mon. Not. R. astr. Soc.* **210**, 223.

Berriman, G., Kenyon, S., & Bailey, J., 1986. *Mon. Not. R. astr. Soc.* **222**, 871.

de Ruiter, H.R. & Lub, J., 1986. *Astr. Astrophys. Suppl. Ser.* **63**, 59.

Horne, K., 1984. *Nature* **312**, 348.

Horne, K. & Cook M.C., 1985. *Mon. Not. R. astr. Soc.* **214**, 317.

Krzeminski, W. & Vogt, N., 1985. *Astr. Astrophys.* **144**, 124 (KV).

Osaki, Y., 1985. *Astr. Astrophys.* **144**, 369.

Papaloizou, J. & Pringle, J.E., 1979. *Mon. Not. R. astr. Soc.* **189**, 293.

Schoembs, R., 1986. *Astr. Astrophys.* **158**, 233.

Shakura, N. & Sunyeav, I.N., 1973. *Astr. Astrophys.* **24**, 337.

Smak, J., 1985. *Acta Astron.* **35**, 1.

Verbunt, F., Hassall, B.J.M., Pringle, J.E., Warner, B., & Marang, F., 1987. *Mon. Not. R. astr. Soc.* **225**, 113.

Vogt, N., 1982. *Astrophys. J.* **252**, 653.

Wade, R.A 1984. *Mon. Not. R. astr. Soc.* **208**, 381.

Wade, R.A. & Rucinski, S.M., 1985. *Astr. Astrophys. Suppl. Ser.* **60**, 471.

Warner, B., 1985. In: *Interacting Binaries* p.367 eds Eggleton, P.P. & Pringle, J.E. D. Reidel, Dordrect, Holland.

Whitehurst, R., Bath, G.T. & Charles, P.A., 1984. *Nature* **309**, 768.

Wood, J., 1986. *Ph.D. thesis,* Cambridge.

Chapter 6

Ultraviolet and X-ray Observations of the May 1985 Superoutburst of OY Carinae

6.1 Introduction

In the last chapter I discussed optical and IR photometry from the May 1985 superoutburst of OY Car; this chapter contains the results from the ultraviolet (*IUE*) and X-ray (*EXOSAT*) observations of the same superoutburst. Section 2 describes the *IUE* observations and Section 3 discusses the analysis of the continuum and line spectra. Section 4 contains details of the *EXOSAT* data and Section 5, its analysis. Section 6 is a more general discussion of the data, and Section 7 summarizes the conclusions.

6.2 IUE data

6.2.1 IUE observations

Figure 5.01 shows the timing of the *IUE* observations relative to the overall optical lightcurve. The first group of observations were made on May 2 (JD 2 446 188) covering 3 hours about 3 days after the peak of the outburst, when the FES magnitude was about 12.2. The second group, covering a total of 16 hours, was obtained roughly two days later on May 5 (JD 2 446 190) when the FES magnitude had declined to about 12.6. Optical observations (Chapter 3) show that the superhumps had already developed by the time of the first *IUE* observation. During both sets of observations, the superhump coincided roughly with the orbital eclipse. (See Table 6.1 for exact beat phases and Section 2 of Chapter 5 and

Table 6.1 Log of *IUE* observations

Date	Image No.	Mid Exposure (HJD-2440000)	Exposure (secs)	Orbital Phase	Beat Phase
May 2	SWP25836	6188.17693	420	0.521-0.598	0.07
	SWP25837	6188.20775	150	0.031-0.058	0.08
	SWP25838	6188.23864	720	0.470-0.602	0.08
	SWP25839(T)	6188.26870	600	0.955-0.065	0.09
	LWP5885	6188.21918	900	0.148-0.313	0.08
May 5	SWP25855	6190.51137	420	0.502-0.579	0.80
	SWP25856	6190.54006	180	0.982-0.015	0.81
	SWP25857	6190.57034	900	0.392-0.557	0.82
	SWP25858	6190.62470	900	0.252-0.417	0.83
	SWP25859	6190.66638	180	0.978-0.011	0.85
	SWP25860	6190.73474	300	0.053-0.108	0.87
	SWP25861	6190.76500	1200	0.450-0.670	0.88
	SWP25862	6190.79260	180	0.979-0.012	0.89
	SWP25863	6190.83238	900	0.547-0.712	0.90
	SWP25864	6190.85571	180	0.980-0.013	0.91
	SWP25865	6190.88435	1200	0.341-0.561	0.92
	SWP25866	6190.91883	180	0.980-0.013	0.93
	SWP25867	6190.96355	1200	0.596-0.816	0.94
	SWP25868	6191.03679	900	0.784-0.949	0.96
	SWP25869(T)	6191.10560	600	0.898-0.008	0.99
	LWP5906	6190.52164	900	0.622-0.787	0.80
	LWP5907	6190.60241	180	0.965-0.998	0.83
	LWP5908	6190.66007	300	0.868-0.923	0.85
	LWP5909	6190.72946	180	0.978-0.011	0.86
	LWP5910	6190.90425	1500	0.628-0.903	0.87
	LWP5911	6190.98192	180	0.981-0.014	0.92
	LWP5912	6191.01278	1200	0.376-0.596	0.95
	LWP5913	6191.07589	1500	0.347-0.622	0.96

Appendix 2 for a discussion of superhump development and adopted ephemeris.) The lack of good beat phase coverage make it impossible to distinguish between modulations on the orbital and superhump periods.

The *IUE* observations presented here are listed in the Journal of Observations in Table 6.1. The exposures were all made in low resolution mode (spectral resolution ≃5Å in SWP, and ≃6Å in LWP) in the large aperture using standard acquisition techniques. On May 2 one LWP and four SWP exposures were made to obtain limited orbital phase coverage. On May 5 a total of 15 SWP spectra were obtained, giving excellent phase coverage and a total of five 3-minute exposures well centred on the predicted times of mid-eclipse according to Wood's (1986) ephemeris. Of the eight LWP spectra taken on this day, three coincide with eclipses and the remaining five only give good phase coverage between orbital phases 0.5 to 0.95. Two spectra (SWP25839 and SWP25869; labelled T in Table 6.1) were produced by trailing the star slowly along the long axis of the large aperture, covering the 20 arcsec in 10 minutes.

6.2.2 IUE data reduction

The spectra were extracted at the ground stations using the standard IUESIPS reduction package for Low Resolution spectra (IUE Image Processing Information Manual, Volume 2.0 New Software). The absolute flux calibration of *IUE* (Bohlin & Holm 1980, for SWP and Cassatella & Harris 1983, for LWP) is accurate to approximately 10%, whilst the internal consistency between spectra is better than this. The absolute wavelength accuracy, after all known camera temperature and time corrections are applied for a star well centred in the aperture, is better than about 1Å. Displacement of the star from the aperture centre

causes a shift of the spectrum both parallel and perpendicular to the dispersion direction. The latter effect is automatically corrected in the IUESIPS extraction process and gave rise to shifts of up to 1 pixel i.e. 1.5Å in our data. Shifts along the dispersion direction can not be corrected but should be no greater than the perpendicular shift, amounting to a total uncertainty of about 2Å. Since all our spectra were obtained within a short space of time, with similar camera temperatures and acquisition procedures the wavelength calibration repeatability is probably better than the 2Å quoted above.

The geocoronal light in the Lyman α emission line is negligible in our data, particularly in the 3 minute exposures during eclipse. This is evident from examination of the expected location of the extended large aperture image in Lyman α in the photowrite. A geocoronal flux of the observed intensity would only be expected after an exposure of several hours under normal circumstances.

The spectra are shown in figures 6.01 to 6.03; instrumental reseaux are marked by an R while prominent line features are identified on the diagram. Spikes near 1260Å and 1370Å due to hot pixels have been omitted from SWP25855 and SWP25861 respectively. A spike in the background near 1640Å in SWP25855 was correctly treated by the extraction software and causes no distortion of the HeII profile. The large gap in the data near 1600Å in SWP25858 is due to omission of those data affected by a particle hit whose "cometary" path crosses the spectrum in this region. The background is slightly overestimated in the neighbouring 50Å and the details of the red wing of the CIV line should be treated with some caution.

In figure 6.01, representative SWP spectra from May 5 are arranged in

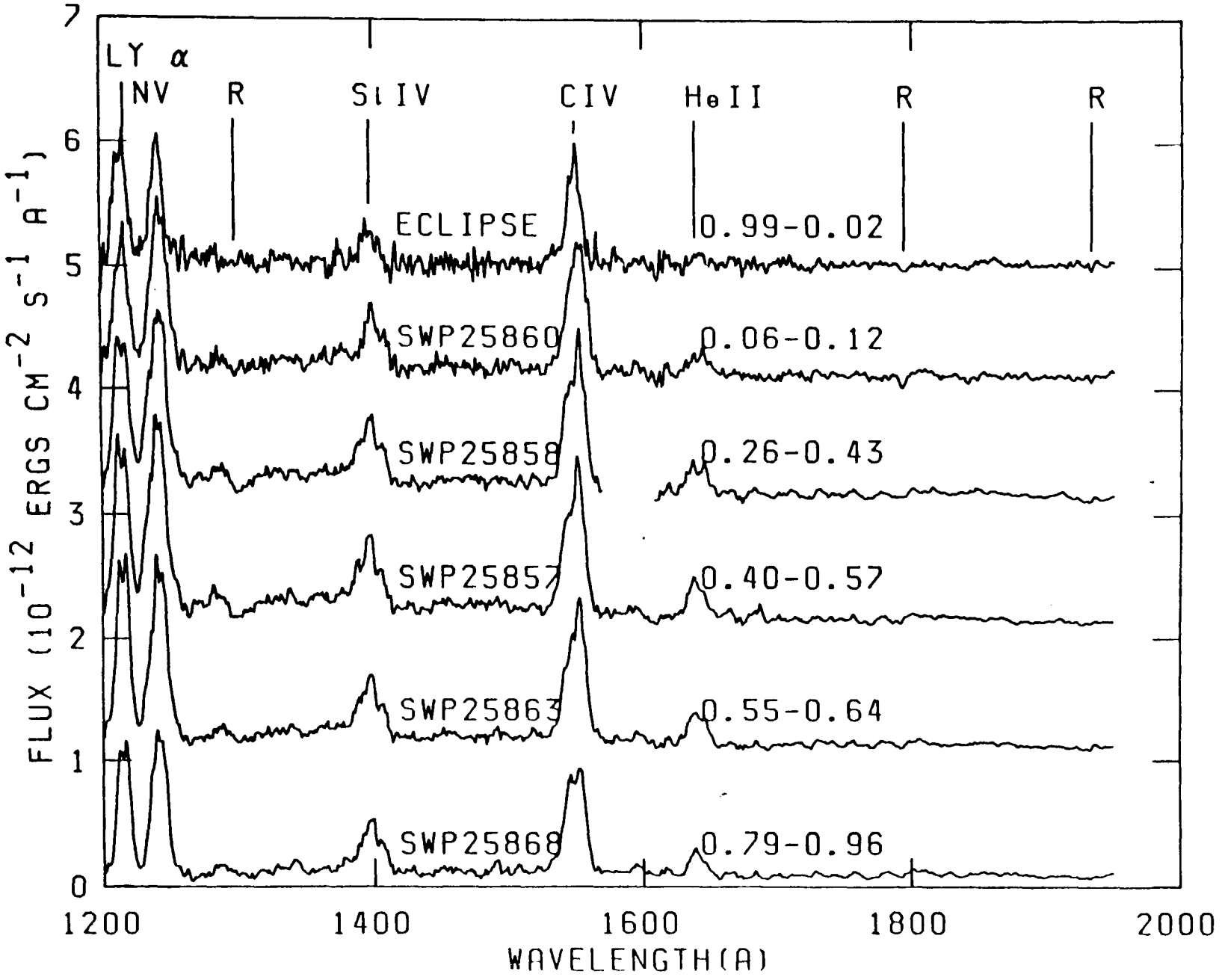

Figure 6.01 Representative SWP spectra for May 5. The spectra are arranged downwards in order of increasing orbital phase as shown by the annotated ranges of phases covered. Each spectrum is offset by 10^{-12} ergs $cm^{-2}s^{-1}Å^{-1}$ and the zero point for each is indicated by tick marks of the y-axis. Prominent emission features and instrumental reseaux (R) are marked on the uppermost spectrum. The eclipse spectrum is the mean of the five eclipse spectra taken on this day.

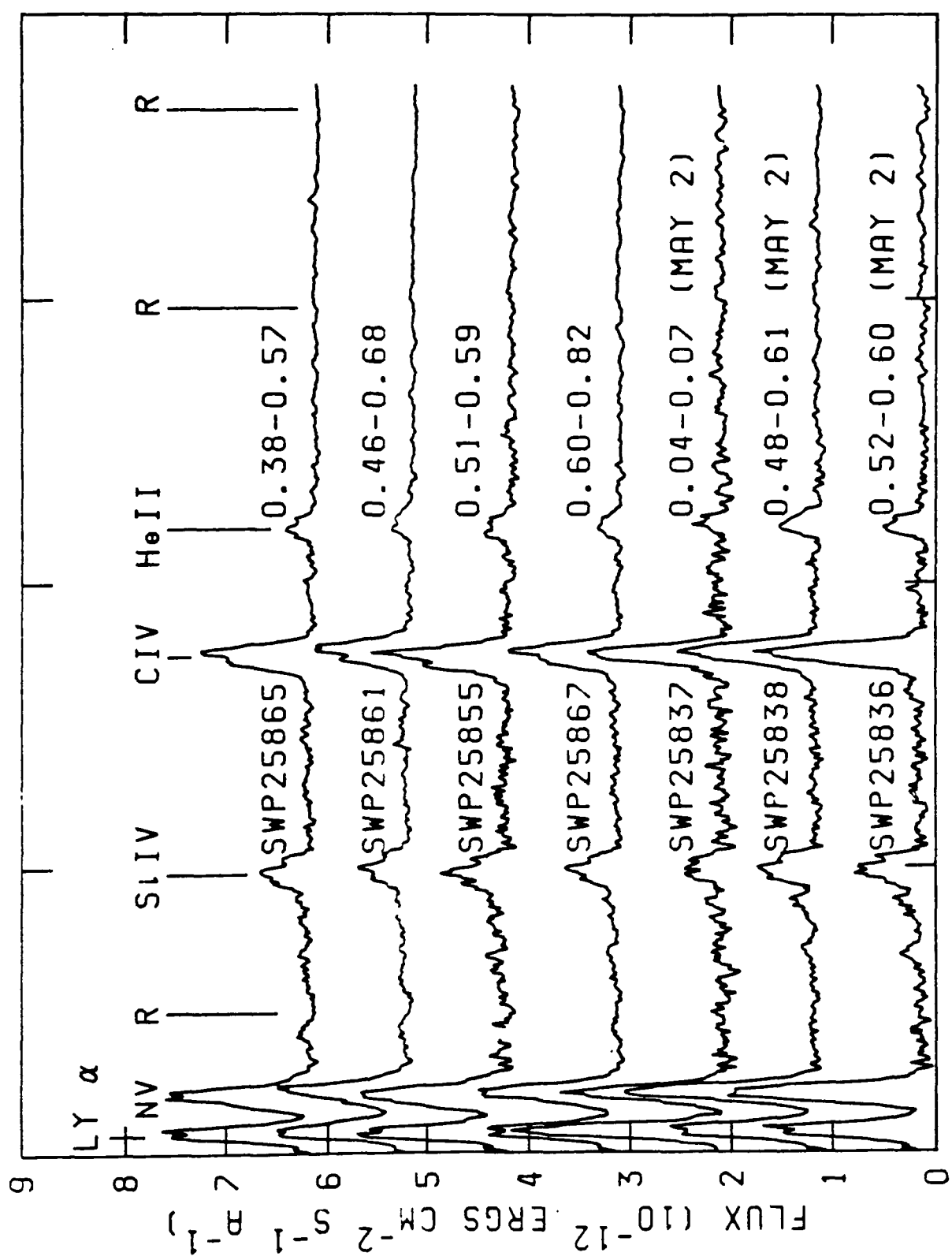

Figure 6.02 The SWP spectra from May 2 and the remaining SWP spectra from May 5, each set arranged in order of increasing orbital phase. Offsets are as for figure 6.01

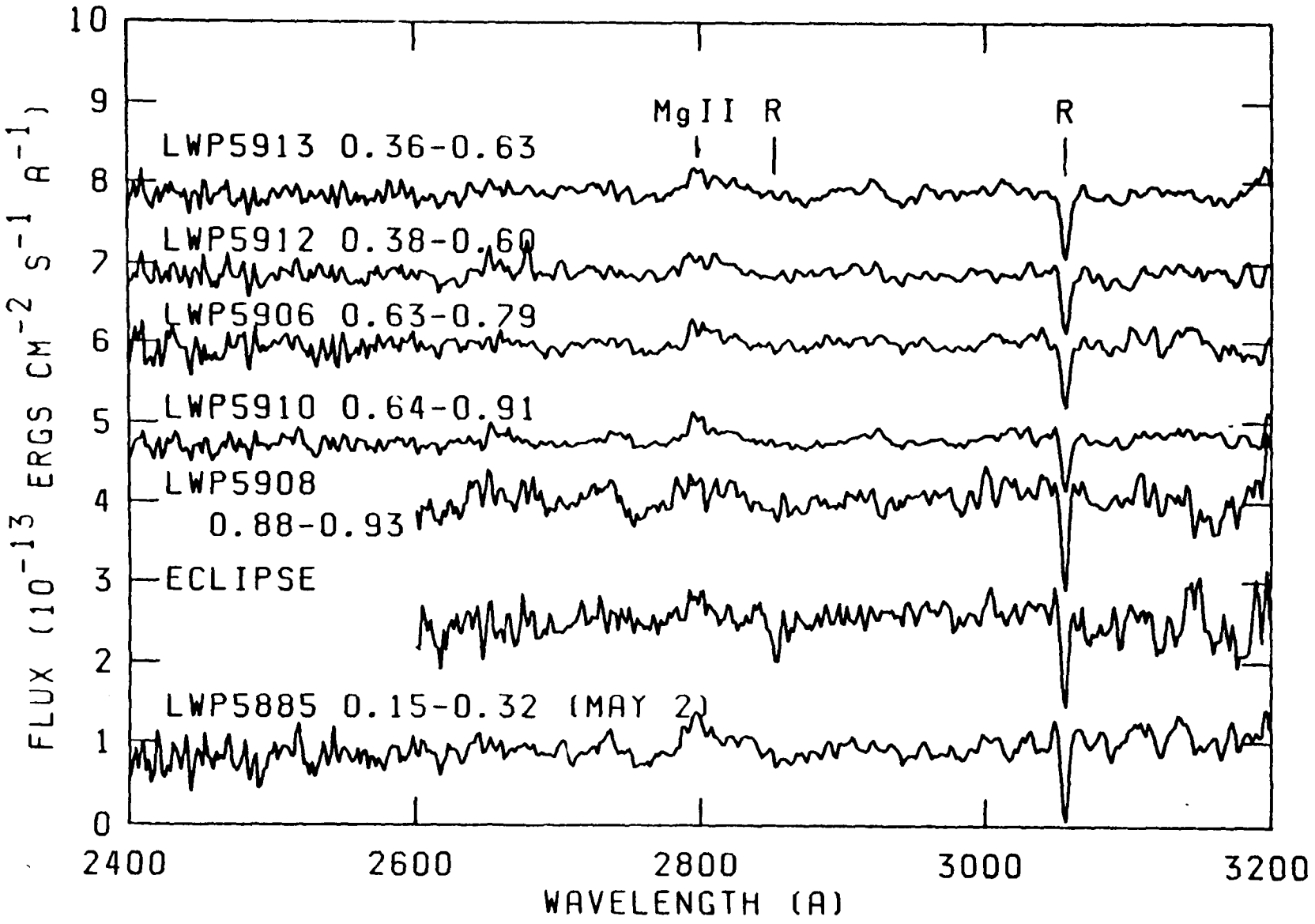

Figure 6.03 The LWP spectra. Those for May 5 are ordered by increasing orbital phase as annotated. The offset in the y-axis is $1x10^{-13}$ergs $cm^{-2}s^{-1}Å^{-1}$ between spectra, except the eclipse spectrum which is offset by $2x10^{-13}$ergs $cm^{-2}s^{-1}Å^{-1}$ from LWP5885. The eclipse spectrum is the mean of 3 spectra on May 5 as described in the text. LWP 5885 is for May 2. All spectra have been truncated at 2200Å and excessively noisy data shortward of 2400Å have been omitted from the plot. R marks reseaux positions.

order of orbital phase. The eclipse spectrum is the mean of the five images SWP 25856, 25859, 25862, 25864 and 25866. The remaining SWP spectra from this date and those from two days earlier are shown in figure 6.02. All the spectra have strong emission lines of Lyman α (1215Å), CIV(1550Å), NV(1240Å), SiIV(1400Å) and weaker HeII (1640Å). There is evidence for variability in several lines and double structure in the CIV and Lyman α lines (see 6.3.2 to 6.3.5). Absorption is seen at 1300Å (Si III) and weakly at 1260Å (SiII) and 1280Å (possibly CI) in some non-eclipse exposures. Particularly evident on the spectra from May 2 are CII emission at 1335Å and an emission feature at about 1370Å (possibly SiIII) on the blue wing of the SiIV 1400Å line. On both days non-eclipse spectra have a strong blue continuum, while during eclipse the continuum is much weaker.

Figure 6.03 displays LWP spectra as a function of orbital phase for May 2 and May 5. The eclipse spectrum is the mean of the three spectra (LWP 5907, 5909 and 5911) centred on phase zero. No strong line features are seen in the LWP range, although all spectra show evidence for MgII emission at 2800Å. Because of the low sensitivity in the short wavelength end of the camera, excessively noisy data shortward of about 2400Å have been omitted from some spectra. The low signal prohibits an analysis of the 2200Å feature to estimate E(B-V). I have therefore adopted E(B-V)=0.0, noting that the known redennings to dwarf novae at ~100pc suggest that E(B-V) for OY Car is likely to be less than 0.1. The flux in the 2700-2900Å region of the weak eclipse exposure LWP 5909 may be adversely affected by a particle hit nearby in the background.

6.2.3 Line fitting technique

The line fitting described in this section was carried out using the Marquardt algorithm (Bevington 1969) for non-linear least-squares fitting. The continuum for up to 50Å on either side of the line was fitted with a linear ($F(\lambda)=a_o+a_1\lambda$) function, where a_o and a_1 are free parameters. Each independent Gaussian component contributes a further 3 free parameters (position, width and height), giving a total of 5 for a single Gaussian fit and 8 for 2 independent Gaussians. Lines treated as intrinsic doublets, such as CIV 1550Å, were fitted by 2 Gaussian profiles with identical FWHM, with the theoretical values of the separation and flux ratios (2:1 for the blue:red). Thus an intrinsic doublet contributes only 3 free parameters to the fit. For clarity, we shall describe such an intrinsic doublet as a "component". So in the case of intrinsic doublets a "two component fit" would still only imply 2 free parameters for the continuum plus 6 for the lines, despite the inclusion of 4 Gaussians in the numerical fit.

Except for NV and Lyman α, all the line fluxes quoted were found by fitting a linear function to the continuum on either side of the line, and then calculating the flux in the line above this continuum. The errors for the fluxes during eclipse were derived by taking the standard deviation of the values from each of the eclipse spectra. The method of calculating the errors associated with each data point is described in Appendix 3. These errors were used in the line fitting, and to calculate the uncertainties given for the fluxes in figures 6.04 to 6.06 and 6.09 to 6.11.

6.3 IUE data analysis

6.3.1 The continuum

The continuum flux for May 5 in the region 1345-1360Å is plotted as a function of orbital phase and of time in figures 6.04a and 6.04b. The eclipse depth is 90±7 per cent of the mean out-of-eclipse flux. Aside from the eclipse, figure 6.04a shows modulation over a large range of orbital phase. However, figure 6.04b suggests the existence of a secular decline in flux by a factor of 2 during the 16 hours of observation, corresponding to ~1mag/day. During the early part of the observation the out-of-eclipse exposures are concentrated around orbital phase 0.5, and subsequently the emphasis shifted to later phases in order to improve phase coverage. With this sampling it is impossible to differentiate between a real orbital modulation and a decline in flux. However, the visual lightcurve (figure 5.01) and the nearly constant FES magnitude (figure 6.05b) which changes less than 0.2 magnitudes, favour orbital modulation.

The flux in the band 2590-2650Å is plotted as a function of orbital phase in figure 6.05a. The eclipse depth is 54±6 per cent of the mean out-of-eclipse flux. There is insufficient phase coverage to discern the overall orbital modulation, although the data does not show any decline before the eclipse, analogous to that in the SWP data. In fact, the high point at phase 0.9 is suggestive of the superhump, and mimics the modulation in the FES.

6.3.2 CIV (1548.2Å and 1550.8Å)

In figure 6.06a I have plotted the total CIV flux against orbital phase.

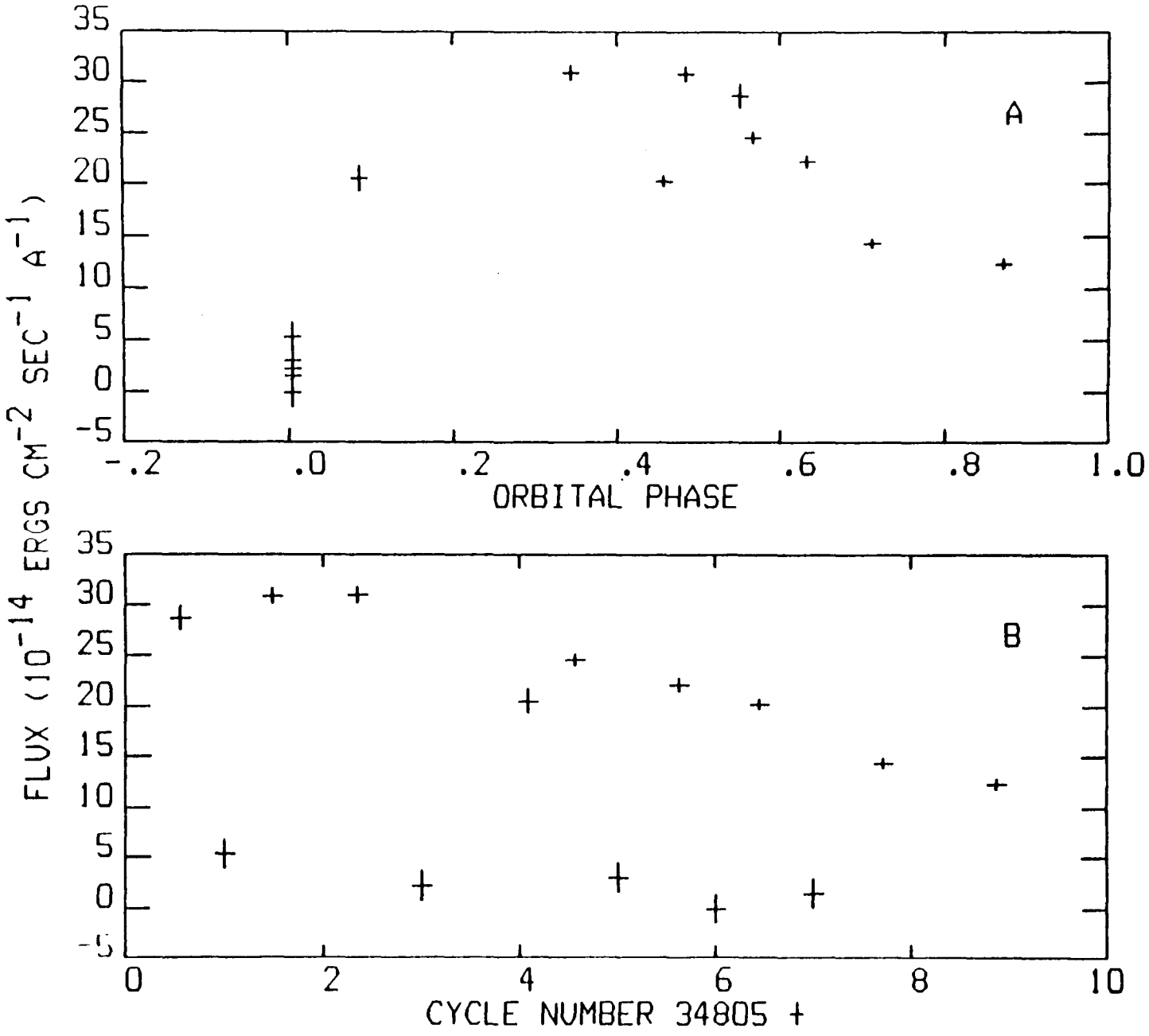

Figure 6.04 Modulation of the continuum flux in the band 1345-1360Å. A) The data folded on orbital phase. B) The data in chronological order. The vertical extent of each cross is the error for that point.

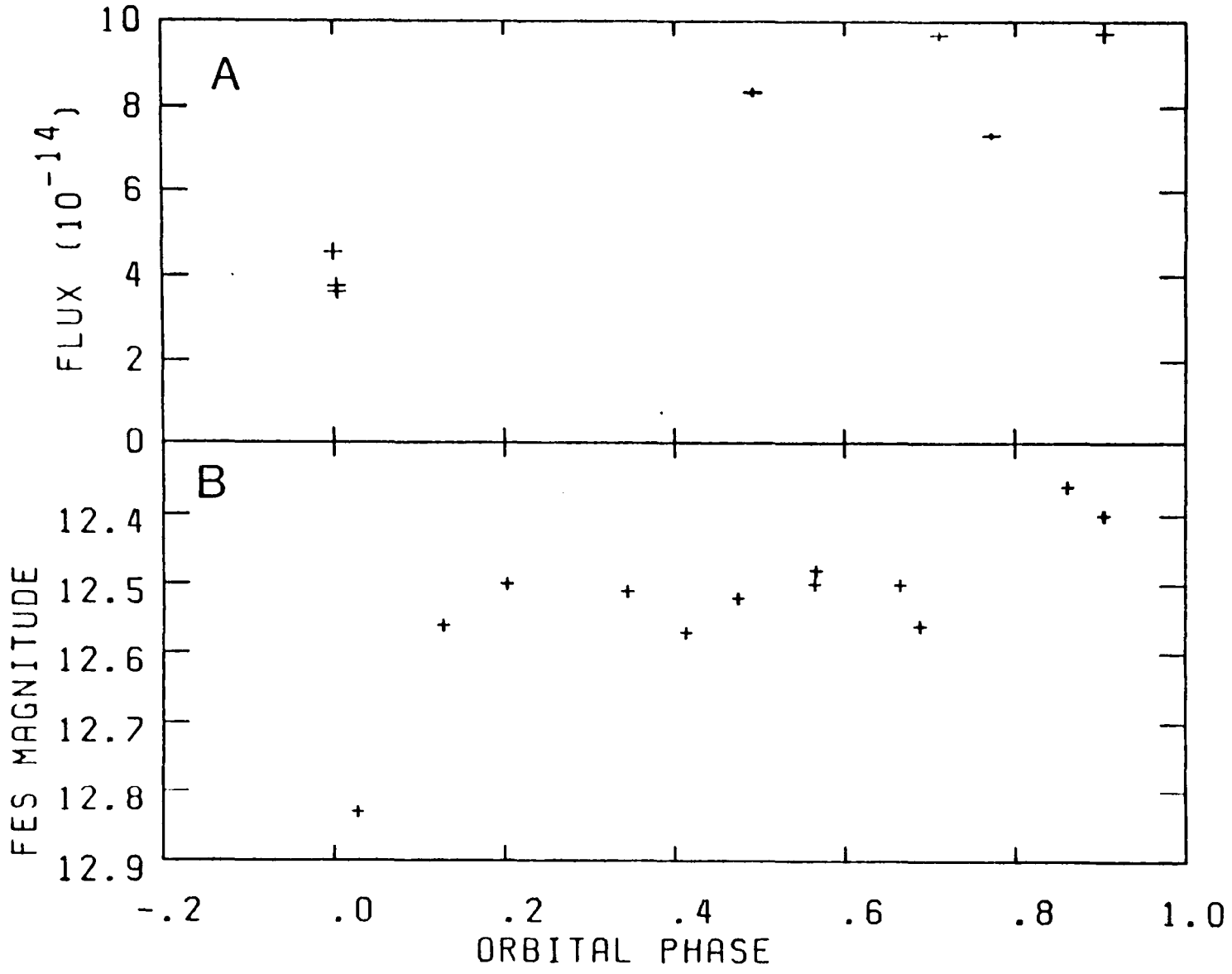

Figure 6.05 A) The continuum flux at 2670Å (bandwidth 40Å) as a function of phase. The vertical extent of each cross in the upper panel is the error for that point, and the flux is in units of ergs $cm^{-2}s^{-1}Å^{-1}$. B) The FES magnitude folded on orbital phase.

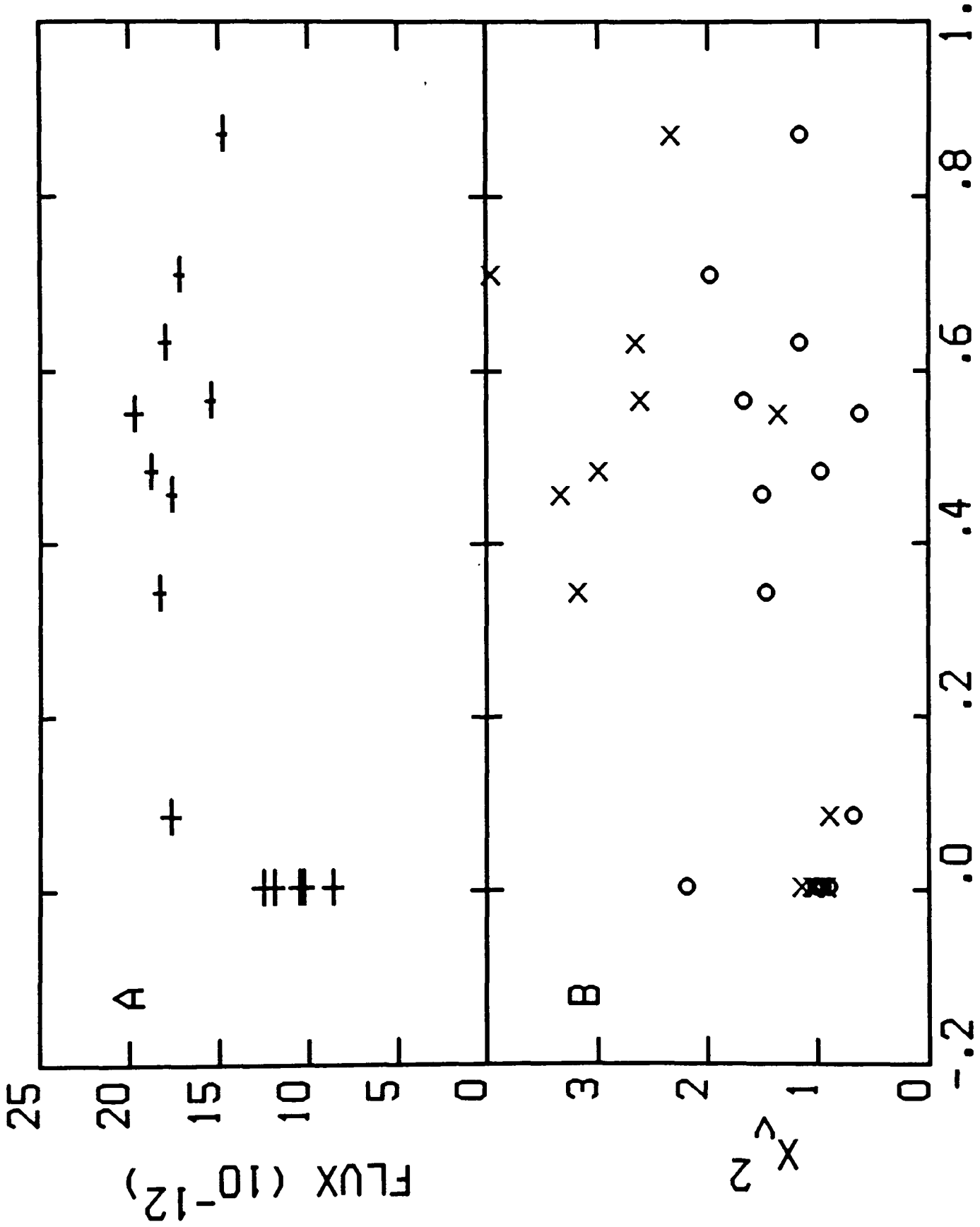

Figure 6.06 A) Flux in the CIV 1550Å line in units of ergs $cm^{-2}s^{-1}Å^{-1}$, plotted as a function of phase. The vertical extent of each cross is the error for that point. B) The reduced χ^2 of the one (crosses) and two (circles) component models, as functions of phase.

The eclipse depth is 38±8 per cent of the out-of-eclipse mean. Figures 6.01 and 6.02 show that the CIV 1550Å line is asymmetric away from eclipse, in the sense that the red wing falls more rapidly than the blue. This is shown more clearly in the sample line fit in figure 6.07. During eclipse, the asymmetry is not apparent and the line narrows significantly (see figure 6.08). Also during eclipse a "pedestal" on the blue wing of the line is seen, which may be either velocity structure in the CIV emission, or a weak blended line. There is some evidence for this feature away from eclipse, but the stronger continuum makes it difficult to distinguish.

In order to test the significance of the line's asymmetry the data were fitted with one and two component models, where "component" refers to velocity structure as described in 6.2.3. All the spectra with orbital phases greater than 0.2 show a decrease in χ^2 between the one and two component fits, which is significant according to an F-test (see figure 6.06b), and thus for these spectra the asymmetry is real. The eclipse spectra, and that at orbital phase 0.1 show no significant change in χ^2 between the two cases. However, it was found that if the errors associated with an out-of-eclipse spectrum were set equal to those for a 3 minute exposure, an acceptable χ^2 resulted from a single component fit. Thus the eclipse data are not of sufficiently high signal-to-noise to discover whether the asymmetry is absent, or masked by the higher noise. Aside from the eclipse effects, none of the fitted parameters varied systematically with phase.

Figure 6.07 shows a sample fit of the two Gaussians to the CIV line profile. In this example, as in nearly every other spectrum the data lie below the fitted curve near 1549Å, implying that the fit cannot

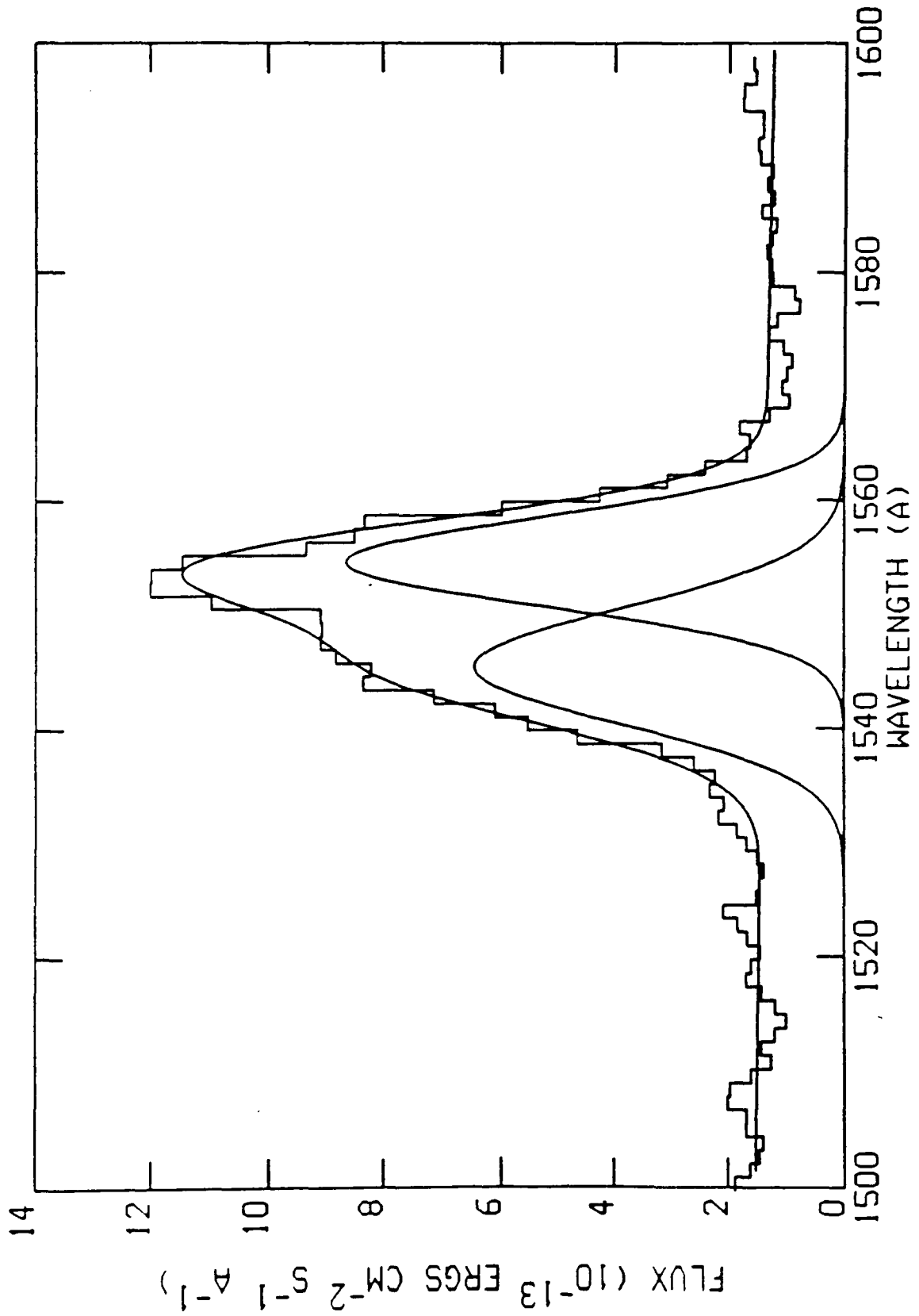

Figure 6.07 Sample fit to CIV line. Each component consists of the intrinsic CIV doublet.

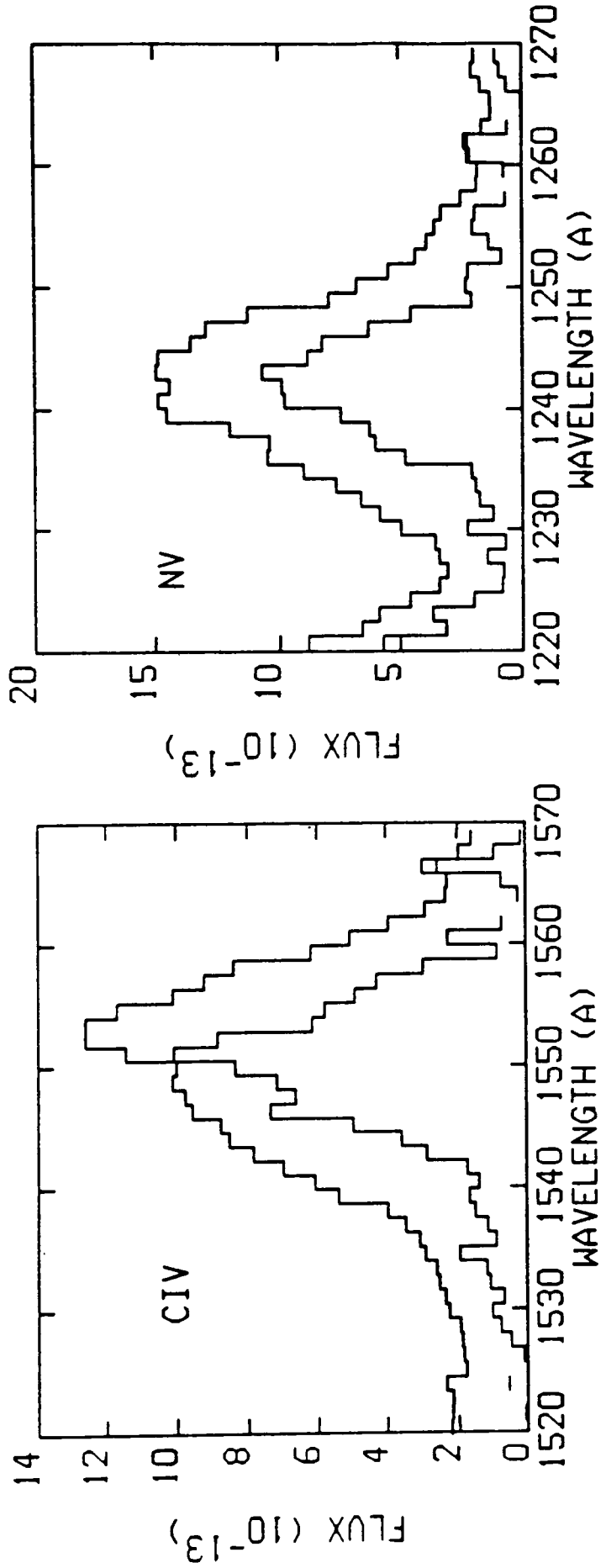

Figure 6.08 The mean of the out-of-eclipse spectra (lower curves) from May 5. The regions around CIV 1550Å (left) and NV 1240Å (right) lines are shown. The fluxes are in units of ergs $cm^{-2}s^{-1}Å^{-1}$.

reproduce the sharp change in gradient just shortward of the line peak. Thus, although the Gaussians are a useful device for demonstrating the asymmetry, they are not an adequate model of the line profile. It might be fitted better by a broad (≃20Å) flat-topped (i.e. non-Gaussian) component at its rest velocity, and a narrow (≃5Å), red shifted (by ≃6Å) component producing the peak. This would reproduce both the line asymmetry and the sharp change in gradient that the Gaussians could not achieve.

6.3.3 HeII (1640.4Å)

The HeII line is deeply eclipsed (see figures 6.01 and 6.02) and in figure 6.09a I show the flux derived by numerical integration as a function of orbital phase. The flux shows some evidence for a decline after phase 0.6. The upper limit to the flux during eclipse is 1.1×10^{-12}ergs $cm^{-2}s^{-1}Å^{-1}$ (90% confidence), i.e. at least 67% of the mean out-of-eclipse flux is eclipsed. The profile is not detectably asymmetric since the difference in χ^2 between the one and two component fits did not justify the inclusion of a second component.

6.3.4 Lyman α and NV (1240.1Å)

Because of blending of their wings, these lines were fitted simultaneously, treating NV as a doublet, Lyman α as a singlet. A continuum of the form $F(\lambda)=a_o$ was used due to the proximity of Lyman α to the short wavelength limit of the flux calibration, and the lack of well-defined continuum longward of NV, where there is a profusion of weak absorption lines. Both Lyman α and NV were fitted with one velocity component, despite the apparent double-peaked nature of Lyman

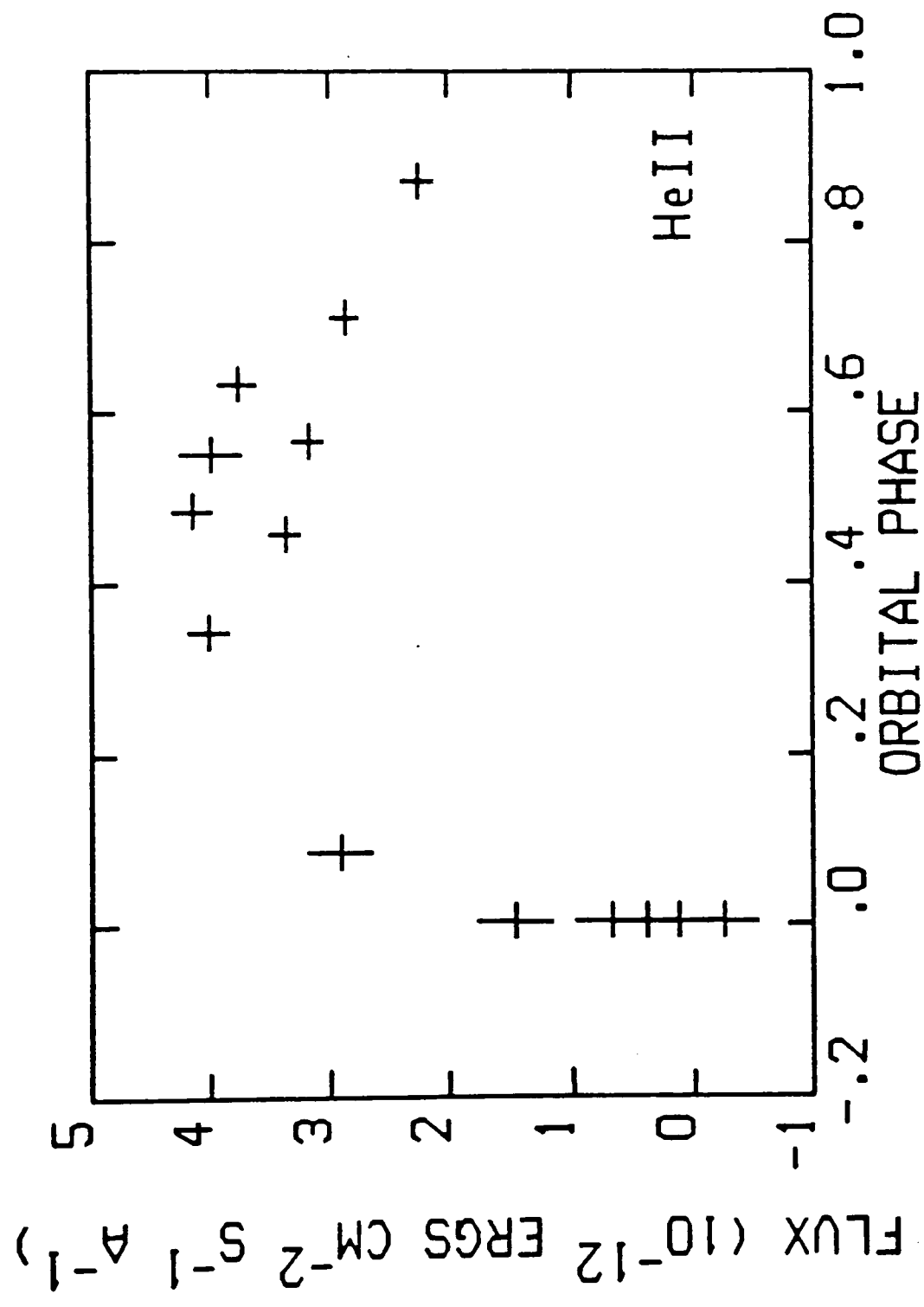

Figure 6.09 The total flux for HeII 1640Å as a function of phase. The vertical extent of each cross is the error for that point.

α. Because of the uncertainties in intrinsic Lyman α flux due to geocoronal contamination, and the difficulties in continuum choice, a more detailed fit would not be justified.

Figure 6.10 shows the line fluxes derived from the Gaussian fits. Lyman α is clearly modulated, but with no sharp eclipse. The NV flux shows no sign of orbital modulation before about phase 0.9, the eclipse depth is 50±4 percent of the mean out-of-eclipse flux. Figure 6.08 shows that the line narrows during eclipse.

6.3.5 SiIV (1393.7Å and 1402.7Å)

The observed line profile is complex, sometimes with three clear peaks. It may be compatible with a 2 component fit, as for CIV, but appears more complicated because of the large separation of the peaks in the intrinsic doublet. Most spectra also show weak line features in the region redward of the SiIV line, which was duly excluded from the continuum fits and line flux estimates. The resulting phase folded flux (figure 6.11) shows an eclipse of 45±6 percent, but no other orbital modulation.

6.4 EXOSAT data

OY Car was observed with the low-energy (LE) telescope (de Korte *et al.* 1981) and the medium-energy (ME) experiment (Turner *et al.* 1981) on board the EXOSAT X-ray observatory (Taylor *et al.* 1981) on three occasions well into the superoutburst as shown in figure 5.01. The journal of observations is given in Table 6.2

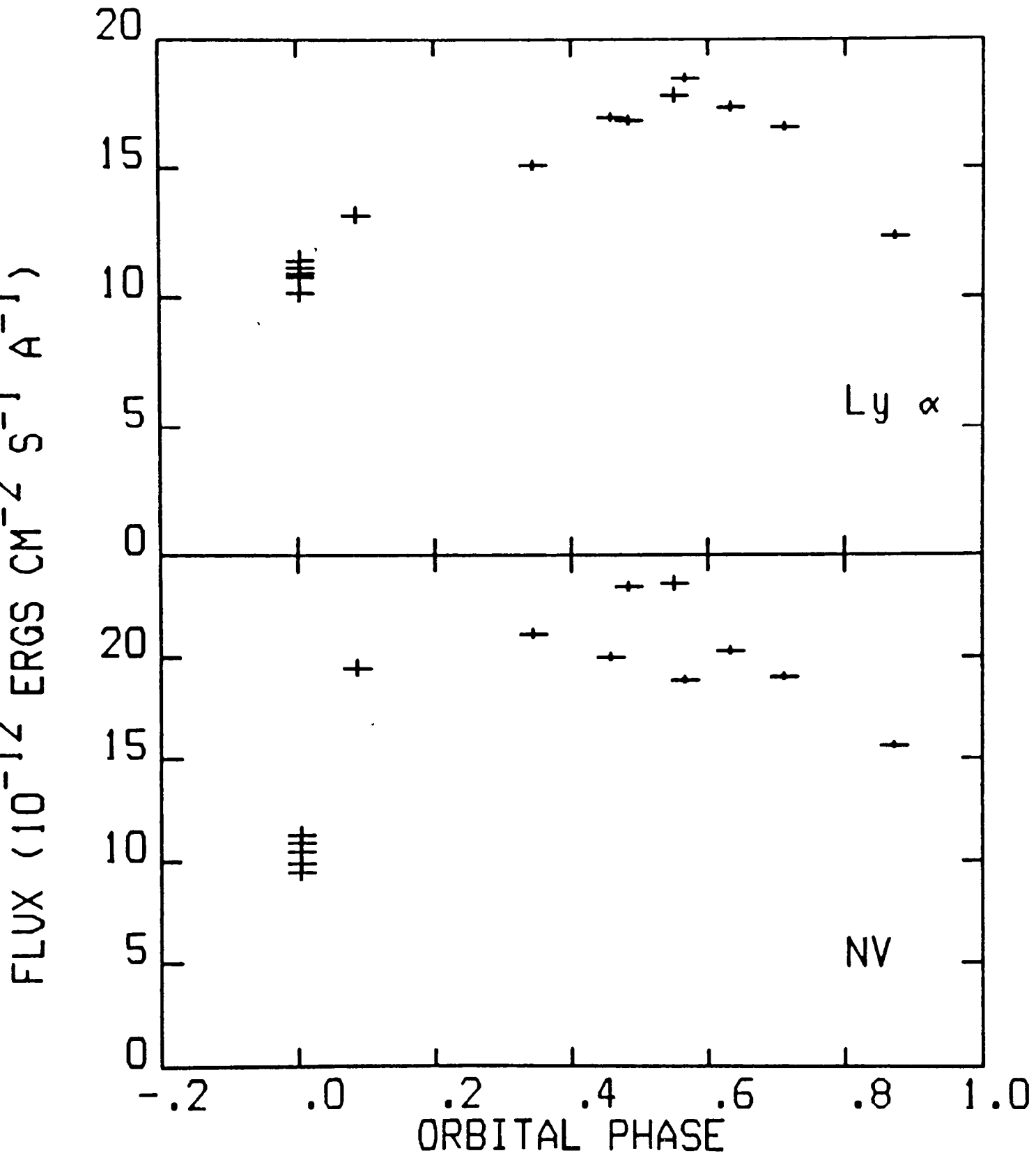

Figure 6.10 The total flux for Lyman α (upper) and NV (lower), as functions of phase. The vertical extent of each cross is the error for that point.

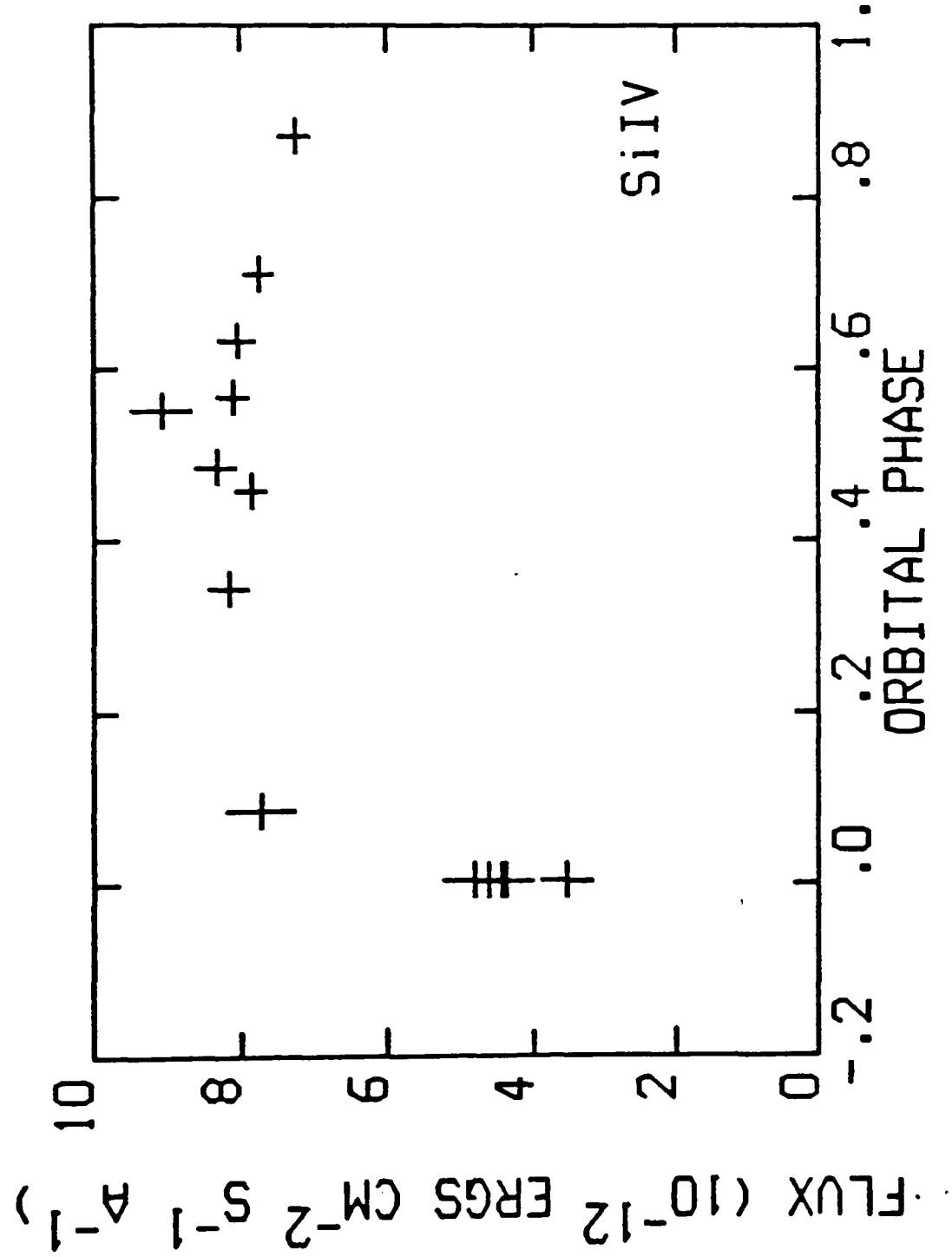

Figure 6.11 The flux for SiIV (1393.7Å; 1402.7Å) as a function of phase. The vertical extent of each cross is the error for that point.

Table 6.2a Log of *EXOSAT* LE observations

Date	Obs	Filter	Mid Exposure (HJD-2440000)	Exposure(s)	Counts/sec	Softness ratio
May 3	1	Al-P	6188.803	1272	0.059 0.007	0.35 0.05
		3000-lexan	6188.866	9280	0.171 0.005	
May 5	2	Al-P	6190.796	3792	0.023 0.003	0.43 0.06
		3000-lexan	6190.707[1] 6190.854	11072 5920	0.053 0.003	
May 10/11	3	Al-P	6196.440	7752	0.003 0.001	0.38 0.16
		3000-lexan	6196.523	6152	0.008 0.002	

The numbers below the count rates and softness ratios are the 1σ errors.

[1]There were two 3000-lexan observations on this day. The count rate is the mean of the two observations.

Table 6.2b Log of *EXOSAT* ME observations

Date	Obs	Mid Exposure (HJD-2440000)	Exposure (s)	Counts/sec
May 3	1	6188.842	12368	0.06 0.07
May 5	2	6190.759	22552	0.15 0.05
May 10/11	3	6196.484	16008	0.13 0.08

The numbers below the count rates are the 1σ errors.

6.4.1 The LE data

The CMA detector was used in combination with the 3000-lexan (7-250Å) or aluminium-parylene (Al-Pa) (7-300Å) filters (de Korte *et al.* 1981). The ratio of the two filters (Al-Pa/3000-Lexan), called the softness ratio, gives an indication of the spectral shape. The count rates quoted are from the ESOC auto-analysis system, and the light curve presented below was extracted with the Starlink data reduction system ASTERIX.

A decay of the soft X-ray flux by a factor of 3 (see Table 6.2a) is observed during the maximum of the optical outburst but the softness ratio (0.39±0.07) does not vary significantly between the observations. The 3000-Lexan light curve from observation 1 (figure 6.12) covers almost two orbital cycles including the predicted times of two optical eclipses. Solar activity disturbed the observation during the last hour. The light curve shows neither obvious X-ray eclipse, nor orbital modulation, although the source shows variability on the timescale of ~1 hour.

6.4.2 The ME data

Simultaneous observations with the argon proportional counter of the ME experiment (Turner *et al.* 1981) gave information in the energy range 1-20keV. During the observation, half of the experiment was pointed at the source, while the other half monitored the variability of the background at an offset of 2 degrees. Halfway through the observation the detector halves were interchanged to correct for instrumental effects caused by the different sensitivity of the two halves. The accurate background correction is taken from these in preference to the slew data obtained just before and after the pointing to the source.

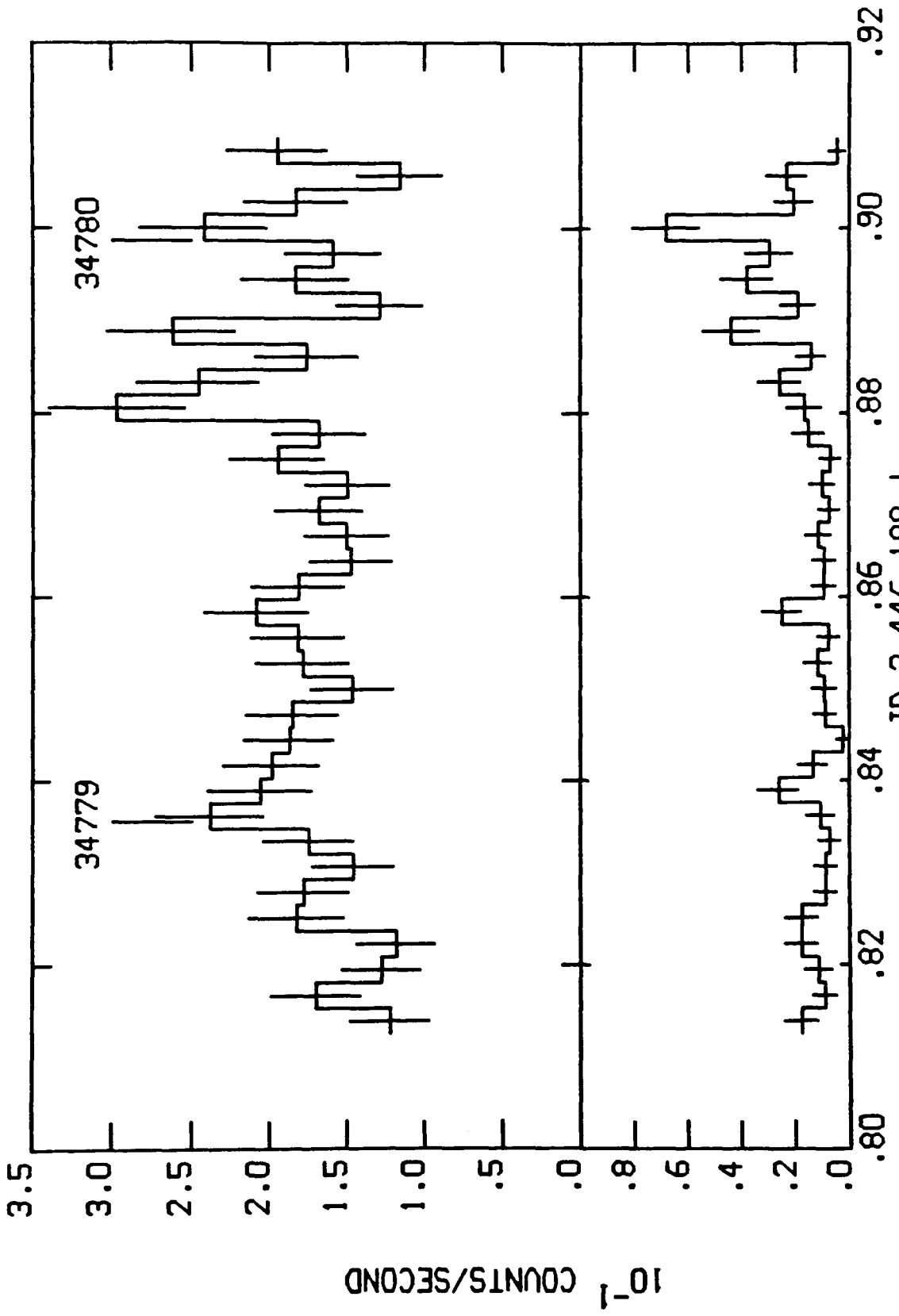

Figure 6.12 The background subtracted *EXOSAT* LE light curve (upper panel), using the 3000-lexan filter, from May 2. Each bin is 240 seconds. The lower panel shows the background.

The count rates quoted in Table 6.2b are for the range 2-6keV and were extracted using the ESOC interactive analysis system. Only on May 5 was there a 3-sigma ME detection.

6.5 EXOSAT analysis

6.5.1 Eclipse analysis

Cook (1985) showed, from optical photometry of OY Car during quiescence, that the eclipse of the white dwarf and boundary layer lasts 274 seconds. If the X-rays originate from the boundary layer, a total eclipse is expected to occur at orbital phase zero (the times marked in figure 6.12). Since no eclipse is apparent in the X-ray data, I assessed the maximum depth of eclipse that could evade detection during this observation. The observation 1 3000-lexan data were binned into 274 second bins, one of which was centered on eclipse 34779 of the Wood (1986) ephemeris. They were also binned such that one bin was centered on eclipse 34780. The overlap in phase resulted in ten duplicated phase bins roughly centred on the eclipse. These pairs of phase bins were added, and the resulting 9 non eclipse phase bins were used to find the mean and standard deviation (see Table 6.3). The standard deviation of the individual bins is an estimate of the errors for each bin, and automatically includes source and background counting statistics as well as intrinsic source fluctuations. Using this as an error estimate eclipses deeper than 24% can be ruled out at the 90% confidence level.

Applying the same method to the 3 eclipses in the 3000-lexan data of observation 2 yielded a maximum allowed eclipse depth of 33%. Finally, the low count rate in the observation 2 Al-P data, means that the

Table 6.3 Allowed eclipse depths in *EXOSAT* LE bands

Obs	Filter	Out-of-eclipse counts Mean	Standard deviation	Eclipse counts	Maximum allowed eclipse depth
1	3000-lex	0.186	0.0272	0.170	24%
2	3000-lex	0.0558	0.0110	0.0421	33%
2	Al-P	0.0261	0.0126	0.00782	80%

All count rates are in cts s^{-1}.
The allowed eclipse depths are 90% confidence limits.

Table 6.4 Summary of observed modulations in OY Car

Line or Band	Orbital Modulation	Light Eclipsed
2590-2650Å	?	54(±6)%
1345-1360Å	yes	90(±7)%
3000-lexan	no	< 24%
Al-P	no	< 80%
CIV	?	38(±8)%
Lyman α	yes	no
NV	?	50(±4)%
HeII	?	> 67%
SiIV	no	45(±6)%

allowed eclipse depth for this data is 80%.

6.5.2 Rapid oscillations

Fourier analysis to search for oscillations similar to those seen in VW Hyi (van der Woerd *et al.* 1986) was carried out on each of the LE data sets. No significant coherent modulation of the soft X-ray flux was found in the period range 1 to 1000 seconds. However, since the lowest limit we can place on any oscillations (<30%, obtained by adding artificial periodicities) is comparable to the largest modulation found in VW Hyi, the prescence of coherent oscillations in OY Car cannot be ruled out.

6.6 Discussion

6.6.1 The UV emission lines

Partially eclipsed asymmetric emission lines in high inclination cataclysmic variables have been interpreted by previous authors as indicating an outflowing wind region (see Holm, Panek & Schiffer (1982) for UX UMa, and Cordova & Mason (1985) for RW Tri and possibly DQ Her).

Calculations of line profiles through eclipse by Drew (1987) show that in the case of a normal, outwardly accelerating wind, the line blue shifts during eclipse. In contrast, in OY Car, both wings of the line are eclipsed, as might be expected during the eclipse of the inner regions of an accretion disc. However, the lack of total eclipse of the CIV, NV and SiIV lines (Table 6.4), indicates that they do not originate entirely within the inner disc; although the lower limit for the eclipsed flux of the HeII line (67%) is consistent with an inner disc

origin for this line. This is supported by the out-of-eclipse width of HeII (HWZI=12Å), which corresponds to a Keplerian orbit of about 2.5 white dwarf radii for a white dwarf of mass $0.685M_{\odot}$ (the mass is that given by Wood 1986).

The widths of the CIV and NV lines show that their broadening is also consistent with inner disc velocities. As they become narrower during eclipse, I suggest that the eclipsed portion of the flux is from the inner disc, and the remainder of their flux originates in a wind region described in Cordova & Mason (1985).

Amongst the UV lines Lyman α is unique in that, despite the absence of a deep eclipse, it shows the most distinct orbital modulation. Since the wind, the outer and inner regions of the disc, and possibly even the secondary (by X-ray heating) are all expected to emit Lyman α, the precise cause of the modulation and shallow eclipse is unclear.

The presence of the lines NV, SiIV, CIV and HeII purely in emission, rather than in absorption or with classical P Cygni profiles, contrasts strongly with observations of other dwarf novae in outburst, and seems to be the result of viewing the wind at high inclination in OY Car. In a system with an accretion disc, the strengths of emission and absorption components are sensitive to the relative extent of the wind and the accretion disc, and the orbital inclination (Drew 1987). An extensive wind viewed at high inclination will tend to lead to a strong emission component, whereas if there were a large disc at low inclination the wind would obscure the emission from the disc while enhancing the absorption. In high inclination cases, the lack of absorption may be exacerbated by a bipolar density distribution within the wind.

The presence of intrinsic disc emission lines poses a problem because the outburst disc itself is expected to be optically thick. Thus there must be a "transition" emission region above the disc, whose physical depth (in order to be eclipsed) must be smaller than, or of the order of, the disc height.

6.6.2 The UV continuum

The observed UV flux distribution of OY Car in superoutburst is unusually cool compared with the lower inclination dwarf novae in outburst. Moreover, in none of those systems have large changes in the flux distribution been observed on orbital timescales, except in the early stages of outburst.

This smooth modulation of the UV continuum is not identifiable with the optical superhump since it peaks near orbital phase 0.4 rather than with the predicted phase of optical superhump near phase zero (see Chapter 5), and so is probably orbital in origin. It coincides with the phase at which the inward face of the secondary is in the line of sight, suggesting that the extra UV flux source may be due to X-ray heating of the secondary by the white dwarf. A major objection to this lies with the improbably high X-ray flux required. To produce a UV modulation of $2x10^{-13}$ergs $cm^{-2}s^{-1}Å^{-1}$ over a 500 Å range from a source 100pc distant $2x10^{32}$ergs s^{-1} is required at the source. This is already a factor of 10^4 greater than the observed X-ray flux, assuming the black body model discussed in 6.6.3, although the flux is strongly dependent on the spectrum assumed. However, after also allowing for the fact that only ~0.25% of the X-ray flux will be intercepted by the secondary for a mass ratio of 10, and that the conversion into UV photons will not be 100%

efficient, this model can probably be ruled out for all likely spectral shapes.

Alternatively we may regard the UV modulation not as an enhancement at phase 0.4, but rather as a deficit at phase ~0.8 due to obscuration by a large cool object in the stream impact area. This could be the "dark spot" proposed in Chapter 5. Further evidence for extended vertical structure in the accretion disc, in addition to that described in Chapter 5 (Section 4), is given by the relatively cool flux distribution of OY Car. In high inclination systems such as OY Car, a large opening angle of the disc would lead to partial obscuration of the central regions of the disc, resulting in an apparently cooler flux distribution. Since the detailed structure in the outer disc is unlikely to be stable over many orbital periods, it is not surprising that minor differences in UV flux are seen on timescales of hours or days at similar orbital phase.

The strong eclipses of the continuum which, are deeper at shorter wavelengths are as expected from a centrally condensed UV emitting accretion disc, with an inwardly increasing temperature distribution.

6.6.3 The X-ray data

Two pieces of evidence indicate that the X-ray flux, like some of the UV line flux, comes from an extended region. Firstly, the absence of an X-ray eclipse suggests that instead of coming from the white dwarf or boundary layer directly, the X-ray flux must originate throughout a volume with linear dimension commensurate with the accretion disc or binary separation, namely 10^{10} cm or more.

Secondly, an optically thick X-ray plasma can be ruled out using the count rates and softness ratio. Assuming a black body emitter, a softness ratio of 0.4 and N_H of 10^{18} atoms cm^{-2}, a temperature of $1.7x10^6$K (kT=0.15 keV) is obtained. This implies an X-ray source radius at 100pc of only $5x10^4$cm. This radius is small compared with that of a white dwarf (~$5x10^8$cm) or even the expected size of the boundary layer (~1% of the white dwarf area, Pringle 1977). Moreover, the white dwarf and boundary layer are precluded as the origin of the observed X-rays by the lack of eclipse.

The conclusion that the X-ray source observed in OY Car is a large optically thin corona is consistent with the shadowing of the inner disc and boundary layer that has been deduced from the UV observations, together with the optical and IR data in Chapter 5. The existence of an optically thin X-ray component has previously been postulated by van der Woerd & Heise (1987). They suggested that the observed X-ray spectrum of VW Hyi in superoutburst might consist of an optically thin component in addition to an optically thick component from the boundary layer. Thus the difference in X-ray flux and softness ratio between OY Car and VW Hyi becomes explicable simply in terms of an inclination effect, explicitly whether or not the boundary layer is hidden from view by the accretion disc.

The UV emitting wind has a temperature of ~20 000K, which is probably too low to generate significant X-ray flux. However, like the X-ray emitting region, it has a volume comparable to the Roche lobe. Since the temperatures are incompatible, we must conclude that physically distinct regions are involved. This can only be achieved if the X-ray region is distributed through the UV wind, as might arise in radiatively

driven shocks. Such models have been proposed for application to early-type stars (e.g. Lucy 1982), but the proposed instability may also occur in dwarf nova winds (Raymond & Mauche 1985).

6.7 Conclusions

The UV and X-ray observations of OY Car during superoutburst have four remarkable properties when compared with other dwarf novae in outburst.

1) The UV spectra show emission lines which become narrower in eclipse.

2) The UV flux distribution is relatively cool and is modulated on the orbital timescale.

3) The X-ray flux is hard compared with VW Hyi in outburst, but comparable to VW Hyi's softness ratio in quiescence.

4) No clear eclipse is seen in the X-ray data.

All these effects are consistent with our expectations of the behaviour of the standard model of a dwarf nova viewed at high inclination; provided that the disc has extensive vertical structure, and that the whole system is embedded in an extensive X-ray corona and UV emitting wind. I suggest that the latter is largely responsible for the differences between the UV spectrum of OY Car and other lower-inclination systems. Whereas emission lines from both the disc transition region and the wind itself dominate in OY Car, wind absorption becomes important in lower inclination systems.

References

Andrews, D. 1985. *Exosat Express* **12**, 67.

Bevington, P.R., 1969. *Data Reduction and Error Analysis for the Physical Sciences* McGraw-Hill, New York.

Bohlin, R.C. & Holm, A.V., 1980. *NASA IUE Newsletter* **10**, 37.

Cassatella, A. & Harris, A. W., 1983. *NASA IUE Newsletter* **23**, 21.

Chiappetti, L. 1984. *Exosat Express* **8**, 27.

Cook, M.C. 1985. *Mon. Not. R. astr. Soc.* **215**, 211.

Cordova, F.A., & Mason, K.O., 1985. *Astrophys. J.* **290**, 671.

de Korte, P.A.J., Bleeker, J.A.M., den Boggende, A.J.F., Branduardi-Roymont, G., Brinkman, A.C., Culhane, J.L., Gronenschild, E.H.B.M, Mason, I., McKechnie, S.P., 1981. *Space Sci. Rev.* **30**, 495.

Drew, J. 1987. *Mon. Not. R. astr. Soc.* **224**, 595.

Hassall, B.J.M., Pringle, J.E., Schwarzenberg-Czerny, A., Wade, R.A., Whelan, J.A.J. and Hill, P.W.,1983. *Mon. Not. R. astr. Soc.* **203**, 865.

Hassall, B.J.M. 1985. *Mon. Not. R. astr. Soc.*, **216**, 335.

Holm, A.V., Panek, R.J., & Schiffer, F.H., 1982. *Astrophys. J.* **252**, L35.

Leahy, D.A., Darbro, W., Elsner, R.F., Weisskopf, M.C., Sutherland, P.G., Kahn, S., & Grindlay, J.E., 1983. *Astrophys. J.* **266**, 160.

Lucy, L.B., 1982. *Astrophys. J.* **255**, 286.

Pringle, J.P., 1977. *Mon. Not. R. astr. Soc.* **178**, 195.

Raymond, J.C., & Mauche, C.W., 1985. In: *Proc. 9th North American Cataclysmic Variable Workshop*, p. 128, ed. Szkody, P., University of Washington.

Taylor, B.G., Andresen, R.D., Peacock, A., Zobl, R., 1981. *Space Sci. Rev.* **30**, 479.

Turner, M.J.L., Smith, A., & Zimmermann, H.U., 1981. *Space Sci. Rev.* **30**, 513.

van der Woerd, H. & Heise, J., 1987. Mon. Not. R. astr. Soc. **225**, 141.

van der Woerd, H., Heise, J., & Bateson, F., 1986. Astron. Astrophys.

156, 252.

van der Woerd, H., Heise, J., Paerels, F., Beuermann, K., van der Klis, M., Motch, C., & van Paradijs, J., 1987. *Astron. Astrophys.* in press.

Wood, J., 1986. *Ph.D. Thesis,* University of Cambridge.

Chapter 7

IUE Observations of Outbursts of WZ Sagittae and EX Hydrae

In this chapter I will present IUE data from the outbursts of two more dwarf novae. The first, WZ Sge, shows obvious UV dips. In the second case, that of EX Hya, the data are less conclusive.

7.1 The 1978 superoutburst of WZ Sge

7.1.1 Observations and data reduction

As was stated in Chapter 4, WZ Sge appears to be an SU UMa star with a long (33 year) recurrence time between superoutbursts, and with no normal outbursts. The overall light curve of its most recent outburst, in December 1978, is shown in figure 7.01, and is described in Mattei (1980). Patterson *et al.* (1980) show that superhump behaviour began on December 13 (JD 2 443 856).

The outburst was extensively studied using *IUE* in both the low resolution (Fabian *et al.* 1980 and Holm *et al.* 1980) and high resolution (Friedjung 1981) modes. Fabian *et al.* (1980) presented the continuum variations as a function of phase, using the data collected at ESA's Villafranca ground station. Since then the NASA data has become available through the *IUE* archive, and Table 7.1 is a log of all the available low resolution SWP observations using the large aperture, aside from those very early in the outburst.

The data were originally extracted by IUESIPS#1 using an incorrect Intensity Transfer Function (ITF). The precise nature of the problem is

Table 7.1 SWP Large Aperture Spectra of WZ Sge From December 1978.

Image Number	Mid Exposure (UT date, hrs:mins)	Exposure (secs)	Orbital Phase
swp3591	14 10:59	240	0.69
swp3592	14 12:33	240	0.84
swp3593	14 14:06	210	0.98
swp3598	15 02:48	90	0.31
swp3599	15 03:12	140	0.61
swp3600	15 03:39	140	0.94
swp3601	15 04:26	140	0.51
swp3602	15 04:54	140	0.85
swp3603	15 05:24	140	0.22
swp3604	15 06:02	280	0.69
swp3672	22 22:26	149	0.22
swp3673	22 22:53	200	0.55
swp3674	22 23:20	200	0.88
swp3675	22 23:48	200	0.22
swp3676	23 00:14	200	0.54
swp3688	24 12:02	240	0.85
swp3689	24 12:55	240	0.50
swp3690	24 13:46	240	0.13
swp3691	24 14:36	240	0.74
swp3701	25 08:04	160	0.58
swp3702	25 09:17	140	0.47
swp3703	25 09:47	200	0.84
swp3678	01 07:12	200	0.42

Table 7.2 EX Hya Spectra From July 1986.

Image Number	Mid Exposure (UT date, hrs:mins)	Exposure (secs)	Orbital Phase	67-Minute Phase
lwp8761	29 4:24	360	0.88	0.30
swp28772	29 4:54	540	0.18	0.75
swp28773	29 5:44	180	0.69	0.50

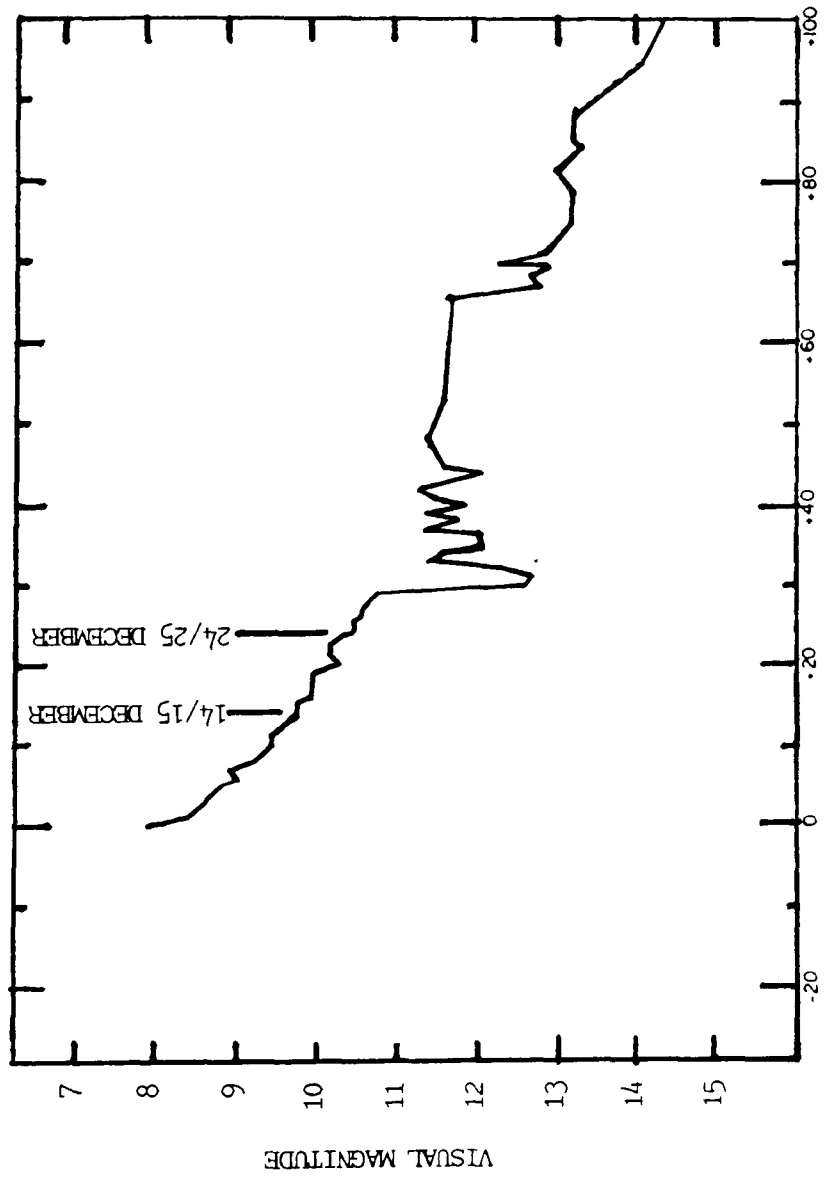

Figure 7.01 The daily averages of the American Association of Variable Star Observers' visual observations of the 1978 outburst of WZ Sge (taken from Mattei 1980). The time axis is in days since peak (December 1), and the dates of the IUE observations used for figures 7.02 and 7.03 are marked.

described in Turnrose & Harvel (1982). I corrected the data using the 3-Agency 4th-file method (Cassatella *et al.* 1980). This method involves correcting the line-by-line image for the ITF error, and re-extracting gross and background spectra. The background was smoothed using one pass of an 82Å (31 pixels of 2.66Å) wide median filter and 2 passes of a 40Å (15 pixel) wide average filter. This procedure is identical to that carried out by IUESIPS#2. After background subtraction the spectra were flux calibrated using the instrumental response from Bolin & Holm (1980). Fabian *et al.* (1980) gave the limit for the reddening as E(B-V) < 0.04, and so no correction has been applied to the spectra.

Figure 7.02 shows the variation of the UV flux in the band 1440-1490Å as a function of orbital phase, on December 14/15 and December 24/25. This band was chosen to avoid strong line features in the spectra. Although some spectra using the small aperture are available in the archive they were not used since its throughput depends on how well centered in the aperture the object is, and on the telescope focus (and thus temperature). The ephemeris used is that of the eclipse-like feature in the quiescent optical light-curve, which is thought to be the eclipse of the bright spot, and is defined as phase zero (see Robinson, Nather & Patterson 1978). The December 14/15 data show a dip near phase 0.7, which is defined by two data points (in the figure 7.02 the two symbols lie in almost exactly the same position). Since these are the first and last spectra taken in the series (see Table 7.1) this cannot be a secular effect.

7.1.2 Interpretation of the dips

The behaviour of the December 14/15 data is strongly reminiscent of the

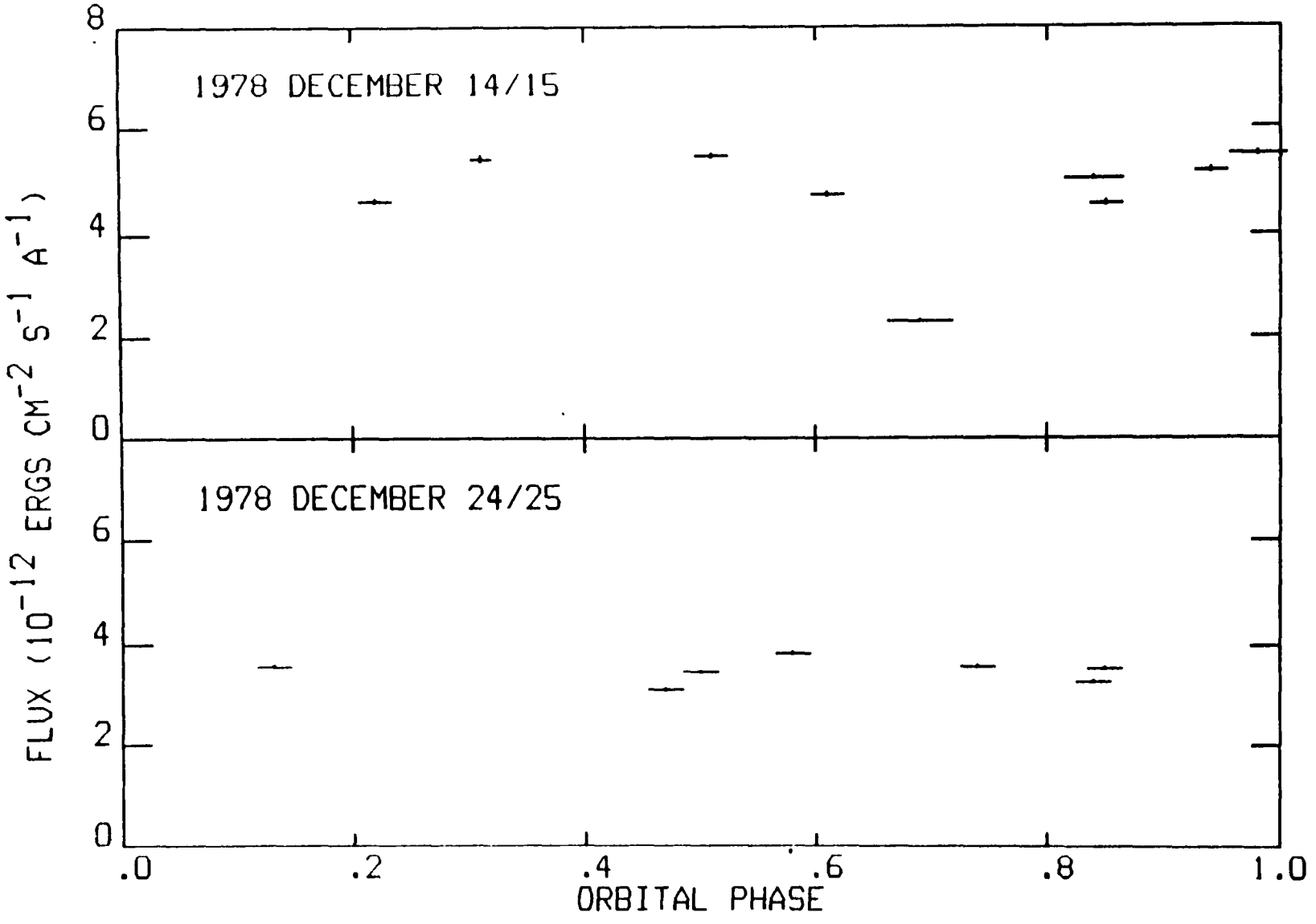

Figure 7.02 Flux in the range 1440-1490Å as a function of phase for WZ Sge, on 1978 December 14/15 and 24/25. The vertical extent of each point is its statistical error, the horizontal extent the length of the integration. On the December 14/15 panel there are two points near phase 0.7, but their values of phase and flux coincide so closely that their symbols have merged.

dips in the pre-superhump optical light curves during the May 1985 superoutburst of OY Car (see Chapter 5, and especially figure 5.02). Like those dips, this effect may be caused by the stream impact region obscuring the inner regions of the disc. If this is the case, then, as discussed in Chapter 5, the blue light should be affected more severely than the red. Figure 7.03 shows the mean of the two spectra near orbital phase 0.7, and the mean of all the remaining data from December 14/15. It is obvious that any colour effect is small. In fact the ratio of the two spectra varies from 2.3 at 1680Å to approximately 2.8 at 1350Å. However, this result should be treated with some caution since the forest of absorption and emission features at short wavelengths make it uncertain whether a particular continuum region is uncontaminated or not.

The CIV flux remains constant between the two spectra in figure 7.03 to within 2%. The changes in Lyman α and NV are more difficult to assess because there is no continuum free of line features near them, and Lyman α suffers from geocoronal contamination in any case. The SiIV line changes from emission during the dip, to absorption during the rest of the orbital cycle.

The behaviour of SiIV can be explained as follows. Part of the wind in WZ Sge will normally be seen projected against the hot inner regions of the disc, and thus will produce an absorption profile, as occurs in the face-on systems. However, the moderately high inclination of WZ Sge means that a significant portion of the wind will be observed with no back illumination, and so be observed in emission, as in OY Car. When the dark spot occults the central regions of the disc from view, the temperature of the region against which some of the wind is seen will

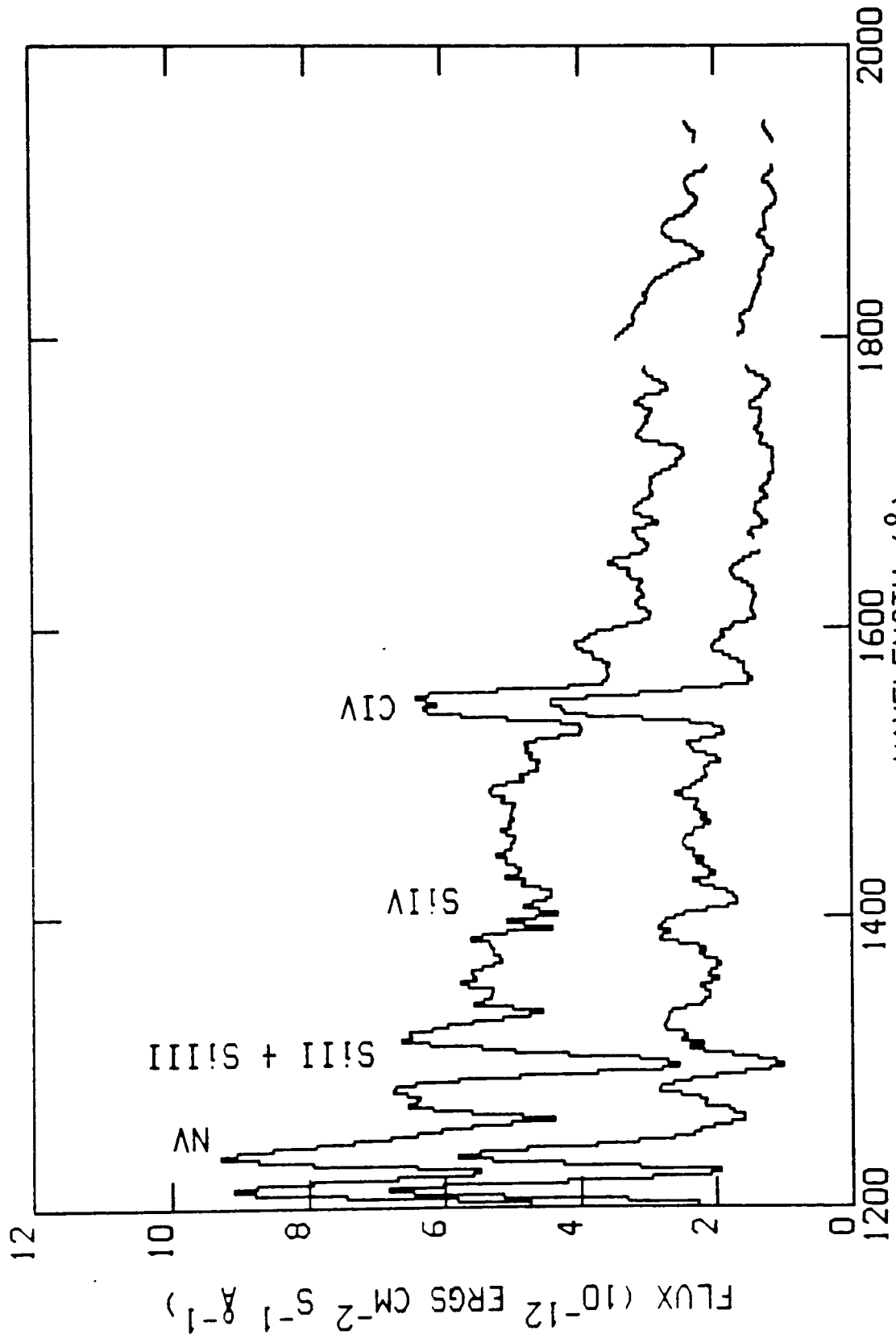

Figure 7.03 The sum of both spectra near phase 0.7 on December 14 (lower curve), and the sum of all the remaining spectra from that date (upper curve). Data from near a reseau have been omitted. The unlabelled emission line on the left is Lyman α.

fall. The spectrum from this part of the wind will change from absorption to emission. Although this explains the changes in the SiIV line, I currently have no explanation for the constancy of the CIV flux.

7.1.3 The December 24/25 UV light curve

The light curve on December 24/25 (figure 7.02, lower panel) shows no dip near phase 0.8. However, there is no point in the light curve corresponding precisely to the two points defining the minimum on December 14/15, although there is a point almost immediately after them. Thus, if the recovery from the dip is extremely rapid, the dips may have escaped detection.

The alternative is that WZ Sge was not showing dipping behaviour at this time. Physically, this would mean that the dark spot had decreased in size such that it could no longer obscure the inner disk. This could be explained if the fall in optical luminosity between these two dates (see figure 7.01) reflects a decline in mass transfer rate into the disc. This, in turn, might reduce the disruption of the disc edge by the stream and so result in smaller vertical disc structure. I shall explore this idea further in Chapter 8.

7.2 The July 1986 outburst of EX Hya.

7.2.1 The geometry of EX Hya.

EX Hya is one of only two known DQ Her stars below the period gap, its orbital period being 98 minutes, derived from timing the eclipse of the white dwarf by the secondary. There is a second periodicity in EX Hya, the white dwarf spin period of 67 minutes (Gilliland 1982). The

geometry is further discussed in the quiescent spectroscopic and photometric studies by Hellier *et al.* (1987) and Cordova, Mason & Kahn (1985) respectively.

Quiescent X-ray studies have been carried out using Einstein (Kruszewski *et al.* 1981) and the *EXOSAT* medium (Beuermann & Osborne 1985) and low (Cordova *et al.* 1985) energy experiments. The data suggest that there is a soft component (< 4 keV) which is modulated in phase with the 67 minute optical modulation. By examining how the depth of the eclipse varied as a function of 67 minute phase, Beuermann & Osborne concluded that the soft component was partially eclipsed. The hard component (> 4 keV) does not show the orbital modulation and does not appear to be eclipsed. Cordova *et al.* found that if the 67 minute period was removed from their data, and the data then folded on the orbital period, it showed a broad ($\simeq$0.5 of a cycle) dip centered near phase 0.8. They interpreted this as due to the accretion stream obscuring the central regions of the source. There is no comparable dip in the medium energy data.

The existence of the eclipse means that the soft X-rays must come from the white dwarf region. The site of the hard X-rays is more controversial. Cordova *et al.* and Beuermann & Osborne independently suggested that they might originate in a stand-off shock in the magnetic funnel, further from the white dwarf surface than the region producing the soft X-rays. However, more extended regions, such as a white dwarf corona, have been suggested, though such a region would have to extend $>$1 white dwarf radius from the white dwarf surface.

7.2.2 The July 1986 IUE data

The optical outbursts of EX Hya are normally of low amplitude (~1 mag) and last approximately two days. In July 1986, however, it showed a dwarf nova type outburst, brightening by about 4 magnitudes in under 1 day, and fading to quiescence over 3 days. Three days later this was followed by a similar outburst. The overall light curve for the outbursts, taken from observations by the Variable Star Section of the Royal Astronomical Society of New Zealand (VSS RAS NZ), is shown in figure 7.04.

G. Sonneborn obtained one LWP and 2 SWP spectra about 20 hours after the star was first observed to be in a bright state. Their timings and phases are shown in Table 7.2. The orbital phases are from the ephemeris of Mumford (1967) and the 67 minute phase from Gilliland (1982). The spectra are shown in figures 7.05 and 7.06. As in the spectra of DQ Her (Cordova & Mason, 1985) they show NV, SiIV, CIV, HeII and MgII emission, although some of these lines are saturated in the EX Hya spectra. The LWP spectrum shows no obvious 2200Å feature, but is rather noisy. I have therefore adopted E(B-V)=0.0.

The continuum of the phase 0.88 spectrum is very similar to that in DQ Her, but at phase 0.18 the continuum is much bluer. This is as might be expected if a dark spot is occulting the region near the white dwarf. The system is bright at phase 0.18, and becomes fainter and redder at phase 0.69. It should be noted that the regions occulted in EX Hya are probably the accretion poles of the white dwarf, since there is no inner disc and boundary layer, as in OY Car. However, the situation is not clear cut because of the 67 minute phase. This phase is defined such that in the optical its maximum occurs at phase zero. The brighter and

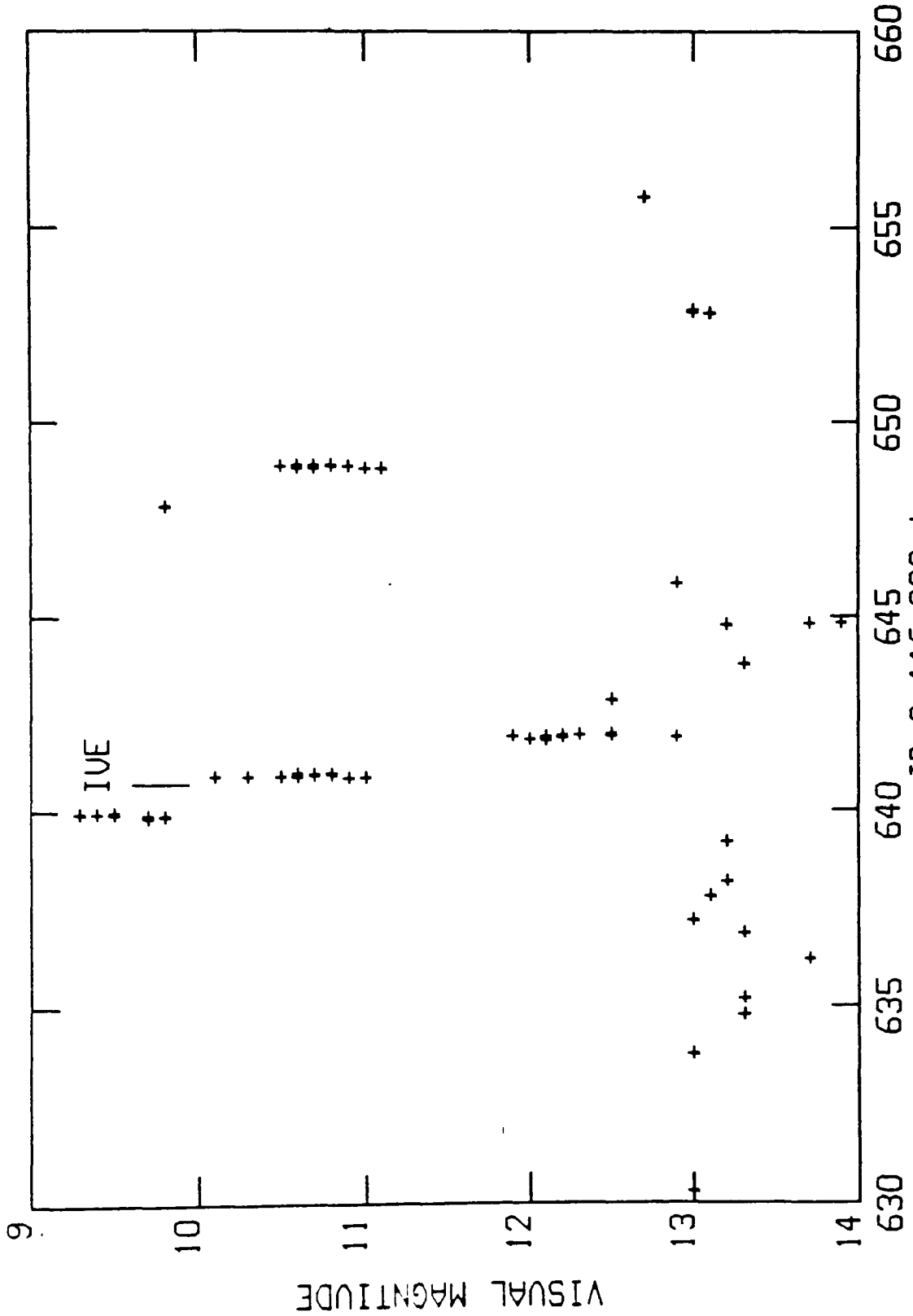

Figure 7.04 The visual light curve of EX Hya during the July 1986 outburst, from observations by the VSS RAS NZ. The time of the IUE observation is marked.

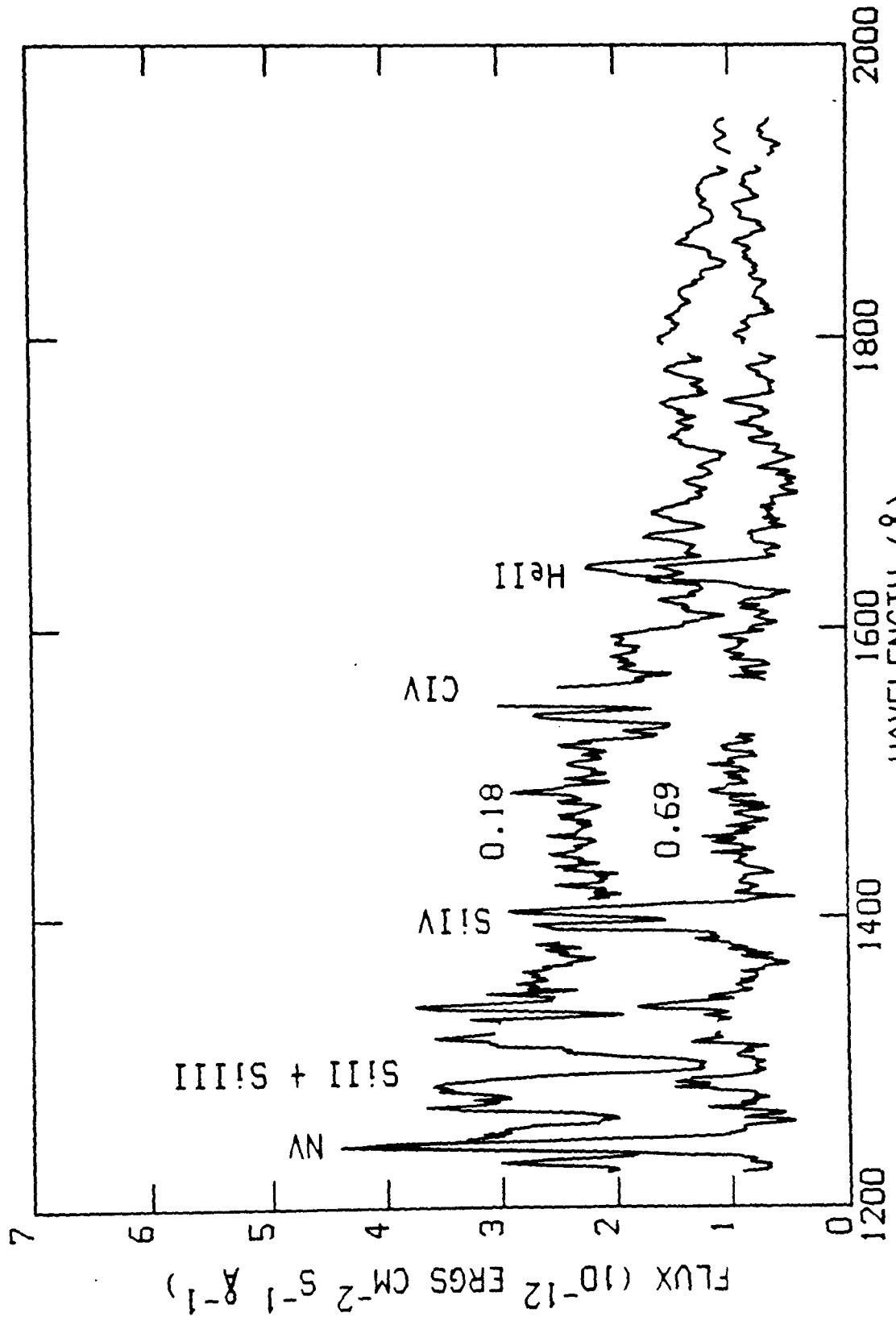

Figure 7.05 The SWP spectra of EX Hya at orbital phase 0.69 (lower curve) and 0.18 (upper curve). Data points which are saturated, or near reseaux have been omitted.

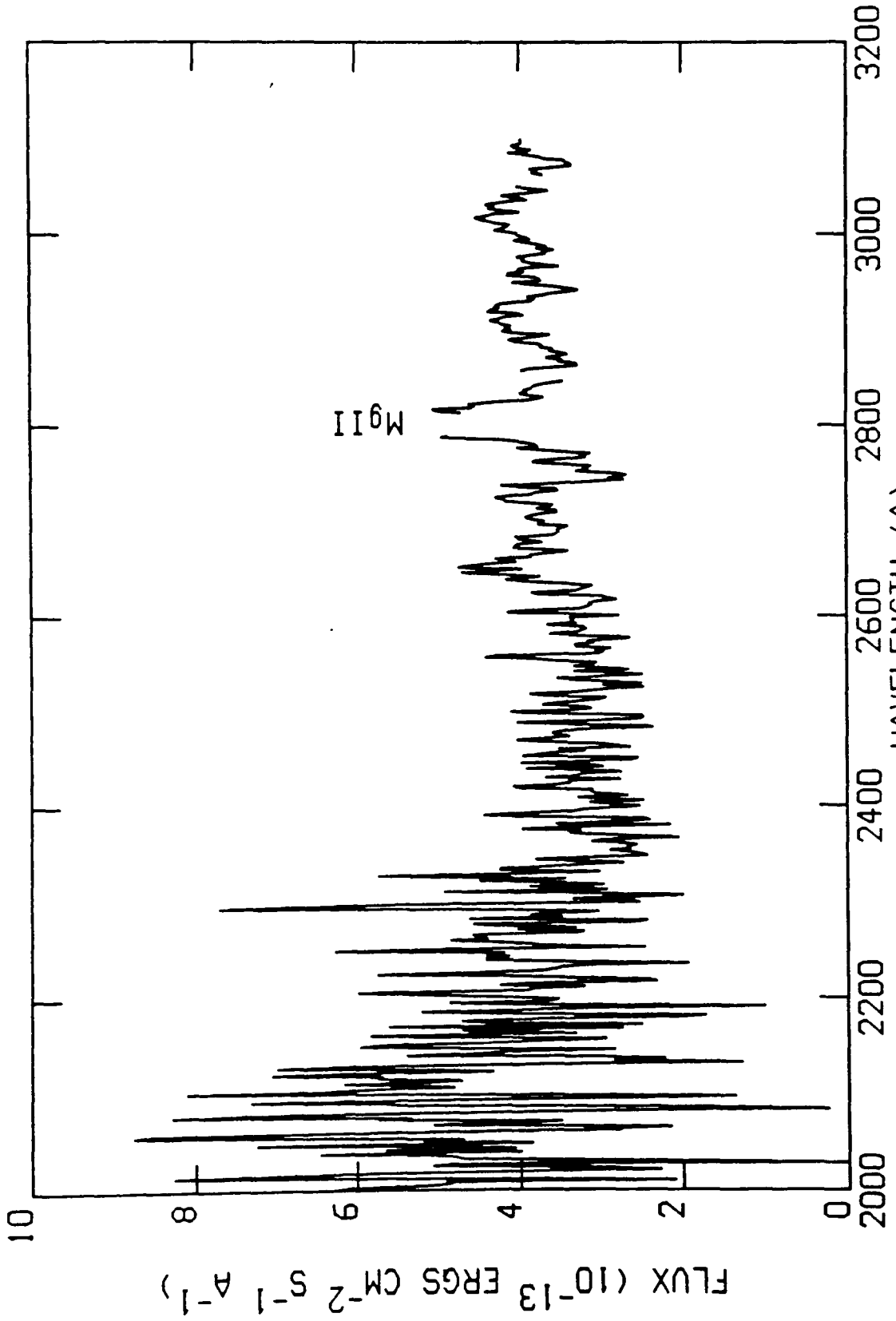

Figure 7.06 The LWP spectrum of EX Hya. Data points which are saturated, such as the MgII line, and data which are near reseaux, have been omitted.

bluer of the SWP spectra is at 67 minute phase 0.75, and the fainter at phase 0.50 (see Table 7.2). Thus, if the UV light curve follows the optical, the 67 minute variation might also produce the observed effect. More observations of EX Hya during outburst are required to disentangle these two effects.

References

Beuermann, K., & Osborne, J., 1985. *Space Sci. Rev.*, **40**, 117.

Bolin, R.C., & Holm, A.V., 1980. *NASA IUE Newsletter*, No. 10, p. 37.

Cassatella, A., Holm, A., Ponz, D., & Schiffer, F.H. III, 1980. *IUE ESA Newletter*, No. 5 p.5.

Cordova, F.A., & Mason, K.O., 1985. *Astrophys. J.*, **290**, 671.

Cordova, F.A., Mason, K.O., & Kahn, S.M., 1985. *Mon. Not. R. astr. Soc.*, **290**, 671.

Fabian, A.C., Pringle, J.E., Stickland, D.J., Whelan, J.A.J., 1980. *Mon. Not. R. Ast. Soc.* **191**, 457.

Friedjung, M., 1981. *Astron. Astrophys.* **99**, 226.

Gilliland, R.L., 1982. *Astrophys. J.*, **258**, 576.

Hellier, C., Mason, K.O., Rosen, S.R., & Cordova, F.A., 1987. *Mon. Not. R. astr. Soc.*, in press.

Holm A.U., Wu, C.C., Sparks, W.M., Schiffer F.H.III, & Bogess, A., 1980. In: *IAU Symp. 88, Close bianry stars: observations and interpretation*, p.447, eds Plavek, M.J., Popper, D.M., & Ulrich, R.K., Reidel, Dordrecht.

Kruszewski, A., Mewe, R., Heise, J., Chlebowski, T., Van Dijk, W., & Bakker, R., 1981. *Space Sci. Rev.*, **30**, 221.

Mattei, J.A., 1980. *J. Roy. Astron. Soc. Can.*, **74**, 53.

Mumford, G.S., 1967. *Astrophys. J. Suppl. Ser.*, **15**, 1.

Patterson, J., McGraw, J.T., Coleman, L., & Africano, J.L., 1980. *Astrophys. J.*, **248**, 1067.

Robinson, E.L., Nather, R.E., & Patterson, J., 1978. *Astrophys. J.*, **219**, 168.

Tunrose, B.E., & Harvel, C.A., 1982. *IUE ESA Newletter*, No. 14 p.1-1.

Chapter 8

Conclusions

8.1 The superhump phenomenon

From the data presented in this thesis, it is now apparent that the region which produces the superhump in the SU UMa stars is large (5.3.2). This confirms the picture presented by Horne (1984), that the superhump region's size allows it to avoid eclipse. This is in agreement with Whitehurst's tidal model, where the entire disc is assumed to produce the superhump light. It is also consistent with Vogt's elliptical disc model; although it requires that the stream is large, which may be the case if it takes the form of a stream penetration zone such as that suggested by Bath, Edwards & Mantle (1983). However, if the stream impact region is instead a dark spot, as it is in OY Car in superoutburst, this might also have the required area to provide the superhump light.

If the structure during superhump maximum (5.7) is caused by vertical structure at the disc edge shadowing the inner disc, it may be that the superhump disrupts the disc in some way. This might be caused either by the stream having more energy, as in Vogt's model, or in the tidal model, it would imply that the same process which causes the disc to become brighter, also disrupts it.

One of the sets of simultaneous optical and IR lightcurves suggest that there is a large asymmetry in distribution of cool material in the disc (5.6). This is consistent with the presence of an asymmetric disc whose positioning matches that required in either Vogt's or Whitehurst's

models of the superhump. Thus I return once again to the problem mentioned in Chapter 4, that an observational test to rule out one or other of these models is difficult to find. A further test which may help, is to find the projected area of the superhump on the plane of the sky for a low inclination system. If this shows that the superhump is not in the plane of the disc (i.e. if the area is significantly smaller than in OY Car) then this would favour Vogt's model. If the area is similar to, or larger than that for OY Car, the test cannot distinguish between the models.

Another test of the models may be contained in the O-C information. I mentioned in Chapter 4 that the Z Cha O-Cs did not match the prediction for an uneclipsed superhump. In Chapter 5 (Section 7) I showed that Krzeminski & Vogt's (1985) O-Cs of OY Car, which had previously been thought to match the prediction for an uneclipsed superhump, are of too low a quality to be a meaningful test. Thus it might be that the Z Cha O-Cs contain information about the partial eclipse of the superhump, specifically the superhump source's location.

8.2 Disc structure

I have shown that the inner disc and boundary layer of an SU UMa system during superoutburst are obscured (5.4, 6.6.2 and 6.6.3). This may be caused by extensive vertical structure in the disc, possibly near its edge. The obscuration of the inner disc allows us to see the wind (which has been seen in other CVs, e.g. Cordova & Mason 1985), and an extended soft X-ray source. The origin of the soft X-rays is unclear, but may be caused by shocks in the wind such as those which Raymond & Mauche (1985) have attempted to model.

The height of the disc structure seems to reach a maximum near the point where the stream interacts with the disc. The effects of this "dark spot" obscuring the inner disc can be seen in the UV (figures 6.04a and 7.02), and sometimes in the optical (figure 5.02). This may well be analogous to the dips seen in the X-ray light curves of the low mass X-ray binary ADC or dip sources. There is some evidence that the size of the dark spot may reflect mass transfer rate through the disc (7.1.3). This may also be the case for the LMXB transient EXO 0748-676 (Parmar *et al.* 1986) where the X-ray dips are deeper when the source is brighter. One might expect this if the spot's size is controlled by the mass transfer rate from the secondary into the disc, since the transfer rate also determines the mass accretion rate onto the compact object, provided that the viscous timescale of the disc is short (~days).

If the depth of the dips is an indicator of mass transfer rate, it should prove to be a very useful diagnostic. For instance, in the case of EXO 0748-676 (Parmar *et al.* 1986) it suggests that the outbursts are mass transfer sustained, since the outbursts decay as the mass transfer rate falls. The OY Car optical data in figure 5.02 show optical dips near the peak of a superoutburst, and yet the data of Cook (1985) show no dips during a normal outburst. This is consistent with the view that superoutbursts are also mass transfer sustained, whilst normal outbursts have relatively short mass transfer events (Bath, Clarke & Mantle 1986), or are caused by a disc instability. One must be cautious about drawing such an important conclusion from so few light curves, but it highlights the importance of obtaining more outburst and pre-superhump superoutburst photometry of Z Cha and OY Car.

The above ideas suggest a support process for the extended vertical disc

structure, especially the dark spot. Since the size of dark spot is related to the mass, and thus the energy in the stream, it may be that some of that energy is released as turbulence, which, in turn, supports the structure. Such an idea is not new (see Mason 1986, and references therein) but has been criticised on the grounds that it is not clear that the stream has sufficient energy to support the disc. However, we can use the estimates of the column density required to produce the HeI absorption in AC211 (see 3.7.2) to find an order of magnitude for the total mass of the vertical structure, which is $\sim 10^{-13} M_{\odot}$. The force required to support this above the plane could easily be supplied by the change of momentum of a mass transfer stream of $\sim 10^{-10} M_{\odot} yr^{-1}$. Since such scant observational evidence as there is lends support to this mechanism, it warrants thorough theoretical investigation.

8.3 Postscript

Despite the analogy drawn in the above section, the essential fact remains that AC211 is an LMXB whose compact object is a neutron star or black hole; it is not a dwarf nova in outburst. However, dealing with the high inclination X-ray binaries as a group, leads one to suppose that the problems associated with them may have a common solution. Specifically; is the mechanism which supports the disc structure similar in both groups of systems; and are superoutbursts, and the outbursts of the LMXB transients mass transfer sustained? As always, more research is needed to discover if the similarities are merely superficial, or if they reflect the same underlying mechanisms.

References

Bath, G.T., Clarke, C.J., & Mantle, V.J., 1986. *Mon. Not. R. astr. Soc.* **221**, 269.

Bath, G.T., Edwards, A.C. & Mantle, V.J., 1983. *Mon. Not. R. astr. Soc.* **205**, 171.

Cook, M.C., 1985. *Mon. Not. R. astr. Soc.* **216**, 219.

Cordova, F.A., & Mason, K.O., 1985. *Astrophys. J.* **290**, 671.

Horne, K., 1985. *Nature*, **312**, 348.

Krzeminski, W. & Vogt, N., 1985. *Astr. Astrophys.* **144**, 124.

Mason, K.O., 1986. In: *Physics of Accretion onto Compact Objects* p. 29, eds. Mason, K.O., Watson, M.G., & White, N.E., Springer-Velag, Heidelberg.

Parmar, A.N., White, N.E., Giommi, P., & Gottwald, M., 1986. *Astrophys. J.*, **308**, 199.

Raymond, J.C., & Mauche, C.W., 1985. In: *Proc. 9th North American Cataclysmic Variable Workshop*, p. 128, ed. Szkody, P., University of Washington.

Appendix 1

Extraction of IPCS Spectra in Crowded Fields

A1.1 Introduction

In Section 2 of Chapter 3 it was pointed out that in the core of a globular cluster the position of a star's spectrum on the IPCS varies with wavelength by an amount comparable with the separation of the stars (see figure 3.01). The aim of this appendix is to show how this problem was overcome, and discuss the limitations of the method devised.

Figure A1.01 shows a schematic view of the IPCS. The position of a star as a function of wavelength varies for two reasons. The first is an instrumental effect called "S waving", which causes the spectrum to take up an "S" shape on the detector. The second is that atmospheric dispersion will cause the blue image to be displaced along the slit relative to the red image.

There are two commonly used methods of extraction for single stars. The first is to sum a sufficiently wide block of spectra that all the flux remains within the block. This does not increase the noise significantly if the sky background is negligible compared with the star. However, the proximity of the cluster core to AC211 (see figure A1.02) means that the background is far from negligible, and so this technique would result in very noisy spectra. Also the core would move in and out of the block of spectra with wavelength, giving a strange, unphysical, continuum shape.

The second approach, for fainter objects, is to sum a large number of pixels perpendicular to the dispersion direction, but weight each one

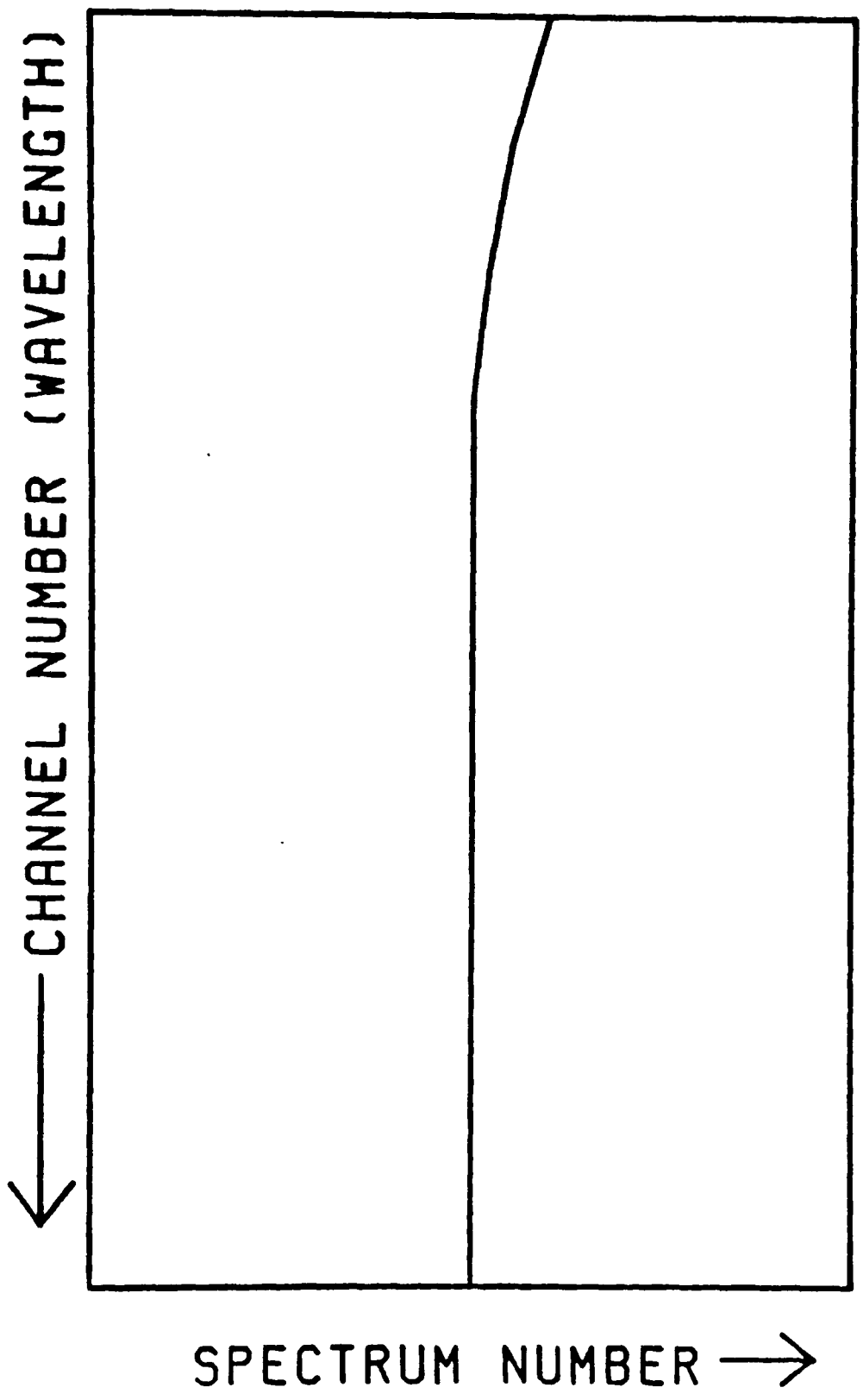

Figure A1.01 A schematic view of the IPCS. The definitions of channel number and spectrum number are marked, wavelength increases down the page. Also shown is the track of a star which suffers atmospheric dispersion.

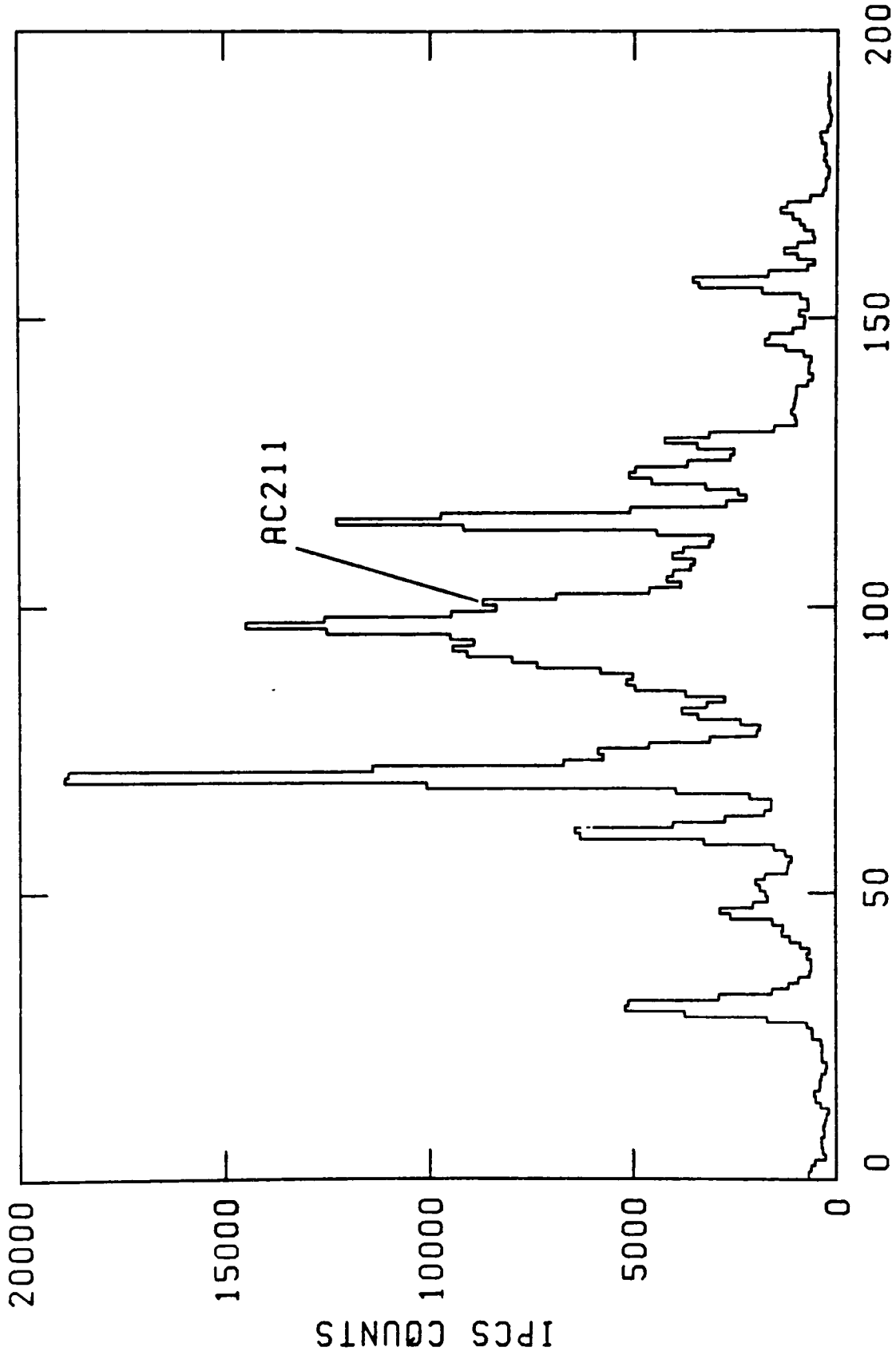

Figure A1.02 A cross section of the IPCS detector near 4500Å, from an image near the start of Night 2. The position of AC211 is marked.

according to the expected flux from the star ("optimal extraction", see for example Horne 1986). Thus channels consisting of mainly sky counts have a low weighting and do not add significantly to the noise. In both cases spectra well clear of the object are used to estimate the sky contribution. Unfortunately, this method can only be used for isolated stars.

The technique I developed was to choose a bright star in the IPCS image, and use this to define the channel number - spectrum number relationship for the entire detector. An offset between this "track" and the object was calculated, and the object spectrum parallel to the track extracted.

A1.2 Finding the position of AC211

The HeII λ4686 line is almost always present in AC211. Therefore the AC211 spectrum was located by searching for the HeII line using a program which found the significance of any spectral line relative to the local continuum. A continuum region was specified (channels 1300 to 1400 for night 2, a total of 50Å) as was a region for the spectral line of interest (channels 1414 to 1442 for night 2 and HeII λ4686). For each spectrum number along the slit the counts in each of the two bands were summed, and then one divided by the other to find a mean line to continuum ratio. Another method of achieving this would be to find the ratio for each spectrum, and take the mean. This has the effect, however, of equally weighting the ratio from spectra with a high number of counts, and those with very few. The method adopted has the advantage that the mean ratio is dominated by the statistically well determined ratios near the core.

From the ratio in each spectrum I then subtracted the mean ratio (see

figure A1.03). The plot is dominated by noise from the low count rate spectra. To overcome this I then divided by the error in each ratio, effectively finding the square root of the significance of any lines detected. This was not squared since the sign defines whether there is a flux excess (positive) or deficit (negative) in the line region region, relative to the other spectra. The result is shown in figure A1.04, where the presence of HeII λ4686 is clearly shown in spectra near 101.

A1.3 Tracking a Star.

The program "Rivoli" tracked a star. (See Chandler 1966 for an explanation of the program names in this appendix.) At each channel number the program found the highest valued spectrum within a given range of spectrum number. The range chosen was usually about 10 spectra wide and included a bright star suitable for tracking. It was chosen using a cross section through the data. Once the highest valued spectrum has been found a parabola was forced through this point and the two pixels adjacent to it to find a floating point value for the center of the star. The result (see figure A1.05) is noisy on a scale of 1 pixel. To overcome this a Fourier filter was used that removed structure on a scale smaller than 200 pixels. A Fourier filtered track is also shown in figure A1.05. The use of a filter means that the track moves away from the position of the star by up to 0.5 pixels in the last ~80 channels near the edge of the detector.

A1.4 Extracting the spectrum

The program "Lodi" extracted the spectrum by summing the counts in a 3

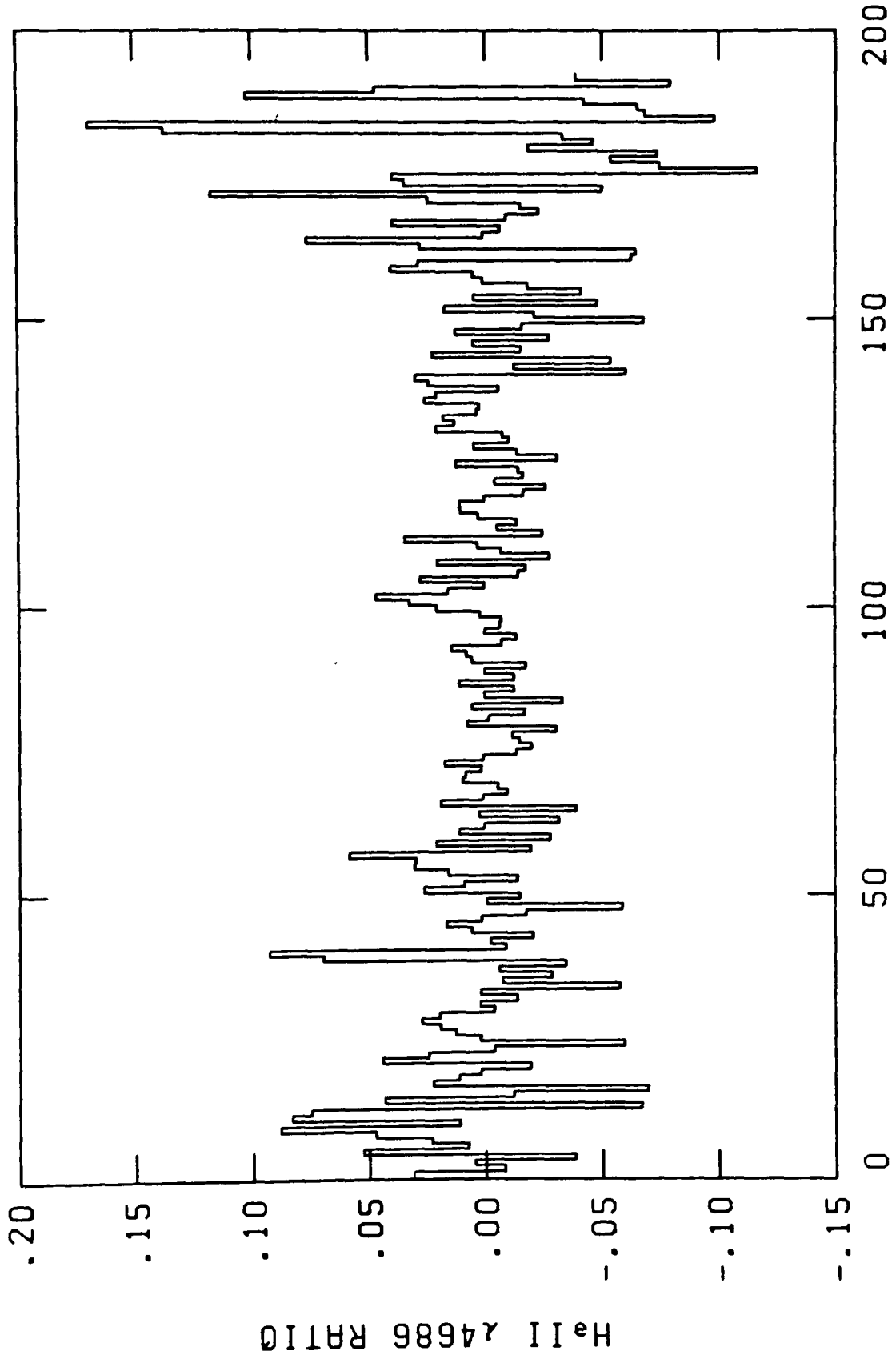

Figure A1.03 The ratio of the flux in a defined band near HeII λ4686 to a continuum band for each spectrum in an IPCS image, after the subtraction of a mean ratio. Note how the ratio becomes much noiser towards the edges of the detector, where the count rate was lower.

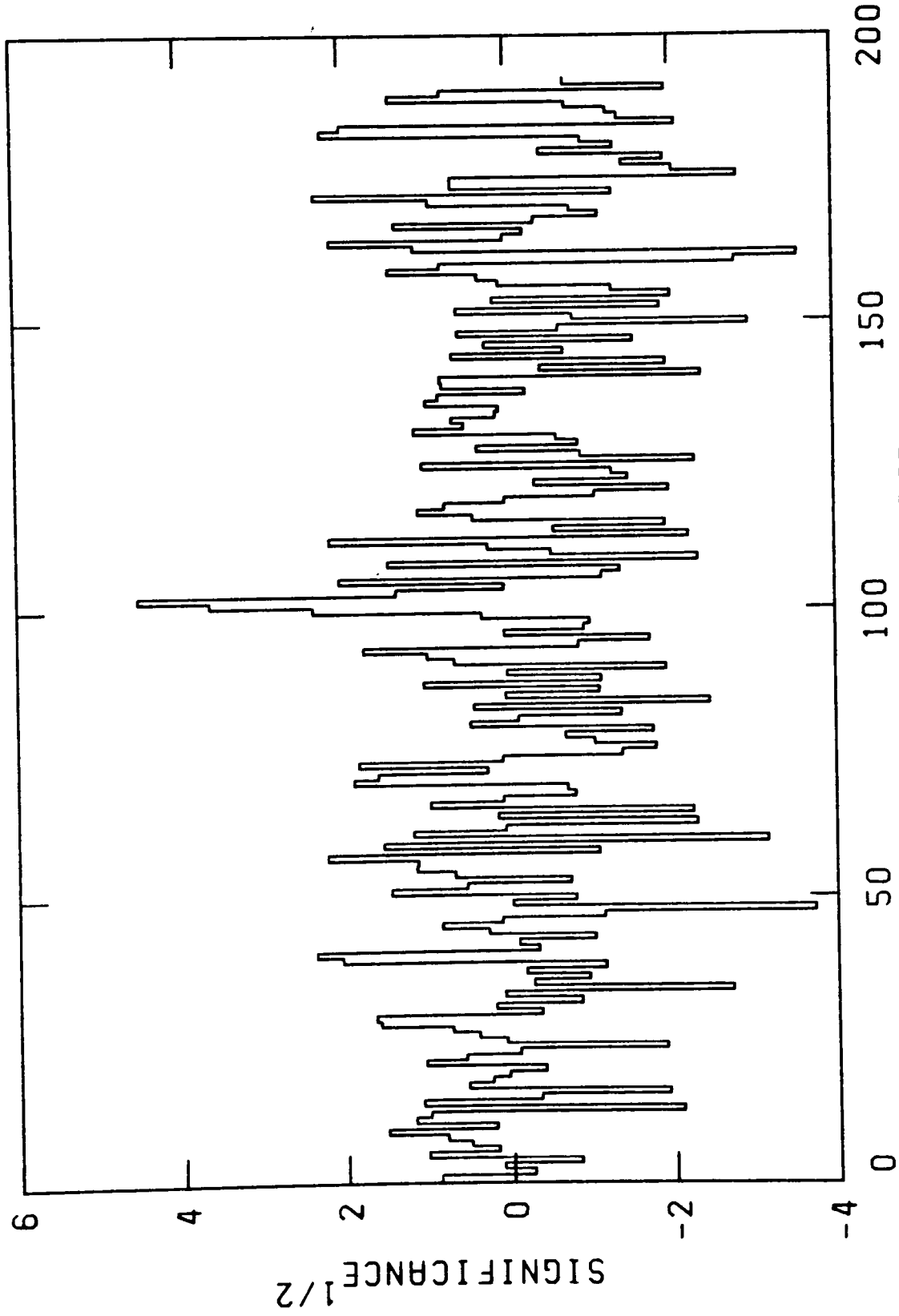

Figure A1.04 The significance of any spectral feature near HeII λ4686 plotted against spectrum number. The peak around spectrum 101 is due to emission from AC211.

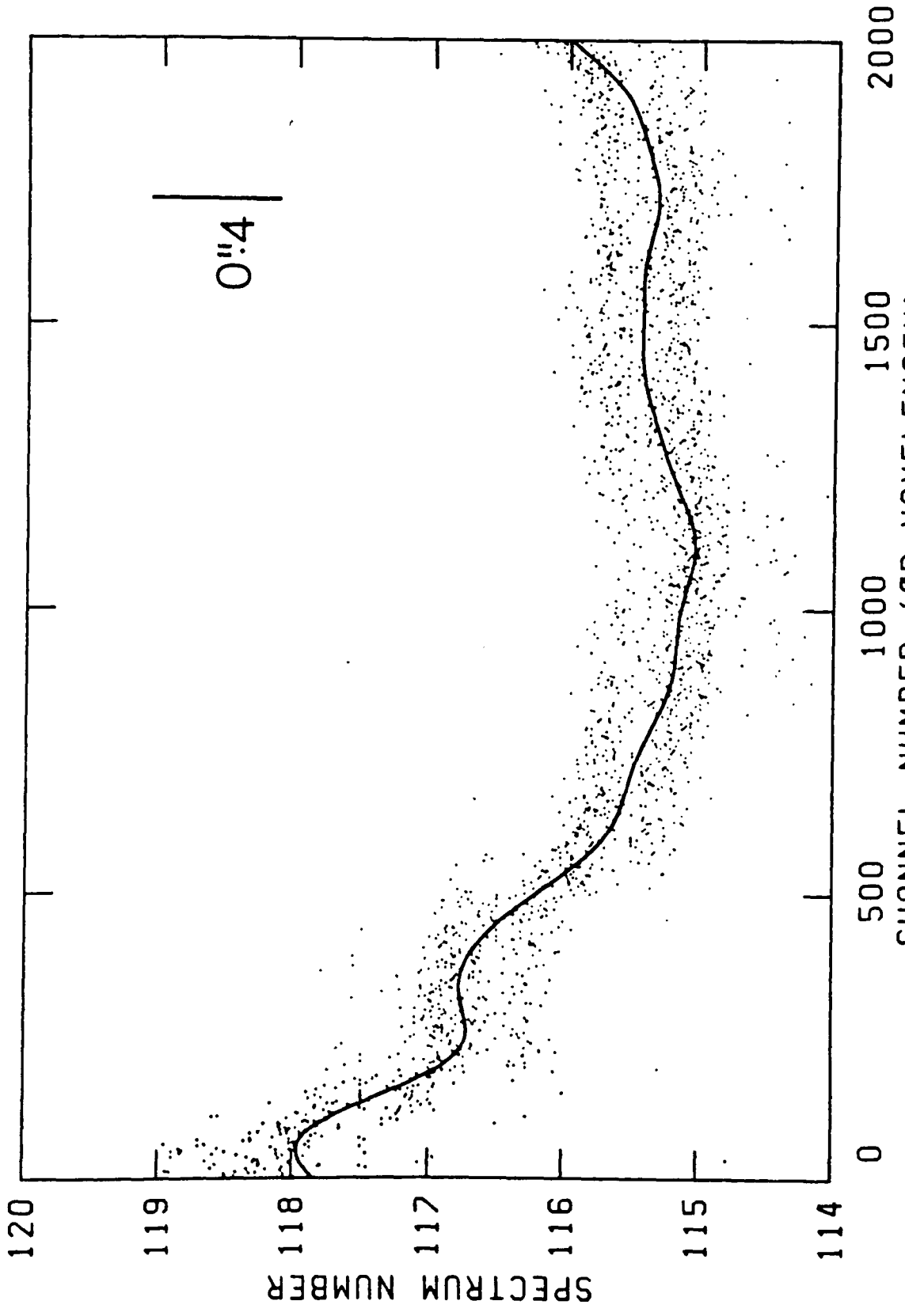

Figure A1.05 The track of a star along the IPCS, from the same image as figure A1.02. The dots show the track generated by forcing a parabola through the highest and two adjacent points, the solid line is the result of Fourier filtering the points.

pixel wide window around the position of AC211. This size was chosen to match the seeing, which was ≃1" throughout the observations.

In order to find the position of the object, the difference between the spectrum number of the HeII emission and the track at the appropriate channel was calculated. This was used as an offset between the track and AC211 to give the position of the latter at all channel numbers. As this was a floating point number, the number of counts in the extracted spectrum was the sum of all the counts in two pixels, and a portion of the counts in two others, as shown in figure A1.06. This method was chosen, as opposed to summing the nearest three pixels, since it ensures that the spectrum is continuous. A whole pixel method would mean that whenever the three spectra being summed changed, the extracted spectrum would show a discontinuity.

The position of the arc lines in an arc image varies slightly (~1 channel = 30km s^{-1} on Nights 2 and 3) with spectrum number. Therefore each spectrum of AC211 was calibrated by an arc spectrum extracted with the same offset as the data and a similar track.

A1.5 Fluxing the spectra

The flux in an extracted spectrum is considerably smaller than the total flux from the object. This is because it was observed through a narrow spectrograph entrance slit, and because the extraction window was only 3 pixels wide. When converting to absolute fluxes this effect was allowed for in the following way.

If the position along the slit is x, and the perpendicular to the slit is y, the seeing disc can be assumed to be;

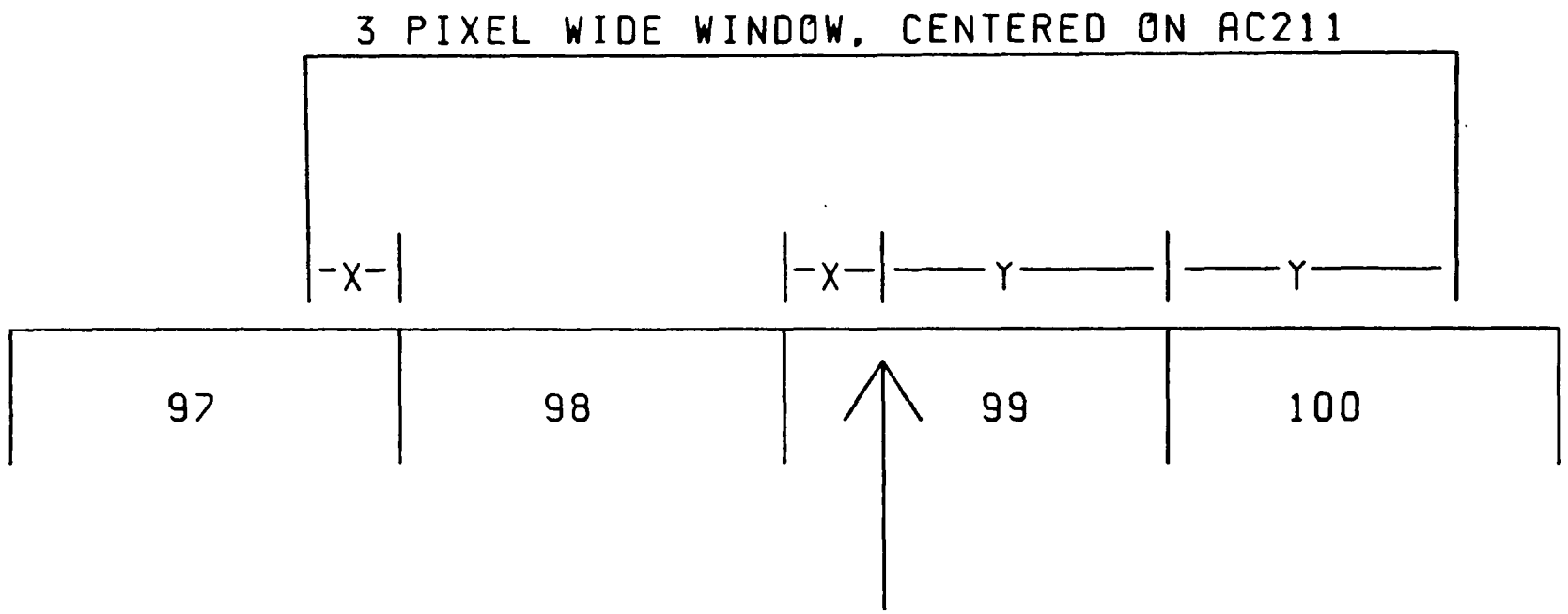

Figure A1.06 A diagrammatic representation of the sum of pixels used to find the counts in AC211. X and Y are defined as the distance between the position of AC211 and the nearest pixel boundaries, measured in pixel lengths. In the case shown, all of the counts in spectra 98 and 99 would be used, with X times the counts in spectrum 97, and Y times the counts in spectrum 100.

$$\text{Flux at } (x,y) = \frac{A \exp(x^2+y^2)}{2\sigma^2} \qquad \ldots \text{(A1.1)}$$

where,

$$1/A = 2\pi\sigma^2. \qquad \ldots \text{(A1.2)}$$

The full-width-half-maximum seeing (s) is given by $s^2=8\sigma^2\ln 2$. The normalisation has been chosen such that the total flux is 1.

In order to find the flux in the extracted spectrum, equation A1.1 must be integrated over the range $-w/2 < y < w/2$, $-1.5 < x < 1.5$, where x and y are measured in pixels, and w is the spectrograph slit width. The integral is separable into the product of two Gaussian integrals. The values for these integrals can be found in tables (see for example Bevington 1969, Table C-2) if the limits are expressed in terms of σ. A Gaussian fit to an isolated star will yield the seeing, and hence σ, in pixels, and w must also be converted into pixels. Thus the correction factor can be calculated.

The flux standards were observed using a wide slit, and a conventional (wide window) extraction technique. AC211 was then fluxed with an instrumental response function defined by the standards, and using the correction factor to allow for the difference in the observation techniques. This method was preferred to attempting to observe the standards with a narrow slit and extraction window, since;
(1) the difference in seeing between the standard star and object observations would still have to be allowed for, and
(2) the standard star may not have been centered on the slit. However, there still remains the uncertainty that AC211 may not have been centered on the slit, in which case the flux is a lower limit.

The seeing profile is, in fact, a Gaussian with a superimposed broad

base. In order to investigate the effect that this has, and to check the method, the integral of equation A1.1 was used to predict the ratio of flux in a narrow window extraction after background subtraction, to that of a conventional extraction for the standard stars. The results (shown in Table A1.1) are within 3% of those predicted by the formula.

Table A1.1

Image #	Seeing (Pixels)	Ratio Predicted	Ratio Measured
40	3.42	0.70	0.67
86	3.33	0.71	0.69
91	4.07	0.61	0.61
153	3.80	0.65	0.62

A1.6 Discussion

In order to simplify data reduction, the tracking and extraction procedures were combined into one program called "Marengo", which required as input the window within which to search for the track star, and the offset to AC211. The offset was calculated for each slit position using an image which was the sum of about 3 IPCS frames at that parallactic angle. Figure A1.07 compares the results of using "Marengo" with a conventional extraction.

Although no background subtraction can be undertaken using this method, the background light remains constant for a given slit position. Thus it is possible to observe how the continuum changes over limited periods of time. The fluxes in lines can similarly be compared, but once the telescope is moved, the narrow slit means that a different proportion of the light from AC211 will enter the spectrograph, and the apparent flux from an intrinsically constant line may change. However, the ratio of the flux in one line to that in another, where the flux is entirely from

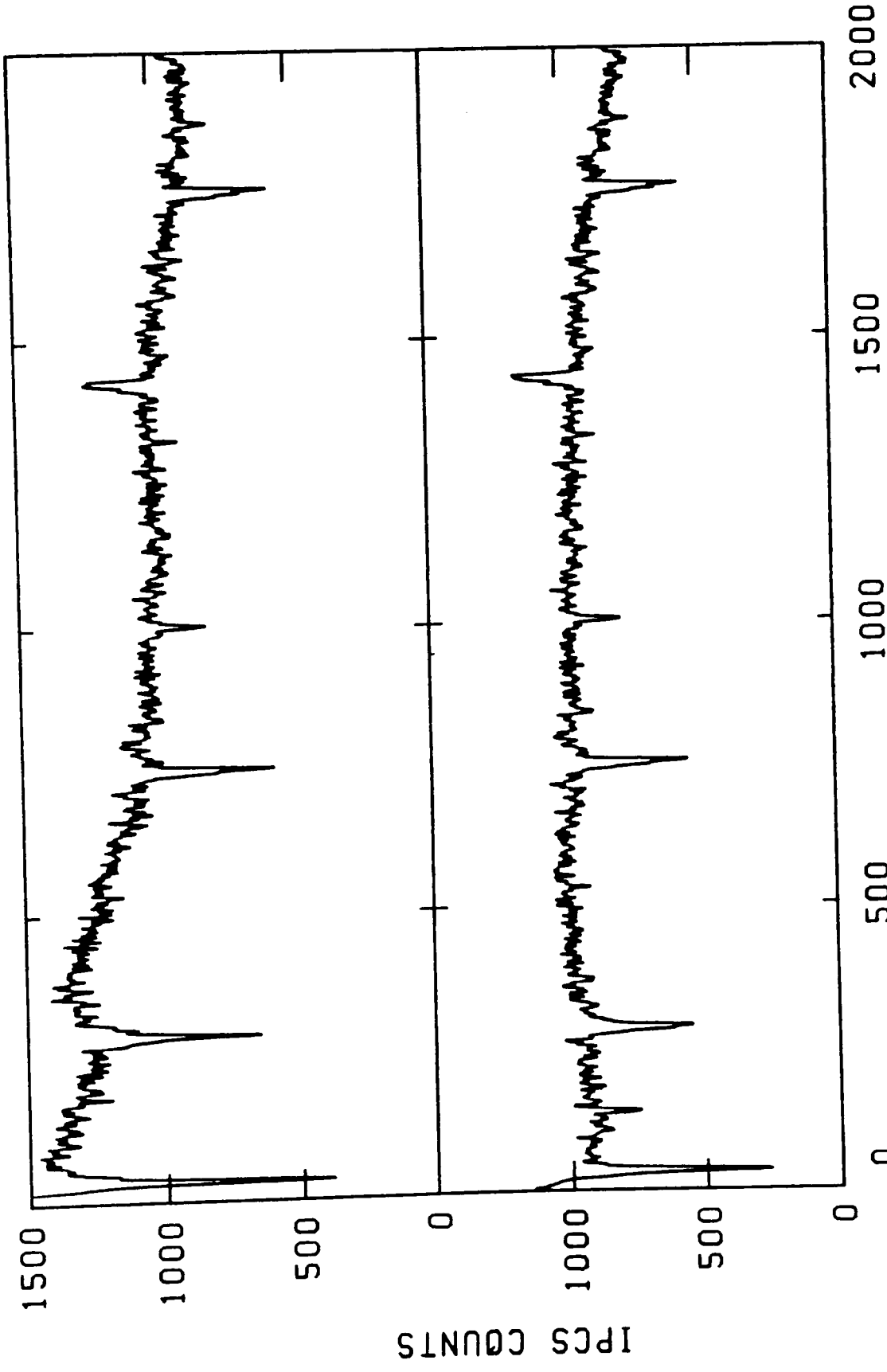

Figure A1.07 A comparison of a simple sum of 3 adjacent spectra (upper panel) and the spectrum extracted by Marengo. Both spectra are the sum of the spectra from the first 7 exposures of Night 2, and have been smoothed by 3 passes of a triangular filter. Note how atmospheric dispersion of the core into the simple sum spectrum gives the impression of a rise towards the blue. Atmospheric dispersion of AC211 out of the block of spectra summed leads to the HeI line near channel 150 being

the object (this will not work for the Balmer lines becuase of the substantial contribution from other cluster stars), is correct. All wavelength information obtained by this method of extraction is, of course, reliable.

The statistical error in a given IPCS pixel is usually assumed to be the square root of the number of counts. Therefore the error (E) for a channel in a spectrum extracted by "Marengo" is given by

$$E^2 = f^2N_1 + N_2 + N_3 + (1-f)^2N_4 \qquad \ldots (A1.2)$$

Where N_i is the counts in spectrum i of the IPCS image, and f is the fraction of spectrum 1 used. If N_i is assumed to be the same in all spectra of the IPCS image at a given channel number, then it is N/3 where N is the number of counts in the extracted spectrum. The maximum error then occurs for f=1, and is the square root of N. The minimum error occurs when f=0.5, and is then $(5/6)^{1/2}N$. Thus, if square root errors are assumed, the χ^2 of any fit should be multiplied by a factor between 1 and 1.2.

Finally it must be remembered that the method is far from automatic. For instance the results of tracking stars must be monitored, and the position of the object found. As a result the extraction process becomes interactive, and as each image is 768 Kbytes, large amounts of interactive CPU and I/O time are required. Also the emission line finding program is less sensitive than the human eye. When it failed, the HeII could often be found by summing the spectra in threes, and making one such sum for each spectrum number around the suspected position of AC211. After smoothing, the HeII could be found by eye in one of the summed spectra.

References

Bevington, P.R., 1969. *Data Reduction and Error Analysis for the Physical Sciences*, McGraw-Hill, New York.

Chandler, D.G., 1966. *The Campaigns of Napoleon*, Weidenfeld & Nicholson, London.

Horne, K., 1986. *Publs. astr. Soc. Pacif.*, **98**, 609.

Appendix 2

Superhump Ephemeris for the May 1985 Superoutburst of OY Carinae

In general the superhump ephemeris in SU UMa stars has the form,

$$HJD(maximum) = T_o + P_sE + CE^2 \qquad ...(A2.1)$$

(see for example Warner 1985). P_s and C are constant for a given system from one superoutburst to the next, but T_o changes. In most cases the quadratic term is negative, and $\sim 5x10^{-6}$, but is unknown in the case of OY Car. As only observation 6 has an unambiguous superhump timing, (HJD = 6190.3353) we have insufficient data to find the quadratic term. Therefore a linear ephemeris was adopted with a period equal to that of a fit to the first 70 superhump cycles of the January 1980 superoutburst, using the data of KV, and assuming that the period in the same range of superhump cycle numbers will be the same.

None of the KV timings deviate from this ephemeris by more than $5.2x10^{-3}$ days (0.08 in phase). Using observation 6 to fix T_o we find

$$HJD(maximum) = 6190.3353 + 0.064400E \qquad ...(A2.2)$$

where the error in any one superhump timing is $\sim 5x10^{-3}$ days (0.08 in phase). This error is due to the difficulty of judging the time of superhump maximum when deriving the ephemeris. In combination with Wood's (1986) ephemeris this gives the beat phase, which we define as the orbital phase at which superhump maximum occurs.

References

Warner, B., 1985. In: *Interacting Binaries* p.367 eds. Eggleton, P.P. & Pringle, J.E. D. Reidel, Dordrect, Holland.

Wood, J., 1986. *Ph.D. Thesis*, Cambridge.

Appendix 3

Calculation of Errors for IUE Low Resolution Data

A3.1 Introduction

The "raw image" from an *IUE* exposure is an image 768 pixels square. The flux in each pixel is recorded as an 8 bit number, the "data number" (DN). In order to correct for the differences in sensitivity from pixel to pixel (the flat field), and the non-linearity of each pixel, this image is converted, by use of the Intensity Transfer Function (ITF), into flux number (FN). FN is proportional to the flux which has fallen on the pixel, and is the same in two pixels on which the same flux, at the same wavelength, has fallen. After the extraction of the spectrum the variation in sensitivity with wavelength is removed using a flux calibration function.

Noise in the spectra comes from two main sources, approximately Poissonian noise in the original DN image, and noise in the ITF, which will affect the FN image. The DN noise will be a function of DN alone. As the ideal exposure time for an image corresponds to approximately 200 DN we can, instead, say that the noise is a function of ideal exposure time divided by real exposure time (T_{ideal}/T_{real}). In fact, ideal DN is a weak function of wavelength, but varies by less than ±10% (IUE Image Processing Manual, Chapter 5). Thus, expressing the noise as a function of T_{ideal}/T_{real} introduces a similar error in our calculated signal to noise. It is unclear what the noise contribution from the ITF is a function of, and so I will assume that it is also a function of DN alone, and test the validity of this assumption later.

A3.2 The program

If the noise in each pixel is a function of T_{ideal}/T_{real} only, then so is the noise in the extracted spectrum. Indeed, at flux levels far above background the form of the T_{ideal}/T_{real} dependence will be identical to that for individual pixels, with a different normalisation. Thus the program for calculating the errors, "iueerr" works from the final extracted spectrum.

From a spectrum the ideal exposure time is calculated as a function of wavelength using the formulae given in the IUE Notes for Applicants. From T_{ideal}/T_{real} the signal to noise is found by interpolation from points in a look up table, and thus the noise can be found for each data point.

A3.3 The signal to noise relationship

The success of the program depends on the signal to noise look up table. This was constructed from two sources. Firstly the Camera User Guide gives signal to noise in single pixels as a function of photons per pixel. Using the fact that T_{ideal}/T_{real} = 1 yields a signal to noise of ~30, this curve is presented as a function of T_{ideal}/T_{real} in figure A3.01 using small circles.

The crosses in figure A3.01 show signal to noise measured from the continua of the SWP spectra presented in Chapter 6. In the overlap region the two sets of points agree. This is important since it shows that assuming the ITF noise to be a function of T_{ideal}/T_{real} alone is a good approximation in this situation. However, it should be emphasised that this does not mean that ITF noise is such a function. For instance, were ITF noise constant in T_{ideal}/T_{real} space, and a weak

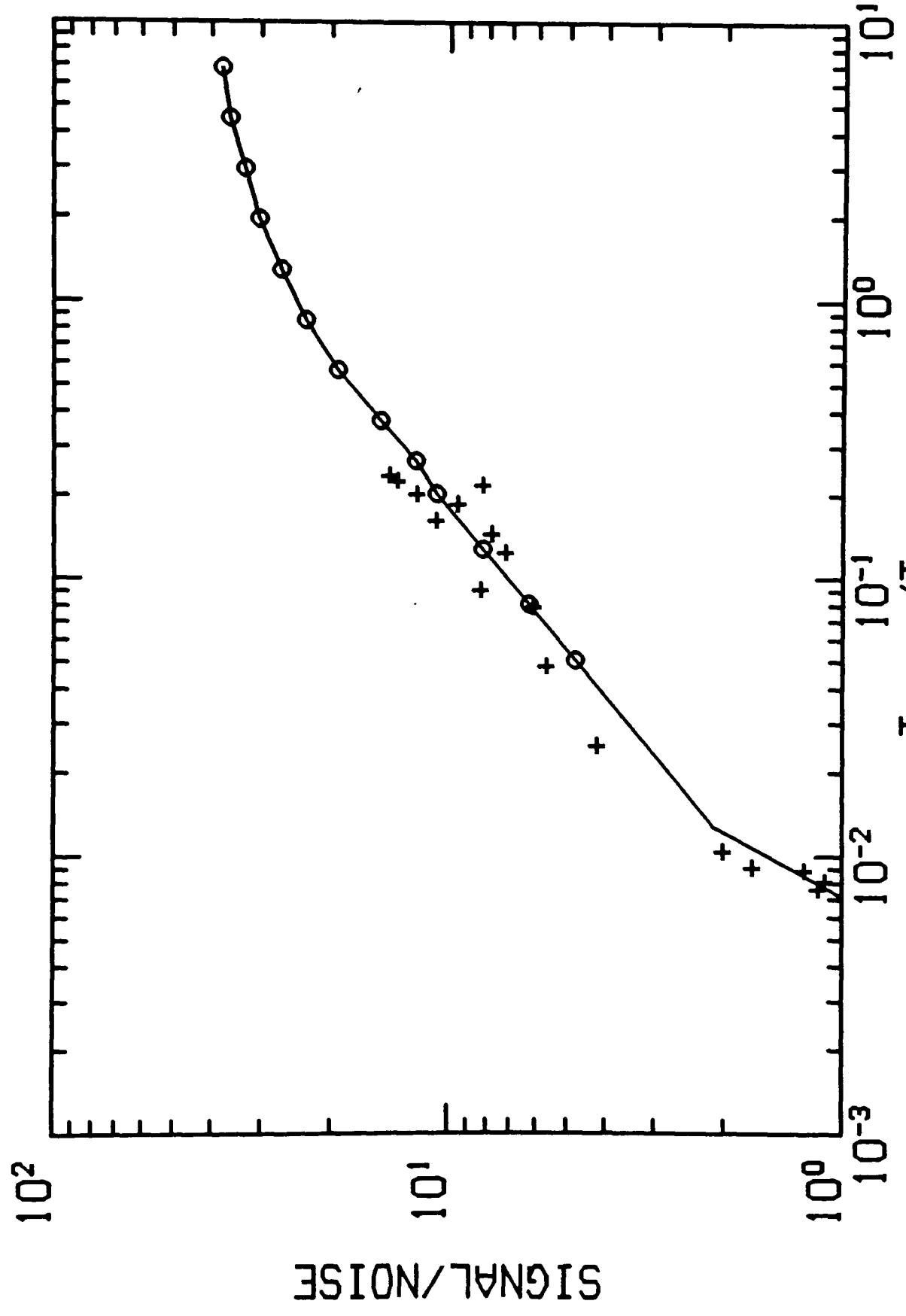

Figure A3.01 Signal to noise in *IUE* spectra as a function of the exposure time divided by the ideal exposure time (T_{real}/T_{ideal}). The circles are points taken from the Camera User Guide, the crosses points measured from spectra and the line is the relationship adopted.

function of detector temperature, the points in figure A3.01 may still have agreed.

At low T_{ideal}/T_{real} the measured points do not lie on the extrapolation of the Camera User Guide data points. This is probably because the noise in the background is now becoming important. The solid curve in figure A3.01 is the signal to noise relationship adopted.

A3.4 Future developments

Differing background count rates will undoubtedly affect the form of figure A3.01, although the small scatter of the points for the Chapter 4 data shows that the background rates for these observations are sufficiently similar for one curve to be used for all the data. If the program is to be made completely general then it should allow for the error due to the background for individual spectra. *IUE* spectra are extracted by summing all the lines of the FN (line-by-line) image near the object spectrum to form the "gross", and subtracting a background spectrum taken from elsewhere in the image. The background is smoothed by one pass of a 63 point median filter followed by two passes of a 31 point mean filter, and thus contains negligible noise. So the noise could be found by working entirely from the gross spectrum, with no need to return to the line-by-line image. Of course the signal to noise relationship would have to be measured from various gross spectra.

Acknowledgments

First and foremost my thanks must go all those people who have helped create the environment in which I have worked for the last 3 years. My supervisor, Phil Charles, instigated of most of the projects in this thesis, and his enthusiasm has helped carry them through. Barbara Hassall has worked tirelessly to improve my prose style, and her knowledge of *IUE*, and the dwarf nova literature has been invaluable. In addition to the above, other people have spent many hours in discussions with me, and passing on their scientific know how. These include Robin Corbet (who also made available the 2S0921-630 data used in Chapter 3), Janet Drew, Geoff Bath, Alan Smale (who also helped with some of the *EXOSAT* data reduction), Koji Mukai and Bill Honey. After carrying out the eclipse fitting in Chapter 5, Graham Berriman spent much time discussing its interpretation with me. The co-authors of the papers which resulted from the data presented in this thesis, Jeremy Bailey, George Sonneborn, Brain Warner and Hans van der Woerd also contributed many useful comments, And, of course, Donald Blackwell, the Savillian Professor of Astronomy, provided the hospitality and facilities of the Department of Astrophysics. Finally, all those friends who, despite my protests, persisted in providing distractions whilst I was writing this thesis; especially Nicola Marples.

To carry out Target of Opportunity observations involves a large organisation. First there is Frank Bateson and the members of the Variable Star Section of the Royal Astronomical Society of New Zealand. These amateur observers have maintained a constant watch on many southern dwarf novae, and informed the Oxford group promptly when OY Car and EX Hya went into outburst; without this information any amount of

Space Age technology would have been useless. Their data also forms figures 5.01 and 7.04. Then there are all the people who organised or carried out the observations. Tony Peacock and Paul Barr (ESOC) and Willem Wamsteker (Vilspa) and their staff organised the *EXOSAT* and *IUE* observations at very short notice. D. Allen carried out the AAT service observations and I.M. Coulson, A.R. Hyland, K. Reinsch and P.A. Whitelock for interrupted their own programmes in order to observe OY Car.

Most of the data reduction was carried out with the ARK software on the Perkin-Elmer computer at the Department of Astrophysics, Oxford. I thank all those who have helped me use this machine for their help. The rest of the data reduction was carried out on the Cambridge and Rutherford Nodes of the STARLINK Network, and I thank Jim Peden for his help with ASTERIX. The new observations in Chapters 2 and 3 were carried out using the Isaac Newton Telescope on the island of La Palma, which is operated by the Royal Greenwich Observatory at the Spanish Observatorio del Roque de los Muchachos of the Instituto de Astrofisica de Canarias. Chapter 5 is based partly on observations collected at the European Southern Observatory, La Silla, Chile. Chapter 6 is based partly on observations by the *International Ultraviolet Explorer* collected at the Villafranca Tracking Station of the European Space Agency and at the Goddard Space Flight Center of the National Aeronautics and Space Administration. The author was supported by a Science and Engineering Research Council postgraduate studentship throughout the preparation of this thesis.